Oceanologia

Official Journal of the Polish Academy of Sciences: Institute of Oceanology and Committee on Maritime Research

This journal is supported by the Ministry of Science and Higher Education, Warsaw, Poland

Indexed in: ISI Journal Master List, Science Citation Index Expanded, Scopus, Current Contents, Zoological Record, Thomson Scientific SSCI, Aquatic Sciences and Fisheries Abstracts, DOAJ

IMPACT FACTOR ANNOUNCED FOR 2017 IN THE 'JOURNAL CITATION REPORTS' IS 1.614; 5-year IF is 1.585

Publisher
Elsevier Sp. z o.o.
22, Jana Pawła II Avenue
00-133 Warsaw, Poland

Associate Publisher
Justyna Kasprzycka
j.kasprzycka@elsevier.com
+31 20 485 3846

ISSN 0078-3234

Oceanologia (2018) 60, 431—445

Available online at www.sciencedirect.com

ScienceDirect

journal homepage: www.journals.elsevier.com/oceanologia/

ORIGINAL RESEARCH ARTICLE

Deposition, return flux, and burial rates of nitrogen and phosphorus in the sediments of two high-Arctic fjords

Katarzyna Koziorowska *, **Karol Kuliński**, **Janusz Pempkowiak**

Institute of Oceanology, Polish Academy of Sciences, Sopot, Poland

Received 4 April 2018; accepted 4 May 2018
Available online 18 May 2018

KEYWORDS
Hornsund;
Kongsfjorden;
Sedimentary nitrogen and phosphorus;
Pore water;
Concentrations;
Nutrients

Summary The aim of this study was to determine the burial rates of nitrogen (N) and phosphorus (P) in the sediments of two high-latitude fjords: Hornsund and Kongsfjorden (Spitsbergen). Both deposition to sediments and the return flux from sediments to the water column of the various species of these elements were, therefore, quantified. The burial rate was then calculated as the difference between deposition and return flux. The required concentrations of N and P species were measured in surface sediments, in pore water extracted from the sediments, and in the above-bottom water at sampling stations situated along the axes of the fjords.

Annual deposition to sediments ranged between 2.3—8.3 g m^{-2} for N and 0.9—2.8 g m^{-2} for P. The nitrogen return fluxes ranged from 0.12 to 1.46 g m^{-2} y^{-1}. At most stations, the N flux was predominantly of dissolved organic (about 60—70%) rather than inorganic N. The P return flux varied between 0.01 and 0.11 g m^{-2} y^{-1}, with organic species constituting 60—97%. The N and P burial rates differed between fjords: 2.3—7.9 g N m^{-2} y^{-1} and 0.9—2.8 g P m^{-2} y^{-1} in Hornsund vs. 0.9—1.3 N g m^{-2} y^{-1} and 1.0—1.2 g P m^{-2} y^{-1} in Kongsfjorden. This was accompanied by a different efficiency of N and P burial — higher in Hornsund than in Kongsfjorden, in both cases. This suggests differences in the quality and quantity of N and P organic species deposited to sediments and therefore differences in the intensity of their mineralization and/or decomposition.

* Corresponding author at: Institute of Oceanology Polish Academy of Sciences, Powstańców Warszawy 55, Sopot, Poland. Tel.: +48 587311931.
E-mail address: kkozio@iopan.gda.pl (K. Koziorowska).
Peer review under the responsibility of Institute of Oceanology of the Polish Academy of Sciences.

Production and hosting by Elsevier

https://doi.org/10.1016/j.oceano.2018.05.001

1. Introduction

Nitrogen (N) and phosphorus (P) limit or co-limit primary production in the global ocean (Moore et al., 2013; Tremblay et al., 2015). Some of the substances containing these elements are deposited to surface sediments, whether as organic or inorganic compounds. The differences in the chemical and physical forms (species) of these substances reflect their different sources. Inorganic species are mostly transported by river runoff, as a result of weathering and anthropogenic activity and/or from the exoskeletons or skeletons of dead marine organisms. In sediments, N is bound in organic substances or occurs as lattice-bound ammonium in clay minerals (Knies et al., 2007), while P is usually present as loosely sorbed phosphate (PO_4^{3-}), iron-bound PO_4^{3-}, authigenic fluorapatite, detrital P, and organic P (Ruttenberg and Goni, 1997). Organic matter (OM) formed during autochthonous production and/or supplied from land is important form of N and P in sediments. Terrestrial OM may be fresh, produced recently on land, or ancient, mobilized by the melting and thawing of the permafrost. Hence, the processes related to OM production, mineralization, and transformation shape the pools of inorganic N and P species in the water column and thus primary production as well. The short loops between the organic and inorganic forms of N and P are strongly evidenced in productive coastal zones, where the inventories of both are supplemented by return fluxes from the sediments (Benitez-Nelson, 2000; Cloern, 2001; Nixon, 1995).

Global warming and its consequences are becoming increasingly evident, especially in the Arctic, where the respective changes have come early and are of particular intensity. Shifts such as a significant reduction in the amount of sea ice extent or, in some parts of the high Arctic, even the complete disappearance of sea ice, have increased the amount of irradiance reaching the water column and therefore the level of primary production (Fernandez-Mendez et al., 2015; Polyakov et al., 2017). Since it is known that, in the Arctic, N is the main element limiting production (Reigstad et al., 2002; Tremblay et al., 2015), studies on the cycling and origin of N have become particularly important.

Despite the many studies on OM cycling in the Arctic Ocean and especially in its fjords, very little is known about N and P deposition and burial in bottom sediments. Sedimentary N is usually analyzed as total nitrogen, without distinguishing between inorganic and organic forms, while phosphorus in sediments has been generally neglected (Carroll et al., 2008; Kim et al., 2011; Koziorowska et al., 2016; Kuliński et al., 2014; Zaborska et al., 2006, 2016). Moreover, investigations into N accumulation and burial rates in fjord sediments usually do not take into account the fraction of organic N that undergoes mineralization and/or hydrolysis in surface sediments and returns to the water column in the form of dissolved compounds. The only available results for the Svalbard region are those of Blackburn et al. (1996) and according to that study, only ~23% of the organic N deposited in surface sediments remains there, which suggests that sediments are a significant source of N in the water column. However, there are no published data on the burial of P in the sediments of the Svalbard region, nor on the return fluxes of phosphates from bottom sediments to the water column. In other regions, sediments were shown to be an important sink for P (burial), although some fraction of sedimentary P diffuses back into the water column in the form of bioavailable PO_4^{3-} (Filippelli, 2001; Rydin et al., 2011; van der Zee et al., 2002).

The goal of this study was to quantify the burial rates of N and P in the surface sediments of two high-latitude fjords located on the west coast of Spitsbergen: Hornsund and Kongsfjorden. This was achieved by measuring the concentrations of total N and total P (TN, TP), organic N and P (ON, OP) and inorganic N and P (IN, IP) in the surface sediments, pore water, and in the seawater overlying the sediments in samples acquired at four sampling stations in Hornsund and three in Kongsfjorden. The stations were situated along the axes of the respective fjords. The return fluxes of both dissolved organic nitrogen (DON) and dissolved organic phosphorus (DOP) as well as inorganic forms of N and P, including nitrate (NO_3^-), nitrite (NO_2^-), and phosphate (PO_4^{3-}) were calculated based on diffusion from the pore water to the bottom water using the Fick's first law of diffusion. N and P burial rates were calculated as the difference between the accumulation in the sediments and the return flux. The results presented in this report supplement those of studies on the deposition and burial of carbon in the same region (Koziorowska et al., 2018).

2. Study area

The study area was already described in sufficient detail by Koziorowska et al. (2018). The important features as regards the study subject are as follows. Both fjords are situated on the west coast of Spitsbergen. Hornsund is the southernmost, medium-size fjord with a complex coastline (Beszczyńska-Moller et al., 1997; Blaszczyk et al., 2013). The largest bay – Brepollen is situated in the innermost part of the fjord and isolated from the central basin by an underwater riffle and the Treskelen Peninsula. Hornsund is influenced by two main current systems: the coastal Sørkapp Current and the West Spitsbergen Current (WSC; Piechura et al., 2001; Promińska et al., 2017). The sediments are composed of sandy mud and mud (Drewnik et al., 2016), with a maximum OC concentration ~20 mg g^{-1} at the inner part of the fjord (Koziorowska et al., 2016; Zaborska et al., 2016). Primary production ranges from 120 to 220 g C m^{-2} y^{-1} (Piwosz et al., 2009; Smoła et al., 2017).

Kongsfjorden, located on the northwestern Spitsbergen coast, is a relatively small fjord, divided into two parts by a chain of islands (Lovénøyane). The outer part is strongly affected by the WSC whereas the inner part is under the influence of tidewater glaciers (Promińska et al., 2017; Svendsen et al., 2002). The large supply of mineral material, arriving with the freshwater from melting glaciers, snow and ice in summer, accounts for the relatively high sediment accumulation rates (SAR). The surface sediments are composed of fairly uniform mud (Włodarska-Kowalczuk and Pearson, 2004), with a sedimentary OC concentrations from 1 to 20 mg g^{-1} (Koziorowska et al., 2017). Annually, primary production is in the range of 20 and 50 g C m^{-2} (Piwosz et al., 2009; Smoła et al., 2017).

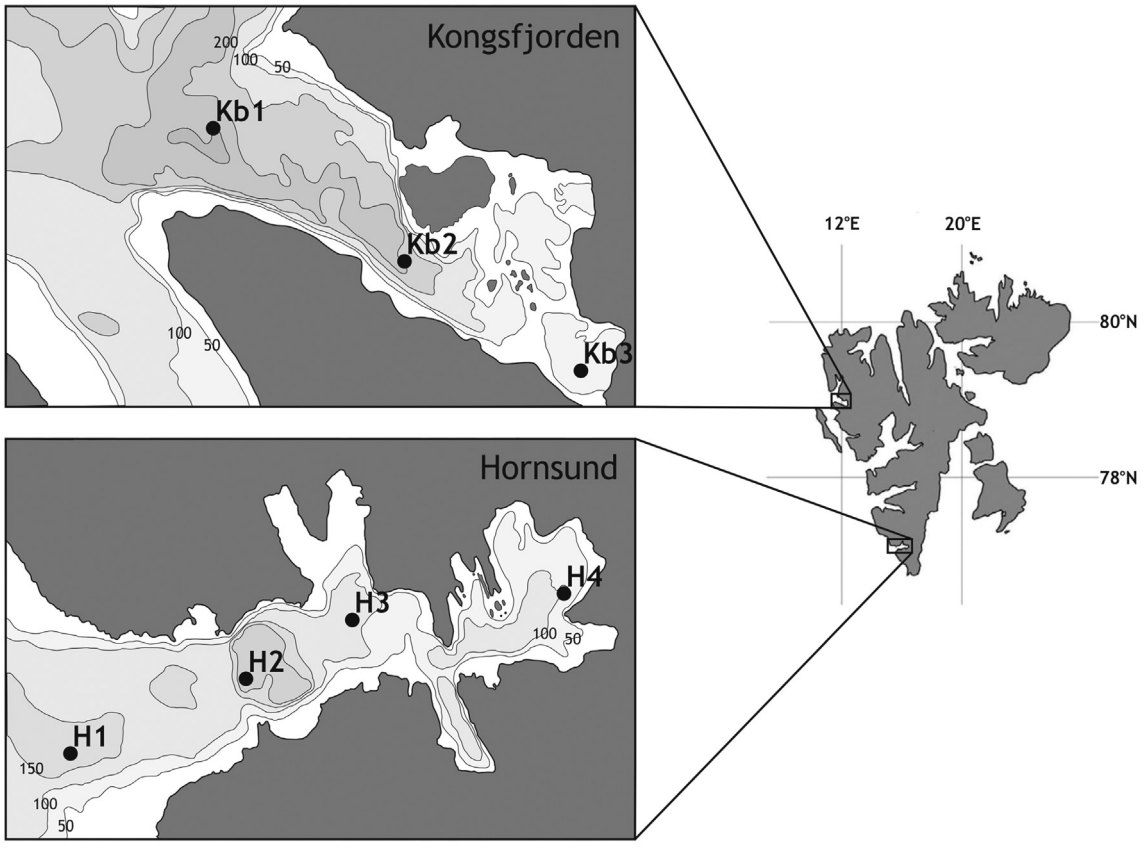

Figure 1 Locations of the sampling stations in Hornsund and Kongsfjorden.

3. Experimental

3.1. Sampling

Surface sediments were collected using a Nemisto gravity corer from onboard the r/v "Oceania" in the summers of 2015 and 2016. Samples were obtained from seven stations: H1, H2, H3, and H4, representing the outer, central, inner, and glacial (Brepollen) parts of Hornsund, and Kb1, Kb2, and Kb3 — the outer, central, and inner parts of Kongsfjorden (Fig. 1). At each sampling station, two undisturbed sediment cores were collected and then combined to increase the amount of material for further analyses. The bottom water overlying the sediment (5 cm above the sediment surface — to avoid collecting pore water caused by possible sediment resuspension) was sampled using a pre-cleaned syringe for nutrients ($N\text{-}NO_2^-$, $N\text{-}NO_3^-$, $P\text{-}PO_4^{3-}$) and DOC analyses. The topmost parts of the sediment cores (0—3 cm) were then sliced into 10-mm-thick layers and frozen (−20°C). In the laboratory, sediment samples were centrifuged (15 min, 5000 g) and the resulting pore water was analyzed for $N\text{-}NO_2^-$, $N\text{-}NO_3^-$, $P\text{-}PO_4^{3-}$ and DOC. Residual sediments were freeze-dried, homogenized, and analyzed for total, organic, and inorganic concentrations of N and P species. All analyses were carried out at the Marine Biogeochemistry Laboratory of the Institute of Oceanology of the Polish Academy of Sciences (Sopot, Poland), using the methods described below.

3.2. Analyses of total, organic, and inorganic nitrogen and phosphorus in sediment samples

Total N and inorganic N (bound as ammonium to fine-grained sediments) were analyzed in an elemental analyzer (Flash EA 1112 series) combined with a Delta V Advantage isotopic ratio mass spectrometer (IRMS; Thermo Electron Corp., Germany). For both TN and IN, ~50 mg (10-μg accuracy) of freeze-dried and homogenized sediment was weighed into silver capsules. The IN sediment samples were first treated with a KOBr-KOH solution to remove ON, according to the method described by Silva and Bremner (1966). Quantitative measurements of TN were calibrated against certified reference materials (marine sediments) provided by HEKAtech GmbH (Germany). The precisions of the TN and IN measurements, reported as the relative standard deviations (RSDs), were better than ±1.7% and ±2.4% (n = 5), respectively. The ON concentration was calculated as the difference between the TN and IN concentrations.

Total P and IP concentrations were measured using a spectrophotometer (TECAN, Switzerland) and the ammonium molybdate method after digestion of the sediment samples according to the procedure described by Aspila et al. (1976). Briefly, the samples for TP analysis were combusted in a muffle furnace at 550°C for 5 h and then extracted with 1 M HCl for 16—18 h. Samples for IP were analyzed as described for TP except the combustion step was omitted. The measurements were calibrated against certified refer-

ence materials (river sediment) provided by BCR® (Community Bureau of Reference, Belgium). The precisions of the TP and IP measurements, reported as the RSDs, were ±4.2% and ±3.8% (n = 5), respectively. The OP concentration was calculated as the difference between the TP and IP concentrations.

3.3. Analyses of dissolved nitrogen and phosphorus species in water samples

3.3.1. Nitrites (N-NO_2^-), nitrates (N-NO_3^-), and phosphates (P-PO_4^{3-})

Nutrient (nitrite, nitrate, and phosphate) concentrations were analyzed colorimetrically on a Dr 2800 spectrophotometer (Hach-Lange, Germany) using the methods described in detail by Strickland and Parsons (1967) and by Salley et al. (1986). The accuracy of the nutrients analyses was confirmed by measurements of certified reference material (RM-BU; National Metrology Institute of Japan). The precisions (RSDs) were ±1.5% for N-NO_2^-, ±1.2% for N-NO_3^-, and ±1.6% for P-PO_4^{3-}.

3.3.2. Dissolved organic carbon (DOC), dissolved organic nitrogen (DON) and dissolved organic phosphorus (DOP)

DOC analyses were carried out using a TOC-L analyzer (Shimadzu Corp., Japan) and a high-temperature (680°C) oxidation method performed in the presence of Pt catalyst. Quality control was based on measurements of reference material (North Atlantic water, obtained from the Hansell Laboratory). The precision (RSD) was ±0.8%; n = 5.

DON and DOP concentrations were calculated from the measured DOC concentrations and the DOC/DON or DOC/DOP ratios characteristics of pore water in marine sediments. The average values of these ratios, as reported in the available literature, were 14.1 ± 3.7 for DOC/DON (Alkhatib et al., 2012, 2013; Burdige, 2001; Burdige and Komada, 2015; Burdige and Zheng, 1998; Lomstein et al., 1998) and 407.0 ± 183.8 for DOC/DOP (Loh and Bauer, 2000; Tremblay et al., 2014; Yasui et al., 2016). As there are no literature data for the DOC/DOP ratio in pore water, we used the results reported for the water column. For each pore water sample, both the range and the average results were calculated (Fig. 3). However, for further calculations of the return fluxes and burial rates only the average values were used.

3.4. Calculations

3.4.1. Nitrogen and phosphorus deposition to sediments

The deposition of N and P, both inorganic and organic, in sediments was calculated as the product of the sediment mass accumulation rate (MAR) and the ON, IN, OP, and IP concentrations in the sediment layers. The MAR values for each sampling station were those reported in the literature (Koziorowska et al., 2017, 2018; Zaborska, 2017) (Table 1).

3.4.2. Nitrogen and phosphorus return fluxes

The diffusion of dissolved N and P species from the sediments into the overlying bottom seawater was estimated based on Fick's first law of diffusion (Ullman and Aller, 1982).

$$J_x = -\varphi \times D_{sed} \times \frac{\Delta c}{\Delta x},$$

where J_x is the diffusion flux of x [N-NO_2^-, N-NO_3^-, P-PO_4^{3-}, DON, or DOP; μg cm^{-2} s^{-1}]; φ is the porosity of the sediment, D_{sed} is the specific sediment diffusion coefficient for NO_2^-, NO_3^-, PO_4^{3-}, DON, or DOP [cm^2 s^{-1}], and $\Delta c/\Delta x$ is the N-NO_2^-, N-NO_3^-, P-PO_4^{3-}, DON, or DOP concentration gradient between the pore water of the surface-most sediment layer and the seawater overlying the sediments [μg cm^{-3}/cm].

The D_{sed} values used in the calculations were derived from the literature and corrected for temperature and sediment porosity according to Boudreau (1997) and Holcombe et al. (2001): 5.54×10^{-6} cm^2 s^{-1} for NO_2^- and NO_3^-, 1.53×10^{-6} cm^2 s^{-1} for PO_4^{3-}, and 1.22×10^{-6} cm^2 s^{-1} for DON and DOP. Since, under oxic conditions, ammonium is oxidized to nitrate, its presence and release from the oxic surface-most sediment layer is unlikely (see Chapter 5.1 for the subject discussion; Glud et al., 1998; Kotwicki et al., 2018) and, therefore, ammonium was disregarded in the analyses described herein.

3.4.3. Burial rates of total nitrogen (TN_{BR}) and total phosphorus (TP_{BR})

TN_{BR} (or TP_{BR}) were calculated as the difference between TN (or TP) deposition in the surface-most sediments and the sum of the return fluxes of N-NO_2^-, N-NO_3^-, and DON for TN_{BR} or P-PO_4^{3-} and DOP for TP_{BR}.

Table 1 Sediment mass accumulation rates (MAR) at the investigated sampling stations.

Station	MAR [g m^{-2} y^{-1}]	Reference
H1	1310	Koziorowska et al. (2018)
H2	2330	Koziorowska et al. (2018)
H3	3070	Zaborska (2017)
H4	6250	Zaborska (2017)
Kb1	1160	Koziorowska et al. (2018)
Kb2	1950	Koziorowska et al. (2018)
Kb3	–[a]	Koziorowska et al. (2017)

[a] See Chapter 4.2 for details.

Table 2 Concentrations [mg g^{-1}] of sedimentary nitrogen: total (TN), organic (ON), and inorganic (IN) and sedimentary phosphorus (TP, OP and IP) in the top-most (0–3 cm) sediment layer.

Station	Concentrations in sediments [mg g^{-1}]					
	TN	ON	IN	TP	OP	IP
H1	2.22	1.49	0.72	0.69	0.30	0.39
H2	1.94	1.26	0.68	0.63	0.23	0.40
H3	1.38	0.67	0.72	0.48	0.15	0.33
H4	1.33	0.47	0.86	0.45	0.14	0.30
Kb1	2.37	2.15	0.23	0.97	0.25	0.72
Kb2	1.19	1.07	0.12	0.68	0.18	0.51
Kb3	0.35	~0.35[b]	<LOD[a]	0.21	0.03	0.18

[a] LOD: limit of detection (LOD: 0.01 mg g^{-1}).
[b] Difference between TN and IN (<LOD).

4. Results

4.1. Nitrogen and phosphorus concentrations

4.1.1. Sedimentary N and P concentrations

The TN concentrations in the surface sediments of Hornsund and Kongsfjorden were 1.33–2.22 mg g^{-1} and 0.35–2.37 mg g^{-1}, respectively (Table 2), and they increased towards the mouths of the fjords. The spatial distribution of the ON concentration was similar to that of TN, with higher concentrations measured at outer regions (1.49 mg g^{-1} and 2.15 mg g^{-1}, respectively) and lower concentrations at inner regions (0.47 mg g^{-1} and 1.07 mg g^{-1}, respectively). By contrast, there was no distinct spatial difference in the IN concentrations measured at stations within the fjords, although the values were significantly higher in Hornsund (0.68–0.86 mg g^{-1}) than in Kongsfjorden (ranging from below the limit of detection [LOD] to 0.23 mg g^{-1}). The TN, ON, and IN concentrations determined in this study were close to those previously reported for the sediments of Arctic fjords. Specifically, TN, ON, and IN concentrations of 0.5–3.7 mg g^{-1}, 0.2–2.9 mg g^{-1}, and 0.2–1.0 mg g^{-1}, respectively, were measured by Knies et al. (2007), 0.5–1.5 mg g^{-1}, 0.3–0.9 mg g^{-1}, and 0.2–0.6 mg g^{-1} by Schubert and Calvert (2001), and 0.7–4.7 mg g^{-1}, 0.4–3.4 mg g^{-1}, and 0.2–1.3 mg g^{-1} by Winkelmann and Knies (2005).

As was the case for the TN and ON concentrations, the concentrations of all P fractions increased towards the mouths of the fjords (Table 2). TP, OP, and IP concentrations were 0.45–0.69 mg g^{-1}, 0.14–0.30 mg g^{-1}, and 0.30–0.40 mg g^{-1}, respectively, in Hornsund and 0.21–0.97 mg g^{-1}, 0.03–0.25 mg g^{-1}, and 0.18–0.72 mg g^{-1} in Kongsfjorden. Slightly higher TP and IP concentrations were measured in Kongsfjorden than in Hornsund. Unlike N, the inorganic P fraction predominated over the organic P fraction. In the only report on sedimentary P in Kongsfjorden (Zhu et al., 2014) available to us, IP concentrations were similar (0.01–0.6 mg g^{-1}) while those of TP and OP were higher (0.2–5.9 mg g^{-1} and 0.01–5.9 mg g^{-1}, respectively).

4.1.2. N and P concentrations in pore and sea water

The concentrations of the measured nutrients in pore water are presented in Fig. 2, and those of the dissolved species of organic C, N, and P – in Fig. 3. The measured N-NO_2 concentrations were generally low and did not exceed 0.1 mg L^{-1}. Concentrations were highest at stations located in the outer parts of the fjords, and were especially high in the pore water extracted from the surface-most layers (Fig. 2a, b, e, and f), while concentrations were much lower in the inner regions (Fig. 2c, d and g). Significantly higher concentrations, reaching 2.0–3.0 mg L^{-1}, were measured for N-NO_3^-. This was observed at all stations except H4 and Kb3, located close to the glacier fronts, where N-NO_3^- concentrations did not exceed 0.20 mg L^{-1}. At all stations, the highest N-NO_3^- concentrations occurred in the surface-most sediment layers and the lowest concentrations in the deeper layers (except stations H1 and Kb1; Fig. 2a and e). These are typical nitrate concentration profiles for surface sediments, where oxic conditions prevail (Schulz and Zabel, 2006). The measured concentrations were higher than the 0.5 mg NO_3^- L^{-1} previously reported for the Arctic region by several teams (Blackburn et al., 1996; Gihring et al., 2010; Hulth et al., 1996; Rysgaard et al., 1998; Thibodeau et al., 2010).

Similarly to nitrates and nitrites, higher concentrations of phosphates (P-PO_4^{3-}) were measured in the outer and central parts of both fjords (up to 0.9 mg L^{-1}; Fig. 2). The vertical distribution of P was more diverse than that of N, as P concentrations decreased towards the sediment surface at stations H1, H3, H4, Kb1, and Kb3. These profiles were in agreement with the PO_4^{3-} concentrations in pore waters reported in the literature (Schulz and Zabel, 2006). However, at stations H2 and Kb2, located in the central part of the fjords, the profiles of P-PO_4^{3-} were reversed and phosphate concentrations decreased with increasing depth (Fig. 2b and f). This reversed gradient of concentrations may suggest more intense organic matter mineralization in surface sediments caused by a larger contribution of fresh OM at these stations, caused by a local increase of primary production or organic matter preferential deposition. The hypothesis is supported by a higher return flux of dissolved inorganic carbon there (Koziorowska et al., 2018). However, further research is required to explain the phenomenon exclusively.

Wide ranging DON and DOP concentrations were found in the pore water of the two fjords (Fig. 3). Like the inorganic fractions, DON and DOP concentrations were higher at stations in the outer and central parts (4.5–23.4 mg L^{-1} and 0.4–1.8 mg L^{-1}, respectively). The low DON and DOP concentrations in the inner parts of the fjords (0.4–5.4 mg L^{-1} and 0.0–0.4 mg L^{-1}, respectively) may have been caused by the proximity of glaciers. Regions characterized by a high freshwater supply usually have lower rates of primary production and thus a smaller supply of fresh OM for deposition to the sediment surface. This is due to the high turbidity of the land-derived, mineral-rich, material discharged in large amounts by glaciers and river runoff, especially during the ablation season in the summer and early autumn (Moskalik et al., 2018). Typically, the concentration of dissolved constituents originating from mineralization and hydrolysis should decrease towards the sediment surface (Alkhatib et al., 2013; Blackburn et al., 1996; Winogradow and Pempkowiak, 2014; Yasui et al., 2016). However, at the investigated stations, the DON and DOP concentrations varied

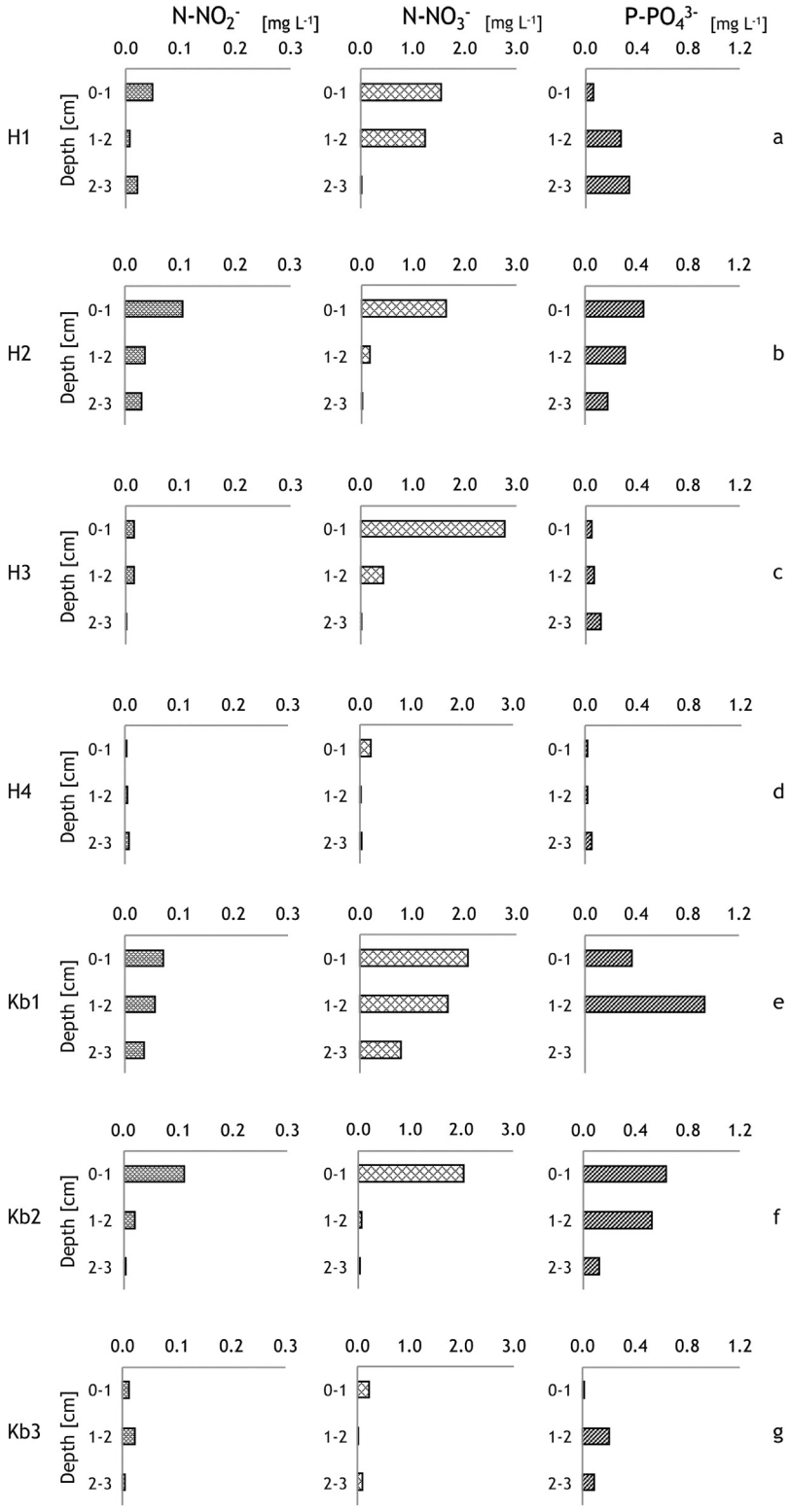

Figure 2 Concentrations of nitrites ($N\text{-}NO_2^-$), nitrates ($N\text{-}NO_3^-$), and phosphates ($P\text{-}PO_4^{3-}$) in the pore water of the surface sediment layers (0—3 cm) at stations (a) H1, (b) H2, (c) H3, (d) H4, (e) Kb1, (f) Kb2, and (g) Kb3.

widely. At stations H1, Kb1 and Kb2 the values decreased towards the surface while at the other stations they increased, which suggested a difference in the quality of the OM supplied to the sediments.

Nutrients (nitrites, nitrates, and phosphates) concentrations were significantly lower in the seawater overlying the sediments than in the pore waters (Table 3). $N\text{-}NO_2^-$ concentrations were below the LOD for all sampling stations, N-

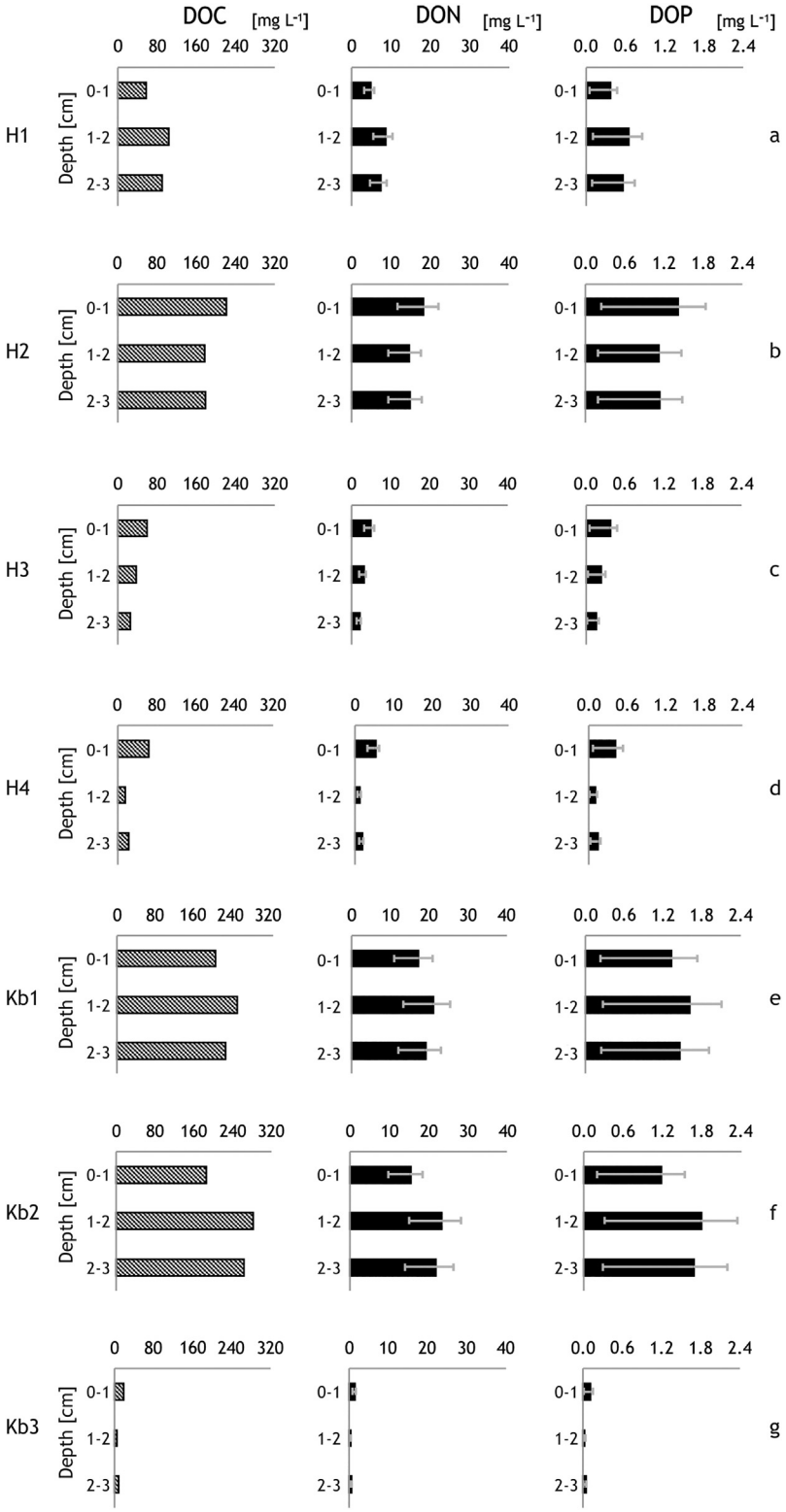

Figure 3 Concentrations of dissolved organic carbon (DOC), dissolved organic nitrogen (DON), and dissolved organic phosphorus (DOP) in the pore water of the surface sediment layers (0—3 cm) at stations (a) H1, (b) H2, (c) H3, (d) H4, (e) Kb1, (f) Kb2, and (g) Kb3. The error bars represent the uncertainty resulting from the use of DOC/DON and DOC/DOP molar ratios to calculate DON and DOP concentrations (see Section 3.3.2 for details).

Table 3 Concentrations [mg L^{-1}] of nitrites ($N\text{-}NO_2^-$), nitrates ($N\text{-}NO_3^-$), phosphates ($P\text{-}PO_4^{3-}$), dissolved organic carbon (DOC), dissolved organic nitrogen (DON) and dissolved organic phosphorus (DOP) in the seawater overlying the sediments.

Station	Concentrations in water [mg L^{-1}]					
	$N\text{-}NO_2^-$	$N\text{-}NO_3^-$	$P\text{-}PO_4^{3-}$	DOC	DON	DOP
H1	<LOD[a]	0.05	0.02	1.90	0.16	0.01
H2	<LOD[a]	0.02	0.02	0.84	0.07	0.01
H3	<LOD[a]	0.05	0.04	1.16	0.10	0.01
H4	<LOD[a]	0.03	0.01	1.34	0.11	0.01
Kb1	<LOD[a]	0.02	0.02	1.09	0.09	0.01
Kb2	<LOD[a]	0.02	0.03	2.28	0.19	0.01
Kb3	<LOD[a]	0.03	0.01	1.60	0.13	0.01

[a] LOD: limit of detection.

NO_3^- varied between 0.02 and 0.05 mg L^{-1}; and $P\text{-}PO_4^{3-}$ ranged from 0.02 to 0.04 mg L^{-1}. These concentrations in the overlying seawater were close to those previously measured in the bottom water of the Arctic Ocean (Blackburn et al., 1996; Gihring et al., 2010; Thibodeau et al., 2010). For the organic fractions, the average concentrations varied between 0.09 and 0.19 mg L^{-1} for DON and ~0.01 mg L^{-1} for DOP. For all dissolved species of C, N, and P (both organic and inorganic) investigated in this study, the differences between the two fjords and the different stations were not significant.

4.2. Deposition rates of nitrogen and phosphorus

4.2.1. Sediment dating

The data indicated a steep gradient along the fjord axis, with low MARs in the outer parts and high MARs in the inner parts of both fjords (Table 1). At station Kb3, the MAR could not be determined due to sedimentation rates that were too fast to be determined using the radiolead method. The differences in the MARs along the axes of the two fjords indicated suspended matter loads differing in their intensity due to differences in their proximity to the sources of the sedimentary material, i.e., glacier fronts and/or rivers.

4.2.2. Deposition of inorganic and organic N and P to sediments

Recent annual rates of total (TN_{AR}), organic (ON_{AR}) and inorganic (IN_{AR}) nitrogen deposition as well as total (TP_{AR}), organic (OP_{AR}) and inorganic (IP_{AR}) phosphorus deposition are presented in Fig. 4. Despite the lower TN concentrations in the surface sediments of the inner stations in Hornsund (Table 2), the high MARs resulted in an increasing TN_{AR} towards the inner part of the fjord (from 2.9 g m^{-2} y^{-1} at H1 to 8.3 g m^{-2} y^{-1} at H4; Fig. 4a). In Kongsfjorden, despite the differences in the MAR and TN concentrations, the TN_{AR} was relatively constant: 2.8 g m^{-2} y^{-1} at Kb1 and 2.3 g m^{-2} y^{-1} at Kb2 (Fig. 4c). In spite of the variance of MARs, ON_{AR} values measured at the two fjords were quite similar, ranging between 2.0 and 2.9 g m^{-2} y^{-1} in Hornsund and between 2.1 and 2.5 g m^{-2} y^{-1} in Kongsfjorden. Moreover, the organic fraction accounted for up to 90% of the total amount of N deposited in the surface sediments of Kongsfjorden, whereas in Hornsund the contribution varied between 35% and 67%. The gradual decrease in the share with increasing proximity to the inner part of the fjord indicated an important role for autochthonous production in the supply of ON. The pattern of IN_{AR} was similar to that of TN_{AR}. Thus, in Hornsund the annual rates increased with increasing distance from the fjord entrance (from 0.9 g m^{-2} y^{-1} at H1 to 2.8 g m^{-2} y^{-1} at H4), while in Kongsfjorden there was a slight decrease in the annual rate (from 0.3 g m^{-2} y^{-1} at Kb1 to 0.2 g m^{-2} y^{-1} at Kb2). These results are consistent with those reported previously by Rysgaard et al. (1998), who estimated TN_{AR} in the Svalbard fjords sediments at 5.6 g m^{-2} y^{-1}, a rate significantly higher than the TN_{AR} reported by Muzuka and Hillaire-Marcel (1999) for the Eastern Canadian Margin (0.06–0.2 g m^{-2} y^{-1}).

Similarly, TP_{AR} values increased along the axes of Hornsund and Kongsfjorden, from 0.9 g m^{-2} y^{-1} at station H1 to 2.8 g m^{-2} y^{-1} at station H4 and from 1.1 g m^{-2} y^{-1} at station Kb1 to 1.3 g m^{-2} y^{-1} at station Kb2, respectively (Fig. 4b, d). The contribution of OP_{AR} to TP_{AR} was much lower than was the case for N, accounting for only ~26% (~0.3 g m^{-2} y^{-1}) in Kongsfjorden and 32–43% (0.4–0.9 g m^{-2} y^{-1}) in Hornsund. However, as for N, the contribution decreased towards the fjord interior. The IP_{AR} values also differed along the fjord axis, with higher IP loads deposited in the inner and central parts (1.9 g m^{-2} y^{-1} and 1.0 g m^{-2} y^{-1} at H4 and Kb2, respectively) and lower loads in the outer region (0.5 g m^{-2} y^{-1} and 0.8 g m^{-2} y^{-1} at H1 and Kb1, respectively). This suggested a larger supply of IP from land and/or melting glaciers. Data on P accumulation rates in marine surface sediments are scarce. According to van der Zee et al. (2002), TP_{AR} in the NE Atlantic varies between 0.4 and 6.7 g m^{-2} y^{-1}, while Rydin et al. (2011) estimated TP_{AR} of 1.7–2.8 g m^{-2} y^{-1} in the Baltic Sea, and Yang et al. (2017) TP_{AR} of 1.9–6.4 g m^{-2} y^{-1} and OP_{AR} of 0.4–1.0 g m^{-2} y^{-1} in the East China Sea.

4.3. Return fluxes of nitrogen and phosphorus (N_{RF} and P_{RF})

Fick's first law of diffusion was applied to estimate the N and P return fluxes from the bottom sediments to the water column. The N return flux (N_{RF}) ranged from 0.43 to 1.38 g m^{-2} y^{-1} in Hornsund and from 0.12 to 1.46 g m^{-2} y^{-1} in Kongsfjorden (Table 4). In Hornsund, higher values were measured at the central stations (H2 and H3), and in Kongsfjorden at the outer and central stations (Kb1 and Kb2). For both fjords (except stations H1 and H3), the contribution of DON to the TN return flux was significant, amounting to 60–70% (0.07–0.97 g m^{-2} y^{-1}). This DON return flux (J_{DON}) was much lower than that reported by Blackburn et al. (1996) for Svalbard sediments (~4.8 g m^{-2} y^{-1}) and generally at the lower limits of the DON fluxes previously reported for other world regions, including Laholmm Bay, Sweden: 0.5–2.0 g m^{-2} y^{-1} (Enoksson, 1993), Chesapeake Bay: 0.2–2.8 g m^{-2} y^{-1} (Burdige and Zheng, 1998), and the Laurentian and Anticosti Channel, Canada: 0.6–2.2 g m^{-2} y^{-1} (Alkhatib et al., 2013). The diffusion flux of DIN (J_{DIN}) was 0.05–0.63 g m^{-2} y^{-1}, which is slightly lower than the fluxes deter-

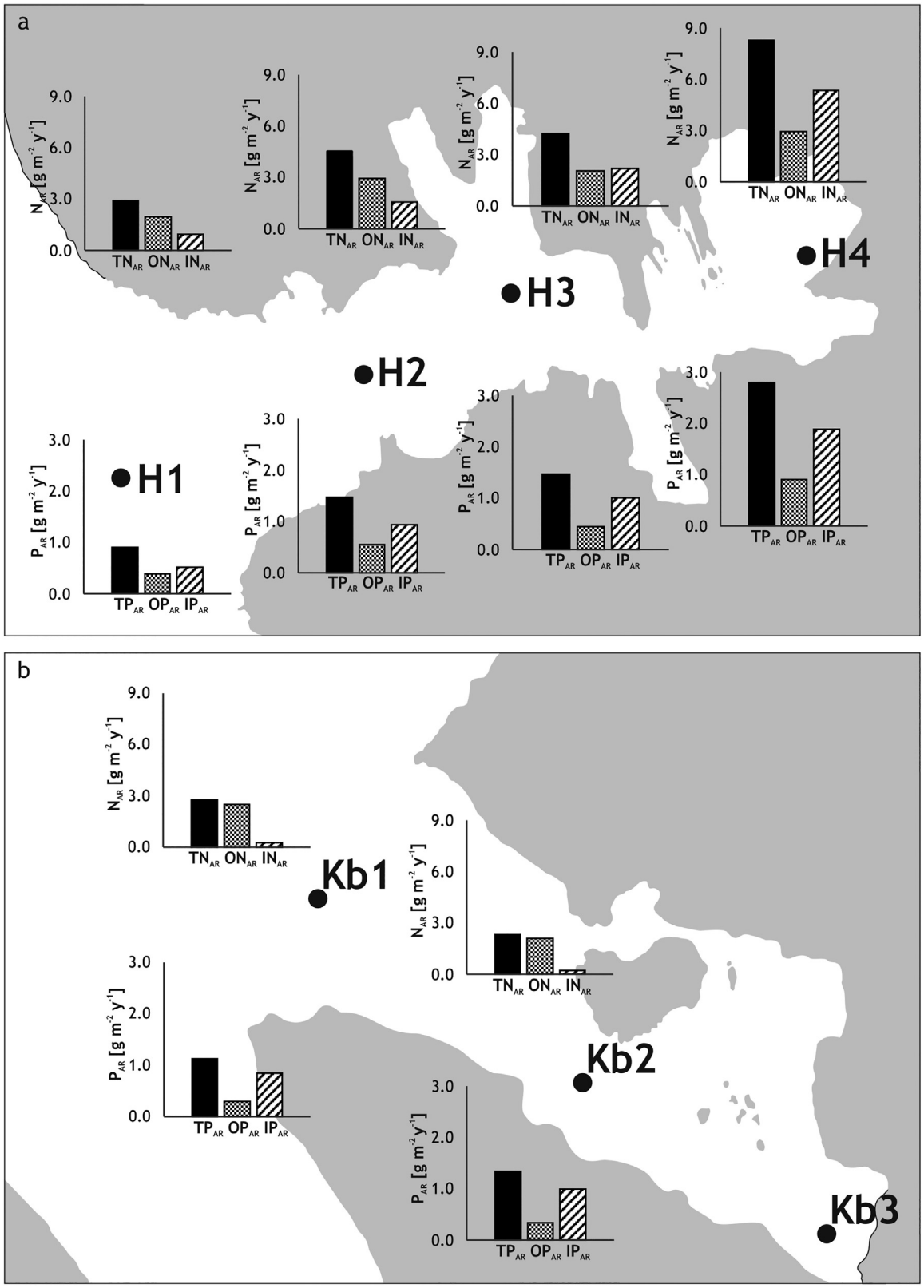

Figure 4 Recent deposition rates of nitrogen: total (TN_{AR}), organic (ON_{AR}) and inorganic (IN_{AR}), and of phosphorus: total (TP_{AR}), organic (OP_{AR}) and inorganic (IP_{AR}) at Hornsund (a) and Kongsfjorden (b). Deposition rates were not calculated at station Kb3.

Table 4 Porosity and the return fluxes (J) of dissolved nitrogen: inorganic (J_{DIN}), organic (J_{DON}) and total (N_{RF}); return fluxes of dissolved phosphorus: inorganic (J_{DIP}), organic (J_{DOP}) and total (P_{RF}).

Stations	Porosity	Return flux [g m^{-2} y^{-1}]					
		J_{DIN}	J_{DON}	N_{RF}	J_{DIP}	J_{DOP}	P_{RF}
H1	0.78	0.39	0.26	0.64	0.002	0.020	0.022
H2	0.76	0.41	0.97	1.38	0.029	0.074	0.103
H3	0.73	0.63	0.24	0.87	0.001	0.019	0.019
H4	0.76	0.15	0.28	0.43	0.001	0.021	0.022
Kb1	0.78	0.52	0.94	1.46	0.024	0.072	0.095
Kb2	0.81	0.55	0.86	1.41	0.043	0.066	0.109
Kb3	0.73	0.05	0.07	0.12	0.001	0.005	0.006

mined for the Svalbard sediments in the Arctic: ~0.7 g m^{-2} y^{-1} (Blackburn et al., 1996) and 0.9–2.0 g m^{-2} y^{-1} (Gihring et al., 2010).

The P return flux (P_{RF}) was much lower than N_{RF} and varied from 0.02 to 0.10 g m^{-2} y^{-1} in Hornsund and from 0.01 to 0.11 g m^{-2} y^{-1} in Kongsfjorden (Table 4). As for N, the highest P values were measured at stations H2, Kb1, and Kb2. In both fjords, the return flux of the organic P fraction accounted for 60–97% (0.02–0.07 g m^{-2} y^{-1}) of the annual TP return flux, while in many places the diffusion flux of DIP (J_{DIP}) was very low. While published data on the P return flux in the Arctic region are lacking, Yasui et al. (2016) estimated the J_{DOP} at Tokyo Bay, reporting a rate of 0.06 ± 0.06 g m^{-2} y^{-1}, close to the value obtained in this study. For P_{RF} our results are similar to those previously reported for the NE Atlantic (van der Zee et al., 2002) and East China Sea (Yang et al., 2017): 0.01–0.20 g m^{-2} y^{-1} and 0.04–0.40 g m^{-2} y^{-1}, respectively.

5. Discussion

The recent reduction in both the spatial extent and the duration of the ice cover in the Arctic Ocean has increased the annual availability of light. Together, these conditions may substantially increase primary production (Fernandez-Mendez et al., 2015). However, the presence of nutrients is also critical, as nitrogen, silica, and phosphorus may limit or co-limit primary production in seawater (Moore et al., 2013; Tremblay et al., 2015). For example, in the Arctic, IN species are the primary yield-limiting nutrient (Reigstad et al., 2002; Tremblay et al., 2002, 2008). Given the importance of nutrient availability for ecosystem functioning, the identification and quantification of nutrient sources have been the focus of considerable research. Benthic fluxes of N and P species from the sediment are an important but still awaiting quantification component of the respective marine cycles, and thus their determination seems of importance.

5.1. Sources of dissolved inorganic N and P species in pore water

In sediments where oxic conditions prevail, ammonia is quantitatively oxidized to nitrate. Below the oxygen penetration depth, where oxygen is depleted, denitrification reduces nitrates to dinitrogen (Schulz and Zabel, 2006). Basing on measurements in single cores Kotwicki et al. (2018) reported that in the Hornsund sediments oxygen penetrates to a depth of 1–2 cm, while in Kongsfjorden – to a depth of 2–3 cm. Within these sediment layers, ammonium is oxidized to nitrate and thus cannot be released from the sediment to the overlying water. Findings of Kotwicki et al. (2018) confirm results of earlier studies (Glud et al., 1998) on diffusive fluxes of NH_4^+ both from sedimentary anoxic zone into the oxic zone and from the sediments to bottom water to be ~0.1–0.5 mmol m^{-2} d^{-1} and 0 ± 0 mmol m^{-2} d^{-1}, respectively. This confirms that ammonia diffusing up from the deeper sediments is quickly nitrified in the oxic zone before it is released from sediments. Surface sediments were not considered a source of ammonia, even when traces of this nitrogen species (mostly in the range ~10–20 μmol L^{-1}) were found in pore water of the surface sediments (Gihring et al., 2010). Kotwicki et al. (2018) also determined rather steep oxygen concentration gradients in the sediment of both fjords, with oxygen saturation falling to below 25% already at a depth of 1.0–1.5 cm. These results correlate well with the distribution of NO_3^- determined in our studies. As oxygen was not measured in our study, we can only presume that the higher NO_3^- concentrations in the deeper sediment layers at stations in the outer parts of the fjords reflected the deeper penetration of oxygen into sediments there. It is worth noting that NO_3^- concentrations in pore waters were much higher than in the seawater overlying the sediments. It is, most likely, caused by organic matter mineralization as concentration of organic matter in sediments is orders of magnitude larger than concentration in bottom water. OM mineralization delivers huge loads of ammonia that is quickly oxidized to nitrate. Subsequently, some part of newly produced nitrate diffuses upward into the water overlaying sediments, and is immediately diluted in a large volume of seawater. Some part of the newly formed NO_3^- diffuses downward to be denitrified. Low NO_2^- concentrations, both in pore waters and bottom water, confirm the above described sequence of processes as NO_2^- is immediately oxidized to NO_3^-. In the case of phosphate, changes in its concentrations were likely caused by its release after previous adsorption to iron and manganese oxyhydroxides and carbonates. This could have occurred both by the anaerobic degradation of the OP adsorbed to the solid phase of sediments and/or reduction of insoluble Fe (III) and Mn (IV) oxy-hydroxides to soluble Fe (II) and Mn (II) species and releasing adsorbed, N and P containing organic compounds. Moreover, a different speciation of the IP that accumulated in the sediments cannot be overruled (Baldwin et al., 2001; Lehtoranta et al., 2015; Schulz and Zabel, 2006; Yasui et al., 2016).

5.2. Burial rates of total nitrogen (TN_{BR}) and total phosphorus (TP_{BR}) and their burial efficiencies

The return fluxes, burial rates, and efficiencies of the burial rates for N and P are presented in Fig. 5. For both TN_{BR} and TP_{BR}, the results differed between the fjords, with higher rates calculated for the Hornsund stations (2.3–7.9 g m^{-2} y^{-1} and 0.9–2.8 g m^{-2} y^{-1}, respectively) than for

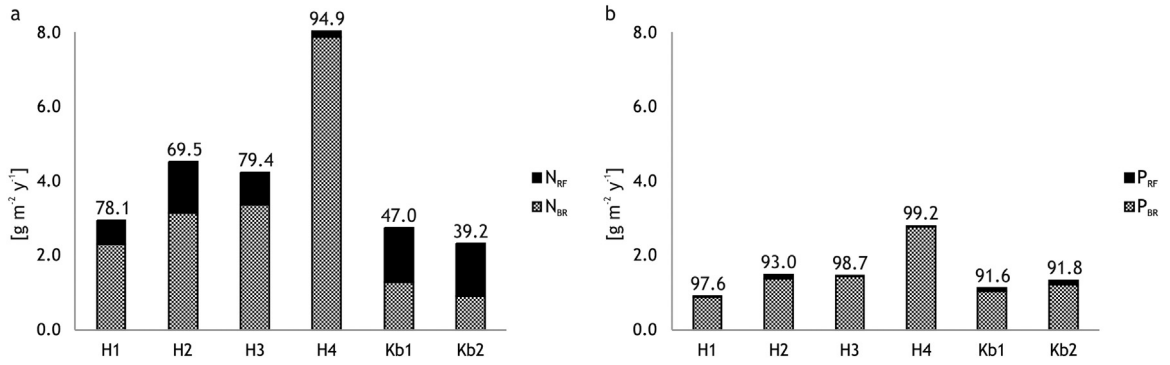

Figure 5 Return fluxes (RFs) and burial rates (BRs) of nitrogen (a) and phosphorus (b) in Hornsund and Kongsfjorden. Values above the bars are the burial efficiencies (%).

the Kongsfjorden stations (0.9–1.3 g m^{-2} y^{-1} and 1.0–1.2 g m^{-2} y^{-1}, respectively). The higher values in Hornsund suggest a larger OM supply from land and/or higher *in situ* production. The two explanations are equally likely, given the higher rate of primary production (Piwosz et al., 2009; Smoła et al., 2017) and greater contribution of terrestrial OM (Koziorowska et al., 2016; Zaborska et al., 2016) in Hornsund than in Kongsfjorden. Another possibility was a larger supply of inorganic species to the Hornsund sediments (higher MAR). Numerous studies (Comans et al., 1989; Muller, 1977; Schubert and Calvert, 2001) have shown that ammonium ions are preferentially fixed in illites, but Knies et al. (2007) reported that this is probably not the case for Spitsbergen sediments, where IN concentrations correlated negatively with the occurrence of illites. Alternative sources of IN are so far unknown, but may be of terrestrial origin. This would agree with the higher IN concentration and accumulation rate measured in Hornsund (especially at H4 station), where the contribution of terrigenous material was higher than in other areas (Koziorowska et al., 2016; Zaborska et al., 2016).

Generally, the burial efficiency determined in our study was much higher for P (92–99%) than for N (39–95%). During OM decomposition, P is released to the pore water in the form of phosphate and diffuses as a return flux to the overlying water. However, phosphates can also be retained in sediments, whether adsorbed to clay minerals, transformed to authigenic carbonate fluorapatite, or bound to iron oxyhydroxides (Cha et al., 2005; Ruttenberg and Goni, 1997; van der Zee et al., 2002). Retention can significantly reduce the return flux of P from sediments and increase the efficiency of P burial. In addition to the different efficiencies of N and P burial, the difference between the two fjords was significant, with the generally lower values in Kongsfjorden (39.2–47.0% for TN and 91.6–91.8% for TP) than in Hornsund (69.5–94.9% and 93.0–99.2%, respectively), indicating a more effective mineralization and/or decomposition during the early stage of diagenesis and therefore a higher return flux from the sediments to the water column. This may have been due to differences in the quality of the OM deposited to the sediments. Literature data (Koziorowska et al., 2016; Zaborska et al., 2016) indicated that Kongsfjorden sediments contain much more marine OM than do Hornsund sediments. Marine OM is considered to be more available for benthic organisms and more efficiently degraded in sediments. In addition, diagenetic processes may be influenced by the oxygen content in the sediments. According to Kotwicki et al. (2018), the slightly deeper oxygen penetration of Kongsfjorden sediments may enhance aerobic mineralization, which is probably more efficient than anoxic mineralization (Schulz and Zabel, 2006). At station H4, the TN_{BR} and TP_{BR} were higher than at any other station (7.9 g m^{-2} y^{-1} and 2.8 g m^{-2} y^{-1}, respectively) as were the efficiencies of N and P burial (94.9% and 99.2%, respectively). Several factors may have contributed to these results. First, a role for the MAR can be assumed because a high MAR causes a high TN_{BR} and TP_{BR} even in the presence of moderate concentrations of N and P in the sediments, as was the case in this study (1.33 mg N g^{-1} and 0.45 mg P g^{-1}). A high MAR also causes a low return flux because freshly deposited material is quickly covered with new material and thus transported below the biologically active surface layer, where OM degradation proceeds at a slower pace (Arndt et al., 2013). Second, Brepollen Bay (where station H4 is located) is separated from the rest of the fjord by an underwater riffle and by the Treskelen Peninsula in addition to being surrounded by glaciers. Its conditions therefore differ from those of the other regions of Hornsund and include an intense freshwater discharge, strong stratification of the water column, and large quantities of suspended material delivered with meltwaters. Consequently, the supply of terrestrial, refractory OM strongly predominates over marine OM production, which is additionally limited by the high turbidity of the water.

5.3. Global perspective

There are few published estimates of N and P burial rates in sediments (Table 5). In the case of N, most studies have focused on the processes occurring in the sediments, including denitrification, nitrification, and the return flux of the inorganic fraction (Alkhatib et al., 2012, 2013; Yasui et al., 2016). Our results (except at station H4, with its significantly different environment and therefore unique results) are consistent with those previously reported for sediments of the Arctic. Blackburn et al. (1996) reported TN_{BR} efficiencies of 51% and Rysgaard et al. (1998) ON_{BR} efficiencies of ~21%. These values are close to those obtained in Kongsfjorden in this study and suggest that the studied areas are rich in autochthonous OM. For other regions investigated throughout the world, very different TN_{BR} rates have been obtained, with higher values measured in

Table 5 Total nitrogen and total phosphorus burial rates (TN_{BR} and TP_{BR}) and burial efficiencies at different locations.

Region	Nitrogen burial characteristics		Reference
	TN_{BR} [g m^{-2} y^{-1}]	TN_{BR} efficiency [%]	
Hornsund, Spitsbergen	2.3–7.9	69–95	This study
Kongsfjorden, Spitsbergen	0.9–1.3	39–42	This study
Svalbard, Norway	1.6[a]	23[a]	Blackburn et al. (1996)
Young Sound, Greenland	2.9	51	Rysgaard et al. (1998)
Chesapeake Bay	9.2 ± 2.0	–	Kemp et al. (1990)
Laurentian Channel, Canada	0.5–1.0	–	Thibodeau et al. (2010)
Yellow Sea	0.01–1.2	16–30	Lu et al. (2005)
Region	**Phosphorus burial characteristics**		**Reference**
	TP_{BR} [g m^{-2} y^{-1}]	TP_{BR} efficiency [%]	
Hornsund, Spitsbergen	0.9–2.8	93–99	This study
Kongsfjorden, Spitsbergen	1.0–1.2	92	This study
NE Atlantic	0.3–7.3	86–100	van der Zee et al. (2002)
Saanich Inlet, Canada	3.1–18.6	35–37	Filippelli (2001)
Baltic Sea	1.7–2.8	51–66	Rydin et al. (2011)
East China Sea	1.9–6.0	93–99	Yang et al. (2017)
Middle Shelf, East China Sea	0.3–7.2	90–95	Fang et al. (2007)

[a] Organic nitrogen burial rate (ON_{BR}).

Chesapeake Bay (9.2 ± 2.0 g m^{-2} y^{-1}; Kemp et al., 1990) and lower values in the sediments of the Yellow Sea (0.01–1.2 g m^{-2} y^{-1}; Lu et al., 2005) and the Laurentian Channel, Canada (0.5–1.0 g m^{-2} y^{-1}; Thibodeau et al., 2010).

By contrast, the P burial rates in the Arctic have yet to be reported. However, the comparable TP_{BR} values reported for other regions, e.g. the Baltic Sea, the East China Sea, and the NE Atlantic (Fang et al., 2007; van der Zee et al., 2002; Yang et al., 2017) suggest that a large share of the P deposited in the sediments is retained there.

5.4. Significance of surface sediments as a source of nitrogen and phosphorus to the water column

In this study, the yearly N and P return fluxes in Hornsund and Kongsfjorden were estimated. First, based on the depth, slope, and type of sediments, the sediment accumulation area in these fjords was estimated to be 100 ± 15 km^2 and 95 ± 15 km^2, respectively, which amounts to 30–40% of their total surface areas. The accumulation areas were then multiplied by the N and P return fluxes of Hornsund and Kongsfjorden, which revealed the annual release into the water column of 0.8 ± 0.4 × 10^5 kg N and 0.04 ± 0.04 × 10^5 kg P in Hornsund and of 1.0 ± 0.8 × 10^5 kg N and 0.07 ± 0.06 × 10^5 kg P in Kongsfjorden. These fluxes largely constitute organic N and P compounds (DON and DOP), which, after their release from the sediments, may enter the microbial loop, undergo mineralization, and finally enrich the inorganic nutrient pool (Nausch et al., 2004). Because there is no information on the amount of dissolved N and P supplied to Svalbard fjords from the atmosphere and via either rivers and melting glaciers or the inflow of shelf water, we were unable to determine the contributions of the return fluxes to the nutrient budget. However, based on the literature data on annual primary production (120–220 g C m^{-2} in Hornsund and 20–50 g C m^{-2} in Kongsfjorden), we calculated the possible contribution of average return flux of N and P to the nutrients loads required to support primary production (assuming that the released dissolved organic species enter the microbial loop, as mentioned above, and turn into bioavailable forms). First, based on the Redfield ratio (106:16:1), the amount of N and P required to support the primary production was calculated to be 20–40 g N m^{-2} and 3–5 g P m^{-2} in Hornsund, and 3–9 g N m^{-2} and 0.5–1.2 g P m^{-2} in Kongsfjorden. Then, the contributions of N and P originating from return fluxes were estimated – much lower in Hornsund (2–4% for N and 0.8–1.4% for P) than in Kongsfjorden (11–33% and 6–14% respectively), mainly because of huge difference in primary production in these fjords. Moreover, it is worth emphasizing that nutrients are used many times during a growing season, so the above calculated contributions are underestimated. While we are aware of the very high uncertainty underlying conclusions on the nutrients loads transfers, and thus the need for further research, our results nevertheless indicate that diffusion flux from sediments is substantial and thus is an important component of the N and P cycling in the fjords.

6. Conclusions

This study provided qualitative and quantitative analyses of the N and P return fluxes from sediments to the bottom-water as well as estimations of the N and P burial rates in the surface sediments of two high-latitude Arctic fjords, Hornsund and Kongsfjorden. The N_{RF} ranged from 0.43 to 1.38 g m^{-2} y^{-1} in Hornsund and from 0.12 to 1.46 g m^{-2} y^{-1} in Kongsfjorden. At most stations, DON was responsible for 60–70% of the N_{RF}. For P_{RF} the corresponding values were 0.02–0.10 g m^{-2} y^{-1} and 0.01–0.11 g m^{-2} y^{-1}, respectively,

with 60—97% of the flux assigned to DOP. Since N is the main limiting factor of primary production in this region, these results supplement already available knowledge on the origins of N and P in the sea water. Up till now most studies have focused on external sources of N (and P), such as delivery with freshwater inputs from rivers or melting glaciers, whereas sediments as a nutrient source have hardly been investigated. According to our results, a large fraction of the deposited N returns to the bottom water, enriching the pool available for phytoplankton. The consequences of this return may be significant, especially as climate warming increases annual light availability and nutrient limitations restrict phytoplankton primary production.

Both TN_{BR} and the TP_{BR} differed between the two fjords, with rates of 2.3—7.9 g N m^{-2} y^{-1} and 0.9—2.8 g P m^{-2} y^{-1} in Hornsund vs. 0.9—1.3 N g m^{-2} y^{-1} and 1.0—1.2 g P m^{-2} y^{-1} in Kongsfjorden. This difference was accompanied by different efficiencies of N and P burial rates, higher in Hornsund (69—95% for TN_{BR} and 93—99% for TP_{BR}) than in Kongsfjorden (39—42% and 92%, respectively). The difference between the two fjords was likely due to the larger contribution of fresh, marine OM to the Kongsfjorden sediments. Additionally, the slightly deeper penetration of oxygen at the Kongsfjorden sediments may enhance aerobic mineralization, which is more efficient than anoxic mineralization. The generally much higher burial efficiency of P than N would suggest the greater retention of P in the sediments. Our TN_{BR} and TP_{BR} results as well as the determined efficiencies indicate significant differences in the quality and quantity of material deposited to the sediments of these two fjords, especially in the case of N. Moreover, the differences followed a pattern similar to that previously determined for carbon burial rates.

Finally, the N and P burial rates determined in this study are characteristic of the present-day conditions. Climate warming may cause the deposition of OM to sediments increase and shifts in the redox conditions and nutrient burial rates.

Acknowledgements

Katarzyna Koziorowska's participation in the study was supported by the Centre for Polar Studies, KNOW—Leading National Research Centre, Sosnowiec, Poland. The financial support from the National Science Centre, Poland, grant no. 2015/19/N/ST10/01652, and the statutory activities of the Institute of Oceanology (Sopot, Poland) are acknowledged.

References

Alkhatib, M., del Giorgio, P.A., Gelinas, Y., Lehmann, M.F., 2013. Benthic fluxes of dissolved organic nitrogen in the lower St. Lawrence estuary and implications for selective organic matter degradation. Biogeosciences 10 (11), 7609—7622, http://dx.doi.org/10.5194/bg-10-7609-2013.

Alkhatib, M., Schubert, C.J., del Giorgio, P.A., Gelinas, Y., Lehmann, M.F., 2012. Organic matter reactivity indicators in sediments of the St. Lawrence Estuary. Estuar. Coast. Shelf Sci. 102, 36—47, http://dx.doi.org/10.1016/j.ecss.2012.03.002.

Arndt, S., Jorgensen, B.B., LaRowe, D.E., Middelburg, J.J., Pancost, R.D., Regnier, P., 2013. Quantifying the degradation of organic matter in marine sediments: a review and synthesis. Earth-Sci. Rev. 123, 53—86, http://dx.doi.org/10.1016/j.earscirev.2013.02.008.

Aspila, K.I., Agemain, H., Chau, A., 1976. A semi-automated method for the determination of inorganic, organic and total phosphorus in sediments. Analyst 101 (1200), 187—197, http://dx.doi.org/10.1039/an9760100187.

Baldwin, D.S., Beattie, A.K., Coleman, L.M., 2001. Hydrolysis of an organophosphate ester by manganese dioxide. Environ. Sci. Technol. 35 (4), 713—716, http://dx.doi.org/10.1021/es001309l.

Benitez-Nelson, C.R., 2000. The biogeochemical cycling of phosphorus in marine systems. Earth Sci. Rev. 51 (1—4), 109—135, http://dx.doi.org/10.1016/S0012-8252(00)00018-0.

Beszczyńska-Moller, A., Węsławski, J.M., Walczowski, W., Zajączkowski, M., 1997. Estimation of glacial meltwater discharge into Svalbard coastal waters. Oceanologia 39 (3), 289—298.

Blackburn, T.H., Hall, P.O.J., Hulth, S., Landen, A., 1996. Organic-N loss by efflux and burial associated with a low efflux of inorganic N and with nitrate assimilation in Arctic sediments (Svalbard, Norway). Mar. Ecol. Prog. Ser. 141 (1—3), 283—293, http://dx.doi.org/10.3354/meps141283.

Blaszczyk, M., Jania, J.A., Kolondra, L., 2013. Fluctuations of tidewater glaciers in Hornsund Fjord (Southern Svalbard) since the beginning of the 20th century. Pol. Polar Res. 34 (4), 327—352, http://dx.doi.org/10.2478/popore-2013-0024.

Boudreau, B.P., 1997. Molecular/ionic diffusion coefficients. In: Boudreau, B.P. (Ed.), Diagenetic Models and Their Implementation: Modelling Transport and Reactions in Aquatic Sediments. Springer, Berlin-Heidelberg, 96—118.

Burdige, D.J., 2001. Dissolved organic matter in Chesapeake Bay sediment pore waters. Org. Geochem. 32 (4), 487—505, http://dx.doi.org/10.1016/s0146-6380(00)00191-1.

Burdige, D.J., Komada, T., 2015. Sediment pore waters. In: Hansell, D.A., Carlson, C.A. (Eds.), Biogeochemistry of Marine Dissolved Organic Matter. 2nd ed. Elsevier Sci. Publ., San Diego, USA, 535—577.

Burdige, D.J., Zheng, S.L., 1998. The biogeochemical cycling of dissolved organic nitrogen in estuarine sediments. Limnol. Oceanogr. 43 (8), 1796—1813, http://dx.doi.org/10.4319/lo.1998.43.8.1796.

Carroll, J., Zaborska, A., Papucci, C., Schirone, A., Carroll, M.L., Pempkowiak, J., 2008. Accumulation of organic carbon in western Barents Sea sediments. Deep-Sea Res. Pt. II 55 (20—21), 2361—2371, http://dx.doi.org/10.1016/j.dsr2.2008.05.005.

Cha, H.J., Lee, C.B., Kim, B.S., Choi, M.S., Ruttenberg, K.C., 2005. Early diagenetic redistribution and burial of phosphorus in the sediments of the Southwestern East Sea (Japan Sea). Mar. Geol. 216 (3), 127—143, http://dx.doi.org/10.1016/j.margeo.2005.02.001.

Cloern, J.E., 2001. Our evolving conceptual model of the coastal eutrophication problem. Mar. Ecol. Prog. Ser. 210, 223—253, http://dx.doi.org/10.3354/meps210223.

Comans, R.N.J., Middelburg, J.J., Zonderhuis, J., Woittiez, J.R.W., De Lange, G., Das, H.A., Van der Weijden, C.H., 1989. Mobilisation of radiocaesium in pore water of lake sediments. Nature 339, 367—369, http://dx.doi.org/10.1038/339367a0.

Drewnik, A., Weslawski, J.M., Wlodarska-Kowalczuk, M., Lacka, M., Prominska, A., Zaborska, A., Gluchowska, M., 2016. From the worm's point of view. I: Environmental settings of benthic ecosystems in Arctic fjord (Hornsund, Spitsbergen). Pol. Biol. 39 (8), 1411—1424, http://dx.doi.org/10.1007/s00300-015-1867-9.

Enoksson, V., 1993. Nutrient recycling by coastal sediments — effects of added algal material. Mar. Ecol. Prog. Ser. 92 (3), 245—254, http://dx.doi.org/10.3354/meps092245.

Fang, T.H., Chen, J.L., Huh, C.A., 2007. Sedimentary phosphorus species and sedimentation flux in the East China Sea. Cont. Shelf Res. 27 (10—11), 1465—1476, http://dx.doi.org/10.1016/j.csr.2007.01.011.

Fernandez-Mendez, M., Katlein, C., Rabe, B., Nicolaus, M., Peeken, I., Bakker, K., Flores, H., Boetius, A., 2015. Photosynthetic production in the central Arctic Ocean during the record sea-

ice minimum in 2012. Biogeosciences 12, 3525—3549, http://dx.doi.org/10.5194/bg-12-3525-2015.

Filippelli, G.M., 2001. Carbon and phosphorus cycling in anoxic sediments of the Saanich Inlet, British Columbia. Mar. Geol. 174 (1—4), 307—321, http://dx.doi.org/10.1016/s0025-3227(00)00157-2.

Gihring, T.M., Lavik, G., Kuypers, M.M.M., Kostka, J.E., 2010. Direct determination of nitrogen cycling rates and pathways in Arctic fjord sediments (Svalbard, Norway). Limnol. Oceanogr. 55 (2), 740—752, http://dx.doi.org/10.4319/lo.2009.55.2.0740.

Glud, R.N., Hoffmann, F., Canfield, D.E., 1998. Benthic mineralization and exchange in Arctic sediments (Svalbard, Norway). Mar. Ecol. Prog. Ser. 173, 237—251, http://dx.doi.org/10.3354/meps173237.

Holcombe, B.L., Keil, R.G., Devol, A.H., 2001. Determination of pore-water dissolved organic carbon fluxes from Mexican margin sediments. Limnol. Oceanogr. 46 (2), 298—308, http://dx.doi.org/10.4319/lo.2001.46.2.0298.

Hulth, S., Hall, P.O.J., Blackburn, T.H., Landen, A., 1996. Arctic sediments (Svalbard): pore water and solid phase distributions of C, N, P and Si. Polar Biol. 16 (6), 447—462.

Kemp, W.M., Sampou, P., Caffrey, J., Mayer, M., Henriksen, K., Boynton, W.R., 1990. Ammonium recycling versus denitrification in Chesapeake Bay sediments. Limnol. Oceanogr. 35 (7), 1545—1563, http://dx.doi.org/10.4319/lo.1990.35.7.1545.

Kim, J.H., Peterse, F., Willmott, V., Kristensen, D.K., Baas, M., Schouten, S., Damste, J.S.S., 2011. Large ancient organic matter contributions to Arctic marine sediments (Svalbard). Limnol. Oceanogr. 56 (4), 1463—1474, http://dx.doi.org/10.4319/lo.2011.56.4.1463.

Knies, J., Brookes, S., Schubert, C.J., 2007. Re-assessing the nitrogen signal in continental margin sediments: new insights from the high northern latitudes. Earth Planet Sci. Lett. 253 (3—4), 471—484, http://dx.doi.org/10.1016/j.epsl.2006.11.008.

Kotwicki, L., Grzelak, K., Opaliński, K., Wesławski, J.M., 2018. Total benthic oxygen uptake in two Arctic fjords (Spitsbergen) with different hydrological regimes. Oceanologia 60 (2), 107—113, http://dx.doi.org/10.1016/j.oceano.2017.11.005.

Koziorowska, K., Kulinski, K., Pempkowiak, J., 2016. Sedimentary organic matter in two Spitsbergen fjords: terrestrial and marine contributions based on carbon and nitrogen contents and stable isotopes composition. Cont. Shelf Res. 113, 38—46, http://dx.doi.org/10.1016/j.csr.2015.11.010.

Koziorowska, K., Kuliński, K., Pempkowiak, J., 2017. Distribution and origin of inorganic and organic carbon in the sediments of Kongsfjorden, Northwest Spitsbergen, European Arctic. Cont. Shelf Res. 150, 27—35, http://dx.doi.org/10.1016/j.csr.2017.08.023.

Koziorowska, K., Kuliński, K., Pempkowiak, J., 2018. Comparison of the burial rate estimation methods of organic and inorganic carbon and quantification of carbon burial in two high Arctic fjords. Oceanologia, http://dx.doi.org/10.1016/j.oceano.2018.02.005.

Kuliński, K., Kędra, M., Legeżyńska, J., Głuchowska, M., Zaborska, A., 2014. Particulate organic matter sinks and sources in high Arctic fjord. J. Mar. Syst. 139, 27—37, http://dx.doi.org/10.1016/j.jmarsys.2014.04.018.

Lehtoranta, J., Ekholm, P., Wahlstrom, S., Tallberg, P., Uusitalo, R., 2015. Labile organic carbon regulates phosphorus release from eroded soil transported into anaerobic coastal systems. Ambio 44 (2), S263—S273, http://dx.doi.org/10.1007/s13280-014-0620-x.

Loh, A.N., Bauer, J.E., 2000. Distribution, partitioning and fluxes of dissolved and particulate organic C, N and P in the eastern North Pacific and Southern Oceans. Deep Sea Res. Pt. 1 47 (12), 2287—2316, http://dx.doi.org/10.1016/S0967-0637(00)00027-3.

Lomstein, B.A., Jensen, A.G.U., Hansen, J.W., Andreasen, J.B., Hansen, L.S., Berntsen, J., Kunzendorf, H., 1998. Budgets of sediment nitrogen and carbon cycling in the shallow water of Knebel Vig, Denmark. Aquat. Microb. Ecol. 14 (1), 69—80, http://dx.doi.org/10.3354/ame014069.

Lu, X.X., Song, J.M., Li, X.G., Yuan, H.M., Zhan, T.R., Li, N., Gao, X. L., 2005. Geochemical characteristics of nitrogen in the southern Yellow Sea surface sediments. J. Mar. Syst. 56 (1—2), 17—27, http://dx.doi.org/10.1016/j.jmarsys.2004.06.009.

Moore, C.M., Mills, M.M., Arrigo, K.R., Berman-Frank, I., Bopp, L., Boyd, P.W., Galbraith, E.D., Geider, R.J., Guieu, C., Jaccard, S. L., Jickells, T.D., La Roche, J., Lenton, T.M., Mahowald, N.M., Maranon, E., Marinov, I., Moore, J.K., Nakatsuka, T., Oschlies, A., Saito, M.A., Thingstad, T.F., Tsuda, A., Ulloa, O., 2013. Processes and patterns of oceanic nutrient limitation. Nat. Geosci. 6, 701—710, http://dx.doi.org/10.1038/ngeo1765.

Moskalik, M., Ćwiąkała, J., Szczuciński, W., Dominiczak, A., Głowacki, O., Wojtysiak, K., Zagórski, P., 2018. Spatiotemporal changes in the concentration and composition of suspended particulate matter in front of Hansbreen, a tidewater glacier in Svalbard. Oceanologia, http://dx.doi.org/10.1016/j.oceano.2018.03.001.

Muller, P.J., 1977. C-N ratios in Pacific deep-sea sediments — effect of inorganic ammonium and organic nitrogen-compounds sorbed by clays. Geochim. Cosmochim. Acta 41 (6), 765—776, http://dx.doi.org/10.1016/0016-7037(77)90047-3.

Muzuka, A.N.N., Hillaire-Marcel, C., 1999. Burial rates of organic matter along the eastern Canadian margin and stable isotope constraints on its origin and diagenetic evolution. Mar. Geol. 160 (3—4), 251—270, http://dx.doi.org/10.1016/S0025-3227(99)00022-5.

Nausch, M., Nausch, G., Wasmund, N., 2004. Phosphorus dynamics during the transition from nitrogen to phosphate limitation in the central Baltic Sea. Mar. Ecol. Prog. Ser. 266, 15—25, http://dx.doi.org/10.3354/meps266015.

Nixon, S.W., 1995. Coastal marine eutrophication — a definition, social causes, and future concerns. Ophelia 41, 199—219, http://dx.doi.org/10.1080/00785236.1995.10422044.

Piechura, J., Beszczynska-Moller, A., Osinski, R., 2001. Volume, heat and salt transport by the West Spitsbergen Current. Polar Res. 20 (2), 233—240, http://dx.doi.org/10.1111/j.1751-8369.2001.tb00061.x.

Piwosz, K., Walkusz, W., Hapter, R., Wieczorek, P., Hop, H., Wiktor, J., 2009. Comparison of productivity and phytoplankton in a warm (Kongsfjorden) and a cold (Hornsund) Spitsbergen fjord in mid-summer 2002. Polar Biol. 32 (4), 549—559, http://dx.doi.org/10.1007/s00300-008-0549-2.

Polyakov, I.V., Pnyushkov, A.V., Alkire, M.B., Ashik, I.M., Baumann, T. M., Carmack, E.C., Goszczko, I., Guthrie, J., Ivanov, V.V., Kanzow, T., Krishfield, R., Kwok, R., Sundfjord, A., Morison, J., Rember, R., Yulin, A., 2017. Greater role for Atlantic inflows on sea-ice loss in the Eurasian Basin of the Arctic Ocean. Science 356 (6335), 285—291, http://dx.doi.org/10.1126/science.aai8204.

Promińska, A., Cisek, M., Walczowski, W., 2017. Kongsfjorden and Hornsund hydrography — comparative study based on a multiyear survey in fjords of west Spitsbergen. Oceanologia 59 (4), 397—412, http://dx.doi.org/10.1016/j.oceano.2017.07.003.

Reigstad, M., Wassmann, P., Riser, C.W., Oygarden, S., Rey, F., 2002. Variations in hydrography, nutrients and chlorophyll *a* in the marginal ice-zone and the central Barents Sea. J. Mar. Syst. 38 (1—2), 9—29, http://dx.doi.org/10.1016/s0924-7963(02)00167-7.

Ruttenberg, K.C., Goni, M.A., 1997. Phosphorus distribution, C:N:P ratios, and delta C-13(oc) in arctic, temperate, and tropical coastal sediments: Tools for characterizing bulk sedimentary organic matter. Mar. Geol. 139 (1—4), 123—145, http://dx.doi.org/10.1016/s0025-3227(96)00107-7.

Rydin, E., Malmaeus, J.M., Karlsson, O.M., Jonsson, P., 2011. Phosphorus release from coastal Baltic Sea sediments as estimated from sediment profiles. Estuar. Coast. Shelf Sci. 92 (1), 111—117, http://dx.doi.org/10.1016/j.ecss.2010.12.020.

Rysgaard, S., Thamdrup, B., Risgaard-Petersen, N., Fossing, H., Berg, P., Christensen, P.B., Dalsgaard, T., 1998. Seasonal carbon and

nutrient mineralization in a high-Arctic coastal marine sediment, Young Sound, Northeast Greenland. Mar. Ecol. Prog. Ser. 175, 261—276, http://dx.doi.org/10.3354/meps175261.

Salley, B.A., Bradshaw, J.B., Neillo, B.J., 1986. Results of comparative studies of preservation techniques for nutrient analysis on water samples. Virginia Inst. Mar. Sci. Gloucester Point 89 pp.

Schubert, C.J., Calvert, S.E., 2001. Nitrogen and carbon isotopic composition of marine and terrestrial organic matter in Arctic Ocean sediments: implications for nutrient utilization and organic matter composition. Deep Sea Res. Pt. 1 Oceanogr. Res. Pap. 48 (3), 789—810, http://dx.doi.org/10.1016/s0967-0637(00)00069-8.

Schulz, H.D., Zabel, M., 2006. Marine Geochemistry. Springer-Verlag, Berlin-Heidelberg, 574 pp.

Silva, J.A., Bremner, J.M., 1966. Determination and isotope-ratio analysis of different forms of nitrogen in soils. 5. Fixed ammonium. Soil Sci. Soc. Am. Proc. 30 (5), 587—594, http://dx.doi.org/10.2136/sssaj1966.03615995003000050017x.

Smoła, Z., Tatarek, A., Wiktor, J., Wiktor Jr., J., Hapter, R., Kubiszyn, A., Węsławski, J.M., 2017. Primary producers and production in two West Spitsbergen fjords (Hornsund and Kongsfjorden) — a review. Pol. Polar Res. 38 (3), 351—373, http://dx.doi.org/10.1515/popore-2017-0013.

Strickland, J.D.H., Parsons, T.R., 1967. A practical handbook of seawater analysis. Fish. Res. Board Canada Bull. 328, 45—138.

Svendsen, H., Beszczynska-Moller, A., Hagen, J.O., Lefauconnier, B., Tverberg, V., Gerland, S., Orbaek, J.B., Bischof, K., Papucci, C., Zajaczkowski, M., Azzolini, R., Bruland, O., Wiencke, C., Winther, J.G., Dallmann, W., 2002. The physical environment of Kongsfjorden-Krossfjorden, an Arctic fjord system in Svalbard. Polar Res. 21 (1), 133—166, http://dx.doi.org/10.1111/j.1751-8369.2002.tb00072.x.

Thibodeau, B., Lehmann, M.F., Kowarzyk, J., Mucci, A., Gelinas, Y., Gilbert, D., Maranger, R., Alkhati, M., 2010. Benthic nutrient fluxes along the Laurentian Channel: impacts on the N budget of the St. Lawrence marine system. Estuar. Coast. Shelf Sci. 90 (4), 195—205, http://dx.doi.org/10.1016/j.ecss.2010.08.015.

Tremblay, J.E., Anderson, L.G., Matrai, P., Coupel, P., Belanger, S., Michel, C., Reigstad, M., 2015. Global and regional drivers of nutrient supply, primary production and CO_2 drawdown in the changing Arctic Ocean. Prog. Oceanogr. 139, 171—196, http://dx.doi.org/10.1016/j.pocean.2015.08.009.

Tremblay, J.E., Gratton, Y., Carmack, E.C., Payne, C.D., Price, N.M., 2002. Impact of the large-scale Arctic circulation and the North Water Polynya on nutrient inventories in Baffin Bay. J. Geophys. Res. 107 (C8), 1—15, http://dx.doi.org/10.1029/2000jc000595.

Tremblay, J.E., Raimbault, P., Garcia, N., Lansard, B., Babin, M., Gagnon, J., 2014. Impact of river discharge, upwelling and vertical mixing on the nutrient loading and productivity of the Canadian Beaufort Shelf. Biogeosciences 11 (17), 4853—4868, http://dx.doi.org/10.5194/bgd-10-16675-2013.

Tremblay, J.E., Simpson, K.G., Martin, J., Miller, L., Gratton, Y., Barber, D., Price, N.M., 2008. Vertical stability and the annual dynamics of nutrients and chlorophyll fluorescence in the coastal, southeast Beaufort Sea. J. Geophys. Res. 113 (C7), 1—14, http://dx.doi.org/10.1029/2007JC004547.

Ullman, W.J., Aller, R.C., 1982. Diffusion-coefficients in nearshore marine-sediments. Limnol. Oceanogr. 27 (3), 552—556, http://dx.doi.org/10.4319/lo.1982.27.3.0552.

van der Zee, C., Slomp, C.P., van Raaphorst, W., 2002. Authigenic P formation and reactive P burial in sediments of the Nazare canyon on the Iberian margin (NE Atlantic). Mar. Geol. 185 (3—4), 379—392, http://dx.doi.org/10.1016/S0025-3227(02)00189-5.

Winkelmann, D., Knies, J., 2005. Recent distribution and accumulation of organic carbon on the continental margin west off Spitsbergen. Geochem. Geophy. Geosy. 6, 1—22, http://dx.doi.org/10.1029/2005gc000916.

Winogradow, A., Pempkowiak, J., 2014. Organic carbon burial rates in the Baltic Sea sediments. Estuar. Coast. Shelf Sci. 138, 27—36, http://dx.doi.org/10.1016/j.ecss.2013.12.001.

Włodarska-Kowalczuk, M., Pearson, T.H., 2004. Soft-bottom macrobenthic faunal associations and factors affecting species distributions in an Arctic glacial fjord (Kongsfjord, Spitsbergen). Polar Biol. 27 (3), 155—167, http://dx.doi.org/10.1007/s00300-003-0568-y.

Yang, B., Song, G.D., Liu, S.M., Jin, J., 2017. Phosphorus recycling and burial in core sediments of the East China Sea. Mar. Chem. 192, 59—72, http://dx.doi.org/10.1016/j.marchem.2017.04.001.

Yasui, S., Kanda, J., Usui, T., Ogawa, H., 2016. Seasonal variations of dissolved organic matter and nutrients in sediment pore water in the inner part of Tokyo Bay. J. Oceanogr. 72 (6), 851—866, http://dx.doi.org/10.1007/s10872-016-0382-0.

Zaborska, A., 2017. Sources of 137Cs to an Arctic fjord (Hornsund, Svalbard). J. Environ. Radioact. 180, 19—26, http://dx.doi.org/10.1016/j.jenvrad.2017.09.021.

Zaborska, A., Pempkowiak, J., Papucci, C., 2006. Some sediment characteristic and sedimentation rates in an Arctic fjord (Kongsfjorden, Svalbard). Rocz. Ochr. Srod. 8, 79—96.

Zaborska, A., Wlodarska-Kowalczuk, M., Legeżyńska, J., Jankowska, E., Winogradow, A., Deja, K., 2016. Sedimentary organic matter sources, benthic consumption and burial in west Spitsbergen fjords — Signs of maturing of Arctic fjordic systems? J. Mar. Syst. 180, 112—123, http://dx.doi.org/10.1016/j.jmarsys.2016.11.005.

Zhu, R.B., Ding, W., Hou, L.J., Wang, Q., 2014. Matrix-bound phosphine and phosphorus fractions in surface sediments of Arctic Kongsfjorden, Svalbard: effects of glacial activity and environmental variables. Chemosphere 103, 240—249, http://dx.doi.org/10.1016/j.chemosphere.2013.12.011.

Oceanologia (2018) 60, 446—463

Available online at www.sciencedirect.com

ScienceDirect

journal homepage: www.journals.elsevier.com/oceanologia/

ORIGINAL RESEARCH ARTICLE

Spatiotemporal changes in the concentration and composition of suspended particulate matter in front of Hansbreen, a tidewater glacier in Svalbard

Mateusz Moskalik [a,*], Joanna Ćwiąkała [a], Witold Szczuciński [b], Aleksander Dominiczak [b], Oskar Głowacki [a], Kacper Wojtysiak [a], Piotr Zagórski [c]

[a] *Institute of Geophysics, Polish Academy of Sciences, Warszawa, Poland*
[b] *Institute of Geology, Adam Mickiewicz University in Poznań, Poznań, Poland*
[c] *Faculty of Earth Sciences and Spatial Management, Maria Curie-Skłodowska University, Lublin, Poland*

Received 31 July 2017; accepted 19 March 2018
Available online 5 April 2018

KEYWORDS
Seasonality;
Suspended particulate matter;
Particulate organic matter;
Tidewater glacier;
Fjord;
Svalbard

Summary Tidewater glaciers supply large amounts of suspended particulate matter (*SPM*) and freshwater to fjords and affect oceanographic, sedimentological and biological processes. Our understanding of these processes, is usually limited to the short summer season. Here, we present the results of a one-year-long monitoring of the spatial variability in *SPM* characteristics in a context of oceanographic and meteorological conditions of a glacial bay next to Hansbreen, a tidewater glacier in Hornsund (southern Spitsbergen). The observed range of *SPM* concentrations was similar to ranges measured in other sub-polar glaciated fjords, especially in Svalbard. The major source of SPM is the meltwater discharge from the glacier. The maximum water column-averaged *SPM* concentrations did not correlate with peaks in freshwater discharge and were observed at the beginning of the autumn season, when the fjord water transitioned from stratified to fully mixed. The observed spatiotemporal variations in the total *SPM*, particulate organic matter (*POM*) and particulate inorganic matter (*PIM*) are likely controlled by a combination of factors including freshwater supply, water stratification and circulation, bathymetry, the presence of sea ice, biological productivity and sediment resuspension. During the ablation season, the *SPM* maximum concentrations were located within the upper water layer, whereas

* Corresponding author at: Institute of Geophysics, Polish Academy of Sciences, Księcia Janusza 64, 01-452 Warszawa, Poland. Tel.: +48 226915883.
E-mail address: mmosk@igf.edu.pl (M. Moskalik).
Peer review under the responsibility of Institute of Oceanology of the Polish Academy of Sciences.

ELSEVIER Production and hosting by Elsevier

https://doi.org/10.1016/j.oceano.2018.03.001

during the winter and spring, the greatest amounts of *SPM* were concentrated in deeper part. Thus, typical remote sensing-based studies that focus on *SPM* distributions may not reflect the real *SPM* levels. *POM* and *PIM* concentrations were correlated with each other, during most of the time suggesting that they may have a common source.

1. Introduction

Glaciers are one of the most sensitive indicators of ongoing climate changes that have commonly resulted in their recent very rapid retreat since the end of the Little Ice Age (e.g., Carr et al., 2017; Radić and Hock, 2011; Solomina et al., 2016). Due to the retreat of marine-terminating tidewater glaciers, at a rate of several tens of metres per year, as in Svalbard (e.g., Błaszczyk et al., 2013), or several hundreds of metres per year, as in Alaska (e.g., Molnia, 2007), new glacial bays have formed and host immature coastal ecosystems. Melting glaciers affect coastal waters in many ways, the most important of which is the delivery of freshwater and suspended particulate matter (*SPM*), which is often called suspended sediment. They are among the key driving factors for coastal glaciomarine ecosystems, as well as oceanographic and sedimentary regimes (e.g., Bennett and Glasser, 2009; Chauche et al., 2014; Motyka et al., 2003; Szczuciński and Zajączkowski, 2012). Their influence can also extend far beyond the coastal zone into the open ocean and affect larger scale circulation and biological processes. For example, *SPM*-rich glacial meltwater can provide critical limiting micronutrients (e.g., Fe) to the ocean and thereby influence its primary production (e.g., Bhatia et al., 2013; Markussen et al., 2016).

Many of the existing records of sediment accumulation rates in fjords suggest that climate warming has enhanced sediment production and export to the fjords (Boldt et al., 2013; Koppes and Hallet, 2002; Szczuciński et al., 2009; Zajączkowski et al., 2004). In addition, the combination of historical data and modelling experiments suggests that present-day sediment fluxes to the polar zone of the coastal ocean have increased. For instance, the suspended sediment supply from Greenland to the ocean is currently approximately 56% higher than it was during the 1961–1990 period (Overeem et al., 2017). Moreover, one may expect that the seasonality of *SPM* delivery, distribution and sedimentation processes will also change. However, this issue is still open to research because present-day seasonal changes in *SPM* distributions are poorly known.

SPM is mainly delivered to fjords by ice-contact processes, including meltwater discharge, rafting by icebergs and sea ice, riverine inputs and exchanges with external water masses (Syvitski, 1989; Winters and Syvitski, 1992). The general model of *SPM* delivery shows the driving role of freshwater and sediment-laden outflows from tidewater glaciers, which, due to density differences, form surface brackish water plumes covering most of the glacial bays during the summer season (Syvitski, 1989). However, a growing number of observations, indicate that other factors are also significant. For example, a study on a large dataset from Greenland found that the delivery of *SPM* is likely mainly a function of the regional glacial dynamics and the resulting intensity of erosion, not freshwater flux (Overeem et al., 2017). Furthermore, oceanographic circulation is important not only in terms of the sediment transport and circulation patterns in glacial bays but also as a driving factor of tidewater glacier stability (e.g., Straneo and Heimbach, 2013). Because field observations on seasonal cycles are sparse, the driving forces that control the *SPM* input and distribution in fjords are still subject to ongoing debate.

The fjords of Svalbard are particularly suitable for studies on climate warming impacts on the supply and fate of *SPM* since they are affected by the northward flowing West Spitsbergen Current (WSC) that transports warm Atlantic Water (AW), resulting in accelerated warming (e.g., Cisek et al., 2017; Osuch and Wawrzyniak, 2016; Promińska et al., 2017). Moreover, these fjords are among the best studied subpolar fjords in the world, and many supplementary data are available (e.g., Drewnik et al., 2016; Forwick et al., 2010; Svendsen et al., 2002). The *SPM* concentrations in the fjords of Svalbard are commonly documented during the summer season in central parts of fjords (e.g., Sagan and Darecki, 2018; Svendsen et al., 2002), in meltwater river-fed bays (e.g., Dowdeswell and Cromack, 1991; Zajączkowski and Włodarska-Kowalczuk, 2007) and in the glacial bays near tidewater glaciers (e.g., Elverhøi et al., 1983; Görlich et al., 1987; Schildt et al., 2017; Szczuciński and Zajączkowski, 2012; Trusel et al., 2010; Urbanski et al., 2017; Zajączkowski, 2002, 2008).

However, observations on the seasonal *SPM* concentration changes and their major controlling factors in the fronts of tidewater glaciers in Spitsbergen are very limited. Szczuciński and Zajączkowski (2012) studied sedimentary processes in the summer and autumn in Adolfbukta next to the calving front of Nordenskiöldbreen. These authors found that in the autumn, the vertical particulate matter fluxes (sedimentation) decrease much more than the *SPM* concentrations and that residence time of the *SPM* in the water increases likely due to less effective flocculation. These authors also suggested a list of factors that affect the sedimentation of *SPM*, such as the positions of freshwater inlets (surface/subsurface), meltwater discharge, *SPM* concentrations in the meltwater, local wind damming effects, tides and resuspension. Moreover, studies conducted in glacier-distal settings revealed that phytoplankton blooms are important factors in the increase of *SPM* concentrations in the spring (Pawłowska et al., 2011; Węsławski et al., 1988).

The goal of the paper is to present a unique time series of the seasonal changes of the *SPM* delivery, distribution and composition in a glacial bay next to the calving front of Hansbreen in Hornsund. This paper presents a

complementary dataset, including supporting meteorological and oceanographic monitoring data, for the period from May 2015 to June 2016. The obtained data are used to identify major *SPM* sources and driving processes responsible for *SPM* spatial distribution and composition during various seasons.

2. Study area

Hornsund is an approximately 34 km long fjord in the southwest part of Spitsbergen. Glaciers cover approximately 60% of its catchment (Błaszczyk et al., 2009, 2013). The most frequently studied glacier in Hornsund is Hansbreen, a polythermal tidewater glacier that ends with a 1.5 km wide calving cliff in Hansbukta (Hans Bay), which is almost 80 m deep. The bay covers an area of 6 km^2, and its outer region, with a maximum depth of less than 25 m, is shallower than its innermost region (Ćwiąkała et al., 2018) (Fig. 1). The bay was formed during the last century due to glacier retreat; presently, the glacier retreats approximately 40 m year^{-1} (Błaszczyk et al., 2013). The Hansbreen area is 56 km^2, and its mean ice thickness is approximately 170 m (Błaszczyk et al., 2013; Grabiec et al., 2012). The bedrock beneath the glacier is composed of various types of low to intermediate grades of metamorphic rocks including schists, gneisses, amphibolites, marbles and quartzites (Birkenmajer, 1990). The meltwater is delivered from Hansbreen to the bay mainly through subglacial tunnels that enter the bay from the central and eastern parts of the glacier cliff (Pälli et al., 2003).

The WSC and East Spitsbergen Current (ESC) influence the oceanographic conditions of Hornsund and make its climate

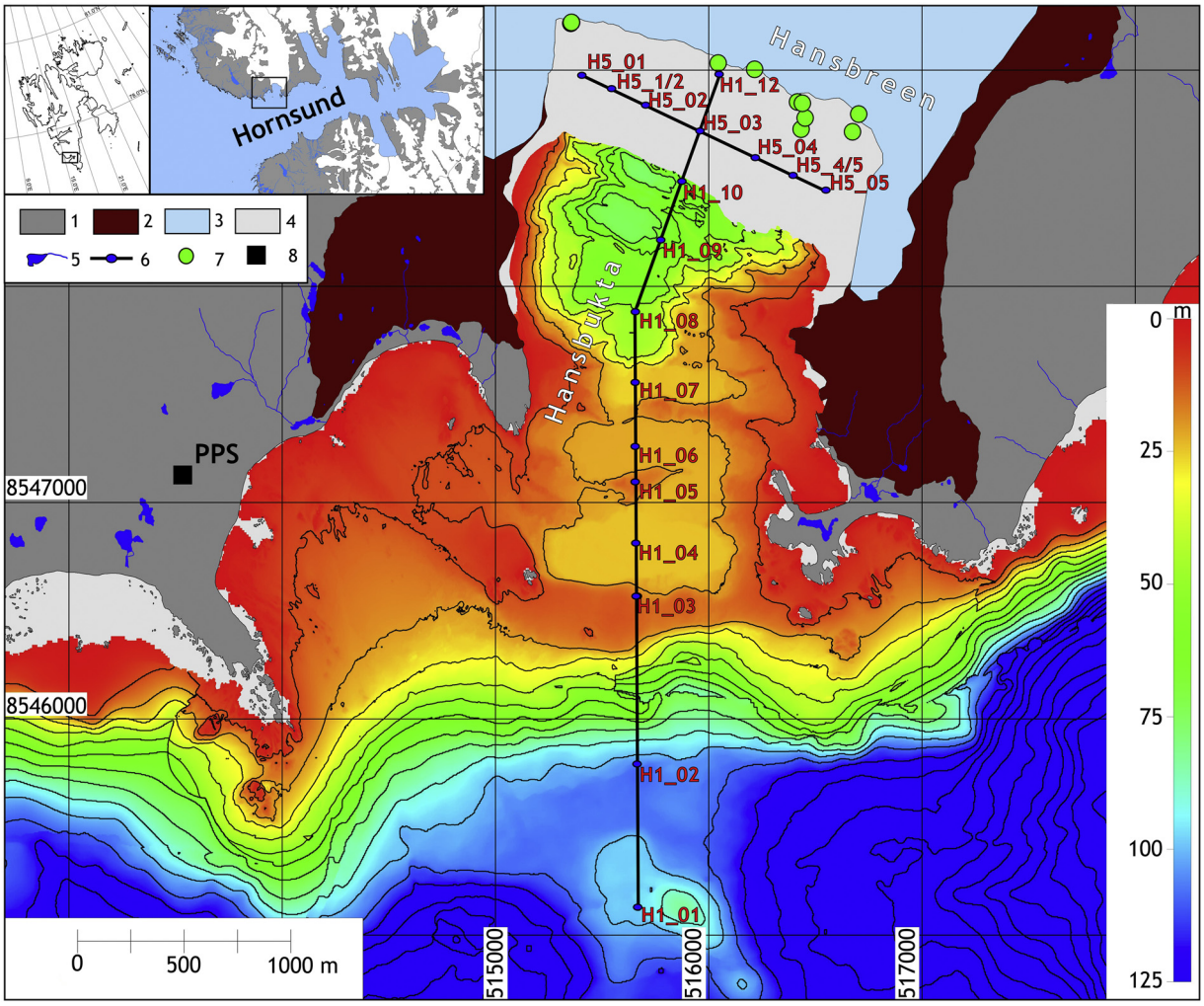

Figure 1 Study area: Hansbukta with transects and monitoring stations marked. Legend: 1 — land, 2 — moraines on land, 3 — glaciers, 4 — marine areas with no bathymetry data, 5 — lakes and rivers, 6 — ADCP transects and monitoring stations, 7 — outflows from the glaciers (based on satellite images collected between the 6th of June and 1st of October 2015), 8 — the meteorological station in the Polish Polar Station (PPS). The inset maps show the location of the study area within the Hornsund Fjord and the location of Hornsund within the Svalbard archipelago.
Sources: Shoreline, lakes, rivers, glaciers and moraines are based on the Norsk Polar Institute data (http://geodata.npolar.no/) (updated for the Hansbreen position in 2015), bathymetric data are from The Norwegian Hydrographic Service (the permit for data use was issued by the Institute of Geophysics, Polish Academy of Sciences no. 13/G722) with isobaths every 10 metres.

mild and maritime (Marsz and Styszyńska, 2013; Osuch and Wawrzyniak, 2016). The mean annual air temperature from 1979 to 2014 was approximately −4.0°C, with the highest temperature recorded in July and the coldest in March. The mean annual precipitation during the same period was approximately 450 mm, with the highest amounts during the late summer and autumn seasons and the lowest during spring (Osuch and Wawrzyniak, 2016). Approximately 60% of the mean total annual precipitation in the region falls as snow or sleet (Łupikasza, 2013). On average, the snow cover occurs approximately 240 days of the year, with maximum mean snow depths in April. However, the snow depths and durations vary strongly from year to year (Kępski et al., 2017).

The fjord water masses are generally stratified during the ablation season, then they are subjected to mixing in the autumn and winter. Moreover they are affected by the inflow of water masses from the Greenland Sea, as documented in previous oceanographic studies (e.g., Drewnik et al., 2016; Görlich, 1986; Promińska et al., 2017; Węsławski et al., 1991, 1995). Consequently, six types of water masses were distinguished according to the classification system for fjords of Svalbard. The AW and Transformed Atlantic Water (TAW) masses enter the fjord from the shelf. The AW comes from the WSC, and its temperature and salinity are higher than 3°C and 34.9 PSU respectively. The TAW is a mix of AW and Arctic-type Water (ArW) from the ESC and has a temperature between 1°C and 3°C and a salinity higher than 34.7 PSU. The third type of water mass is Surface Water (SW), which is the uppermost layer formed from the glacial melt water. SW is common from late spring to autumn and has a water temperature higher than 1°C and a salinity lower than 34.7 PSU. Mixing of the SW and AW or TAW forms Intermediate Water (IW), with a temperature higher than 1°C and a salinity between 34 and 34.7 PSU. Cooling during the winter generates Local Water (LW), with a temperature lower than 1°C and Winter Cooled Water (WCW) with a temperature lower than −0.5°C and salinity higher than 34.4 PSU (Nilsen et al., 2008). The circulation in the fjord is enhanced by the Coriolis force (Jakacki et al., 2017; Pawłowska et al., 2017) and the tides with mean spring tidal range of over 1 m. Lately, the fast ice cover in Hornsund usually covers more than 40% of the fjord and last for approximately 45 days per year (Muckenhuber et al., 2016).

3. Material and methods

3.1. Meteorology

The meteorological data, including air temperature (Fig. 2A) and precipitation (Fig. 2B), from the period from May 2015 to June 2016 were obtained from the Polish Polar Station Hornsund (PPS), which is located 2 km west from Hansbukta. The daily mean air temperatures were smoothed by a robust local regression using a weighted least squares method and second degree polynomial model with a 45-day duration (LOESS model implemented in MATLAB software).

3.2. Oceanography

The water temperature and salinity values were measured using a Valeport miniCTD probe (CTD) during 22 surveys at 18 monitoring stations along 2 transects (Fig. 1). Due to equipment failure, CTD measurements were not made from December 2015 to March 2016. Most of the figures in this paper are based on data from monitoring station H1_09 (Fig. 2C and D), which is considered a representative station because it is located in the deepest central part of the bay, almost 1000 m from the glacier cliff (Fig. 1). At that station, the freshwater from all the meltwater outflows is mixed. The temperature and salinity data from that station were smoothed by a robust local regression using a weighted least squares method and second degree polynomial model for 10 m depth sections (LOESS model implemented in MATLAB software) and interpolated over time using a cubic Hermite spline (method implemented in MATLAB software) to obtain the seasonal fluctuations in the water properties (Fig. 3A and C).

To obtain information about seasonal water stratification changes, the water temperature standard deviation (σ_T) for the depth profile at station H1_09 was calculated from the measured and interpolated data (Fig. 3B). Higher values of σ_T imply greater temperature ranges in the depth profile and, consequently, the development of stratification. Values of σ_T close to zero indicate no stratification in the water column.

To determine the input by the meltwater discharge from the glacier, the freshwater fraction (*FWF*) was calculated for the interpolated and measured salinity (Fig. 3D). Guided by Ketchum (1950) and Nut and Coachman (1956), the *FWF* was calculated using the equation:

$$FWF = \frac{(S_0 - S)}{S_0} \cdot 100\%, \quad (1)$$

where S_0 = 34.92 PSU, which was the highest measured salinity (from H1_01, which is the point nearest to the mouth of the Hornsund Fjord), and S is the average salinity in the water column at station H1_09.

To identify the circulation pattern in the bay, a Teledyne RD Instruments Workhorse Sentinel 600 kHz Acoustic Doppler Current Profiler (ADCP) was used twice during the summer, on the 13th of July, and the 1st of September 2015, along transects perpendicular and parallel to Hansbreen cliff (Fig. 1). The velocity (Fig. 4B, E, H, K) and the direction (Fig. 4A, D, G, J) of the flow were directly measured by the ADCP.

The positions of meltwater outflows from Hansbreen were marked on satellite images collected by Landsat 8 (images from U.S. Geological Survey Department of Interior for the years 2015 and 2016) based on the method outlined by Dowdeswell et al. (2015), in order to compare them with water circulation and *SPM* concentration data.

Information about the sea ice conditions in Hansbukta during the measurement period were based on the observations that were made by the authors and PPS staff (Fig. 2C).

3.3. Suspended particulate matter

Spatial and temporal changes in *SPM* were obtained from the ADCP measurements and filtered water samples. The echo strength (in counts) measured by the ADCP provided insight into the acoustic intensity Int_{ADCP} (in dB):

$$Int_{ADCP} = 20 \cdot \log_{10}(R) + 2 \cdot \alpha \cdot R + K_C \cdot E + C_K, \quad (2)$$

where R is the range along the beam (in m), α is the attenuation coefficient due to water absorption (in dB m^{-1}),

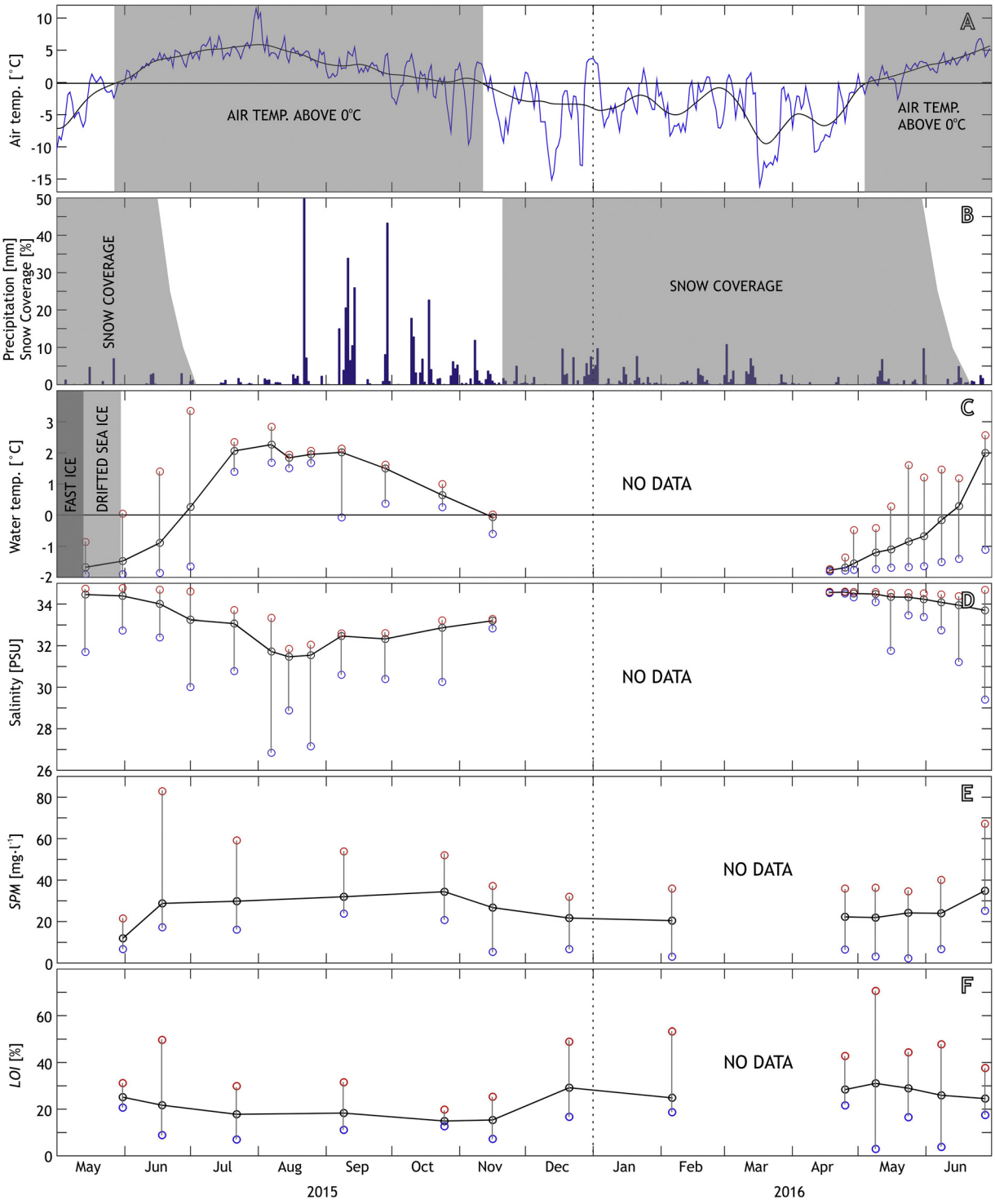

Figure 2 Annual course of the meteorological conditions at the Polish Polar Station (PPS), including oceanographic conditions from station H1_09, and suspended particulate matter (*SPM*) with loss on ignition (*LOI*) data from all the sampling stations (see Fig. 1 for site locations). (A) Daily mean (blue line) and smoothed (black line) air temperature; (B) daily precipitation and snow coverage (based on Kępski et al., 2017); (C) mean (black circles linked by black line), minimum (blue circles) and maximum (red circles) water temperatures and sea ice conditions; (D) mean (black circles linked by black line), minimum (blue circles) and maximum (red circles) water salinity; (E) mean (black circles linked by black line), minimum (blue circles) and maximum (red circles) *SPM* concentrations; (F) mean (black circles linked by black line), minimum (blue circles) and maximum (red circles) *LOI* in *SPM*. (For interpretation of the references to color in this figure legend, the reader is referred to the web version of this article.)

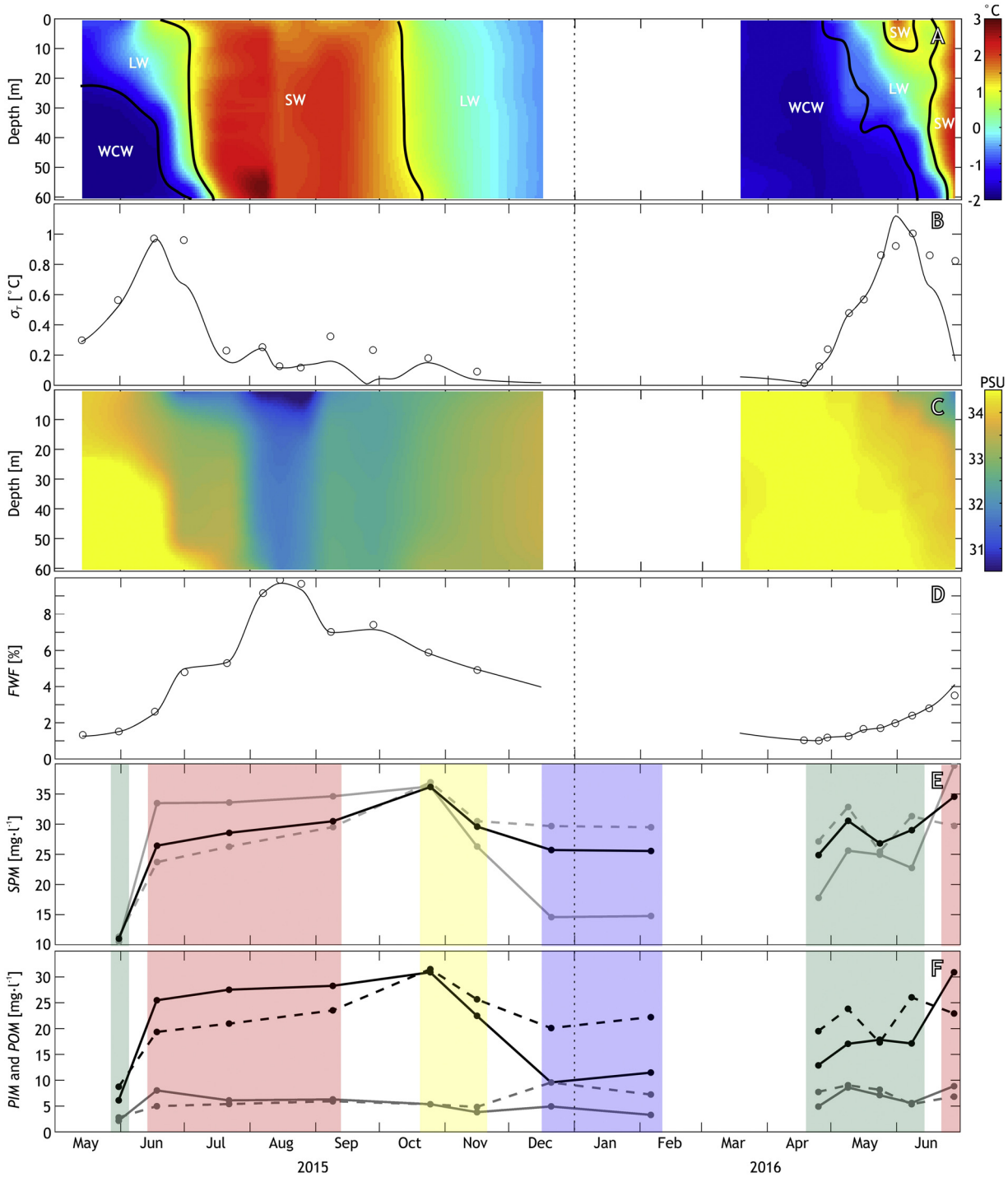

Figure 3 Annual changes in the oceanographic conditions of station H1_09 (for station location see Fig. 1) and mean interpolated suspended particle matter (*SPM*) concentration and composition data. (A) Interpolated water temperature depth profile changes over time. The abbreviations refer to water mass types. WCW — winter-cooled water, LW — local water, and SW — surface water (see text for details); (B) standard deviations of water temperature (σ_T) from interpolated (black line) and measured (black circles) values; (C) interpolated water salinity depth profile changes over time; (D) the freshwater fraction (*FWF*) calculated from interpolated (black line) and measured (black circles) values; (E) the mean concentration of *SPM* from interpolated data over the total water column (black line), its surface concentration (grey line) and deeper subsurface concentration (dashed grey line). The surface part of the water column refers to the layer from the surface to a depth of 10 m, and deep water refers to the layer from 20 to 50 m below surface; (F) average concentrations of the interpolated particulate inorganic matter (*PIM* — black lines) and particulate organic matter (*POM* — grey lines) within the surface (solid lines) and deeper subsurface (dashed lines) parts of water. The time intervals coloured on (E) and (F) represent measurements assigned to the spring (green), summer (red), autumn (yellow), and winter (blue) seasons. (For interpretation of the references to color in this figure legend, the reader is referred to the web version of this article.)

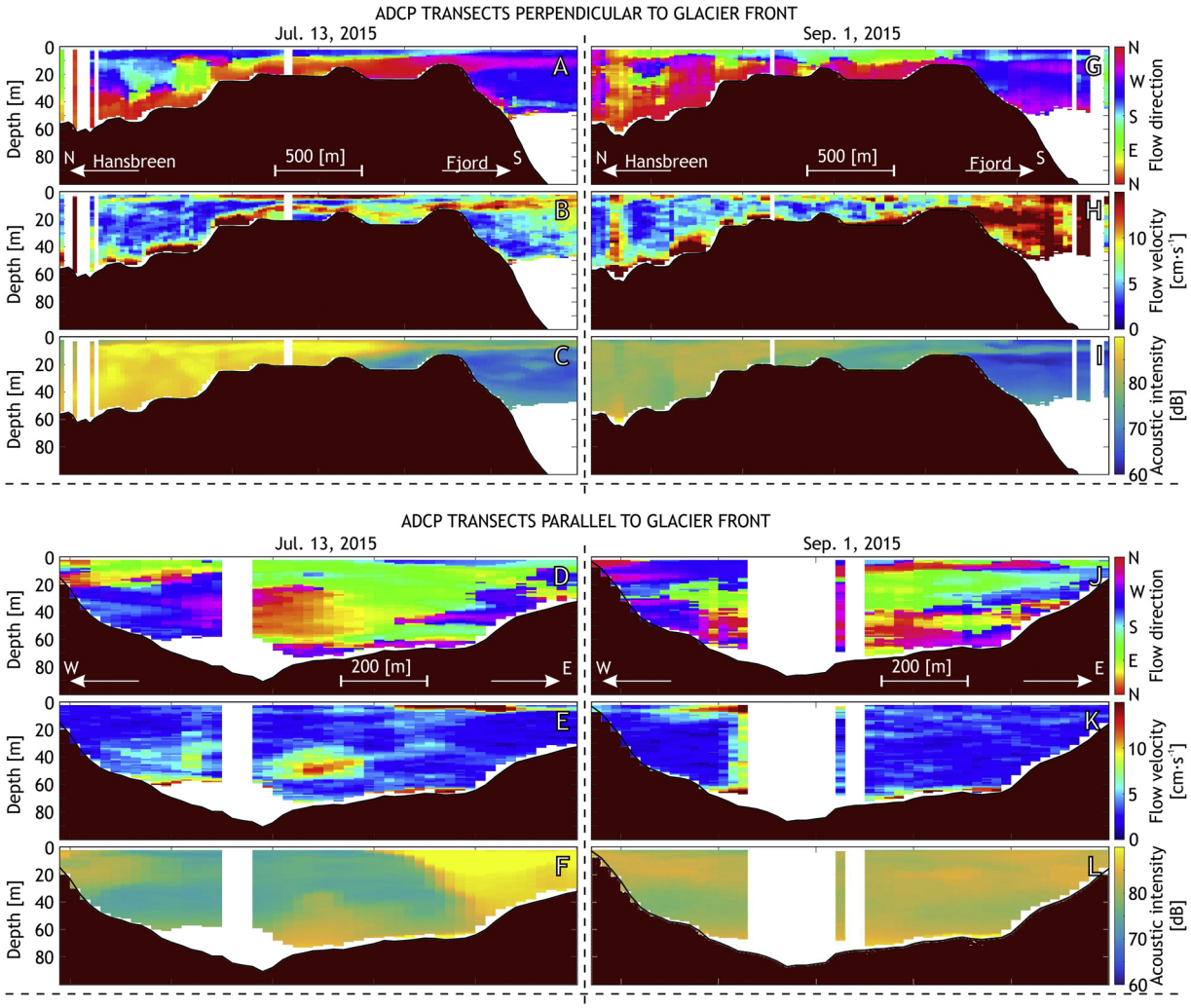

Figure 4 Acoustic Doppler Current Profiler (ADCP) measurements made on the 13th of July 2015 (A–F) and 1st of September 2015 (G–L) on transects perpendicular (A–C, G–I) and parallel (D–F, J–L) to the glacier front (for locations see Fig. 1). A, D, G and J present the flow directions, B, E, H and K show the flow velocity, and C, F, I and L represent the acoustic intensity.

E is the echo strength measured by the ADCP (in counts), and K_C (in dB counts^{-1}) and C_K (in dB) are constants. The values of the constants are calculated during the calibration procedure. The K_C value ranges from 0.35 to 0.55 dB counts^{-1} and is typically 0.45 dB counts^{-1} (Deines, 1999; Kim and Voulgaris, 2003). Using the latter value a modified acoustic intensity (*Int*) may be calculated from:

$$Int = Int_{ADCP} - C_K = 20 \cdot \log_{10}(R) + 2 \cdot \alpha \cdot R + 0.45 \cdot E, \quad (4)$$

Int is related to *SPM* (concentration) (Deines, 1999; Kim and Voulgaris, 2003):

$$10 \cdot \log_{10}(SPM) = Int_{ADCP} \quad (5)$$

and based on Eqs. (4) and (5) the *SPM* (concentration) is expressed as:

$$SPM = 10^{0.1 \cdot C_K} \cdot 10^{0.1 \cdot Int}. \quad (6)$$

In this study, no calibration procedure was performed, so only *Int* was calculated (Fig. 4C, F, I, L).

Water samples were taken 13 times at regular intervals between the 31st of May 2015 and the 28th of June 2016, except of March 2015, using a Hydrobios Free Flow 1l Niskin Bottle at several water depths at the monitoring stations (Fig. 1). The samples (approximately 1 l each) were filtered through Whatman GF/F 0.7 μm filters that had been previously dried for 2 h at 200°C and weighed. There were no animals or plant fragments visible on the filters. After filtering, the filters were rinsed with fresh water and were dried for 24 h at 40°C and weighed again to calculate the *SPM* (Appendix 1, Fig. 2E). Subsequently, all filters were heated at 550°C for 3 h to calculate the loss on ignition (*LOI*), according to the Heiri et al. (2001) equation:

$$LOI = \frac{DW - DW_{550}}{DW} \cdot 100\%, \quad (7)$$

where *DW* is the dry weight of the sediments before heating and DW_{550} is the dry weight of the sediments after heating (Appendix 2, Fig. 2F). With the total *SPM* concentration and *LOI* values, particulate organic matter (*POM*) and particulate inorganic matter (*PIM*) concentrations were calculated:

$$\begin{aligned} POM &= SPM \cdot LOI \\ PIM &= SPM \cdot (1 - LOI) \end{aligned}. \quad (8)$$

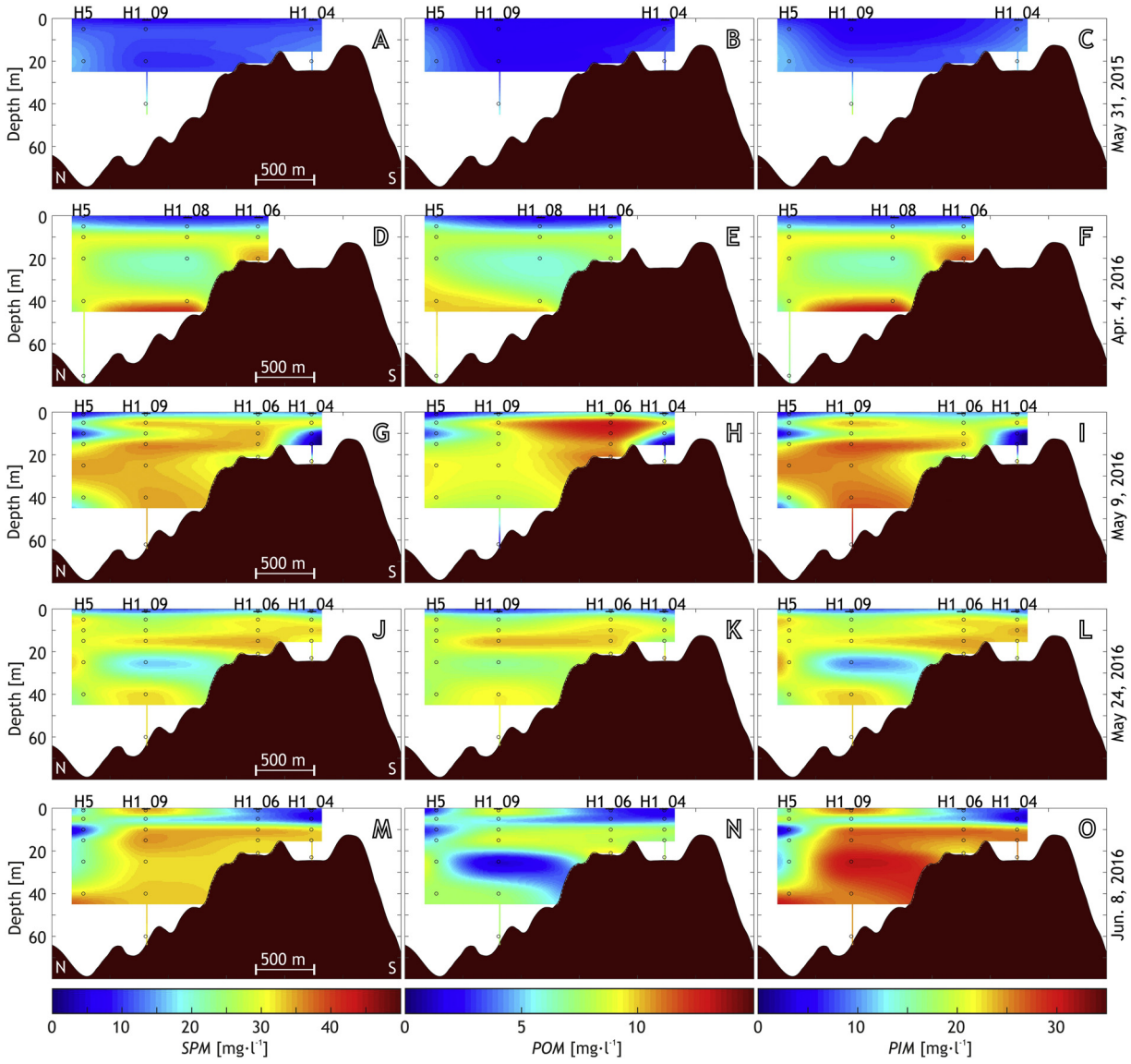

Figure 5 Interpolated distributions of suspended particulate matter (*SPM*) (A, D, G, J, M), particulate organic matter (*POM*) (B, E, H, K, N), and particulate inorganic matter (*PIM*) (C, F, I, L, O), during the spring season in Hansbukta. The interpolations are based on data from measurements taken on the 31st of May 2015 (A, B, C), 25th of April 2016 (D, E, F), 9th of May 2016 (G, H, I), 24th of May 2016 (J, K, L) and 8th of June 2016 (M, N, O). For the location of monitoring stations see Fig. 1.

To determine the spatial distribution of *SPM*, *POM* and *PIM*, the calculated data were interpolated using a cubic Hermite spline (a method implemented with MATLAB software) for the depth profile and between the profiles (Figs. 5–7). In the interpolated profiles perpendicular to the glacier cliff (Figs. 5–7), the data presented for station H5_03 (the closest station to the glacier cliff) are the average values from all the stations along a transect parallel to the glacier cliff. All the interpolated *SPM*, *PIM*, and *POM* data were used to represent the annual variability of the inner part of Hansbukta, up to 2000 m from the glacier. The data were averaged for two water layers: the surface (0–10 m depth) and deeper layer (20–50 m depth) (Fig. 3E and F) and analysed for the particular calendar seasons. Accordingly, the relationship of *POM* to *PIM* (Fig. 8A) and the *LOI* distributions (Fig. 8B–E) were analysed. The correlation coefficient and regression analysis using robust regression (each implemented within MATLAB software) were calculated for the *PIM* and *POM* values in the particular seasons (Fig. 8A, Table 1).

4. Results

4.1. Meteorological conditions

The daily mean air temperatures, precipitation and snow coverage during the study period (2015–2016) are presented in Fig. 2A and B. The air temperature was the highest (11.5°C) at the end of July and beginning of August 2015. The lowest daily mean air temperatures (down to −16.1°C) occurred in March 2016. The ablation season, defined as the period with positive air temperatures, lasted from the end of May 2015 to

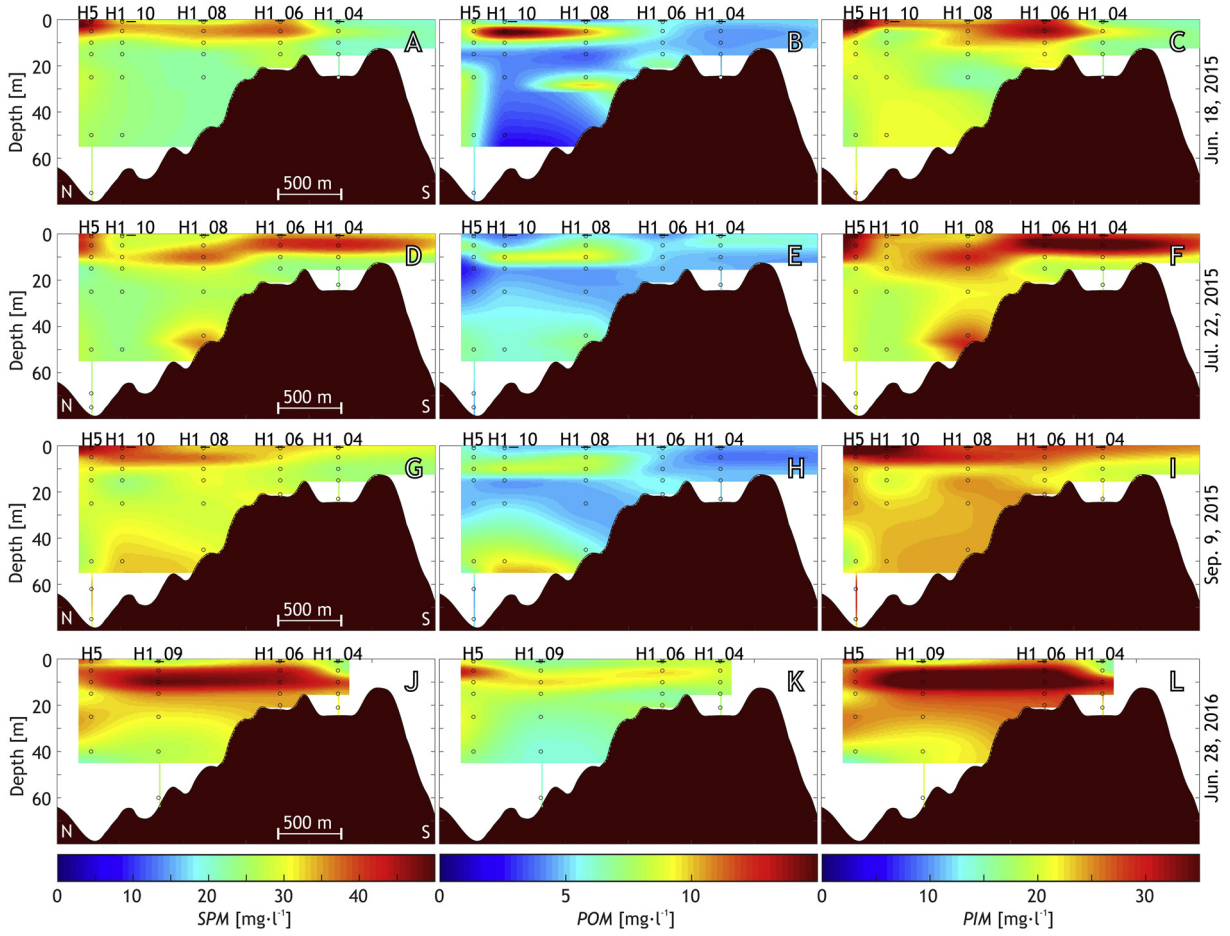

Figure 6 Interpolated distributions of suspended particulate matter (*SPM*) (A, D, G, J), particulate organic matter (*POM*) (B, E, H, K), and particulate inorganic matter (*PIM*) (C, F, I, L) during the summer season in Hansbukta. The interpolations are based on data taken on the 18th of June 2015 (A, B, C), 22nd of July 2015 (D, E, F), 9th of September 2015 (G, H, I), and 28th of June 2016 (J, K, L). For the location of monitoring stations see Fig. 1.

the middle of October 2015 and from the beginning of May 2016 to the end of the study period. However, during the winter, the daily average temperatures were above 0°C several times, particularly at the end of December and the beginning of January (Fig. 2A). Average daily air temperatures were close to 0°C during the second half of October and first half of November. The daily precipitation was low until the middle of August 2015, then precipitation values increased significantly and slowly decreased in autumn 2015 (Fig. 2B). In 2015, the snow coverage percentage was less than 50% in the middle of June and completely disappeared from coastal zone during the beginning of July. The snow coverage pattern in 2016 was similar, but the snow melting occurred about half a month earlier (Fig. 2B).

4.2. Oceanography

The oceanographic conditions revealed clear seasonal variations. The water temperature measured at station H1_09 ranged from −1.8°C during winter and early spring to more than 2°C at the end of July and beginning of August 2015 (Figs. 2C and 3A). The seasonality of the mean water temperature was characterised by a rapid increase from late spring to early summer, small fluctuations during summer and a gradual decrease during autumn. The water temperature increase during the spring/summer transition occurred about one month earlier in 2016 than in 2015 (Figs. 2C and 3A).

Water salinity ranged from less than 30 to almost 35 PSU (Figs. 2D and 3C). The highest salinity was measured during the early spring (May 2015, April and May 2016) and the lowest was measured during the summer (August 2015).

During the study period, three types of water masses were observed in the inner part of Hansbukta. In the spring, the WCW dominated (in 2015, it dominated below a 25 m depth, and in 2016 was present in complete water column). The dominant water mass became LW by the end of June in 2015 and by the middle of June in 2016. Then, in the span of a few days the LW mass was replaced with SW. The latter completely filled the inner part of Hansbukta during the summer of 2015, and it was replaced by LW in the autumn (mid-October 2015). The late autumn/winter period, during which WCW became the dominant water mass, was not documented due to a gap in the measurements. The periods of WCW transformation into LW and then into SW coincided with periods of distinct water stratification (Fig. 3A and C) with maximum σ_T values in June 2015, as well as at the end of May and beginning of June 2016 (Fig. 3B). During the summer (from mid-July to October 2015), stratification was less

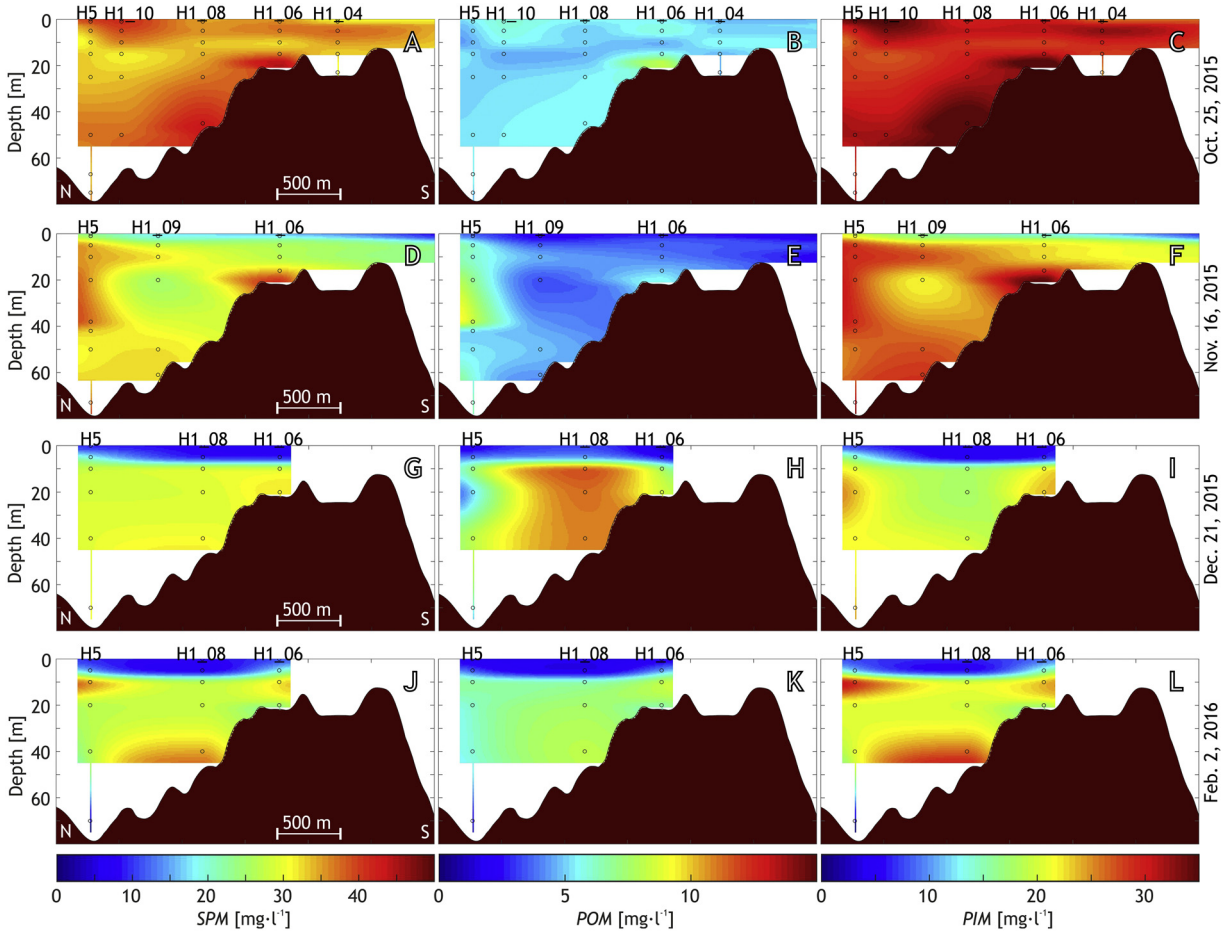

Figure 7 Interpolated distributions of suspended particulate matter (*SPM*) (A, D, G, J), particulate organic matter (*POM*) (B, E, H, K), and particulate inorganic matter (*PIM*) (C, F, I, L) during the autumn (A to F) and winter (G to L) seasons in Hansbukta. The interpolations are based on data taken on the 25th of October 2015 (A, B, C), 16th of November 2015 (D, E, F), 21st of December 2015 (G, H, I), and 6th of February 2016 (J, K, L). For the location of monitoring stations see Fig. 1.

pronounced and was restricted to the surface water layers. During the late autumn of 2015 and the early spring of 2016, the waters were well mixed (Fig. 3A–C).

The calculated *FWF* ranged from nearly 1% in spring 2015 and 2016 to almost 10% in summer, with a maximum in August 2015 (Fig. 3D). A rapid increase in the *FWF* was observed from the late spring (beginning of June) to the middle of the summer (beginning of August) 2015. The *FWF* slowly decreased in the autumn. During the spring of 2016, the increase in *FWF* was slower and started earlier than in the spring of 2015 (Fig. 3D).

The ADCP data from the mid-July, revealed two main flow directions in the inner part of Hansbukta (Fig. 4A, B, D, E). Surface flux, with a velocity between 10 and 15 cm s^{-1}, moved from the NE (east part of ice cliff) to SW (into the fjord), while near-bottom and mid-water depth flux, faster than 15 cm s^{-1}, had the opposite direction. In early September the fluxes were weaker and originated mainly from the western part of glacier cliff (Fig. 4G, H, J, K). The high flow velocity was observed in subsurface water and near the bottom, where current velocities along the bay were over 15 cm s^{-1} (Fig. 4A, B, D, E).

Fast ice was observed inside Hansbukta until the middle of May 2015. After this period, the bay and almost entire Hornsund fjord was covered by drifting sea ice until the end of May 2015. Almost no sea ice was observed during the 2016 season (Fig. 2C).

4.3. Suspended particulate matter

Information on the *SPM* distribution was obtained from satellite images and ADCP surveys for the mid- and late summer and from water sampling throughout the study period. The satellite images revealed the location of major freshwater sediment-laden subglacial outflows from the tide-water glacier cliff. The outflows were observed in the images from the 6th and 31st of June; 8th, 15th, and 17th of September; and the 1st of October 2015 as *SPM*-rich surface water plumes. In the case of the other available images, the weather was cloudy or outflows were not identified. The most prominent outflow was from the eastern part of the Hansbreen cliff, and it was seen in all the described satellite images. Moreover, a number of images contain emerging plumes from outflows located in the western (the 6th and 31st of June, the 15th and 17th of September and the 1st of October 2015) and central (the 15th of September and 1st of October 2015) parts of the glacier cliff (Fig. 1).

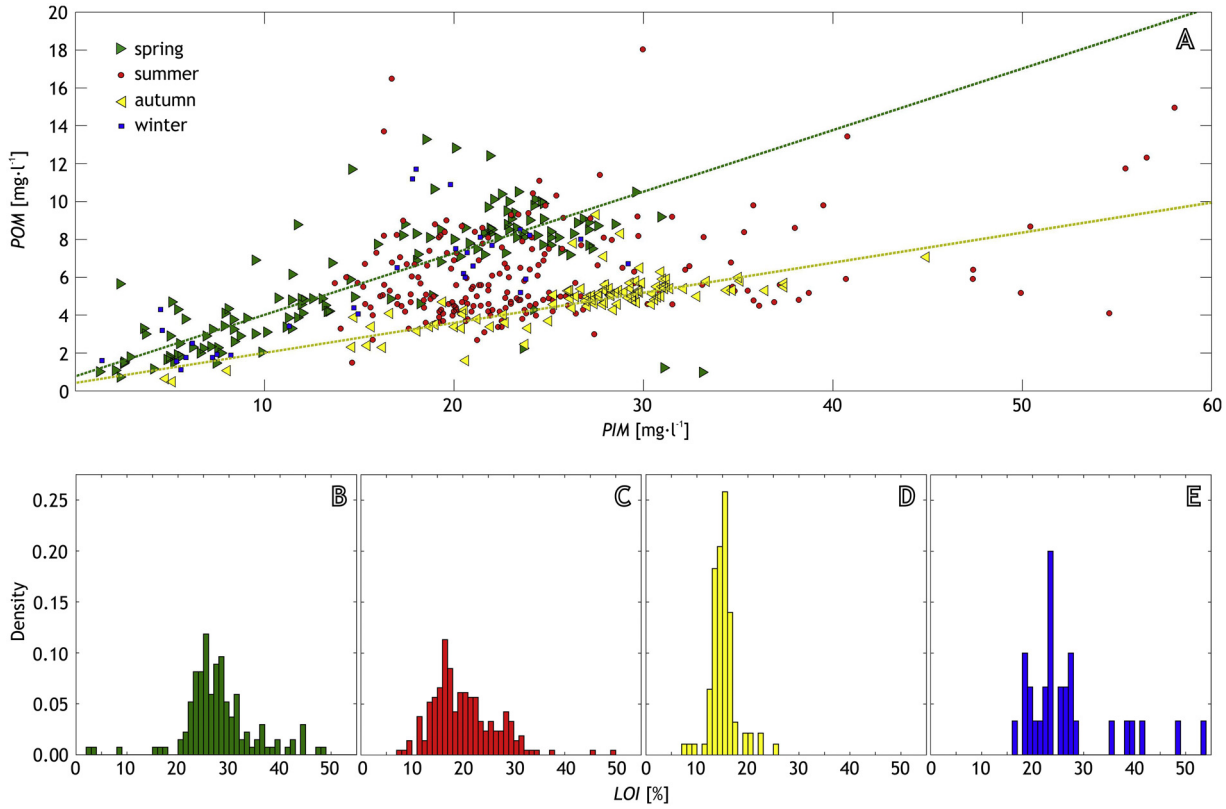

Figure 8 Changes in the composition of suspended particulate matter (*SPM*) over time. (A) Scatter plot of particulate inorganic matter (*PIM*) and particulate organic matter (*POM*) concentrations with linear regressions for the spring (green dotted line) and autumn seasons (yellow dotted line). The data from spring season are marked as green right triangles, summer as red circles, autumn as yellow left triangles and winter as blue squares. The B–D) present probability density distribution of loss on ignition (*LOI*) in the following seasons: (B) spring, (C) summer, (D) autumn, and (E) winter. (For interpretation of the references to color in this figure legend, the reader is referred to the web version of this article.)

Table 1 The correlation coefficient R^2, number of measurements and robust linear regression for particulate inorganic matter (*PIM*) and particulate organic matter (*POM*) for different seasons.

	R^2	Number of measurements	Robust linear regression
Spring	0.56	135 during 5 days	$POM = 0.78 + 0.33 \cdot PIM$
Summer	0.08	212 during 4 days	No correlation
Autumn	0.59	93 during 2 days	$POM = 0.43 + 0.16 \cdot PIM$
Winter	0.59	30 during 2 days	Low number of measurements

In the ADCP surveys, the outflow from the eastern part of Hansbreen was the most evident, while the western and central outflows were only partly resolved (Fig. 4D–F, J–L). The values of *Int*, which reflect *SPM* concentration, were higher in July than in September. However, while both surveys showed that most of the *SPM* was contained to Hansbukta and that only a small amount escaped from the bay (Fig. 4C and I), the *SPM* distributions within the bay was different. In July, the *SPM* maximum was related to the major outflow from the eastern part of Hansbreen, while the two secondary maxima of *Int* were likely related to the outflow from the western part of Hansbreen and to the region in axial part of the bay, below 40 m deep, with rapid flow towards the glacier (Fig. 4D–F). In September, although the outlined maxima in *Int* were still visible, the *SPM* distribution was more uniform (Fig. 4L).

The *SPM* concentrations measured in the water samples ranged from 2.3 mg l^{-1} on the 24th of May 2016 at station H1_09 on the water surface to 82.8 mg l^{-1} on the 18th of June 2015 at station H5_05, which is close to main glacier outflow, at a 1 m depth. The mean *SPM* concentrations averaged for the daily data were the highest during the ablation season in the summer and early autumn, with a maximum average concentration in October 2015 (over 35 mg l^{-1}). The lowest average concentrations were measured during the winter and spring, and a minimum averaged concentration was documented in the 2015 spring season (below 10 mg l^{-1}) in a period shortly after the sea ice disappeared (Appendix A1,

Fig. 2E). The annual course of the changes in the *SPM* mean concentration is characterised by a rapid increase at the end of May and beginning of June 2015 (from 10 to more than 25 mg l^{-1}). After June, the mean concentration increased gradually until the end of October. The mean *SPM* concentration decreased during the late autumn and beginning of winter to approximately 25 mg l^{-1} in December. In April 2016, the mean *SPM* concentration was approximately 25 mg l^{-1} and increased to 35 mg l^{-1} in the second part of June. Moreover, an episodic increase of the *SPM* concentration was observed in the first half of May 2016 (Fig. 3E).

A comparison of the *SPM* distribution (Figs. 5–7) and mean *SPM* concentration in the surface waters (0–10 m) and deeper layers (below 20 m) (Fig. 3E) reveals clear seasonal variability. From June to September, the *SPM* was predominantly in the surface layer, while from November until May, it was predominantly in the deeper water. In October 2015, the amount of *SPM* in the surface waters was very similar to the amount in the deeper layers.

The *LOI* in the *SPM* ranged from 2.9% on the 9th of May 2016 at station H1_09 near the bottom of the bay to 70.6% on the same day at station H1_04 at a depth of 10 m. During the spring, the measured *LOI* mostly ranged between 20 and 40%, with a mode of approximately 25% (Fig. 8B). The highest average *LOI* (approximately 30%) was observed during the spring of 2016 (Appendix A2, Fig. 2F). During the summer season, the *LOI* achieved its lowest values and varied between 10 and 30% with a mode of approximately 15% (Fig. 8C). The values of *LOI* in the *SPM* during the autumn were similar to the values in the summer and ranged from 10 to 20% with a mode of approximately 15% (Fig. 8D). In the winter, the *LOI* in the *SPM* was slightly higher, ranging from 20 to 30% (Fig. 8E).

The highest concentrations of *POM* were measured during the spring and summer, and the highest concentrations of *PIM* were measured during the summer and autumn (Fig. 8A). No correlation was observed between the measured *POM* and *PIM* during the summer (R^2 = 0.08). During the winter, the correlation between *POM* and *PIM* was 0.59; however, there were too few measurements for linear regression to be calculated. The correlations between *POM* and *PIM* were 0.56 during the spring and 0.59 during the autumn (Table 1, Fig. 8A). The seasonal spatial variability of the *POM* and *PIM* distributions (Figs. 3F and 5–7) was similar to the total *SPM* concentration pattern.

5. Discussion

5.1. The studied seasons in the context of multiyear variability

During previous decades, due to specific oceanographic or meteorological conditions like the massive intrusion of AW into fjords, some years and seasons were exceptional (e.g. Cottier et al., 2005). However, the study period from 2015 to 2016 appears to be representative of typical conditions during the past decade when it is considered in a context of multiyear analyses of meteorological conditions from the PPS in Hornsund (Cisek et al., 2017; Osuch and Wawrzyniak, 2016, 2017), as well as snow coverage variability analyses (Kępski et al., 2017). A comparison of the study period to the general summer oceanographic condition in Hornsund also proved that the studied summer was similar to those observed in the previous years (Promińska et al., 2017). In the studied period, sea ice occurred in the spring of 2015 and was absent in 2016. However, as documented by Muckenhuber et al. (2016), the irregular presence of sea ice in Hornsund was also noticed during previous seasons. In terms of the range of the *SPM* concentrations, the measured summer values are similar to the concentrations that have been previously reported from tidewater glacier-affected bays in Svalbard, which usually have values ranging from a few to approximately 100 mg l^{-1} (Elverhøi et al., 1983; Görlich, 1986; Görlich et al., 1987; Svendsen et al., 2002; Szczuciński and Zajączkowski, 2012; Zajączkowski, 2008). Thus, the conditions during the studied period can be considered to be typical for contemporary subpolar fjords of Svalbard.

5.2. Sources of *SPM*

In Hansbukta, the *SPM* is mainly delivered through subglacial meltwater outflows from the cliff of Hansbreen. Based on satellite images (Fig. 1) and ADCP measurements (Fig. 4), we found that the positions of the outflows fluctuated during the studied period. However, the major subglacial meltwater discharge came from the eastern part of the ice cliff (Fig. 1), which was also predicted by a sub-glacial water flow model by Pälli et al. (2003). Hansbreen is a polythermal glacier (Jania et al., 1996); thus, meltwater discharge is possible throughout the year. However, the discharge becomes significant only during the ablation season (Fig. 2A), when the major glacial channels are unblocked due to the high pressure of the meltwater (Pälli et al., 2003). The available data does not allow for precise estimates of suspended sediment discharge. However, assuming that the documented near-surface *SPM*-rich brackish layer contains mainly sediment delivered from the outflows, a simple estimate can be made based on the July ADCP profile (Fig. 4D and E). Using the cross-sectional area of a *SPM*-rich surface water plume of approximately 2500 m^2, multiplying this value by a minimum southward flow velocity of 0.12 m s^{-1} and an average *SPM* concentration of 50 mg l^{-1}, the obtained minimum estimate of the sediment flux is in the order of 15 kg s^{-1}. If this value is multiplied by the three months of the effective ablation season that have relatively high discharge rates and divided by Hansbreen drainage basin area of approximately 55 km^2, it provides a sediment yield in order of 2000 t km^{-2} $year^{-1}$ (for the ablation season). This value is in the same order of magnitude as the sediment yields reported for subpolar and temperate glaciers (e.g., Gurnell et al., 1996; Koppes et al., 2015). Thus, it is very likely that the overwhelming majority of the *SPM* is delivered by the meltwater outflows and that the other *SPM* sources are secondary and may be important only seasonally.

Approximately one-fourth of the total ablation of Hansbreen is due to icebergs calving and ice front melting processes (Grabiec et al., 2012). The icebergs that are produced by Hansbreen are relatively small, and many of them are grounded and melted in the shallow parts of the Hansbukta (Ćwiąkała et al., 2018). Their contribution to the total *SPM* in the bay is relatively small. In the period from 2000 to 2008,

approximately 25.5 × 10^6 m^3 of ice was released as icebergs annually (Grabiec et al., 2012). Except in specific zones, such as 1–2 m thin basal ice layers or shear zones, the average percentage of debris in Hansbreen ranges from 0.05 to 0.5% (Rachlewicz and Szczuciński, 2000). Assuming an average rock density of approximately 2.5 kg m^{-3}, the annual sediment supply from melting icebergs is approximately 65; 5% of the daily supply from the meltwater outflows.

The remaining potential sources of *SPM* include transport by wind and surface runoff from the non-glaciated part of the Hansbukta drainage basin, coastal erosion, rafting by sea ice, biological production (e.g., phytoplankton blooms), import from the main fjord basin due to water exchange (e.g., due to tides) and the resuspension of previously deposited sediments. The supply of sediment from the non-glaciated land is negligible because it has a very small area and low relief. The majority of the terrestrial marginal zone of Hansbreen drains to adjacent bays (Fig. 1). In Hansbukta, no major coastal erosion is observed, although when the *SPM* concentrations from spring 2015 and 2016 are compared (Fig. 3D and E), they are higher in 2016, which is when no wave-protecting shore ice was observed.

The *POM* comes at least from two sources: supply of old organic matter from land and delivery of modern organic matter produced in marine environment. The recent works in Hornsund fjord applying carbon isotopes in organic matter in fjord sediments (Koziorowska et al., 2016; Szczuciński et al., 2017) and in *SPM* (Apolinarska et al., 2017) suggest that significant portion of organic carbon is delivered from erosion of older organic-rich sediments and rocks. This may also apply to the Hansbukta. However, the *POM* is at least partly derived from modern biological production, particularly in specific periods, for instance on the 9th of May 2016 (Fig. 5H) and on the 21st of December 2015 (Fig. 7H), when phytoplankton blooms and massive zooplankton advection likely occurred, respectively. Such phenomenons are commonly reported in the Arctic during the spring and autumn–winter seasons (e.g., Cowan et al., 1998; Görlich et al., 1987; Kwaśniewski et al., 2003; Rabindranath et al., 2008; Walkusz et al., 2003; Weydmann et al., 2013; Węsławski et al., 1988).

The *SPM* is also delivered by sediment resuspension from sill and shallow water regions. The resuspension is due to waves as well as water flow over the sill related to water exchange processes between Hansbukta and the main part of the Hornsund. The water exchange is driven by the tides, Coriolis-driven circulation patterns, as well as by water replacement due to freshwater supplies from meltwater outflows. This exchange of water is a typical oceanographic phenomenon in glacial bays separated by sills (e.g., Motyka et al., 2003; Rignot et al., 2010). The water exchange results in relatively fast near-bottom water flows (Fig. 4), in order of 15 cm s^{-1}, and sediment resuspension. The bottom of the bay around sill has relatively high *SPM* concentrations throughout the year (Figs. 5–7), which suggests that sediment resuspension from the sill is an important factor contributing to the *SPM* distribution in the bay.

5.3. Seasonality in *SPM* distribution

The seasonal changes in the *SPM* concentration, spatial distribution and composition (*POM*/*PIM*) result from the overlapping influences of a number of factors. The drivers discussed here include the duration of the ablation season, freshwater supply, glacial dynamics, *SPM* supply, water stratification and circulation in the bay, the bay bathymetry, presence of sea ice, light availability (polar day and night), biological productivity and sedimentary processes. Moreover, there are also several factors that were found important for *SPM* distribution in similar environments (Cowan and Powell, 1990; Gilbert et al., 2002; Görlich et al., 1987; Syvitski, 1989; Szczuciński and Zajączkowski, 2012) but cannot be here accurately evaluated due to the applied monthly sampling resolution. These factors include tides, storm events, daily fluctuations in the suspended sediment discharge and local wind damming effects.

5.3.1. Summer season

The summer distribution of *SPM*, with *SPM*-rich surface brackish water layer, is generally similar to the patterns that have been previously reported for tidewater glacier fronts (e.g., Curran et al., 2004; Görlich, 1986; Görlich et al., 1987; Syvitski, 1989; Szczuciński and Zajączkowski, 2012; Zajączkowski, 2002), although the 3D pictures provided by ADCP surveys (Fig. 4) showed the circulation to be more complex than previously believed. The intensive freshwater outflows that start in the spring-summer transition period (during June 2015 and May–June 2016) caused slight increase in the water temperature (Figs. 2C and 3A), a decrease in salinity (Fig. 2D and 3C) (transformation of WCW to LW), the development of water stratification (Fig. 3B), and increases in the *FWF* (Fig. 3D) and *SPM* concentration (Fig. 2E and 3E) in Hansbukta.

The large amount of *SPM* that was delivered to the bay was mainly confined to the approximately 10 m thick (Fig. 6) brackish surface water layer. Considering the total *SPM* supply, one could expect even higher *SPM* concentrations in the surface water; however, this water mass is in motion (Fig. 4A and B), and the *SPM* is partly exported from the bay by the surface currents. Moreover, *SPM* in surface layer is removed due to fast settling of flocculated particles.

The flocculation (aggregation) of *SPM*, documented by Laser In Situ Scattering and Transmissometry measurements (Szczuciński and Moskalik, 2017), is enhanced by high *SPM* concentrations, turbulence related to fast flow velocity and the mixing of saline water with freshwater. The *SPM* is composed of approximately 85% of grains smaller than 60 μm, as inferred from the bottom sediments (Görlich, 1986). However, the suspended aggregates that were observed during summer in the surface water layer had a mean floc grain size ranging from 30 to over 120 μm, and below the pycnocline were transferred only aggregates with a mean floc size over 125 μm, which is an equivalent of fine sand grain size fraction (Szczuciński and Moskalik, 2017).

Thus the well-developed pycnocline serves as a barrier for settling particles and is likely the major reason for the higher *SPM* concentrations in the surface water, in particular close to pycnocline (Figs. 3E and 6). During the summer, a steady increase in *FWF* (Fig. 3D) and a weakening of the stratification (Fig. 3B) reduced the role of pycnocline. Simultaneously faster increases in the *SPM* concentration in the deeper water was observed than in the nearby surface (Fig. 3E), which was possibly related to the longer residence time (slower settling rate) of smaller aggregates, which could settle through a smaller density gradient of the pycnocline.

The *SPM* concentration near the bottom of the bay (Fig. 6) is likely a result of resuspension due to the fast water flow over the sill separating Hansbukta from the main Hornsund basin, which was observed during the ADCP surveys (Fig. 4).

The *SPM* in the summer is mostly composed of *PIM*, while the *POM* concentration reaches a similar level to the *POM* concentration during the remaining part of the year. There is no correlation between the *POM* and *PIM* (Fig. 8A and C), which suggests various *SPM* sources or segregation processes. In the summer, *POM* is mainly concentrated along the lower boundary of the surface brackish layer (Fig. 6). According to a commonly reported model (e.g., Lydersen et al., 2014), the *POM* maximum is likely related to zooplankton, which is pumped to Hansbukta at depth with fjord water in exchange for the exported brackish surface water. The fjord waters upwell next to the ice front and the zooplankton population experiences massive mortality rates due to osmotic shock (Węsławski and Legeżyńska, 1998; Zajączkowski and Legeżyńska, 2001). Consequently, such settings are well-known feeding grounds for birds and mammals (Lydersen et al., 2014; Urbanski et al., 2017).

5.3.2. Autumn season

The annual maximum mean *SPM* concentration occurred in the middle of the autumn season (Fig. 3E). During that time, the *SPM*, *POM* and *PIM* distributions were relatively uniform (Fig. 7) in the surface and deeper water masses (Fig. 3E and F). This is likely due to several processes: the density-driven vertical mixing of water in the bay and disappearance of the water stratification (Fig. 3B), enhanced resuspension and mixing during frequent in autumn storms (Wojtysiak et al., 2018), and a reduction in flocculation processes that elongates the residence time of the *SPM* in the water column. The latter was reported also for autumn season in the glacial bay of Adolfbukta (central Spitsbergen) by Szczuciński and Zajączkowski (2012). They compared the summer and autumn conditions and found that the vertical particulate matter fluxes measured with sediment traps decreased by an order of magnitude in the autumn, while the *SPM* concentrations decreased only two-fold. Szczuciński and Zajączkowski (2012) interpreted these observations as a result of a decrease in *SPM* flocculation, resulting in the slowing of the settling rate and the elongation of *SPM* residence times in the water column. However, in contrary to their study, in Hansbukta the *SPM* concentration increased in the autumn. The major reason for the difference may be the fact that Adolfbukta lacks a shallow sill, thus *SPM* may be easily exported from the bay and potential sediment resuspension is limited. In Hansbukta, the presence of a shallow sill causes the *SPM* to be trapped in the bay and enriched in resuspended sediment due to accelerated water flow over the sill.

In November, the *SPM* concentration decreased, particularly in the surface water layer (Figs. 3E and 7A, D), which was depleted of *SPM* due to successive *SPM* settling that was not compensated by the delivery of new *SPM*.

POM and *PIM* concentrations are correlated in autumn (Table 1, Fig. 8A and D). The correlation is likely due to efficient mixing of the *SPM* during the autumn. In December and at the end of autumn (Fig. 7H), an increase in the *POM* concentration in the subsurface waters of the central part of the bay was observed. At that time, the supply from the land had already ceased, air temperatures were well below 0°C, and the primary production in the water was at its lowest level due to the polar night conditions, so the most likely source of the elevated *POM* was the advection of rich in zooplankton fjord and/or shelf waters, as was mentioned in other studies (e.g.: Rabindranath et al., 2008; Walkusz et al., 2009; Weydmann et al., 2013; Węsławski et al., 1988; Zajączkowski et al., 2010).

5.3.3. Winter season

During the winter, the mean *SPM* concentrations reached minimum values in the surface layer, but the water column average remained same as during the summer season (Fig. 3E). The *SPM* was mainly concentrated in the deeper part of the bay (Fig. 7G and J), particularly above the sill, on the sill slope and near the glacier. This may suggest that a major source of *SPM* is the resuspension of sediments, particularly in shallow areas. In the winter, the *SPM* largely comes from the recycling of previously delivered material. The partial exposure of the bay to oceanic swell, the tidal currents and the relatively shallow sill that confines the bay and accelerates flow may all contribute to resuspension of sediments and sustain the *SPM* in suspension. Since Hansbreen is a polythermal glacier (Jania et al., 1996), it is also possible that there are some minor subglacial discharges of suspended sediment in winter.

5.3.4. Spring season

The studied period encompassed two spring seasons, which differed in terms of sea ice conditions. During the spring of 2016, which had no sea ice cover, the average *SPM*, *POM* and *PIM* concentrations were similar to the concentrations of the previous autumn and winter seasons (Figs. 2E and 3E, F). The spatial *SPM* distribution was also the same as the distribution in the winter before the onset of ablation (April) and developed into the summer distribution by an increase in the surface water layer in the weeks following the ablation onset (Fig. 6D–O). The conditions were different in spring 2015, when sea ice cover and well-developed shore ice occurred (Figs. 2, 3 and 6) and the *SPM*, *POM* and *PIM* were the lowest. In both of the spring seasons, the *PIM* and *POM* were correlated (Table 1, Fig. 8A and B), which may suggest that the *SPM* is largely composed of the same material, which is reworked over time. The difference between the 2015 and 2016 spring seasons is likely mainly due to sea ice occurrence during 2015 and limited wave action during this season.

Although *POM* and *PIM* generally correlate, there were also some differences. This was most likely a result of a phytoplankton bloom increasing suspended *POM* concentrations, as commonly occur in the Arctic during the spring season (e.g., Cowan et al., 1998; Görlich et al., 1987; Pawłowska et al., 2011; Węsławski et al., 1988; Zajączkowski et al., 2010). Such situation was documented on the 9th of May 2016 (Fig. 5H).

5.4. Implications for remote sensing based studies

The estimates of freshwater and *SPM* delivery to the coastal ocean from tidewater glaciers and the assessment of their global importance require the application of remote sensing methods that allow simultaneous measurements over large

areas. While these methods appeared to be successful in estimating the sediment supplies of meltwater rivers (e.g., Overeem et al., 2017), they are still of limited use in the case of fjords. The in situ investigations of *SPM* deliveries and distributions near tidewater glacier fronts are often dangerous, expensive and time-consuming, so investigations applying analyses of satellite images are particularly useful (e.g., Hodgkins et al., 2016; Hudson et al., 2014; Schildt et al., 2017; Urbanski et al., 2017). However, they have a number of restrictions. For example, they are usually limited to the short summer season, they must be calibrated with in situ data and they only provide information about surface water. It is commonly assumed that the major *SPM* discharge near tidewater glacier fronts is limited to the brackish surface layer of the water in front of tidewater glaciers. However, the present study shows that a maximum amount of the *SPM* during the summer is at the lower boundary of the surface brackish water layer, which is approximately 10 m thick. Moreover, during the majority of the year, most of the *SPM* is located in deeper waters (>20 m), which is also the case during the period with maximum average *SPM* concentrations in early autumn (Fig. 3E). Thus, the remote sensing data must be carefully interpreted when water surface reflectance is used to estimate the *SPM* concentration because subsurface *SPM* concentrations may be even higher than at the surface.

6. Conclusions

The study presents the first monitoring data of *SPM* concentrations in a sub-polar glacial bay in context of its local oceanographic and meteorological conditions over almost one year. The observed seasonal *SPM* concentration variations appear to result not only from the dominant glacial meltwater input that delivers the vast majority of *SPM* but also from the intensity of flocculation processes that control the residence period of the particles in the water, the resuspension of *SPM* and biological productivity. The documented circulation pattern appears to be more complex than the patterns typically assumed in simple 2D models and is strongly affected by the presence of shallow sill at the entrance. In Hansbukta, the highest single *SPM* concentration value was measured at the beginning of the summer, but the mean *SPM* value gradually increased during the summer with a peak in the autumn, long after the freshwater discharge maximum. During the summer, the *SPM* was mainly concentrated in the surface water layer; during the rest of the year, the opposite occurred, with higher *SPM* levels observed in the deep water layer. Generally, the *POM* content of the *SPM* was stable, except during spring phytoplankton blooms (maximum *POM* concentration) and spring periods with sea ice cover (minimum *POM* concentration).

Author contributions

Mateusz Moskalik and Witold Szczuciński wrote the final version of the manuscript. Mateusz Moskalik made all the data calculations and analyses, prepared the material for the figures and led the discussions. Joanna Ćwiąkała participated in laboratory work and partly wrote the manuscript. Aleksander Dominiczak participated in laboratory work. All authors helped prepare the discussion and conclusion sections.

Acknowledgements

This publication was financed by the statutory activities No 3841/E-41/S/2016 of the Ministry of Science and Higher Education of Poland and by the funds of the Leading National Research Centre (KNOW), received by the Centre for Polar Studies, for the period 2014—2018. W.S., A.D., P.Z. and partly M.M. were supported by the Polish National Science Centre (NCN) grant No. 2013/10/E/ST10/00166.

We thank the Institute of Geophysics PAS (especially Tomasz Wawrzyniak, Maciej Błaszkowski, Mariusz Czarnul) for providing meteorological and oceanographical data used in this investigation and the Polish Polar Station Hornsund staff for establishing and maintaining the meteorological site and oceanographical monitoring. We also thank Urszula Hordyjewska-Cejko and Kamila Jarosz from Marie Curie Skłodowska University in Lublin and Paweł Kaczmarek from Adam Mickiewicz University in Poznań for their help with laboratory work. Constructive comments by two anonymous reviewers and the editor — Prof. Janusz Pempkowiak, contributed to the improvement of the manuscript and are gratefully acknowledged.

Appendix A. Supplementary data

Supplementary data associated with this article can be found, in the online version, at doi:10.1016/j.oceano.2018.03.001.

References

Apolinarska, K., Szczuciński, W., Moskalik, M., Dominiczak, A., 2017. Seasonal changes, spatial variability and origin of suspended organic matter in Hornsund, Spitsbergen. EGU General Assembly 2017. Geophys. Res. Abstracts 19, EGU2017-10283.

Bennett, M., Glasser, N., 2009. Glacial Geology: Ice Sheets and Landforms. Wiley Blackwell, 385 pp.

Bhatia, M.P., Kujawinski, E.B., Das, S.B., Breier, C.F., Henderson, P. B., Charette, M.A., 2013. Greenland meltwater as a significant and potentially bioavailable source of iron to the ocean. Nat. Geosci. 6, 274—278, http://dx.doi.org/10.1038/ngeo1746.

Birkenmajer, K., 1990. Geology of Hornsund Area, Spitsbergen. Map 1:75000 and Explanations. Silesia Univ, Katowice.

Błaszczyk, M., Jania, J., Hagen, J.O., 2009. Tidewater glaciers of Svalbard: recent changes and estimates of calving fluxes. Polish Polar Res. 30 (2), 85—142.

Błaszczyk, M., Jania, J.A., Kolondra, L., 2013. Fluctuations of tidewater glaciers in Hornsund Fjord (Southern Svalbard) since the beginning of the 20th century. Polish Polar Res. 34 (4), 327—352, http://dx.doi.org/10.2478/popore-2013-0024.

Boldt, K.V., Nittrouer, C.A., Hallet, B., Koppes, M.N., Forrest, B.K., Wellner, J.S., Anderson, J.B., 2013. Modern rates of glacial sediment accumulation along a 15° S-N transect in fjords from the Antarctic Peninsula to southern Chile. J. Geophys. Res.-Earth 118, 2072—2088, http://dx.doi.org/10.1002/jgrf.20145.

Carr, R., Stokes, C.R., Vieli, A., 2017. Threefold increase in marine-terminating outlet glacier retreat rates across the Atlantic Arctic: 1992—2010. Ann. Glaciol. 58 (74), 72—91, http://dx.doi.org/10.1017/aog.2017.3.

Chauche, N., Hubbard, A., Gascard, J.C., Box, J.E., Bates, R., Koppes, M., Sole, A., Patton, H., 2014. Ice-ocean interaction and calving front morphology at two west Greenland tidewater

outlet glaciers. Cryosphere 8, 1457—1468, http://dx.doi.org/10.5194/tc-8-1457-2014.

Cisek, M., Makuch, P., Petelski, T., 2017. Comparison of meteorological conditions in Svalbard fjords: Hornsund and Kongsfjorden. Oceanologia 59 (4), 413—421, http://dx.doi.org/10.1016/j.oceano.2017.06.004.

Cottier, F.R., Tverberg, V., Inall, M.E., Svendsen, H., Nilsen, F., Griffiths, C., 2005. Water mass modification in an Arctic fjord through cross-shelf exchange: the seasonal hydrography of Kongsfjorden, Svalbard. J. Geophys. Res. 110, C12005, http://dx.doi.org/10.1029/2004JC002757.

Cowan, E.A., Cai, J., Powell, R.D., Seramur, K.C., Spurgeon, V.L., 1998. Modern tidal rhythmites deposited in a deep-water estuary. Geo-Mar. Lett. 18 (1), 40—48, http://dx.doi.org/10.1007/s003670050.

Cowan, E., Powell, R.D., 1990. Suspended sediment transport and deposition of cyclically interlaminated sediment in a temperate glacial fjord, Alaska, U.S.A. In: Dowdeswell, J.A., Scourse, J.D. (Eds.), Glacimarine Environments: Processes and Sediments. Geol. Soc. Spec. Publ. 53, 75—89.

Curran, K.J., Hill, P.S., Milligan, T.G., Cowan, E.A., Syvitski, J.P.M., Konings, S.M., 2004. Fine-grained sediment flocculation below the Hubbard Glacier meltwater plume, Disenchantment Bay, Alaska. Mar. Geol. 203, 83—94, http://dx.doi.org/10.1016/S0025-3227(03)00327-X.

Ćwiąkała, J., Moskalik, M., Forwick, M., Wojtysiak, K., Giżejewski, J., Szczuciński, W., 2018. Submarine geomorphology at the front of the retreating Hansbreen tidewater glacier Hansbreen, Hornsund fjord, southwest Spitsbergen. J. Maps 14 (2), 123—134, http://dx.doi.org/10.1080/17445647.2018.1441757.

Deines, K.L., 1999. Backscatter estimation using Broadband acoustic Doppler current profilers. In: Anderson, S.P., Terray, E.A., Rizoli White, J.A., Williams, A.J. (Eds.), Proceedings of the IEEE Sixth Working Conference on Current Measurement, San Diego, CA, 249—253.

Dowdeswell, J.A., Cromack, C., 1991. Behavior of a glacier-derived suspended sediment plume in a small Arctic inlet. J. Geol. 99, 111—123, http://dx.doi.org/10.1086/629477.

Dowdeswell, J.A., Hogan, K.A., Arnold, N.S., Mugford, R.I., Wells, M. J., Hirst, P.P., Decalf, C., 2015. Sediment-rich meltwater plumes and ice-proximal fans at the margins of modern and ancient tidewater glaciers: observations and modelling. Sedimentology 62 (6), 1665—1692, http://dx.doi.org/10.1111/sed.12198.

Drewnik, A., Węsławski, J.M., Włodarska-Kowalczuk, M., Łącka, M., Promińska, A., Zaborska, A., Gluchowska, M., 2016. From the worm's point of view. I: Environmental settings of benthic ecosystems in Arctic fjord (Hornsund, Spitsbergen). Polar Biol. 39 (8), 1411—1424, http://dx.doi.org/10.1007/s00300-015-1867-9.

Elverhøi, A., Lønne, Ø., Seland, R., 1983. Glaciomarine sedimentation in a modern fjord environment, Spitsbergen. Polar Res. 1 (2), 127—149, http://dx.doi.org/10.1111/j.1751-8369.1983.tb00697.x.

Forwick, M., Vorren, T.O., Hald, M., Korsun, S., Roh, Y., Vogt, C., Yoo, K.-C., 2010. Spatial and temporal influence of glaciers and rivers on the sedimentary environment in Sassenfjorden and Tempelfjorden, Spitsbergen. In: Howe, J.A., Austin, W.E.N., Forwick, M., Paetzel, M. (Eds.), Fjords Systems and Archives, vol. 344. Geological Soc., Spec. Publ., London, 165—195, http://dx.doi.org/10.1144/SP344.13.

Gilbert, R., Nielsen, N., Möller, H., Desloges, J.R., Rasch, M., 2002. Glaciomarine sedimentation in Kangerdluk (Disko Fjord), West Greenland, in response to a surging glacier. Mar. Geol. 191, 1—18, http://dx.doi.org/10.1029/2002GC000441.

Görlich, K., 1986. Glacimarine sedimentation of muds in Hornsund Fjord, Spitsbergen. Ann. Soc. Geol. Pol. 56, 433—477.

Görlich, K., Węsławski, J.M., Zajączkowski, M., 1987. Suspension settling effect on macrobenthos biomass distribution in the Hornsund fjord, Spitsbergen. Polish Polar Res. 5, 175—192, http://dx.doi.org/10.1111/j.1751-8369.1987.tb00621.x.

Grabiec, M., Jania, J., Puczko, D., Kolondra, L., Budzik, T., 2012. Surface and bed morphology of Hansbreen, a tidewater glacier in Spitsbergen. Polish Polar Res. 33 (2), 111—138, http://dx.doi.org/10.2478/v10183-012-0010-7.

Gurnell, A., Hannah, D., Lawler, D., 1996. Suspended sediment yield from glacier basins. In: Erosion and Sediment Yield: Global and Regional Perspectives. IAHS Publ. 236, 97—104.

Heiri, O., Lotter, A.F., Lemcke, G., 2001. Loss on ignition as a method for estimating organic and carbonate content in sediments: reproducibility and comparability of results. J. Paleolimmnol. 25, 101—110, http://dx.doi.org/10.1023/A:100811961.

Hodgkins, R., Bryant, R., Darlington, E., Brandon, M., 2016. Pre-melt-season sediment plume variability at Jökulsárlón, Iceland, a preliminary evaluation using in-situ spectroradiometry and satellite imagery. Ann. Glaciol. 57 (73), 39—46, http://dx.doi.org/10.1017/aog.2016.20.

Hudson, B., Overeem, I., McGrath, D., Syvitski, J.P.M., Mikkelsen, A., Hasholt, B., 2014. MODIS observed increase in duration and spatial extent of sediment plumes in Greenland fjords. Cryosphere 8, 1161—1176, http://dx.doi.org/10.5194/tc-8-1161-2014.

Jakacki, J., Przyborska, A., Kosecki, S., Sundfjord, A., Albretsen, J., 2017. Modeling of the Svalbard Fjord Hornsund. Oceanologia 59 (4), 473—495, http://dx.doi.org/10.1016/j.oceano.2017.04.004.

Jania, J., Mochnacki, D., Gądek, B., 1996. The thermal structure of Hansbreen, a tidewater glacier in southern Spitsbergen, Svalbard. Polar Res. 15, 53—66.

Ketchum, B.H., 1950. Hydrographic factors involved in the dispersion of pollutants introduced into tidal waters. J. Boston Soc. Civ. Eng. 37, 296—314.

Kępski, D., Luks, B., Migała, K., Wawrzyniak, T., Westermann, S., Wojtuń, B., 2017. Terrestrial remote sensing of snowmelt in a diverse High-Arctic tundra environment using time-lapse imagery. Remote Sens. 9 (7), 733, http://dx.doi.org/10.3390/rs9070733.

Kim, Y.H., Voulgaris, G., 2003. Estimation of suspended sediment concentration in estuarine environments using acoustic backscatter from an ADCP. In: Davis, R.A., Sallenger, A., Howd, P. (Eds.), Proc. International Conference on Coastal Sediments, Sheraton Sand Key Resort, 18—23 May 2003, Clearwater Beach, FL, USA.

Koppes, M.N., Hallet, B., 2002. Influence of rapid glacial retreat on the rate of erosion by tidewater glaciers. Geology 30 (1), 47—50, http://dx.doi.org/10.1130/0091-7613(2002)030<0047:IORGRO>2.0.CO;2.

Koppes, M., Hallet, B., Rignot, E., Mouginot, J., Wellner, J.S., Boldt, K., 2015. Observed latitudinal variations in erosion as a function of glacier dynamics. Nature 526, 100—103, http://dx.doi.org/10.1038/nature15385.

Koziorowska, K., Kuliński, K., Pempkowiak, J., 2016. Sedimentary organic matter in two Spitsbergen fjords: terrestrial and marine contributions based on carbon and nitrogen contents and stable isotopes composition. Cont. Shelf Res. 113, 38—46, http://dx.doi.org/10.1016/j.csr.2015.11.010.

Kwaśniewski, S., Hop, H., Falk-Petersen, S., Pedersen, G., 2003. Distribution of Calanus species in Kongsfjorden, a glacial fjord in Svalbard. J. Plankton Res. 25 (1), 1—20, http://dx.doi.org/10.1093/plankt/25.1.1.

Lydersen, C., Assmy, P., Falk-Petersen, S., Kohler, J., Kovacs, K.M., Reigstad, M., Steen, H., Strøm, H., Sundfjord, A., Varpe, Ø., Walczowski, W., Weslawski, J.M., Zajaczkowski, M., 2014. The importance of tidewater glaciers for marine mammals and seabirds in Svalbard, Norway. J. Mar. Sys. 129, 452—471, http://dx.doi.org/10.1016/j.jmarsys.2013.09.006.

Łupikasza, E., 2013. Atmospheric precipitation. In: Marsz, A.A., Styszyńska, A. (Eds.), Climate and Climate Change at Hornsund, Svalbard. Gdynia Maritime Univ., Gdynia, 402 pp.

Markussen, T.N., Elberling, B., Winter, C., Andersen, T.J., 2016. Flocculated meltwater particles control Arctic land-sea fluxes

of labile iron. Sci. Rep. 6, 24033, http://dx.doi.org/10.1038/srep24033.

Marsz, A.A., Styszyńska, A., 2013. Climate and Climate Change at Hornsund, Svalbard. Gdynia Maritime Univ., Gdynia, 402 pp.

Molnia, B.F., 2007. Late nineteenth to early twenty-first century behavior of Alaskan glaciers as indicators of changing regional climate. Global Planet. Change 56, 23—56, http://dx.doi.org/10.1016/j.gloplacha.2006.07.011.

Motyka, R.J., Hunter, L., Echelmeyer, K.A., Connor, C., 2003. Submarine melting at the terminus of a temperate tidewater glacier, LeConte Glacier, Alaska, U.S.A. Ann. Glaciol. 36, 57—65, http://dx.doi.org/10.3189/172756403781816374.

Muckenhuber, S., Nilsen, F., Korosov, A., Sandven, S., 2016. Sea ice cover in Isfjorden and Hornsund, Svalbard (2000—2014) from remote sensing data. Cryosphere 10 (1), 149—158, http://dx.doi.org/10.5194/tc-10-149-2016.

Nilsen, F., Cottier, F., Skogseth, R., Mattsson, S., 2008. Fjord-shelf exchanges controlled by ice and brine production: the interannual variation of Atlantic Water in Isfjorden, Svalbard. Cont. Shelf Res. 28, 1838—1853, http://dx.doi.org/10.1016/j.csr.2008.04.015.

Nut, D.C., Coachman, L.K., 1956. The oceanography of Hebron Fjord, Labrador. J. Fish. Res. Board. Can. 13 (5), 709—758, http://dx.doi.org/10.1139/f56-043.

Osuch, M., Wawrzyniak, T., 2016. Inter- and intra-annual changes in air temperature and precipitation in western Spitsbergen. Int. J. Climatol. 37 (7), 3082—3097, http://dx.doi.org/10.1002/joc.4901.

Osuch, M., Wawrzyniak, T., 2017. Variations and changes in snow depth at meteorological stations Barentsburg and Hornsund (Spitsbergen). Ann. Glaciol. 58 (75 pt 1), 11—20, http://dx.doi.org/10.1017/aog.2017.20.

Overeem, I., Hudson, B.D., Syvitski, J.P.M., Mikkelsen, A.B., Hasholt, B., van den Broeke, M.R., Noël, B.P.Y., Morlighem, M., 2017. Substantial export of suspended sediment to the global oceans from glacial erosion in Greenland. Nat. Geosci. 10, 859—863, http://dx.doi.org/10.1038/ngeo3046.

Pawłowska, J., Włodarska-Kowalczuk, M., Zajączkowski, M., Nygård, H., Berge, J., 2011. Seasonal variability of meio- and macrobenthic standing stocks and diversity in an Arctic fjord (Adventfjorden, Spitsbergen). Polar Biol. 34, 833—845, http://dx.doi.org/10.1007/s00300-010-0940-7.

Pawłowska, J., Zajączkowski, M., Szczuciński, W., Zaborska, A., Kucharska, M., Jernas, P.E., Forwick, M., 2017. The influence of Coriolis force driven water circulation on the palaeoenvironment of Hornsund (S Spitsbergen) over the last century. Boreas 46 (4), 737—749, http://dx.doi.org/10.1111/bor.12249.

Pälli, A., Moore, J.C., Jania, J., Kolondra, L., Głowacki, P., 2003. The drainage pattern of Hansbreen and Werenskioldbreen, two polythermal glaciers on Svalbard. Polar Res. 22 (2), 355—371, http://dx.doi.org/10.1111/j.1751-8369.2003.tb00117.x.

Promińska, A., Cisek, M., Walczowski, W., 2017. Kongsfjorden and Hornsund hydrography — comparative study based on a multiyear survey in fjords of west Spitsbergen. Oceanologia 59 (4), 397—412, http://dx.doi.org/10.1016/j.oceano.2017.07.003.

Rabindranath, A., Daase, M., Falk-Peteresen, S., Wold, A., Wallace, M.I., Berge, J., Brierley, A.S., 2008. Seasonal and diel vertical migration of zooplankton in the High Arctic during the autumn midnight sun of 2008. Mar. Biodivers. 41 (3), 365—382, http://dx.doi.org/10.1007/s12526-010-0067-7.

Rachlewicz, G., Szczuciński, W., 2000. Ice tectonics and bedrock relief control on glacial sedimentation — an example from Hansbreen, Spitsbergen. In: Polish Polar Studies. 27th Polar Symposium. 259—275.

Radić, V., Hock, R., 2011. Regionally differentiated contribution of mountain glaciers and ice caps to future sea-level rise. Nat. Geosci. 4, 91—94, http://dx.doi.org/10.1038/ngeo1052.

Rignot, E., Koppes, M., Velicogna, I., 2010. Rapid submarine melting of the calving faces of West Greenland glaciers. Nat. Geosci. 3, 187—191, http://dx.doi.org/10.1038/ngeo765.

Sagan, S., Darecki, M., 2018. Inherent optical properties and particulate matter distribution in summer season in waters of Hornsund and Kongsfjordenen, Spitsbergen. Oceanologia 60 (1), 65—75, http://dx.doi.org/10.1016/j.oceano.2017.07.006.

Schildt, K.M., Hawley, R.L., Chipman, J.W., Benn, D.I., 2017. Quantifying suspended sediment concentration in subglacial sediment plumes discharging from two Svalbard tidewater glaciers using Landsat-8 and in-situ measurements. Int. J. Remote Sens. 38, 6865—6881, http://dx.doi.org/10.1080/01431161.2017.1365388.

Solomina, O.N., Bradley, R.S., Jomelli, V., Geirsdottir, A., Kaufman, D.S., Koch, J., McKay, N.P., Masiokas, M., Miller, G., Nesje, A., Nicolussi, K., Owen, L.A., Putnam, A.E., Wanner, H., Wiles, G., Yang, B., 2016. Glacier fluctuations during the past 2000 years. Quat. Sci. Rev. 149, 61—90, http://dx.doi.org/10.1016/j.quascirev.2016.04.008.

Straneo, F., Heimbach, P., 2013. North Atlantic warming and the retreat of Greenland's outlet glaciers. Nature 504, 36—43, http://dx.doi.org/10.1038/nature12854.

Svendsen, H., Beszczynska-Møller, A., Lefauconnier, B., Tverberg, V., Gerland, S., Jon Børre Ørbæk, J., Bischof, K., Pappuci, C., Zajączkowski, M., Azzolini, R., Bruland, O., Wiencke, Ch., Winther, J.G., Dallmann, W., 2002. The physical environment of Kongsfjorden-Krossfjorden, an Arctic fjord system in Svalbard. Polar Res. 21 (1), 133—166, http://dx.doi.org/10.1111/j.1751-8369.2002.tb00072.x.

Syvitski, J.P.M., 1989. On the deposition of sediment within glacier-influenced fjords: oceanographic controls. Mar. Geol. 85, 301—329, http://dx.doi.org/10.1016/0025-3227(89)90158-8.

Szczuciński, W., Dominiczak, A., Apolinarska, K., Forwick, M., Goslar, T., Moskalik, M., Strzelecki, M., Woszczyk, M., 2017. Climate-driven variations in source-to-sink fluxes of sediment and carbon in High Arctic fjord (Hornsund, Svalbard). In: 33rd International Meeting of Sedimentology and 16ème Congrés Français Sédimentologie, Toulouse. 10—12 October 2017 Abstract Book, 863.

Szczuciński, W., Moskalik, M., 2017. Sediment flocculation in fjords: tidewater glacier bay vs river-dominated bay. In: 33rd International Meeting of Sedimentology and 16ème Congrés Français Sédimentologie, Toulouse. 10—12 October 2017 Abstract Book, 864.

Szczuciński, W., Zajączkowski, M., Scholten, J., 2009. Sediment accumulation rates in subpolar fjords — impact of post-Little Ice Age glaciers retreat, Billefjorden, Svalbard. Estuar. Coast. Shelf Sci. 83 (3), 345—356, http://dx.doi.org/10.1016/j.ecss.2009.08.021.

Szczuciński, W., Zajączkowski, M., 2012. Factors controlling downward fluxes of particulate matter in glacier-contact and non-glacier contact settings in a subpolar fjord (Billefjorden, Svalbard). In: Li, M., Sherwood, C., Hill, P. (Eds.), Sediments, Morphology and Sedimentary Processes on Continental Shelves. IAS Spec. Publ., vol. 44. Wiley-Blackwell Publ., 369—385, http://dx.doi.org/10.1002/9781118311172.ch18.

Trusel, L.D., Powell, R.D., Cumpston, R.M., Brigham-Grette, J., 2010. Modern glaciomarine processes and potential future behaviour of Kronebreen and Kongsvegen polythermal tidewater glaciers, Kongsfjorden, Svalbard. In: Howe, J.A., Austin, W.E.N., Forwick, M., Paetzel, M. (Eds.), Fjord Systems and Archives, vol. 344. Geological Soc., Spec. Publ., London, 89—102, http://dx.doi.org/10.1144/SP344.9.

Urbanski, J.A., Stempniewicz, L., Węsławski, J.M., Dragańska-Deja, K., Wochna, A., Goc, M., Iliszko, L., 2017. Subglacial discharges create fluctuating foraging hotspots for sea birds in tidewater glacier bays. Sci. Rep. 7, 43999, http://dx.doi.org/10.1038/srep43999.

Walkusz, W., Storemark, K., Skau, T., Gannefors, C., Lundberg, M., 2003. Zooplankton community structure; a comparison of the fjords, open water and ice stations in the Svalbard area. Polish Polar Res. 24, 149—165.

Walkusz, W., Kwaśniewski, S., Falk-Petersen, S., Hop, H., Tverberg, V., Wieczorek, P., Weslawski, J.M., 2009. Seasonal and spatial changes in the zooplankton community of Kongsfjorden, Svalbard. Polar Res. 28, 254—281, http://dx.doi.org/10.1111/j.1751-8369.2009.00107.x.

Weydmann, A., Søreide, J.E., Kwaśniewski, S., Leu, E., Falk-Petersen, S., Berge, J., 2013. Ice-related seasonality in zooplankton community composition in a high Arctic fjord. J. Plankton Res. 35 (4), 831—842, http://dx.doi.org/10.1093/plankt/fbt031.

Węsławski, J.M., Legeżyńska, J., 1998. Glacier induced zooplankton mortality? J. Plankton Res. 20, 1233—1240.

Węsławski, J.M., Jankowski, A., Kwaśniewski, S., Swerpel, S., Ryg, M., 1991. Summer hydrology and zooplankton in two Spitsbergen fjords. Polish Polar Res. 12, 445—460.

Węsławski, J.M., Koszteyn, J., Zajaczkowski, M., Wiktor, J., Kwaśniewski, S., 1995. Fresh water in Svalbard fjord ecosystems. In: Skjodal, H.R., Hopking, C., Erikstad, K.E., Leinaa, H.P. (Eds.), Ecology of Fjords and Coastal Waters. Elsevier, Amsterdam, 229—241.

Węsławski, J.M., Zajączkowski, M., Kwaśniewski, S., Jezierski, J., Moskal, W., 1988. Seasonality in an Arctic fjord ecosystem: Hornsund, Spitsbergen. Polar Res. 6, 185—189.

Winters, G.V., Syvitski, J.P.M., 1992. Suspended sediment character and distribution in McBeth Fiord, Baffin Island. Arctic 45 (1), 25—35.

Wojtysiak, K., Herman, A., Moskalik, M., 2018. Wind wave climate of west Spitsbergen: seasonal variability and extreme events. Oceanologia, http://dx.doi.org/10.1016/j.oceano.2018.01.002.

Zajączkowski, M., Legeżyńska, J., 2001. Estimation of zooplankton mortality caused by an Arctic glacier outflow. Oceanologia 43 (3), 341—351.

Zajączkowski, M., Nygård, H., Hegseth, E.N., Berge, J., 2010. Vertical flux of particulate matter in an Arctic fjord: the case of lack of the sea-ice cover in Adventfjorden 2006—2007. Polar Biol. 33, 223—239, http://dx.doi.org/10.1007/s00300-009-0699-x.

Zajączkowski, M., Szczuciński, W., Bojanowski, R., 2004. Recent changes in sediment accumulation rates in Adventfjorden, Svalbard. Oceanologia 46 (2), 217—231.

Zajączkowski, M., Włodarska-Kowalczuk, M., 2007. Dynamic sedimentary environments of Arctic glacier-fed river estuary (Adventfjorden, Svalbard). I. Flux, deposition, and sediment dynamics. Estuar. Coast. Shelf Sci. 74, 285—296, http://dx.doi.org/10.1016/j.ecss.2007.04.015.

Zajączkowski, M., 2002. On the use of sediment traps in sedimentation measurements in glaciated fjords. Polish Polar Res. 23, 161—174.

Zajączkowski, M., 2008. Sediment supply and fluxes in glacial and outwash fjords, Kongsfjorden and Adventfjorden, Svalbard. Polish Polar Res. 29 (1), 59—72.

Oceanologia (2018) 60, 464—477

Available online at www.sciencedirect.com

ScienceDirect

journal homepage: www.journals.elsevier.com/oceanologia/

ORIGINAL RESEARCH ARTICLE

Partitioning of solar radiation in Arctic sea ice during melt season

Peng Lu [a,*], **Bin Cheng** [b], **Matti Leppäranta** [c], **Zhijun Li** [a]

[a] *State Key Laboratory of Coastal and Offshore Engineering, Dalian University of Technology, Dalian, China*
[b] *Finnish Meteorological Institute, Helsinki, Finland*
[c] *Institute of Atmospheric and Earth Sciences, University of Helsinki, Helsinki, Finland*

Received 28 December 2017; accepted 22 March 2018
Available online 10 April 2018

KEYWORDS
Arctic sea ice;
Melt pond;
Radiation transfer;
Mass balance;
Numerical modelling

Summary The partitioning of solar radiation in the Arctic sea ice during the melt season is investigated using a radiative transfer model containing three layers of melt pond, underlying sea ice, and ocean beneath ice. The wavelength distribution of the spectral solar irradiance clearly narrowed with increasing depth into ice, from 350—900 nm at the pond surface to 400—600 nm in the ocean beneath. In contrast, the net spectral irradiance is quite uniform. The absorbed solar energy is sensitive to both pond depth (H_p) and the underlying ice thickness (H_i). The solar energy absorbed by the melt pond (Ψ_p) is proportional only to H_p. However, the solar energy absorbed by the underlying ice (Ψ_i) is more complicated due to the counteracting effects arising from the pond and ice to the energy absorption. In September, Ψ_p decreased by 10% from its August value, which is attributed to more components in the shortwave band (<530 nm) of the incident solar radiation in September relative to August. The absorption coefficient of the sea ice only enhances the absorbed energy in ice, while an increase in the ice scattering coefficient only enhances the absorbed energy in the melt pond, although the resulted changes in Ψ_p and Ψ_i are smaller than that in the albedo and transmittance. The energy absorption rate with depth depends strongly on the incident irradiance and ice scattering, but only weakly on pond depth. Our results are comparable to previous field measurements and numerical simulations. We conclude that the incident solar energy was largely absorbed by the melt pond rather than by the underlying sea ice.

* Corresponding author at: State Key Laboratory of Coastal and Offshore Engineering, Dalian University of Technology, Dalian 116024, China. Tel.: +86 411847085208303; Fax: +86 41184708526.
E-mail addresses: lupeng@dlut.edu.cn (P. Lu), bin.cheng@fmi.fi (B. Cheng), matti.lepparanta@helsinki.fi (M. Leppäranta), lizhijun@dlut.edu.cn (Z. Li).
Peer review under the responsibility of Institute of Oceanology of the Polish Academy of Sciences.

https://doi.org/10.1016/j.oceano.2018.03.002

1. Introduction

A steady decline in Arctic sea ice, especially during the melt seasons since 2000, has been well demonstrated (e.g. Comiso et al., 2017). An increase in solar radiation absorbed by the Arctic Ocean was also observed by satellite instruments during the same period (NASA, 2014). The partitioning of solar radiation in an ice-covered sea is a central issue of the energy budget of the Arctic Ocean and the mass balance of Arctic sea ice (Lei et al., 2016; Wang et al., 2014, 2016). The solar energy absorbed by the sea ice cover largely determines the rate of ice melting (Hudson et al., 2013), while the backscattering part provides heats to the atmosphere (Perovich, 2005). Energy penetrating through the sea ice cover warms up the ocean beneath the ice, which is a primary source of ocean heat (Katlein et al., 2015). The apparent optical properties (AOPs) — albedo (reflectance) and transmittance — determine the partitioning of solar radiation into backscattering, absorption and transmittance in the Arctic sea ice (Perovich, 1996).

Extensive field observations have been carried out to measure the AOPs of first-year (FYI) and multiyear sea ice (MYI), and were employed to parameterize the distribution of solar energy in numerical models (e.g. Taskjelle et al., 2015). In Arctic summer, melt ponds pose notable impacts on the AOPs of sea ice. Not only is the albedo of the melting ice significantly lower than that of dry or snow-covered ice, but melt ponds take more solar radiation which then penetrates the ice (Webster et al., 2015). Even a skim layer of liquid water on an ice surface can change the AOPs considerably (Light et al., 2015). For example, the transmittance through FYI is almost three times larger than through MYI because of the larger melt-pond coverage of FYI, and the energy absorption is also 50% larger in FYI than in MYI (Nicolaus et al., 2012). Ponded ice transmits roughly 4.4 times more total energy into the ocean than nearby bare ice. The ubiquitous surface-scattering layer and drained layer present on bare sea ice are responsible for its relatively high albedo and low transmittance, while light transmittance through ponded ice depends on its physical thickness and the magnitude of the scattering coefficient in the ice interior (Light et al., 2015).

Radiative transfer models (RTM) are another approach to determine the partitioning of solar radiation in melting sea ice. A plane-parallel melt pond model with either a Lambertian or a non-Lambertian reflector for the pond bottom was developed to estimate the pond albedo and radiance distribution in ponded ice (Podgorny and Grenfell, 1996). Solar-radiation flux transfer in melt ponds was simulated by Skyllingstad et al. (2009), and variations in the pond albedo with pond depth and the underlying ice albedo were proposed. Influences of different impact factors on the pond albedo and transmittance were investigated, and a parameterized pond albedo as a function of both pond depth and ice thickness was suggested (Lu et al., 2016). This parameterization is more suitable for thinning Arctic sea ice than the exponential relationship between albedo and pond depth (Morassutti and Ledrew, 1996), which is valid for thicker ice.

A summary of previous field and numerical studies on the AOPs of melting sea ice is listed in Table 1, where α and T denote the percentage of solar energy backscattered by the pond surface and transmitted into the ocean beneath ice, respectively, and Ψ_p and Ψ_i are the fractions absorbed by the melt pond and the underlying ice layer, respectively. Some studies combined the absorption of melt ponds and the underlying ice, and present it as the sum of Ψ_p and Ψ_i.

The results of the studies that considered the partitioning of solar energy in melting sea ice differ widely from each other, as seen in Table 1. One can attribute the variations to the different ice conditions in the studies. As such, a systemic investigation on the various factors that affect the energy distribution is still needed. In addition, the portion of solar energy absorbed by meltwater is obviously larger than that absorbed by underlying sea ice, which argues for the notable capacity of melt ponds in energy absorption, and which also implies the possible complicated processes associated with the allocation of energy to the air, pond, ice, and the water below. However, melt ponds are always treated as a controller of surface albedo, and are not individually considered in numerical models (Pedersen et al., 2009); hence, an investigation of their full physics is required.

To achieve these goals, an RTM initially developed to parameterize melt-pond albedo (Lu et al., 2016) was used. The framework of the RTM is summarized in Section 2. In Section 3 we investigate the distribution of solar radiation, the energy budget in the melting sea ice, and the absorption ratio of solar energy. Discussions on the surface transmission parameter, ice internal melt, and photosynthetically active radiation (PAR) beneath the ice are presented in Section 4. Conclusions are drawn in Section 5.

2. Model description

Radiation transfer in a plane-parallel medium can be simplified as two streams: upwelling and downwelling irradiances. These are governed by two coupled first-order differential equations under the assumptions of diffuse incident solar radiation and isotropic scattering (Flocco et al., 2015):

$$\begin{cases} dF^{\downarrow}(z,\lambda) = -k_\lambda F^{\downarrow}(z,\lambda)dz - \sigma_\lambda F^{\downarrow}(z,\lambda)dz + \sigma_\lambda F^{\uparrow}(z,\lambda)dz \\ dF^{\uparrow}(z,\lambda) = k_\lambda F^{\uparrow}(z,\lambda)dz + \sigma_\lambda F^{\uparrow}(z,\lambda)dz - \sigma_\lambda F^{\downarrow}(z,\lambda)dz \end{cases}, \quad (1)$$

where σ_λ is the wavelength-dependent scattering coefficient and k_λ is the absorption coefficient, which defines the inherent optical properties (IOP) of the medium. $F^{\uparrow}(z, \lambda)$ and $F^{\downarrow}(z, \lambda)$ are the upwelling and downwelling irradiances, respectively, z is the depth in the medium and λ is the wavelength.

The RTM developed by Lu et al. (2016) contains three layers: the melt pond, the underlying ice, and the ocean beneath the ice. Assuming the continuity of radiation flux at each interface between the layers, the irradiance in both directions in the melt pond and underlying ice can be calculated. Two AOPs, the spectral albedo of the melt pond α_λ, and the spectral transmittance T_λ, are determined accordingly.

A two-stream model is employed instead of a more advanced RTM such as the one given by Podgorny et al. (2018) using Monte Carlo approach. This is because the two-stream model is mathematically straightforward, and an analytical solution is available for model validation. Moreover, different studies have revealed that the results of the two-stream RTM using Eq. (1) agree well with field measurements on sea ice (Flocco et al., 2015; Taylor and Feltham, 2004). The drawbacks of such model lie to assumptions of

Table 1 Partitioning of incident solar energy in melting sea ice in Arctic summer, including the fractions reflected back by the ice surface α, absorbed by the melt pond Ψ_p, absorbed by the underlying ice Ψ_i, and transmitted into the ocean beneath ice T. Note that $\alpha + \Psi_p + \Psi_i + T = 100\%$. The sum of Ψ_p and Ψ_i is presented if their individual values were not reported in the references.

References	α [%]	$\Psi_p + \Psi_i$ [%]	T [%]	Ice conditions	
Hudson et al. (2013)	15	46	39	Dark pond on FYI	FM
	34	46	20	Bright pond on FYI	FM
Perovich et al. (2001)	15	73	12	Pond on MYI, August	FM
	35	58	7	Pond on MYI, June	FM
Light et al. (2015)	18	30 + 30	22	Pond on FYI	FM
	25	40 + 25	10	Pond on MYI	FM
Nicolaus et al. (2012)	21	57	22	Pond on FYI	FM
	29	56	15	Pond on MYI	FM
Perovich and Tucker (1997)	24	69	7	Pond on MYI, July	FM
Perovich (2005)	26	57	17	Pond on MYI	FM
Ebert et al. (1995)	20	66 + 12	2	Pond on FYI, July	NS
Podgorny and Grenfell (1996)	13	38 + 38	11	Old pond with LBR	NS
	26	38 + 29	7	Young pond with LBR	NS
	–	38 + 37	–	Old pond with non-LBR	NS
	–	39 + 28	–	Young pond with non-LBR	NS

FM – field measurements. NS – numerical simulation. LBR – Lambertian bottom reflection.

diffuse incident solar radiation in the air and isotropic scattering in the ice. The former assumption is not a major problem in Arctic summer because sky is often covered with low stratus cloud. The latter one is also not badly biased for melting sea ice, because the geometric structure of porous sea ice becomes more irregular that can favour isotropic scattering in the ice (Leppäranta et al., 2003).

The IOPs of sea ice and water are prescribed in this study and follow the previous results in Lu et al. (2016). The wavelength-dependent absorption coefficient of water ($k_{\lambda,w}$) employs the pure water values from Kou et al. (1993) and Smith and Baker (1981). The absorption coefficient of sea ice ($k_{\lambda,i}$) is determined by combining the contributions from pure ice and brine pockets, where absorption in the gas inclusions can be neglected. Scattering in meltwater and the ocean beneath the ice is neglected ($\sigma_{\lambda,w} = 0$) according to previous studies (e.g. Taylor and Feltham, 2004). This has been shown to be a valid approximation for melt ponds with a depth less than 1 m (Podgorny and Grenfell, 1996). And the upwelling radiation backscattered by the ocean beneath ice is also extremely small (~1% of the total upwelling radiative flux) because the scattering coefficient of water is 2–3 orders of magnitude lower than that of sea ice (Smith and Baker, 1981). The scattering coefficient of sea ice is independent of wavelength, and a value of $\sigma_i = 2.5\ m^{-1}$ was promoted for summer Arctic sea ice. The incident solar irradiance $F_0(\lambda)$ measured by Grenfell and Perovich (2008) under a completely overcast sky in August with the solar disc not visible, is employed as a representation of Arctic summer. The considered wavelength range covers the solar spectrum from $\lambda_1 = 300$ nm to $\lambda_2 = 2500$ nm.

3. Results

3.1. Vertical distribution of the spectral irradiance

Different to sea ice, irradiance in the ocean can be expressed by Beer's absorption law if the transmitted irradiance $F_w^{\downarrow}(z_w = 0, \lambda)$ is known, since the ocean may be regarded as a semi-infinite medium with a negligible scattering coefficient:

$$\begin{cases} F_w^{\downarrow}(z_w, \lambda) = F_w^{\downarrow}(0, \lambda)\exp(-k_{\lambda,w} z_w) \\ F_w^{\uparrow}(z_w, \lambda) = 0 \end{cases} \quad (2)$$

The upwelling irradiance beyond the pond surface may also be deduced as $\alpha_\lambda F_0(\lambda)$. Then the distributions of the downwelling and upwelling irradiances in the pond–ice–ocean system are obtained. A typical case with $H_p = 0.3$ m and $H_i = 1.0$ m, corresponding to FYI in Arctic summer season, was implemented to calculate the spectral irradiance distribution. The net irradiance distribution across the ice sheet, $F_{net}(z, \lambda)$, was also calculated, which is the difference between the downwelling and upwelling streams (Fig. 1).

The irradiance in Fig. 1 is continuous in magnitude and spectrum within the three regimes (melt pond, underlying ice and the ocean beneath the ice), and discontinuities occur only at the interface between the air and the pond because of reflections there.

Most of the downwelling incident irradiance in the visible band is dissipated in the pond water and the upper ice layer, and only an irradiance of ~0.1 $W{\cdot}m^{-2}{\cdot}nm^{-1}$ (15% of the maximum in melt pond) at wavelengths 400–600 nm reaches the bottom of the ice (Fig. 1a). The downwelling irradiance in the near-infrared (NIR) band is completely absorbed in the pond water, with none reaching the bottom of the ice. The amount of ultraviolet (UV) radiation is nearly constant in the melt pond, however 80% of its energy is dissipated by the underlying sea ice, leaving only ~0.05 $W{\cdot}m^{-2}{\cdot}nm^{-1}$ in 350–400 nm band transmitting through the sea ice to the ocean below.

The maximum amount of downwelling irradiance exists in the melt pond at a wavelength of 450 nm, 0.6 $W{\cdot}m^{-2}{\cdot}nm^{-1}$, which is even greater than the incident solar radiation. It can be explained by the total reflection of light at the air-pond interface, where the downwelling irradiance, $F_p^{\downarrow}(0, \lambda)$, is the sum of the fraction of the $F_0(\lambda)$ entering the pond and the

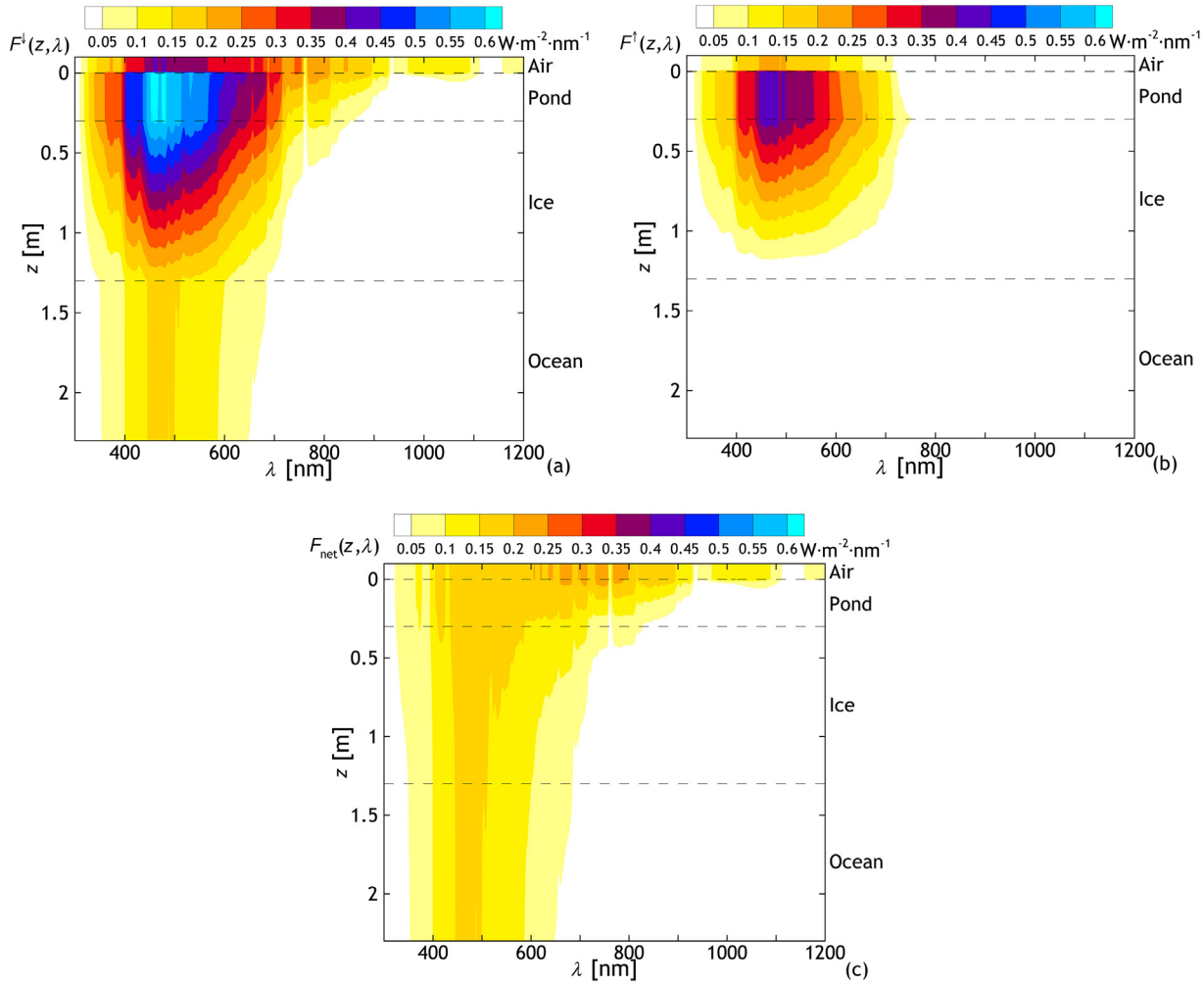

Figure 1 Spectral irradiance distribution in the pond–ice–ocean system with H_p = 0.3 m and H_i = 1.0 m: (a) downwelling irradiance $F^{\downarrow}(z, \lambda)$, (b) upwelling irradiance $F^{\uparrow}(z, \lambda)$, and (c) net irradiance $F_{net}(z, \lambda) = F^{\downarrow}(z, \lambda) - F^{\uparrow}(z, \lambda)$. The colour denotes the spectral value in units of W·m^{-2}·nm^{-1}. Irradiances beyond 1200 nm are truncated in the plots because of their very small quantities. (For interpretation of the references to color in this figure legend, the reader is referred to the web version of this article.)

fraction of the upwelling irradiance reflected downwards by the pond-air interface, $F_p^{\downarrow}(0, \lambda) = (1 - R_1)\, F_0(\lambda) + R_1'\, F_p^{\uparrow}(0, \lambda)$. R_1 = 0.05, which is the Fresnel reflection coefficient at the air-water interface under diffuse sky conditions (Perovich, 1990), and R_1' = 0.54, which is the specular reflectance of the upwelling irradiance at the water-air interface (Dera, 1992). Hence, 95% of the incident solar radiation enters the melt pond, and half of the backscattering irradiance from the underlying ice is reflected back again at the pond surface, where both contribute to a maximum downwelling irradiance that is even greater than $F_0(\lambda)$. On the other hand, the maximum value changes slightly with pond depth because the absorption is very limited ($\sim 10^{-3}$) at 450 nm, and scattering is also negligible in water.

Upwelling irradiance was found only in the pond and ice layers in the visible band (Fig. 1b), because scattering in the ice is the only source of an upwelling stream, and backscattering from water is negligible. Most of the downwelling irradiance into the ice lies in the visible band, so backscattering also occurs in this band. The peak of the upwelling irradiance ($\sim$0.4 W·m^{-2}·nm^{-1} at 450–550 nm) occurs in the upper ice layer and is constant with pond depth owing to the accumulative contributions from the backscatters in the lower ice layer.

The net irradiance is more uniform (0.1–0.2 W·m^{-2}·nm^{-1}) than the downwelling and upwelling irradiances throughout the pond–ice–ocean volume (Fig. 1c). However, the wavelength range clearly narrowed with increasing depth, from 350–900 nm at the pond surface to 400–600 nm in the ocean. The enhanced absorption in ice and water at longer wavelengths is the primary reason for this, which also implies that visible-band radiation is the main contributor to the heat balance in the underlying ice volume and the ocean further below.

3.2. Radiation partitioning in the pond–ice–ocean system

To account for the partitioning of solar energy in the pond–ice–ocean system, the broadband albedo α and transmittance T are defined as:

$$\begin{cases} \alpha = \int_{\lambda_1}^{\lambda_2} \alpha_\lambda F_0(\lambda) d\lambda / Q \\ T = \int_{\lambda_1}^{\lambda_2} T_\lambda F_0(\lambda) d\lambda / Q \\ Q = \int_{\lambda_1}^{\lambda_2} F_0(\lambda) d\lambda \end{cases} \quad (3)$$

We assume that the energy budget in the pond–ice system, and the portion of solar radiation absorbed can be determined by $\Psi = 1 - \alpha - T$. Then, the fraction absorbed by the melt pond Ψ_p, and by the underlying ice Ψ_i, can be individually determined by:

$$\begin{cases} \Psi_p = \int_{\lambda_1}^{\lambda_2} [F_{net}(z_p = 0, \lambda) - F_{net}(z_p = H_p, \lambda)] d\lambda / Q \\ \Psi_i = \int_{\lambda_1}^{\lambda_2} [F_{net}(z_i = 0, \lambda) - F_{net}(z_i = H_i, \lambda)] d\lambda / Q \end{cases} . \quad (4)$$

It is clear that $\Psi = \Psi_p + \Psi_i$. The dependence of the solar energy partitioning in different parts of the melting sea ice with pond depth, H_p, and underlying ice thickness, H_i, is shown in Fig. 2.

The broadband albedo depends mainly on H_i for thin ice ($H_i < 1$ m), but as H_i increases, α is initially sensitive to both H_i and H_p and finally just on H_p for $H_i > 3$ m (Fig. 2a). In contrast, the broadband transmittance depends mostly on H_i, and slightly on H_p (Fig. 2b). This result agrees well with Lu et al. (2016). That is, the portion of solar energy that penetrates all the way to the ocean beneath the ice increases only when the ice becomes thinner, because the extinction effect of ice to the penetrating radiation (absorption + scattering) is stronger than that of water (absorption). However, the portion backscattered by melting ice increases with H_i for thin ice and decreases with H_p for thick ice. This dependence is complicated because a deeper pond poses a negative impact (absorption) on the backscattering, while thicker ice poses both negative (absorption) and positive (scattering) impacts on the backscattering. The overall effect of the ice is positive, however, owing to the larger value of the scattering coefficient relative to the absorption coefficient in the visible band (Fig. 1). The various factors of radiative transfer within the pond and ice cause the backscattering to depend on both H_p and H_i, rather than just one factor, in the whole regime.

The portion of solar energy absorbed by melting sea ice seen in Fig. 2c, increases with both H_i and H_p because either a deeper pond or a thicker underlying ice benefits the absorption of solar radiation. It is interesting if this portion is divided into two. The portion of solar energy absorbed by the melt pond increases only with increasing pond depth (Fig. 2d). The positive effect of backscattering in thicker underlying ice on absorption in melt ponds seems negligible. While the portion absorbed by underlying ice varies in a more complicated way, although the contour lines in Fig. 2e are similar with those seen in Fig. 2a. This can be explained by the counteracting effect of pond and ice to the energy absorption in ice. For a deep pond on thin ice, an increase in ice thickness will significantly enhance the absorbed energy of the underlying ice. For a shallow pond with thick ice, a decrease in pond depth also greatly benefits the absorption by ice. However, for medium values of H_p and H_i, the positive effect of an increase in H_i can be completely counteracted by the negative effect of an increase in H_p. For example, the portion of solar energy absorbed by the underlying ice for H_i = 2 m and H_p = 0.2 m is close to that of the case with H_i = 3 m and H_p = 0.3 m (Fig. 2e).

The relative dominance between the absorbed energy by the pond and ice, namely the ratio of Ψ_p to Ψ_i, is shown in Fig. 2f. It is surprising that the solar energy absorbed by the melt pond is much larger than that by the underlying ice, except for some very shallow ponds with $H_p < 0.1$ m. Indeed, the ratio Ψ_p/Ψ_i even approaches 5–7 for a deep pond on a thin ice layer (Fig. 2f). That is, among the 40–60% solar energy absorbed by melting sea ice (Fig. 2c), a large portion is attributed to the surface water rather than the underlying ice. This again pronounces the importance of melt ponds in enhancing the absorption of sea ice to solar radiation, although part of Ψ_p conducts to the underlying ice.

The solar energy absorbed by melting sea ice ($\Psi_p + \Psi_i$) is dominant with a portion of 40–70%, as seen in Table 1, which agrees with the results in Fig. 2c. Ψ_p/Ψ_i varies within the 1–5.5 range in Table 1, which also approximately agrees with Fig. 2f. The remaining difference can be attributed to the different ice conditions when the field observations were conducted and the definitions used in the numerical modelling. Nevertheless, both results in Table 1 and in Fig. 2 strongly argue for the dominance of solar energy absorption in the melt pond rather than in the underlying ice.

3.3. Impact of other factors on the energy partitioning

Except for the influence of pond depth and the underlying ice thickness, the impacts of other factors to the energy partitioning merit investigation. The values of H_i and H_p are consistent with those in Fig. 1. Variations of the energy partitioning with incident solar irradiance, ice absorption coefficient and ice scattering coefficient are shown in Figs. 3–5, respectively.

Six different incident solar spectra were selected according to Grenfell and Perovich (2008). They were measured near solar noon of the days during the HOTRAX cruise in 2005, and we used them to represent Arctic summer conditions for a completely overcast sky in August and September (Fig. 3a). These six cases differ widely with respect to $F_0(\lambda)$. The broadband albedo and transmittance are slightly higher in September than in August (Fig. 3b). Meanwhile, the portion of solar energy absorbed by the melting sea ice decreases significantly from August to September, in which Ψ_p has a similar trend with Ψ, but Ψ_i is nearly constant in time. This can be attributed to the distribution of the relative energy $F_0(\lambda)/Q$ with wavelength. Although the level of $F_0(\lambda)$ decreases gradually with date (Fig. 3a), more relative energy is contained in the shortwave band (<530 nm) and less in the longwave band (>530 nm). This trend becomes more pronounced with date. As a result, the amount of longwave radiation that can be easily absorbed by surface meltwater decreases significantly with date, and the portion absorbed by the underlying sea ice changes slightly because of the small absorption coefficient of ice in the shortwave band.

Variations in the absorption coefficient of sea ice in Fig. 4a can be attributed to the different combinations of volume fractions of pure ice and brine pockets. However, the difference between the maximum and minimum values of $k_{\lambda,i}$ is

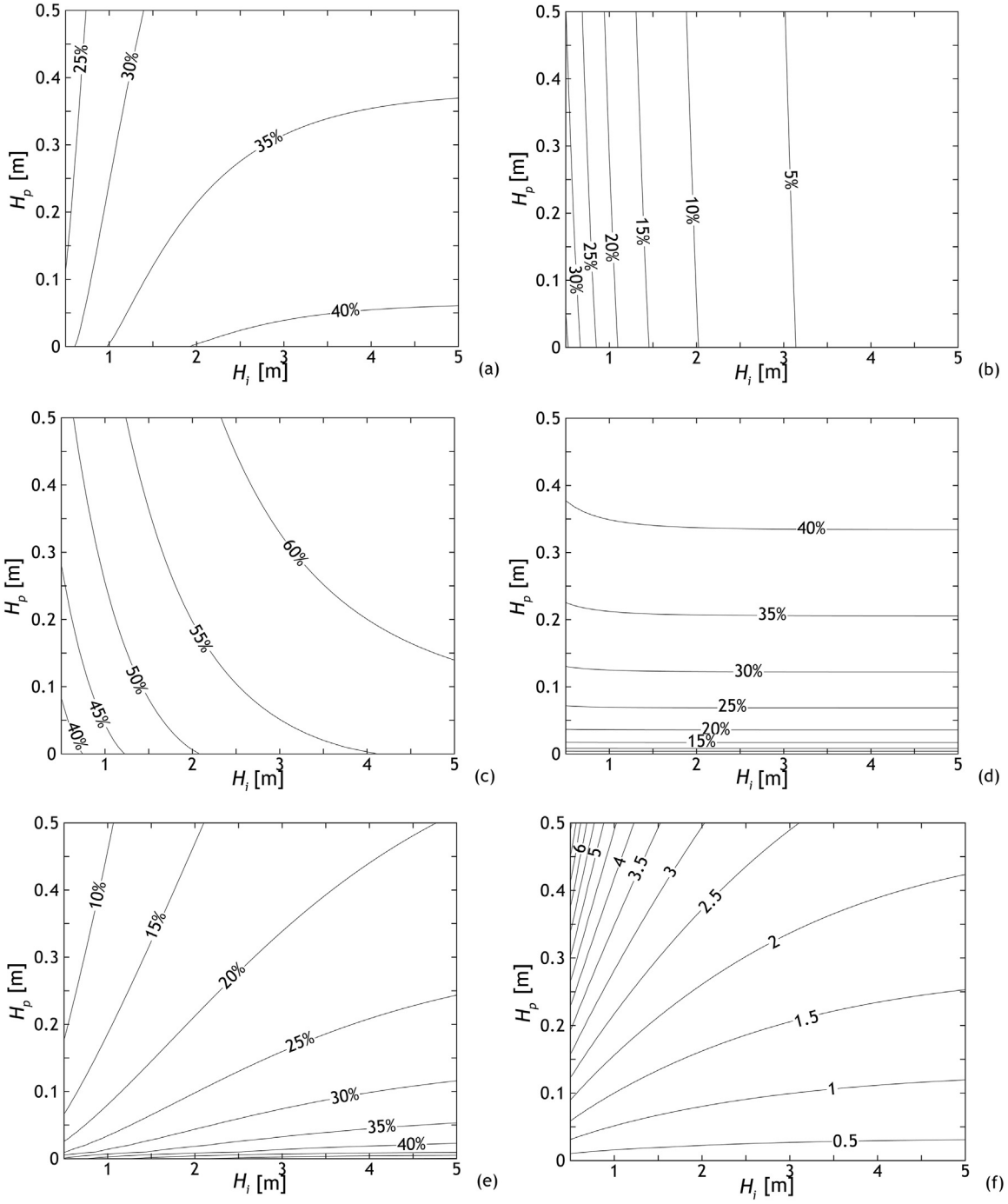

Figure 2 Variations in the portion of solar energy in relation to: (a) the albedo α, (b) transmittance T, (c) the amount absorbed by the melting sea ice Ψ, (d) the amount absorbed by the melt pond Ψ_p, (e) the amount absorbed by the underlying ice Ψ_i, and (f) the ratio of Ψ_p to Ψ_i, with pond depth H_p and the underlying ice thickness H_i. There is $\alpha + T + \Psi = 100\%$, and $\Psi = \Psi_p + \Psi_i$.

still limited, although ν_{pi} and ν_{bp} vary within a relative large range according to the field observations (Huang et al., 2013). As such, variations in the AOPs of the melting sea ice in Fig. 4b are also small. The most obvious change among them is the increase of Ψ_i with increased absorption in the ice. The concurrent slight decrease in Ψ_p is mainly attributed to the enhanced portion of absorption in the ice rather than the decrease in the absolute values of absorption in the melt ponds. Meanwhile, both the broadband albedo and transmittance decrease slightly with increasing absorption in ice, consistent with Lu et al. (2016).

The scattering coefficient of sea ice ranges from 0 to 2.5 m^{-1} in Fig. 5, which corresponds to sea ice from an idealized purely absorbing medium, to melting blue ice with a small content of gas bubbles (1.2 m^{-1}), and then to porous white ice containing large quantities of gas bubbles according to Perovich (1990). Compared with the obvious changes in the broadband albedo and transmittance, variations in the

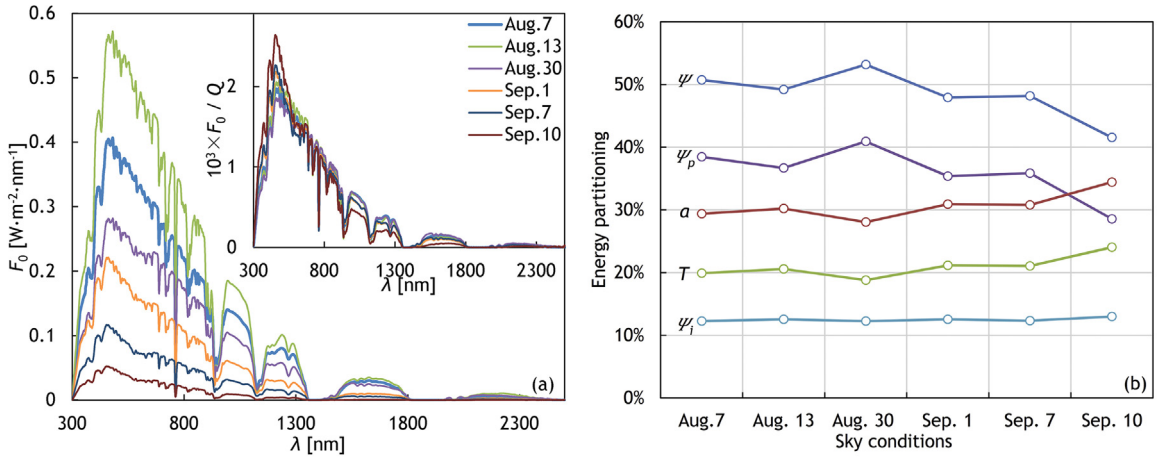

Figure 3 (a) Typical spectral incident solar irradiance in the Arctic summer for a completely overcast sky, according to Grenfell and Perovich (2008). The subplot denotes the normalized values of spectral incident irradiance, which are equal to the ratio of F_0 to the wavelength-integrated incident irradiance Q. (b) The influence on the portion of solar energy in the melting sea ice for H_p = 0.3 m and H_i = 1.0 m. Recall $\alpha + T + \Psi = 1$, and $\Psi = \Psi_p + \Psi_i$. The spectral irradiance on August 7 in (a) is the default value of F_0 defined previously.

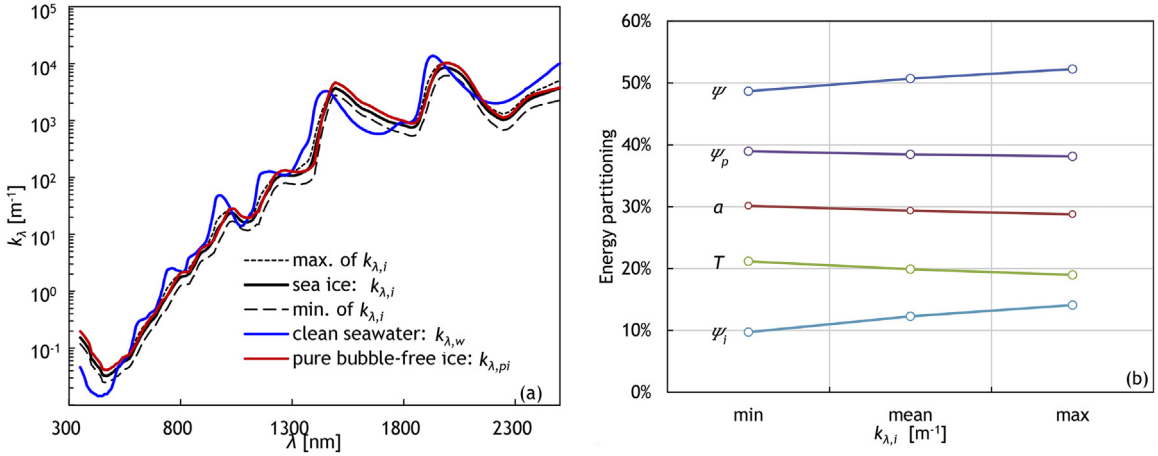

Figure 4 (a) Absorption coefficients of clean seawater, pure bubble-free ice and sea ice. The value of $k_{\lambda,i}$ value is calculated as $k_{\lambda,i} = \nu_{pi}k_{\lambda,pi} + \nu_{bp}k_{\lambda,w}$, which is based on volume fractions of $\nu_{pi} \geq 60\%$ and $\nu_{bp} \leq 20\%$, as determined from field observations of summer Arctic sea ice (Huang et al., 2013). (b) The influence of the ice absorption coefficient on the portion of solar energy in the melting sea ice for H_p = 0.3 m and H_i = 1.0 m.

portion of solar energy absorbed by the melting sea ice are relative small. The portion of absorption in ice is nearly constant in Fig. 5 because the increasing ice-scattering coefficient only causes more upwelling irradiance through backscattering. However, the portion of absorption in the surface meltwater increases consequently owing to the enhanced backscattering irradiance that is absorbed again by the meltwater. Both contribute to the small increase in the portion of solar energy absorbed by melting sea ice.

3.4. Energy absorption rate

The rate of energy absorbed per unit volume (ω) is noteworthy because it is an important source term in the equation of heat conduction, which describes the contribution of solar radiative heating to warming and melting in sea ice. The energy absorption rate ω is given by (Taylor and Feltham, 2004):

$$\omega = -\int_{\lambda_1}^{\lambda_2} \frac{\partial F_{net}(z,\lambda)}{\partial z} d\lambda. \quad (5)$$

Variations in ω vertically downwards in the pond–ice–ocean system for different values of the incident solar radiation, pond depth and underlying ice thickness, and IOPs of the sea ice, are shown in Fig. 6.

Generally, the rate of energy absorption is greatest at the pond surface, which then drops off rapidly by an order of magnitude in the first 0.3 m owing to the loss of radiation in the NIR band, and then decreases more gradually with the attenuation of the remaining radiation. Sudden changes in ω seen at the pond–ice and ice–ocean interfaces in Fig. 6 are mainly attributed to the different IOPs of the two media.

Scattering in ice weakens the energy absorption rate of ice, although the energy fluxes are continuous at the interfaces.

Variations in sky conditions do not alter the relative magnitude of the energy absorption curves to any extent (Fig. 6a), but the absolute values of ω are strictly sorted according to the sequence of the incident energy (Fig. 3a).

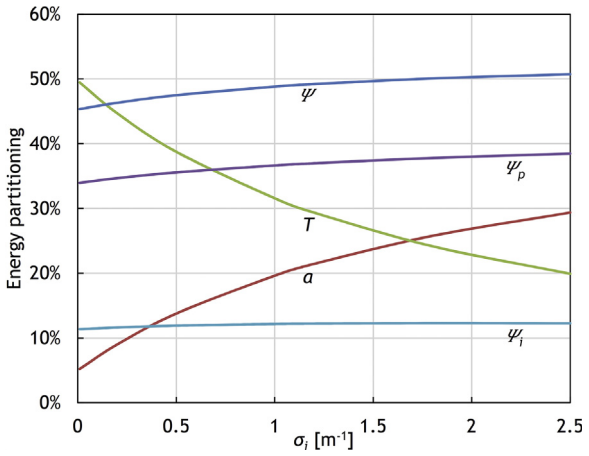

Figure 5 The influence of the ice scattering coefficient on the portion of solar energy in the melting sea ice for H_p = 0.3 m and H_i = 1.0 m.

Near the pond surface, the absorption in August 7 is about 15 times greater than in September 10. This decreases gradually to 10 at a depth of about 0.7 m, and then remains at a relatively constant level, which approximates the ratio of the integrated irradiance for these two sky conditions, namely 10.3 in Fig. 3a.

The influence of scattering in ice is more interesting (Fig. 6b). The energy absorption in the pond water and upper ice layer is greatest for ice with the largest quantity of gas bubbles—that is, the highest scattering coefficient—but it falls below the value for ice with fewer bubbles at a depth of about 0.9 m. This is because the higher scattering in ice results in greater extinction in the upper layer of the pond–ice system and lower transmission to the interior of the ice, whereas more radiation penetrates deep into ice with fewer bubbles, adding to the energy input to the interior of the ice.

Increasing pond depth reduces the energy absorption at the pond's bottom (Fig. 6c) because more radiation is dissipated in the pond water. However, the ice layer acts as a filter, so that the energy absorption at the bottom of the ice, and the consequent transfer of energy into the underlying ocean, is almost uniform. An increase in the ice thickness (Fig. 6d) does not alter the energy absorption by the pond water, but it significantly reduces the absorption at the bottom of the ice and the transfer into the underlying ocean.

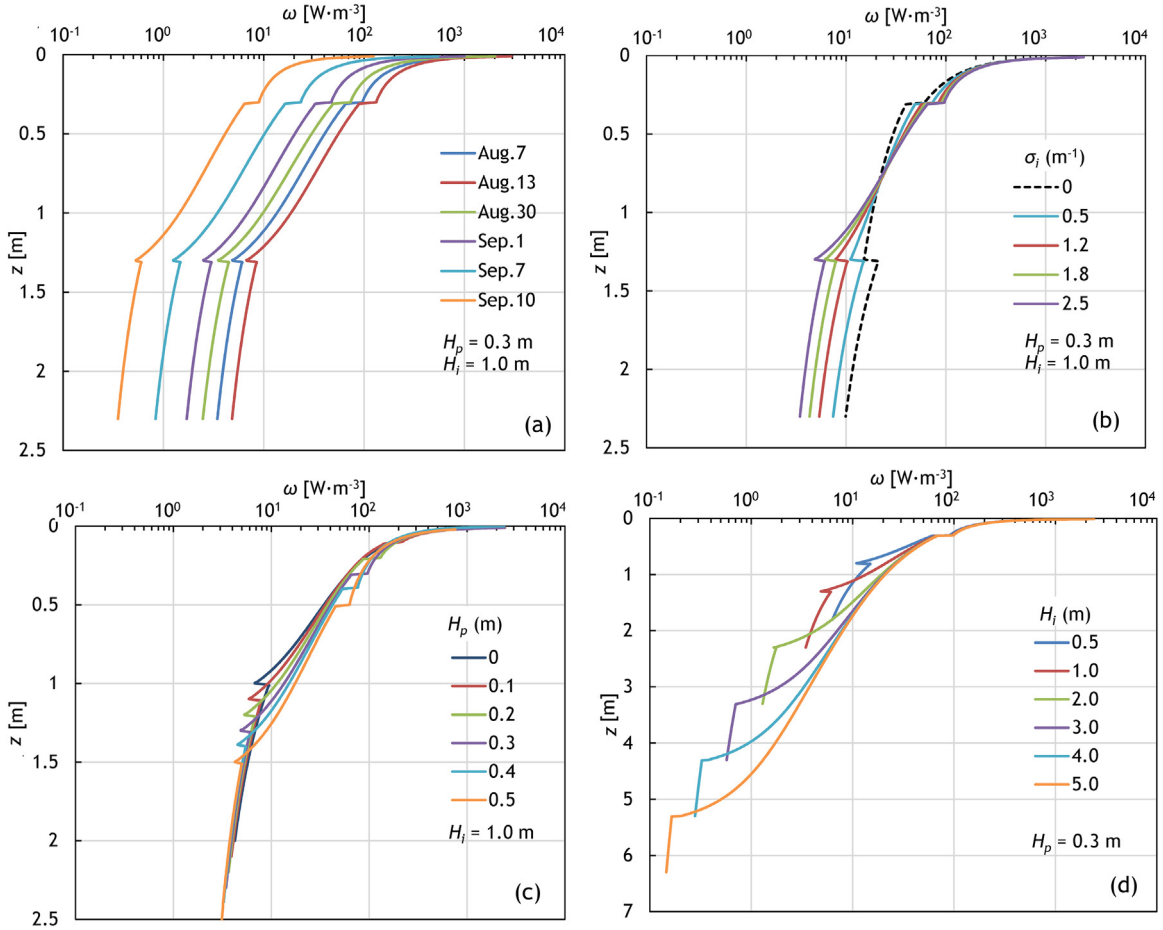

Figure 6 Variations in the rate of absorbed energy ω in the pond–ice–ocean system vertically downwards for different: (a) incident solar irradiance, (b) ice scattering coefficient, (c) pond depth, and (d) underlying ice thickness.

At the same depth, however, due to scattering by the ice, the energy absorption rate within the ice volume is higher when the underlying ice is thicker.

4. Discussion

4.1. The surface transmission parameter I_0

I_0 was designed to quantitatively measure the fraction of radiation transmitted through the highly scattering surface of the ice (Hoffman et al., 2014; Light et al., 2008), and it permits the calculation of shortwave solar radiation within the ice in global climate models (GCMs). The equation for I_0 is given by:

$$I_0 = \frac{\int_{\lambda_1}^{\lambda_2} F_{net}(z = 0.1\,\mathrm{m}, \lambda) d\lambda}{\int_{\lambda_1}^{\lambda_2} F_{net}(z = 0, \lambda) d\lambda}, \quad (6)$$

where $F_{\mathrm{net}}(\lambda,\ z = 0.1\ \mathrm{m})$ is the spectral net flux at 0.1 m depth, and $F_{\mathrm{net}}(\lambda,\ z = 0)$ is the spectral net flux at the surface, which is equal to $F_0(1 - \alpha_\lambda)$. The surface layer thickness is 0.1 m, which was first defined by Maykut and Untersteiner (1971) to conform to their grid spacing and then inherited in following studies.

In most GCMs, I_0 is a constant. For example, values of 0.7 and 0 for I_0 in the visible and NIR bands, respectively, were suggested in CCSM3 (Briegleb et al., 2004). However, I_0 should be variable for ponded sea ice according to Eq. (6). Both H_i and H_p pose an impact on the values of the spectral net flux, and then on the value of I_0. The results are shown in Fig. 7, where the values of I_0 for the visible band were determined with Eq. (6) using $\lambda_1 = 400$ nm to $\lambda_2 = 700$ nm, while $\lambda_1 = 300$ nm to $\lambda_2 = 400$ nm for the UV band, and $\lambda_1 = 700$ nm to $\lambda_2 = 2500$ nm for the NIR band.

Variations of I_0 in the given ranges of H_i (0.5–5 m) and H_p (0–0.5 m) are limited, with broadband values of 0.59 ± 0.03, 0.97 ± 0.01 for the UV band, 0.94 ± 0.01 for the visible band and 0.36 ± 0.02 for the NIR band, respectively (Fig. 7). These are different to the recommendations in CCSM3 (Briegleb et al., 2004), but close to the results of Light et al. (2008), where $I_0 = 0.99$ and 0.48 for ponded MYI in the UV and visible band and NIR band, respectively.

For shallow ponds with depths < 0.1 m, the surface transmission parameter I_0 decreases significantly with increasing H_i for thin ice ($H_i < 2$ m) but with increasing H_p for thick ice

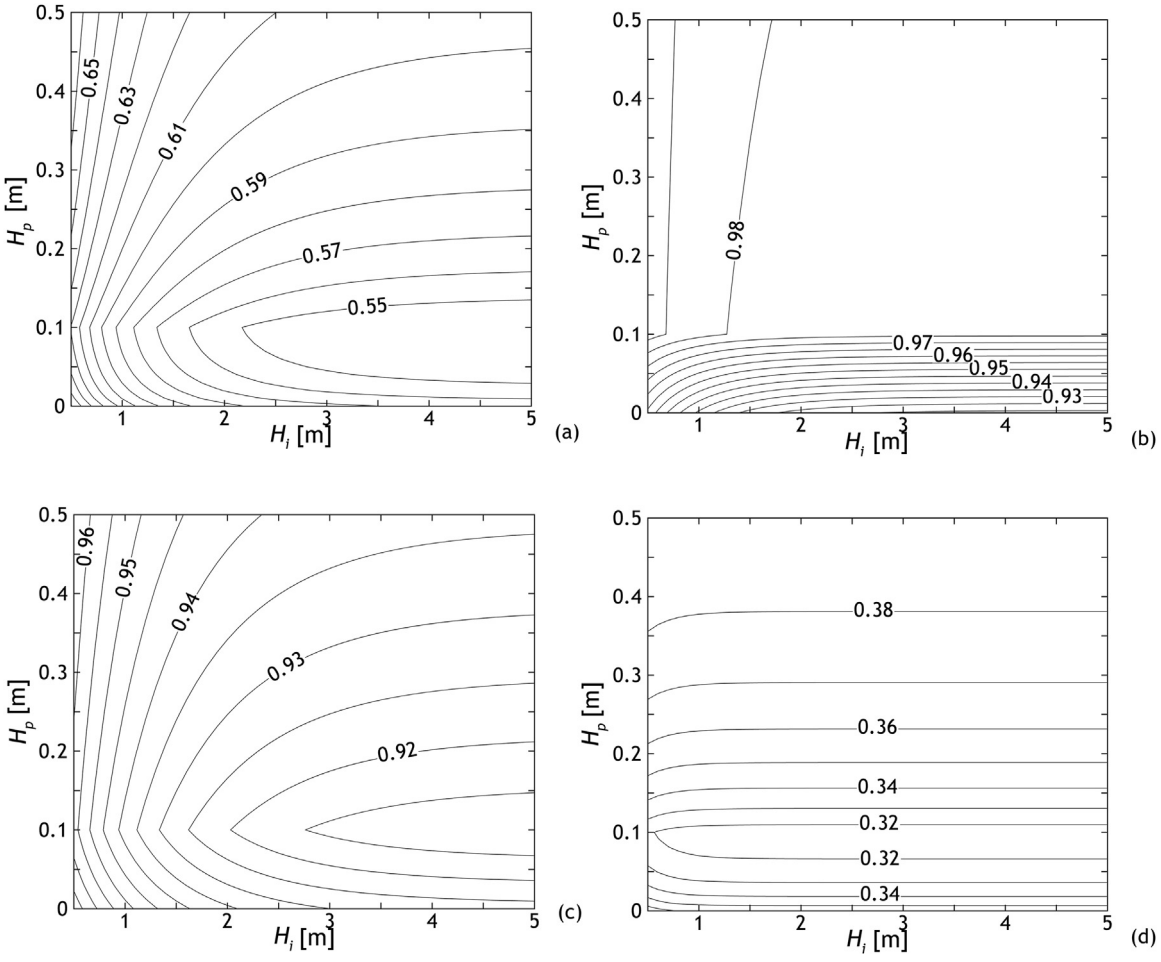

Figure 7 Variations of the surface transmission parameter I_0 with pond depth, H_p, and underlying ice thickness, H_i. In (a) we can see the broadband value of I_0, while in (b), (c), and (d) the results for the UV band (300–400 nm), visible band (400–700 nm), and NIR band (700–2500 nm) are respectively shown. Note that the 0.1-m-thick surface layer contains surface meltwater and upper underlying ice for $H_p < 0.1$ m, and only upper meltwater layer as $H_p \geq 0.1$ m.

($H_i > 3$ m) (Fig. 7a). For ponds deeper than 0.1 m, the behaviour of I_0 is different: it still decreases with increasing H_i for thin ice, but increases with increasing H_p for thick ice. That means that the impact of H_p on I_0 is opposite for shallow and deep ponds. Such a trend is also argued by Fig. 7c and significantly in Fig. 7d, where the value of I_0 in the NIR band depends almost on H_p. However, variations in the UV band are different (Fig. 7b): I_0 in the UV band is almost constant (0.98) as $H_p > 0.1$ m, but it increases with pond depth as $H_p < 0.1$ m, opposite to that in Fig. 7a. A weak dependence on H_i can be only detected for thin ice ($H_i < 1$ m) in Fig. 7b.

It is easy to understand the impact of H_i on I_0, because a thicker ice layer introduces more backscattering, thus weakening transmission through the surface layer. However, for very thick ice, most of the incident radiation in the NIR band is absorbed in the first few centimetres into the meltwater or ice because of the large absorption in this band (Fig. 4a), so that any further increase in H_i will not further alter the value of I_0 (Fig. 7d). Similarly, backscattering in the UV band is very small because less incident radiation in the UV band can penetrate into deeper ice (Fig. 1c), i.e. for a UV absorption coefficient of $\sim 10^{-1}$ m^{-1}, therefore the value of I_0 in the UV band does not depend on H_i for thick ice (Fig. 7b).

The impact of H_p on I_0 is more complicated. For a deep pond ($H_p > 0.1$ m), a further increase in H_p will reduce the amount of incident radiation reaching the underlying ice, which results in less backscattering into the melt pond. Transmission through the 10-cm meltwater layer increases as a result. In contrast, an increase in H_p for a shallow pond ($H_p < 0.1$ m) will significantly enhance the absorption in meltwater because of the large absorption coefficient in the NIR band (Fig. 4a), therefore less incident radiation will reach the lower boundary of the 10-cm surface layer. This also explains why the impact of H_p on I_0 is enhanced in the NIR band (Fig. 7d). However, there is little difference in the UV band. The incident radiation is nearly constant in the melt pond (Fig. 1a) because of the small absorption coefficient of water in the UV band (Fig. 4a), and any increase in H_p will not change the situation very much. So, I_0 in the UV band is constant as $H_p > 0.1$ m. For $H_p < 0.1$ m, a larger H_p causes a smaller H_i within the 10-cm-thick surface layer, and less backscattering due to ice, and finally more transmission through the surface layer (Fig. 7b).

4.2. The internal melting of ponded ice

Internal melting is an important process of sea ice in the melting season (Huang et al., 2016). Different to the surface and basal melting which changes the ice thickness directly, internal melting changes the internal inclusions in sea ice, and ice crystals transform into liquid water pockets (Leppäranta, 2015) that further affect the mechanical and thermal properties of the sea ice (Light et al., 2003). To properly account for internal melting necessitates the inclusion of ice porosity as a dependent model variable. Leppäranta (2009) considered a two-phase approach with liquid phase and solid phase portions considered in each grid cell in addition to the temperature.

The same approach can be employed when considering the internal melting of the sea ice below a melt pond. For simplicity, the temperature profile is taken as isothermal in the underlying ice, which is equal to the freezing point, and the salinity profile is also uniform in depth. These assumptions are acceptable for melting sea ice according to field observations (Polashenski et al., 2012). Then, the amount of absorbed solar energy by the underlying ice will increase the porosity only, and the heat fluxes from the melt pond and the ocean beneath the ice will alter the pond–ice and ice–ocean interfaces, respectively. Consequently, the model physics can be presented as:

$$\begin{aligned} &\text{Surface}: Q_p = -\rho_i L \frac{dH_i^s}{dt}, \\ &\text{Internal}: \quad \omega = \rho_i L \frac{d\nu}{dt}, \\ &\text{Bottom}: \quad Q_w = -\rho_i L \frac{dH_i^b}{dt}, \end{aligned} \tag{7}$$

where Q_p and Q_w are the heat fluxes from the melt pond and the ocean beneath the ice, respectively, ρ_i is the ice density, L is the latent heat of fusion, ν is the liquid water content (essentially the porosity of ice), and ω is the energy absorption rate defined in Eq. (5). Superscripts s and b denote the change of ice thickness H_i occurring on ice surface and bottom, respectively.

For the initial condition of $H_p = 0.3$ m and $H_i = 1.0$ m, evolutions of the ice porosity and thickness can be estimated according to Eq. (7). At each time step, the solar energy absorbed by the melt pond and the ocean beneath the ice for a constant F_0 (same with that in Fig. 2) can be determined by Eq. (7). Half of the solar energy absorbed by the melt pond, $\Psi_p Q$, is assumed to conduct to sea ice according to Zhang et al. (2014), and 5% of the transmitted energy, TQ, contribute to basal melt, which approximately agrees with the oceanic heat flux of 2 W m^{-2} in most GCMs. That is, $Q_p = 0.5\ \Psi_p Q$ and $Q_w = 0.05\ TQ$. Surface melting of the underlying ice contributes only to an increase of pond depth, and the drainage of meltwater into the ocean is neglected as in Lu et al. (2016). That is, $\Delta H_p = \Delta H_i^s \cdot \rho_i / \rho_w$, where ρ_w is the water density. Our result is shown in Fig. 8.

During the modelled one-month melt season, the underlying ice thickness decreased from 1 m to 0.46 m, which includes a surface melt of 0.44 m and a basal melt of 0.02 m (Fig. 8). Consequently, the ice porosity increased from idealized zero with depth, to 0.29 at the surface and 0.06 at the bottom. It is noticeable that once the porosity of the ice reaches 0.3–0.5, the ice can no longer bear its own weight, and subsequently breaks into smaller pieces into the water (Leppäranta, 2009). Hence, in the real initial case with $\nu > 0$, sea ice tends to break up before the thickness decreases to half of its initial value during the melting process. Structural defects will appear first in the upper layer of ice because of the larger ice porosity there, as according to Fig. 8. Additionally, the oceanic heat flux used for the basal melt of sea ice comes only from the transmitted solar radiation in Eq. (7). However, an upwelling heat stream seasonally of up to 10 W m^{-2} due to mixing with warmer underlying water has been also observed in the Arctic Ocean (Polyakov et al., 2017). If the extra heat flux is added to Q_w, the basal melt rate in Fig. 8 will increase by roughly 3 mm day^{-1}, resulting in 0.1 m more basal melt in the one-month melt season. However, the extra heat flux from deep ocean has only a minor impact on the surface melt and

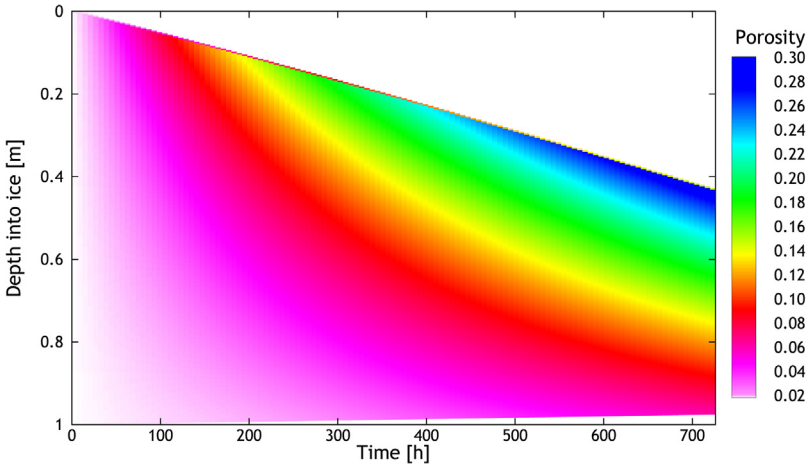

Figure 8 Evolutions of the porosity and thickness of the underlying ice in the model defined by Eq. (7). The *y*-axis denotes the vertical position relative to the initial ice thickness, whereby the changes in ice thickness due to surface melt and basal melt with time can be presented.

porosity evolution of sea ice, because Ψ_p is only sensitive to H_p and the extra decrease in H_i affects T more significantly than Ψ_i (Fig. 2).

The results in Fig. 8 also argue for the importance of including ice porosity in numerical models in addition to temperature and salinity. First, ice porosity describes the phase changes between ice crystal and liquid water, which agree more with actual physical conditions that occur in interior ice during melting and freezing (Light et al., 2003). This is particularly important for melting ice in the summer, because when the ice temperature is close to the freezing point, any additional heat flux will introduce phase changes that alter the ice porosity. Secondly, ice porosity has an upper limit, as mentioned earlier, so modelled ice thickness actually cannot decrease to zero as ice has already broken into pieces due to its weight. Finally, some thermal properties, such as the latent heat of fusion and the specific heat capacity, are also sensitive to the phase components in the sea ice (Shokr and Sinha, 2015). They are constants in most models, but they can be treated as variables that contribute to the ice mass balance if ice porosity changes during the melt process in future.

4.3. The PAR beneath ice

The solar radiation transmitted to the ocean beneath the sea ice impacts not only the physical properties of the system, but also biological processes and biogeochemical fluxes in the sea ice and the uppermost ocean (Arndt et al., 2017). However, only the solar radiation in the visible band can be employed by photosynthetic organisms to the process of photosynthesis. This spectral region corresponds to the range of light visible to the human eye, which is also consistent with the wavelength range in Fig. 1c that most of the transmitted radiation lies in. There are two different ways to quantify PAR: the power of the irradiance, from the point of view of energy transfer, and quantum irradiance q, from the point of view of the flow of light quanta. The total scalar irradiance $E_0(z, \lambda)$, usually employed in biological studies and defined as the irradiance on a point from all directions weighted equally, can be estimated from the planar irradiance $F(z, \lambda)$ employed in Eq. (1):

$$E_0(z,\lambda) = a_u F^{\uparrow}(z,\lambda) + a_d F^{\downarrow}(z,\lambda), \tag{8}$$

where $1 \le a_u,\ a_d \le 2$, and for diffuse radiation, the coefficients are 2. Then, in the ocean beneath ice, there are:

$$\begin{cases} E_0(z_w,\lambda) = 2F_w^{\downarrow}(z_w,\lambda) \\ \hat{E}(z_w) = \int_{\lambda_1}^{\lambda_2} E_0(z_w,\lambda)\,d\lambda \quad q(z_w) = \int_{\lambda_1}^{\lambda_2} E_0(z_w,\lambda)\frac{\lambda}{hc_0}d\lambda, \end{cases} \tag{9}$$

where $h = 6.2566 \times 10^{-34}$ J s is the Planck constant, and $c_0 = 2.9979 \times 10^8$ m s^{-1} is the velocity of light in a vacuum. $\lambda_1 = 400$ nm and $\lambda_2 = 700$ nm are employed in the calculation of PAR.

The ratio $q/\hat{E}$ changes with variations in the spectral distribution of the irradiance rather than its level (Leppäranta et al., 2003; Reinart et al., 1998). So, it is interesting to see how the ratio changes with the properties of the melt pond and the underlying ice. Our results are shown in Fig. 9.

The quantum irradiance q of the PAR transmission drops from 460 μmol·m^{-2}·s^{-1} to 30 μmol·m^{-2}·s^{-1} as H_i increases from 1.3 m to 5.0 m, and the influence of H_p is limited (Fig. 9a). The weakening transmission due to increasing ice thickness is the direct reason for this, and therefore the variations in q are similar with those seen for the transmittance (Fig. 2b). A threshold level of q for primary production is around 10 μmol·m^{-2}·s^{-1}; therefore the PAR transmission for melting Arctic sea ice can of course satisfy this standard.

Within the given range of H_p and H_i, $q/\hat{E}$ = 4.27 ± 0.10 μmol·J^{-1}. The dependence of $q/\hat{E}$ on H_i is obviously greater than on H_p. With increasing ice thickness, the transmitted PAR into the ocean beneath the ice decreases accordingly, and the ratio $q/\hat{E}$ also decreases. In air it is normally assumed that the spectrum of sunlight PAR is even, thus $q/\hat{E}$ = 4.60 μmol·J^{-1}. Here we have a lower value, which means longer wavelengths rather than short ones penetrate the ice. This is an important parameter as such.

Vertical distributions of the ratio $q/\hat{E}$ with depth for different combinations of H_i and H_p are shown in Fig. 9b.

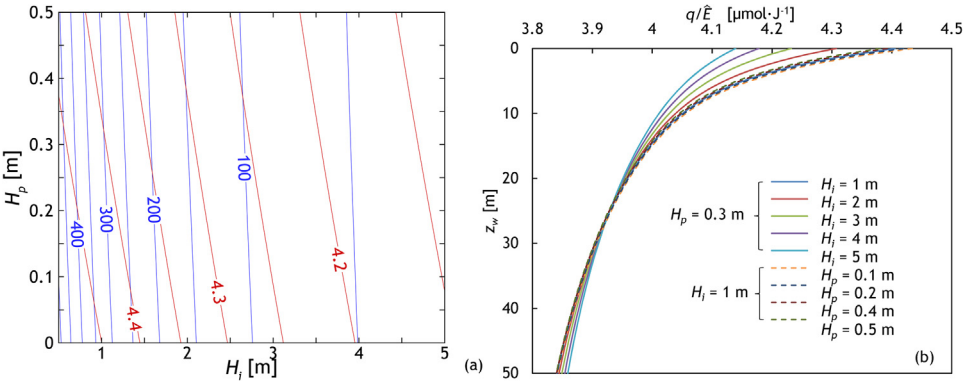

Figure 9 (a) Variations of the quantum irradiance q (blue lines), and the ratio $q/\hat{E}$ (red lines) at the bottom of the ice for a pond depth of H_p and an underlying ice thickness of H_i. (b) Vertical profiles of the ratio $q/\hat{E}$ in the ocean beneath ice. The units of q are μmol·m^{-2}·s^{-1} and μmol·J^{-1} for $q/\hat{E}$. (For interpretation of the references to color in this figure legend, the reader is referred to the web version of this article.)

It is found that a thicker ice layer gives a smaller $q/\hat{E}$ value at the ice bottom, but the value drops slower with depth as compared with that of a thinner ice layer. Thus, at a depth of 25 m beneath the ice, $q/\hat{E}$ = 3.93 for all cases. Below this depth, the $q/\hat{E}$ value for thicker ice is gradually beyond that for thinner ice. The influence of H_p on the profile of $q/\hat{E}$ can be neglected.

5. Conclusions

A two-stream RTM was employed to study the partitioning of solar radiation in the Arctic sea ice during the melt season. Variations of the incident irradiance with depth into the melting sea ice were obtained. Portions of the backscattered solar energy, the fraction absorbed by the melt pond and the underlying ice, and that which penetrates into the ocean beneath the ice were investigated together with their variations due to difference impact factors. Changes in the energy absorption rate were also determined, which were shown to be a contribution of solar radiative heating to thermodynamic equilibrium of sea ice.

The spectral downwelling irradiance distribution clearly narrowed in wavelength, and decreased in value, with increasing depth into the pond–ice–ocean system. Upwelling irradiance resulting from backscattering in ice occurred only in the visible band. The net irradiance was quite uniform, but its wavelength range also narrowed with increasing depth, from 350–900 nm at the pond surface to 400–600 nm in the ocean water. The solar radiation that contributed to the heat balance in the underlying ice volume and the ocean beneath the ice occurred only in the visible band.

Both pond depth, H_p, and the underlying ice thickness, H_i, pose an important impact on the partitioning of solar radiation. The transmitted solar energy into the ocean is sensitive only to H_i, while the backscattered solar energy depends more on H_i than on H_p for thin ice, consistent with the previous results in Lu et al. (2016). The portion absorbed by melting sea ice increased with both H_i and H_p. Among them, the portion in melt pond increased only with H_p, and the variations in the portion in the underlying ice were seen to be complex because of the counteracting effects of pond and ice to the energy absorption in ice. Moreover, the solar energy absorbed by the melt pond was several times larger than that by the underlying ice except for some very shallow ponds ($H_p < 0.1$ m).

The influence of the level of the incident solar irradiance was limited, but the portion of solar energy absorbed by the melt pond decreased by 10% from August to September, which is attributed to the more energy contained in the shortwave band (<530 nm) relative to the longwave band (>530 nm) in September than in August. The portion of solar energy absorbed by the underlying ice increased by 5% as the ice-absorption coefficient increased. As the ice-scattering coefficient increased, the portion of absorption in the ice was nearly constant, but the portion of absorption in the melt pond consequently increased by 5%, in contrast to the obvious changes in the albedo (25%) and transmittance (30%).

Variations in the profile of the energy absorption rate in the melting sea ice showed a strong dependence on the incident irradiance and scattering in ice, but only a weak dependence on pond depth. The increasing ice thickness only reduced the absorption rate in the ocean beneath the ice. Discussions on the surface transmission parameter showed that I_0 decreased with an increase in H_i, but the effect of H_p on I_0 was opposite for shallow and deep ponds. Moreover, variations of I_0 in the UV band were different to those in the visible and NIR bands. Increasing the ice thickness reduced both the quantum irradiance and the ratio $q/\hat{E}$ for the PAR transmission, and also slowed down the attenuation rate of $q/\hat{E}$ in the ocean. The impact of H_p on the PAR beneath ice was limited. Our idealized modelling of the evolution of ice porosity argues for the importance of including ice porosity in numerical models especially for melting sea ice in summer.

Our results agree well with previous field measurements and numerical simulations. More importantly, we demonstrated that the amount of solar energy absorbed by the melt ponds is much larger than that by the underlying ice. Contrary to bare ice, which reflects most of the incident solar radiation, a thin layer of meltwater not only makes the underlying ice absorb more solar energy, but it also creates a situation where the ice is surrounded by two warm water

layers. The upper layer is the melt pond absorbing most solar radiation, and the lower is the ocean mixed layer absorbing nearly 10% more transmitted radiation. Both enhance the melting of sea ice. However, we still have little knowledge on the assignment of absorbed solar energy by melt ponds. Further investigations on how this large part of solar energy is assigned to warm the underlying ice, diffuse to the upper atmosphere, and warm the pond water are still need.

Acknowledgements

This research was supported by the Global Change Research Programme of China (2015CB953901), the National Natural Science Foundation of China (41676187 and 41376186). B.C. was supported by the NSFC research facility mobility (41428603) and the Academy of Finland (283101). M.L. was supported by the EU FP7 Project EuRuCAS (European-Russian Centre for Cooperation in the Arctic and Sub-Arctic Environmental and Climate Research, Grant no. 295068) and the Academy of Finland (11409391).

References

Arndt, S., Meiners, K.M., Ricker, R., Krumpen, T., Katlein, C., Nicolaus, M., 2017. Influence of snow depth and surface flooding on light transmission through Antarctic pack ice. J. Geophys. Res. Oceans 122 (3), 2108—2119, http://dx.doi.org/10.1002/2016JC012325.

Briegleb, B.P., Bitz, C.M., Hunke, E.C., Lipscomb, W.H., Holland, M. M., Schramm, J.L., Moritz, R.E., 2004. Scientific Description of the Sea Ice Component in the Community Climate System Model, version 3. Natl. Cent. for Atmos. Res., Boulder, Colo., NCAR/TN-463+STR, 70 pp.

Comiso, J.C., Meier, W.N., Gersten, R., 2017. Variability and trends in the Arctic Sea ice cover: results from different techniques. J. Geophys. Res. Oceans 122 (8), 6883—6900, http://dx.doi.org/10.1002/2017JC012768.

Dera, J., 1992. Marine physics. Elsevier Oceanogr. Ser. 53, Amsterdam-Oxford-New York-Tokyo-Warsaw, 510 pp.

Ebert, E.E., Schramm, J.L., Curry, J.A., 1995. Disposition of solar radiation in sea ice and the upper ocean. J. Geophys. Res. 100 (C8), 15965—15975, http://dx.doi.org/10.1029/95JC01672.

Flocco, D., Feltham, D.L., Bailey, E., Schroeder, D., 2015. The refreezing of melt ponds on Arctic sea ice. J. Geophys. Res. Oceans 120 (2), 647—659, http://dx.doi.org/10.1002/2014JC010140.

Grenfell, T.C., Perovich, D.K., 2008. Incident spectral irradiance in the Arctic Basin during the summer and fall. J. Geophys. Res. 113 (D12), 13 pp., http://dx.doi.org/10.1029/2007JD009418.

Hoffman, M.J., Fountain, A.G., Liston, G.E., 2014. Near-surface internal melting: a substantial mass loss on Antarctic Dry Valley glaciers. J. Glaciol. 60 (220), 361—374, http://dx.doi.org/10.3189/2014JoG13J095.

Huang, W., Lei, R., Ilkka, M., Li, Q., Wang, Y., Li, Z., 2013. The physical structures of snow and sea ice in the Arctic section of 150°—180°W during the summer of 2010. Acta Oceanol. Sin. 32 (5), 57—67, http://dx.doi.org/10.1007/s13131-013-0314-4.

Huang, W., Lei, R., Han, H., Li, Z., 2016. Physical structures and interior melt of the central Arctic sea ice/snow in summer 2012. Cold Reg. Sci. Technol. 124 (1), 127—137, http://dx.doi.org/10.1016/j.coldregions.2016.01.005.

Hudson, S.R., Granskog, M.A., Sundfjord, A., Randelhoff, A., Renner, A.H.H., Divine, D.V., 2013. Energy budget of first-year Arctic sea ice in advanced stages of melt. Geophys. Res. Lett. 40 (11), 2679—2683, http://dx.doi.org/10.1002/grl.50517.

Katlein, C., Arndt, S., Nicolaus, M., Perovich, D.K., Jakuba, M.V., Suman, S., Elliott, S., Whitcomb, L.L., McFarland, C.J., Gerdes, R., Boetius, A., German, C.R., 2015. Influence of ice thickness and surface properties on light transmission through Arctic sea ice. J. Geophys. Res. Oceans 120 (9), 5932—5944, http://dx.doi.org/10.1002/2015JC010914.

Kou, L., Labrie, D., Chylek, P., 1993. Refractive indices of water and ice in the 0.65- to 2.5-μm spectral range. Appl. Opt. 32 (19), 3531—3540, http://dx.doi.org/10.1364/AO.32.003531.

Lei, R., Tian-Kunze, X., Leppäranta, M., Wang, J., Kaleschke, L., Zhang, Z., 2016. Changes in summer sea ice, albedo, and portioning of surface solar radiation in the Pacific sector of Arctic Ocean during 1982—2009. J. Geophys. Res. Oceans 121 (8), 5470—5486, http://dx.doi.org/10.1002/2016JC011831.

Leppäranta, M., 2009. A two-phase model for thermodynamics of floating ice. In: Proceedings of the 6th Workshop on Baltic Sea Ice Climate, Report Series in Geophysics, 61. Dept. Physics, Univ. Helsinki, Finland, 146—154.

Leppäranta, M., 2015. Freezing of Lakes and the Evolution of their Ice Cover. Springer, Heidelberg, 301 pp., http://dx.doi.org/10.1007/978-3-642-29081-7.

Leppäranta, M., Reinart, A., Arst, H., Erm, A., Sipelgas, L., Hussainov, M., 2003. Investigation of ice and water properties and under-ice light fields in fresh and brackish water bodies. Nord. Hydrol. 34 (3), 245—266.

Light, B., Grenfell, T.C., Perovich, D.K., 2008. Transmission and absorption of solar radiation by Arctic sea ice during the melt season. J. Geophys. Res. 113 (C3), 19 pp., http://dx.doi.org/10.1029/2006JC003977.

Light, B., Maykut, G.A., Grenfell, T.C., 2003. Effects of temperature on the microstructure of first-year Arctic sea ice. J. Geophys. Res. 108 (C2), 16 pp., http://dx.doi.org/10.1029/2001JC000887.

Light, B., Perovich, D.K., Webster, M.A., Polashenski, C., Dadic, R., 2015. Optical properties of melting first-year Arctic sea ice. J. Geophys. Res. Oceans 120 (11), 7657—7675, http://dx.doi.org/10.1002/2015JC011163.

Lu, P., Leppäranta, M., Cheng, B., Li, Z., 2016. Influence of melt-pond depth and ice thickness on Arctic sea-ice albedo and light transmittance. Cold Reg. Sci. Technol. 124 (1), 1—10, http://dx.doi.org/10.1016/j.coldregions.2015.12.010.

Maykut, G.A., Untersteiner, N., 1971. Some results from a time dependent, thermodynamic model of sea ice. J. Geophys. Res. 76 (6), 1550—1575, http://dx.doi.org/10.1029/JC076i006p01550.

Morassutti, M.P., Ledrew, E.F., 1996. Albedo and depth of melt ponds on sea-ice. Int. J. Climatol. 16 (7), 817—838, http://dx.doi.org/10.1002/(SICI)1097-0088(199607)16:7<817::AID-JOC44>3.0.CO;2-5.

NASA/Goddard Space Flight Center, 2014. Satellites Measure Increase of Sun's Energy Absorbed in the Arctic. Science Daily, http://www.sciencedaily.com/releases/2014/12/141217154124.htm (retrieved 10.10.17).

Nicolaus, M., Katlein, C., Maslanik, J., Hendricks, S., 2012. Changes in Arctic sea ice result in increasing light transmittance and absorption. Geophys. Res. Lett. 39 (24), 6 pp., http://dx.doi.org/10.1029/2012GL053738.

Pedersen, C.A., Roeckner, E., Lüthje, M., Winthere, J.-G., 2009. A new sea ice albedo scheme including melt ponds for ECHAM5 general circulation model. J. Geophys. Res. 114 (D8), 15 pp., http://dx.doi.org/10.1029/2008JD010440.

Perovich, D.K., 1990. Theoretical estimates of light reflection and transmission by spatially complex and temporally varying sea ice covers. J. Geophys. Res. 95 (C6), 9557—9567, http://dx.doi.org/10.1029/JC095iC06p09557.

Perovich, D.K., 1996. The optical properties of sea-ice. Cold Reg. Res. and Eng. Lab. (CRREL) Report 96-1, Hanover, NH, 31 pp.

Perovich, D.K., 2005. On the aggregate-scale partitioning of solar radiation in Arctic sea ice during the Surface Heat Budget of the

Arctic Ocean (SHEBA) field experiment. J. Geophys. Res. 110 (C3), 12 pp., http://dx.doi.org/10.1029/2004JC002512.

Perovich, D., Richter-Menge, J., Tucker, W., 2001. Seasonal changes in Arctic sea-ice morphology. Ann. Glaciol. 33 (1), 171—176, http://dx.doi.org/10.3189/172756401781818716.

Perovich, D., Tucker, W., 1997. Arctic sea-ice conditions and the distribution of solar radiation during summer. Ann. Glaciol. 25 (1), 445—450, http://dx.doi.org/10.3189/S0260305500014439.

Podgorny, I., Grenfell, T.C., 1996. Partitioning of solar energy in melt ponds from measurements of pond albedo and depth. J. Geophys. Res. 101 (C10), 22737—22748, http://dx.doi.org/10.1029/96JC02123.

Podgorny, I., Lubin, D., Perovich, D.K., 2018. Monte Carlo study of UAV-measurable albedo over Arctic sea ice. J. Atmos. Oceanic Technol. 35 (1), 57—66, http://dx.doi.org/10.1175/JTECH-D-17-0066.1.

Polashenski, C., Perovich, D., Courville, Z., 2012. The mechanisms of sea ice melt pond formation and evolution. J. Geophys. Res. 117 (C1), 23 pp., http://dx.doi.org/10.1029/2011JC007231.

Polyakov, I.V., Pnyushkov, A.V., Alkire, M.B., Ashik, I.M., Baumann, T. M., Carmack, E.C., Goszczko, I., Guthrie, J., Ivanov, V.V., Kanzow, T., Krishfield, R., Kwok, R., Sundfjord, A., Morison, J., Rember, R., Yulin, A., 2017. Greater role for Atlantic inflows on sea-ice loss in the Eurasian Basin of the Arctic Ocean. Science 356 (6335), 285—291, http://dx.doi.org/10.1126/science.aai8204.

Reinart, A., Arst, H., Blanco-Sequeiros, A., Herlevi, A., 1998. Relation between underwater irradiance and quantum irradiance in dependence on water transparency at different depths in the water bodies. J. Geophys. Res. 103 (C4), 7749—7752, http://dx.doi.org/10.1029/97JC03645.

Shokr, M., Sinha, N., 2015. Sea Ice: Physics and Remote Sensing. John Wiley & Sons, Inc., Hoboken, NJ, 99—137, http://dx.doi.org/10.1002/9781119028000.

Skyllingstad, E.D., Paulson, C.A., Perovich, D.K., 2009. Simulation of melt pond evolution on level ice. J. Geophys. Res. 114 (C12), 15 pp., http://dx.doi.org/10.1029/2009JC005363.

Smith, R.C., Baker, K.S., 1981. Optical properties of the clearest natural waters (200—800 nm). Appl. Opt. 20 (2), 177—184, http://dx.doi.org/10.1364/AO.20.000177.

Taskjelle, T., Hudson, S.R., Granskog, M.A., Nicolaus, M., Lei, R., Gerland, S., Stamnes, J.J., Hamre, B., 2015. Spectral albedo and transmittance of thin young Arctic sea ice. J. Geophys. Res. Oceans 121 (1), 540—553, http://dx.doi.org/10.1002/2015JC011254.

Taylor, P.D., Feltham, D.L., 2004. A model of melt pond evolution on sea ice. J. Geophys. Res. 109 (C12), 19 pp., http://dx.doi.org/10.1029/2004JC002361.

Wang, C., Granskog, M.A., Gerland, S., Hudson, S.R., Perovich, D.K., Nicolaus, M., Karlsen, T.I., Fossan, K., Bratrein, M., 2014. Autonomous observations of solar energy partitioning in first-year sea ice in the Arctic Basin. J. Geophys. Res. Oceans 119 (3), 2066—2080, http://dx.doi.org/10.1002/2013JC009459.

Wang, C., Granskog, M.A., Hudson, S.R., Gerland, S., Pavlov, A.K., Perovich, D.K., Nicolaus, M., 2016. Atmospheric conditions in the central Arctic Ocean through the melt seasons of 2012 and 2013: Impact on surface conditions and solar energy deposition into the ice—ocean system. J. Geophys. Res. Atmos. 121 (3), 1043—1058, http://dx.doi.org/10.1002/2015JD023712.

Webster, M.A., Rigor, I.G., Perovich, D.K., Richter-Menge, J.A., Polashenski, C.M., Light, B., 2015. Seasonal evolution of melt ponds on Arctic sea ice. J. Geophys. Res. Oceans 120 (9), 5968—5982, http://dx.doi.org/10.1002/2015JC011030.

Zhang, S., Zhao, J., Shi, J., Jiao, Y., 2014. Surface heat budget and solar radiation allocation at a melt pond during summer in the central Arctic Ocean. J. Ocean Univ. China 13 (1), 45—50, http://dx.doi.org/10.1007/s11802-014-1922-0.

Oceanologia (2018) 60, 478—487

Available online at www.sciencedirect.com

ScienceDirect

journal homepage: www.journals.elsevier.com/oceanologia/

ORIGINAL RESEARCH ARTICLE

Acid volatile sulphide estimation using spatial sediment covariates in the Eastern Upper Gulf of Thailand: Multiple geostatistical approaches

Pasicha Chaikaew [a,c,*], **Penjai Sompongchaiyakul** [b,c]

[a] *Department of Environmental Science, Faculty of Science, Chulalongkorn University, Bangkok, Thailand*
[b] *Department of Marine Science, Faculty of Science, Chulalongkorn University, Bangkok, Thailand*
[c] *Center of Excellence on Hazardous Substance Management, Chulalongkorn University, Bangkok, Thailand*

Received 6 October 2017; accepted 26 March 2018
Available online 12 April 2018

KEYWORDS
Spatial estimation;
Acid volatile sulphide;
Sediment;
Geostatistical analysis;
Gulf of Thailand

Summary Acid volatile sulphide (AVS), one of the most reactive phases in sediments, is a crucial link in explaining a dynamic biogeochemical cycle in a marine ecosystem. Research gaps exist in describing the spatial variation of AVS and interconnections with sediment covariates in the Eastern Upper Gulf of Thailand. Measurements of AVS and auxiliary parameters followed the standard protocol. A comparison of ordinary kriging (OK), cokriging (CK), and regression kriging (RK) performance was evaluated based on the mean absolute error (MAE) and root mean square error (RMSE). The concentrations of AVS ranged from 0.003 to 0.349 mg g^{-1} sediment dry weight. Most parameters contained short range spatial dependency except for oxidation—reduction potential (ORP) and pH. The AVS tended to be both linearly and non-linearly related to ORP and readily oxidisable organic matter (ROM). The RK model, using inputs from the tree-based model, was the most robust of the three kriging methods. It is suggested that nonlinear interactions should be taken into account when predicting AVS concentration, and it is expected that this will further increase the model accuracy. This study helps establish a platform for ecological health and sediment quality guidelines.

* Corresponding author at: Department of Environmental Science, Faculty of Science, Chulalongkorn University, 254 Payathai Rd., Wang Mai, Pathumwan, Bangkok 10330, Thailand. Tel.: +66 2 218 5191; fax: +66 2 218 5180.
E-mail address: pasicha.c@chula.ac.th (P. Chaikaew).
Peer review under the responsibility of Institute of Oceanology of the Polish Academy of Sciences.

Production and hosting by Elsevier

https://doi.org/10.1016/j.oceano.2018.03.003

1. Introduction

The Upper Gulf of Thailand (UGoT) receives water from four major rivers, namely the Mae Klong and Tha Chin rivers in the western part, and the Chao Phraya and Bang Pakong in the eastern zone. These rivers bring sediment, which is predominantly of detrital derivation, that originates from the rivers (Emery and Niino, 1963; Milliman and Farnsworth, 2011).

The upper part of the Gulf of Thailand provides considerable marine resources and other ecosystem services; however, human activities have altered the environment in this region, in particular shoreline and sediment processes. For a long time, the UGoT has increasingly been threatened by both natural and anthropogenic forces impacting coastal areas and marine waters. Major impacts include pollution from industrial waste and domestic runoff, heavy metals, chemical residues from agriculture, and oil spills (Wattayakorn, 2006).

A major portion of organic matter in oxygen deprived aquatic sediments undergoes oxidation processes where microbes utilise sulphate as the electron receptor, producing hydrogen sulphides and other reduced-sulphur compounds (Morse et al., 1987). The study of sulphur compound in sediments is based on acid extraction (Allen et al., 1993; Morse and Cornwell, 1987). Acid volatile sulphides (AVS) have been shown to be an important metal-binding phase in sediments. It has been reported in various works (Allen et al., 1993; Simpson et al., 2012) that the sediments which contain excess AVS over simultaneously extracted metal (SEM) concentrations show a great reduction of toxicity. Exposure to high levels ($>1\ mg\ L^{-1}$) of dissolved oxygen during resuspension may oxidise the AVS and release metals to more bioavailable forms (Caetano et al., 2003).

The AVS is produced within moderately- to strongly-reducing conditions where redox potential is generally less than −100 mV (van Griethuysen et al., 2003). Variability of AVS in vertical patterns and on a point basis has been addressed in various studies. However, little is known about the spatial variation of AVS in sediments across a large area and its relationships to other sediment parameters. In addition, there are several geostatistical mapping techniques which have been used, but gaps still exist in estimating spatial sediment variables. This study aims to address the following questions: (1) how the spatial variability of AVS and sediment covariates are explicitly expressed across the marine ecology of interest, (2) to what extent are the sediment covariates associated with AVS, and (3) can sediment covariates help improve the predictive accuracy of the models when compared to the point-based interpolation technique.

To answer these questions, our objectives include describing the spatial auto-correlation pattern and variation of AVS and selected sediment covariates, determining the relationships between AVS and sediment covariates, and comparing the predictive performance of AVS derived from ordinary kriging (OK), cokriging (CK), and regression kriging (RK). Current knowledge suggests that no one technique is clearly preferable. The performance of spatial prediction is related to data-driven and multiple variable factors that need to be investigated more in this area. Information on the spatial distribution of AVS and various sediment parameters could be a crucial link to understanding the magnitude of sulphide and sediment transport. This would become a platform for further study, including risk assessment and toxicological studies, and the establishment of sediment quality guidelines (Jiwarungrueangkul et al., 2015).

2. Study area

The Eastern Upper Gulf of Thailand (EUGoT) (Fig. 1), located on the east side of the UGoT (latitude 13°20′N, longitude 100°45′E), receives an enormous amount of freshwater from the Chao Phraya and Bang Pakong estuaries, with annual average river discharge of $482\ m^3\ s^{-1}$ (Burnett et al., 2007) and $267\ m^3\ s^{-1}$ (Boonphakdee et al., 1999), respectively. Strong stratification develops due to high discharge during September and November. Water circulation patterns are variable where a counter-clockwise circulation occurs in the dry season during the northeast monsoon (November–January) and is then clockwise in the wet season of the southwest monsoon (May–August) (Buranapratheprat, 2008). Due to its comparatively static and poorly-flushing condition, the upper gulf is prone to the accumulation of nutrients and other contaminants (Wattayakorn, 2006). The average depth is 14.5 m and the average wind speed is about $5\ m\ s^{-1}$. Annual air temperature data collected from the Thai Meteorological Department at two meteorological stations within the study area between 2007 and 2016 showed a minimum mean temperature of 24.7°C, a mean temperature of 28.64°C, and a maximum mean temperature of 31.2°C. Activities in the area include fishing, aquaculture, recreation, tourism, ports, and shipping, as well as residential areas.

3. Material and methods

3.1. Field data collection

The sampling design was performed on $8 \times 8\ km^2$ grids, covering nearly $2000\ km^2$. A total of 39 sediment samples were collected in July 2016. Surface sediments were taken by the Smith McIntyre grab sampler on board r/v *Kasetsart-1*. The water depth was measured by the on-board depth sounding system. Each sediment sample was subsampled, placed in a zip-locked plastic bag, and stored in a cooler box containing dry ice until it was received by the laboratory. A portion of each sample was immediately checked for AVS on board the vessel.

3.2. On-site parameter analyses

Some parameters were analysed on board. pH and temperature were measured using a pH meter (Hanna HI98127, Hanna Instruments, USA), oxidation–reduction potential (ORP) was determined using an ORP meter (Oakton ORPTestr 10, Eutech instruments, USA), and salinity was measured with a YSI multi-parameter water quality sonde (EXO2, YSI Inc./Xylem Inc., USA). To prevent oxidation, the sediments were placed in polyethylene zipped-bags that contained as little air as possible. The AVS was determined on site using a gas detector

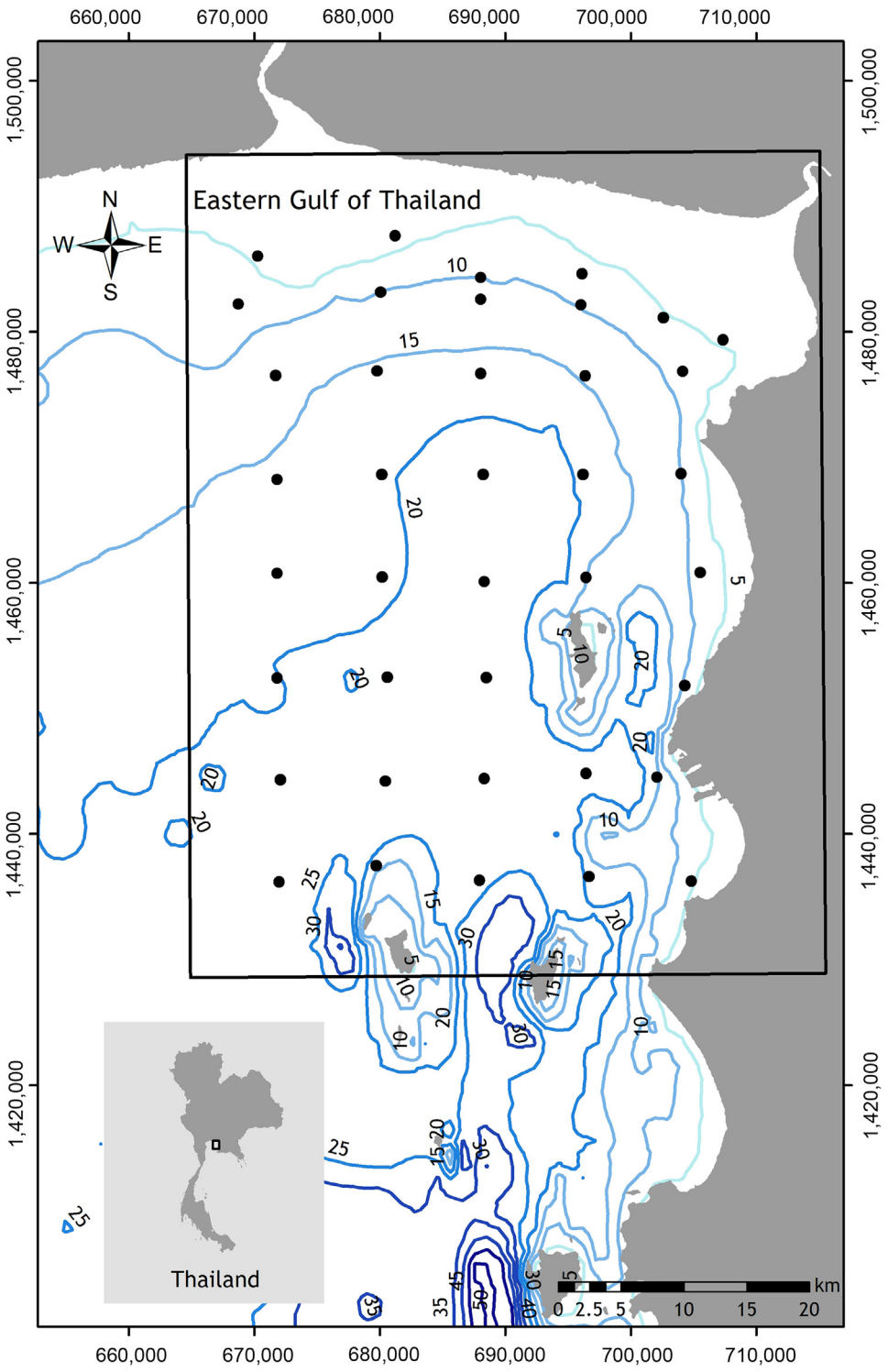

Figure 1 The Eastern Upper Gulf of Thailand. Black dots represent 39 sediment sampling observations. The bathymetry contours are digitised from the nautical charts, Royal Thai Navy No. 001 (1:240,000, 2014) and No. 102 (1:240,000, 2007).

tube. This low-cost and accurate method has recently been used to measure hydrogen sulphide content in marine sediments (Kanaya, 2014; Moqsud and Shigenori, 2016; Wu et al., 2003). The Gastec tube detection complies with international industrial standards and other standards i.e., industrial standard JIS M 7605/JIS M 7650, the International Organisation for Standardisation (ISO) 17621:2015, and the International Union of Pure and Applied Chemistry (IUPAC) (Gastec Corporation, 2017). In the field, the sampled sediments were put in the generation tube and 5 ml of distilled water was added. A gas detector tube (model 201H, Gastec Co., Japan) with a detection range of 0.02–0.2 mg (detection

limit = 0.002 mg, relative standard deviation = 5%) was connected to the gas generator tube and the other end was connected to a vacuum pump. 18 N 2 ml of sulfuric acid (H_2SO_4) was then added to the sediment in order to liberate hydrogen sulphide (H_2S) from the solid-phase sulphide in the sediment. The gas formed by this process, accumulated in the gas detector tube, allowing the AVS values to be read directly on the scale in a mg unit. AVS analysis was performed in triplicate via this method at each location.

3.3. Laboratory analyses

The oven-dry weight from a well-mixed sediment sample was determined. The wet weight AVS concentration was converted in response to the sediment dry weight basis. The water content was simply calculated from the percentage difference in the sample weight before and after oven drying at 105°C. ROM was measured following the modified Walkley-Black method using dextrose as the reference standard, as described in Loring and Rantala (1992). The particle size was analysed using a wet sieving and sedimentation technique with a slight modification from Carver (1971). In this study, fine-grain particles were considered for model inputs i.e., clay (0.002 mm) and clay + silt (<0.063 mm). All analyses were done in triplicate for every sample.

3.4. Statistical and geostatistical analyses

In this study, exploratory statistics were used to check data consistency, distribution of observed data, and outliers. The Anderson–Darling test was used to test the normality of data. The *p*-value should be greater than 0.05 to confirm that the data were normally distributed. According to the test, the AVS data were right-skewed, thus log-transformation was carried out to normalise the distribution. The ORP value was removed from the dataset, because it was considered an extreme outlier—the value was greater than three times the interquartile range away from the 75th percentile. To analyse the relationships among variables, a scatterplot matrix and Pearson's correlation were performed. The spatial behaviours of AVS and covariates were assessed using kriging (Krige, 1951), based on a 150-m resolution. The UTM_Zone_47N projected coordinate system was applied throughout the geospatial analysis. This study applied three kriging techniques to explicitly and spatially predict AVS. The statistical and geostatistical software packages used in this study included R 3.4.1 (R Core Team) and ArcGIS® 10.3.1 (Environmental Systems Research Institute (ESRI), Redlands, CA).

3.4.1. Ordinary kriging

Ordinary kriging (OK) or point kriging is the most common kriging practice in modelling spatial data. This method is based on two assumptions. First, the local mean of the data is unknown and is assumed constant within the domain of stationarity. Second, the variance between two observations is assumed to depend on the separation distance between the two points (Goovaerts, 1997). The spatial dependence can be expressed by semivariograms—half the expected squared difference between two points to the lag distance. The function of estimation is given as:

$$\gamma(h) = \frac{1}{2N(h)} \sum_{i=1}^{N(h)} \{Z(x_i) - Z(x_i + h)\}^2, \quad (1)$$

where $\gamma(h)$ is the semivariogram at distance interval h. $Z(x_i)$ represents measured variable values at sample locations of x_i and $Z(x_i + h)$ represents measured values of the neighbour at distance $x_i + h$. $N(h)$ is the total number of observation pairs separated by distance interval h. When the separation distance between two points increases, the spatial correlation shown in the semivariogram decreases. The OK predictions are based on the model:

$$\hat{Z}_{OK}(x_0) = \sum_{i=1}^{N} W_i(x_0) \cdot Z(x_i) = \lambda_0 \cdot Z, \quad (2)$$

where $\hat{Z}_{OK}(x_0)$ is the predicted value from the OK model. W_i is the kriging weight and λ_0 is the vector of kriging weights. Z is a vector of N observations. The characterisation of the semivariogram involves three parameters: nugget, sill, and range. The nugget C_0 informs the measurement error among observations at zero distance. The sill $C_0 + C$ is the upper boundary of second order stationarity or the maximum variance between observations. The spatial autocorrelation range r is the maximum distance of observations, thus spatial dependency no longer increases beyond the range (Grunwald, 2006; Webster and Oliver, 2001).

3.4.2. Cokriging

Cokriging (CK) is the multivariate extension of kriging that incorporates secondary data (Goovaerts, 1997). Sample correlations over 0.5 are recommended to be included in the CK model to improve the accuracy of the estimation (Taghizadeh-Mehrjardi et al., 2016). Besides the close relationships between covariates, their spatial patterns of continuity are also a key for model performance (Goovaerts, 1999). The CK predictions are made by:

$$\hat{Z}_{CK}(x_i) = \sum_{i=1}^{N} \lambda_i Z^s(x_i) + \sum_{j=1}^{M} \eta_j S(x_j), \quad (3)$$

where $\hat{Z}_{CK}(x_i)$ is the estimation of $Z^s(x_i)$ and $S(x_j)$ (j = 1, 2, 3, ..., M) are available data from auxiliary covariates. λ_i and η_j are kriging weights obtained from the CK computation.

3.4.3. Regression kriging

An application of regression kriging (RK) involves a fitted trend model along with residuals and then adds them back together to produce a final interpolation surface of estimates. The AVS at a new location (x) is estimated by RK as follows:

$$\hat{Z}_{RK}(x) = m(x) + r(x), \quad (4)$$

where the trend $m(x)$ is commonly fitted by linear regression, such as ordinary least squares (OLS), multiple linear regression (MLR), and generalised linear models (GLMs). The residuals, $r(x)$, are computed based on OK. In most cases, the connections between variables in an aqua system are much more complex and sometimes they are non-linearly related. This study extended a linear regression model to a tree-based technique which allowed for the possibility of nonlinear interactions between variables. The tree model successively splits a dataset into a series of decision rules, then creates uniform groupings (Prasad et al., 2006). The output from the

decision tree was used as a conditional statement in the raster calculation tool in the ArcGIS software. The prediction residuals of the regression tree (RT) were interpolated using OK and added to the predictions of RT.

3.5. Model evaluation

A 'cross-validation' or 'leave-one-out' process was used to validate the semivariogram model (Goovaerts, 1997). The evaluation of model performances was based on accuracy on a point-by-point basis. The mean absolute error (MAE) and the root mean square error (RMSE) of OK, BK, and RK were compared. The MAE is a measure of the sum of the absolute residuals, which indicates model performance bias. The MAE value should be approximately 0 to identify unbiased predictions. The RMSE reveals the magnitude of error that might happen at any point in terms of a measure of the sum of the squared residuals. The smaller the RMSE, the more accurate the predictions present. The equations are as follows (Webster and Oliver, 2001):

$$\mathrm{MAE} = \frac{1}{N}\sum_{i=1}^{N}|Z(x_{\mathrm{obs}}) - \hat{Z}(x_{\mathrm{pred}})|, \quad (5)$$

$$\mathrm{RMSE} = \sqrt{\frac{1}{N}\sum_{i=1}^{N}\left[Z(x_{\mathrm{obs}}) - \hat{Z}(x_{\mathrm{pred}})\right]^2}, \quad (6)$$

where $Z(x_{\mathrm{obs}})$ represents the values obtained from the empirical field and $\hat{Z}(x_{\mathrm{pred}})$ is the estimated values from the kriging models. N is the number of observed values with $i = 1, 2, 3, \ldots, N$.

4. Results and discussion

4.1. Descriptive statistics

The AVS and sediment variables data are shown in Table 1. Results from the table indicate that the EUGoT is considered a reducing environment favouring sulphate reduction. According to Barton (1995), general conditions that favour sulphate-reducing bacteria are 25°C to 35°C, ORP of −150 to −400 mV, pH between 4–5 and 8, and low oxygen (<1 mg L^{-1}).

The AVS concentrations in this study (mean 0.06 mg g^{-1}, range 0.003–0.35 mg g^{-1}) were found to be slightly higher than the mean of 0.03 mg g^{-1} and range of 0.0001–0.20 mg g^{-1} (Khaodon et al., 2011) in the same region; but lower than those found in the mangrove sediments (mean 0.62 mg g^{-1}, range 0.14–0.49 mg g^{-1}) on the east coast of the Gulf (Chaikaew et al., 2017). Our findings were close to the AVS content in the southern region (0.008–0.379 mg g^{-1} in summer; 0.001–0.282 mg g^{-1} in the rainy season) (Wongsin et al., 2015). During the wet season, rivers play a major role in contributing freshwater through the estuaries, thus salinity in the upper gulf shows a mixed state of brackish water and mild salt water, as explained in Johnson and Allen (2012), where a salinity of 0.5–30 psu is classified as a brackish condition and >30 psu is classified as seawater. The average water depth of the study area is 14.5 m, with the shallowest depth being 3.5 m and the deepest 27.7 m. Sediments contain a high percentage of clay + silt content with a mean of 61.81% and median of 61.42%, while the average clay content was 12.72%. ROM ranged from 0.46% to 4.84%.

Table 1 Description of AVS and sediment parameters.

Parameters	Unit	Min	Max	Mean	SD	Median	Skewness
AVS	mg g^{-1}	0.003	0.35	0.06	0.10	0.04	2.22
ORP	mV	−379	−126	−210	68	−204	−0.90
Temperature	°C	28.8	31.2	30.2	0.6	30.1	−0.03
pH	−log[H^+]	7.10	7.90	7.48	–	–	−0.36
Salinity	psu	29.0	33.2	32.4	1.1	32.8	−1.76
ROM	%	0.46	4.84	2.33	1.35	2.22	0.25
Clay	%	4.2	27.1	12.7	5.0	11.7	0.81
Clay + silt	%	8.0	99.6	61.8	33.4	61.4	−0.25

Table 2 Semivariogram metrics of log-transformed acid volatile sulphide (AVS) and sediment parameters based on the ordinary kriging (OK) model.

Variables	Samples [n]	Model	Nugget	Sill	Nugget/sill	No of lags	Lag size [m]	Range [m]
AVS	39	Spherical	0.17	1.15	0.15	10	2136	17,492
ORP	38	Exponential	3097	5333.33	0.58	10	3345	33,446
pH	39	Stable	0.02	0.06	0.33	12	5363	63,256
Salinity	39	Stable	0.46	1.91	0.24	10	5363	53,627
ROM	39	Stable	0.09	3.59	0.03	10	5363	53,627
Clay	39	Gaussian	0.01	0.10	0.10	10	1953	14,143
Clay + silt	39	Gaussian	42	2684.82	0.02	10	5363	64,353

4.2. Geospatial analysis of AVS and sediment parameters

The most appropriate models were chosen based on the lowest nugget and RMSE. Thus, different types of fitted models were implemented. A spherical model was used to fit the empirical semivariogram model of log-transformed AVS, while a stable model was used for pH, salinity, and ROM. A Gaussian model was applied to perform clay and clay + silt spatial distributions. The ORP semivariogram was the variable that used the exponential model. According to Cambardella et al. (1994), the degree of spatial dependency in the scale of sampling can be described by the nugget to sill ratio. When the ratio <0.25, the spatial structure is indicated as strong, 0.25–0.75 is moderate spatial dependency, and when >0.75 the spatial structure is weak. In this study, the spatial autocorrelation for OM, clay, and clay + silt was very strongly spatially dependent with a nugget/sill ratio ≤ 0.10. The spatial relationships were strong for AVS and salinity with nugget/sill values of 0.15 and 0.24, respectively. Medium-range spatial dependency was detected for pH and ORP with nugget/sill ratios of 0.33 and 0.58, respectively (Table 2).

The spatial patterns derived from OK were illustrated in Fig. 2a for AVS and Fig. 3 for sediment parameters. High concentrations of AVS appeared in the eastern region of the study area and gradually declined towards the middle of the Gulf. High AVS suggested an anoxic condition relating to high ROM from river discharge, anoxic water mass, and biomass residuals transported into the UGoT by high flow in the wet season (Morimoto, 2015). As noticed from the field observations, in the locations where a high AVS was identified, a rotten egg smell was recorded along with extensive algal blooms. This variation was likely to be influenced by the clockwise water circulation in which poor water circulation increased the vulnerability to AVS accumulation in the downwind direction. In addition, the eastern coast has a land-based source of nutrient inputs from domestic waste (Chaikaew et al., 2017) and various activities such as local food markets and aquaculture. The ORP, interestingly, showed a hot spot in the centre of the study area which slowly decreased towards the shore. From visual observation, the AVS and ORP appear to have an inverse spatial relationship. The water depth was shallow near the river mouth and deeper when entering the open ocean. Salinity was low near the estuaries because of fresh water discharge during the wet season and was high in the lower part of the study area. Spatial pH values between 7.2 and 7.8 were found in the northwest and east of the study area, and then increased towards the deep sea. A high percentage of clay and clay + silt was found near the shoreline and shallow water. These findings coincided with those of Qiao et al. (2015) and affirm that the fine-grained sediment is mostly deposited near the north coast. However, the sediment types in the UGoT have changed during the last two decades from clay, sandy clay, and sand sediment from north to south in the UGoT (Srisuksawad et al., 1997) to silt, sandy silt, and silty sand (Qiao et al., 2015).

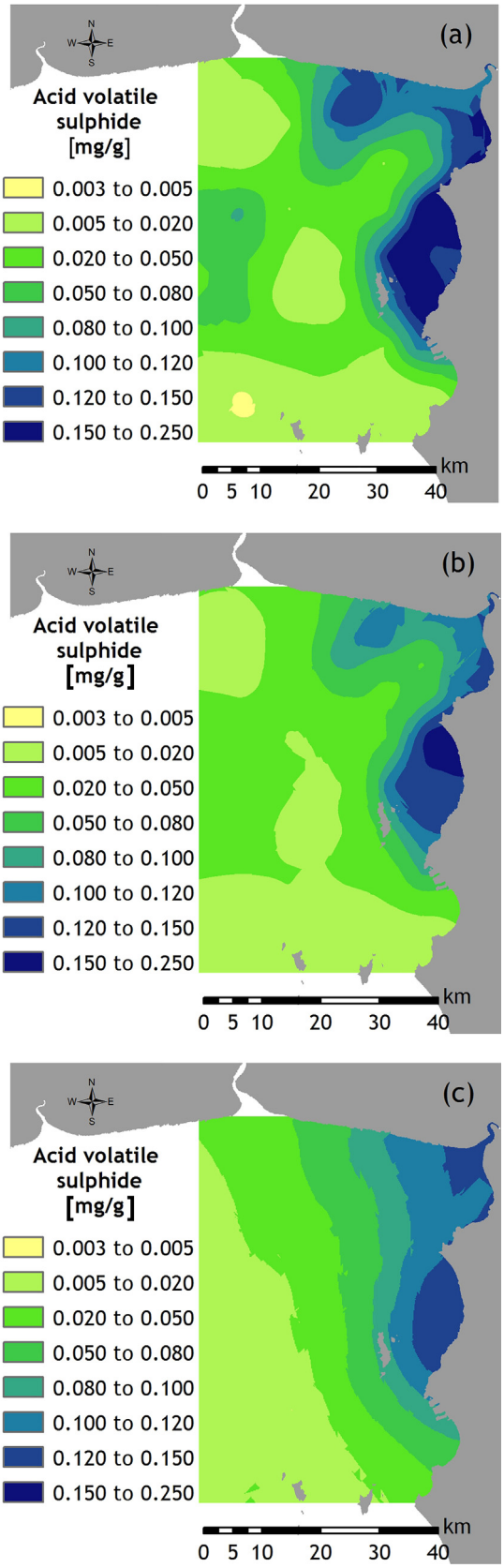

Figure 2 Spatial pattern of acid volatile sulphide (AVS) in the Eastern Upper Gulf of Thailand sediment generated by: (a) ordinary kriging (OK), (b) cokriging (CK), and (c) regression kriging (RK).

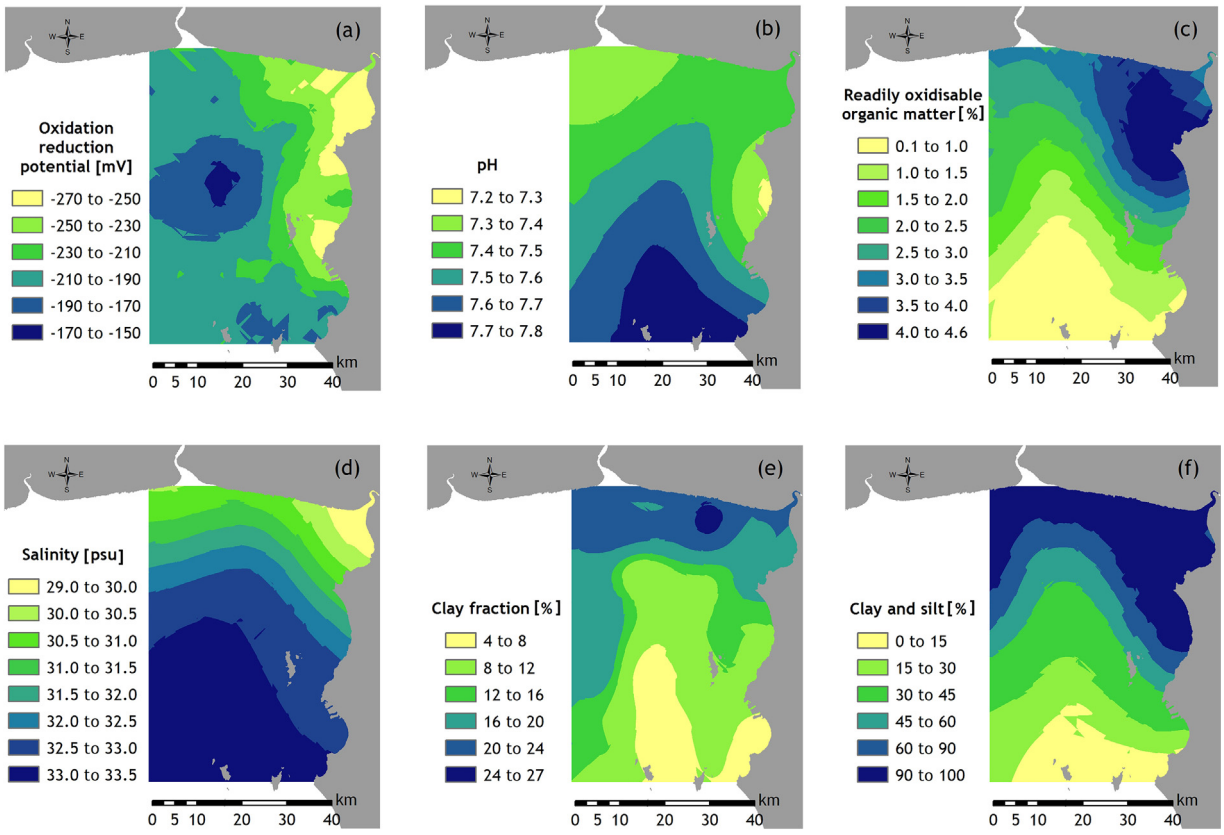

Figure 3 Spatial distribution of (a) oxidation–reduction potential (ORP), (b) pH, (c) readily oxidisable organic matter (ROM), (d) salinity, (e) clay fraction, and (f) clay and silt fraction in the Eastern Upper Gulf of Thailand sediment obtained by ordinary kriging (OK).

4.3. Relationships between AVS and bio-physical parameters

Of all the selected sediment parameters, two variables (ORP and ROM) contributed to the correlation strength with a Pearson's coefficient (r) greater than 0.5. A strong negative correlation was observed between AVS and ORP ($r = -0.73$, $p < 0.0001$). The AVS concentration was positively significantly correlated with ROM ($r = 0.53$, $p = 0.0008$), while the relationship between AVS and clay + silt fraction was found to be slightly weaker ($r = 0.49$, $p = 0.002$) than ORP and ROM. Fine sediment particles (clay + silt) and ROM were significantly correlated ($r = 0.89$, $p < 0.0001$), implying that small fractions are major controlling factors for ROM content. In the marine sediment, this positive correlation can be explained due to the stabilisation of ROM by adsorption (Mayer, 1994; Xing et al., 2011) or by the hydrodynamic equivalence between organic fractions and the high density of fine-grained particles (Mayer et al., 1993). In the EUGoT region, clay + silt content indirectly influenced AVS, as high surface areas of fine-grained particles were able to adsorb high levels of dissolved organic matter, which subsequently undergoes decomposition via sulphate reduction to produce sulphides. The correlation coefficient for each of ORP and ROM with AVS was greater than 0.5 and was selected as secondary covariates in CK analysis. The spatial pattern of AVS derived by CK (Fig. 2b) was marginally different from the OK model (Fig. 2a) yet reflected a similar pattern with a narrow range of predictions. The non-linear characteristics of each pair were further determined using a locally-weighted scatterplot smoothing (LOWESS) function, a non-parametric technique, for the best fit (Fig. 4).

A supervised machine learning, tree-based model was then applied to find the best decision based on values that minimise a loss function (McBratney et al., 2003). Results showed that only ORP and ROM were used in the tree construction. Three terminal nodes represented a classification of estimated AVS concentrations. The summary of the model showed a deviance of 0.002 (RMSE = 0.04), which indicated that the tree had a minimal error of model prediction. The simplicity of nodes identified a great deal of variation in estimating AVS means (Fig. 5). From the outputs of the terminal nodes, it can be interpreted that, for example, when the ORP was lower than −284 mV, a mean AVS concentration was 0.184 mg g^{-1}. When ORP was greater than −284 mV and ROM was lower than 2.98%, sediments contained 0.02 mg g^{-1} of AVS. The spatial pattern of AVS generated by RK is illustrated in Fig. 2c, which shows the high to low AVS concentrations from the east to the west obtained by RK.

4.4. Comparisons of kriging methods

When comparing the three interpolation methods visually, the spatial patterns generally show differences in the

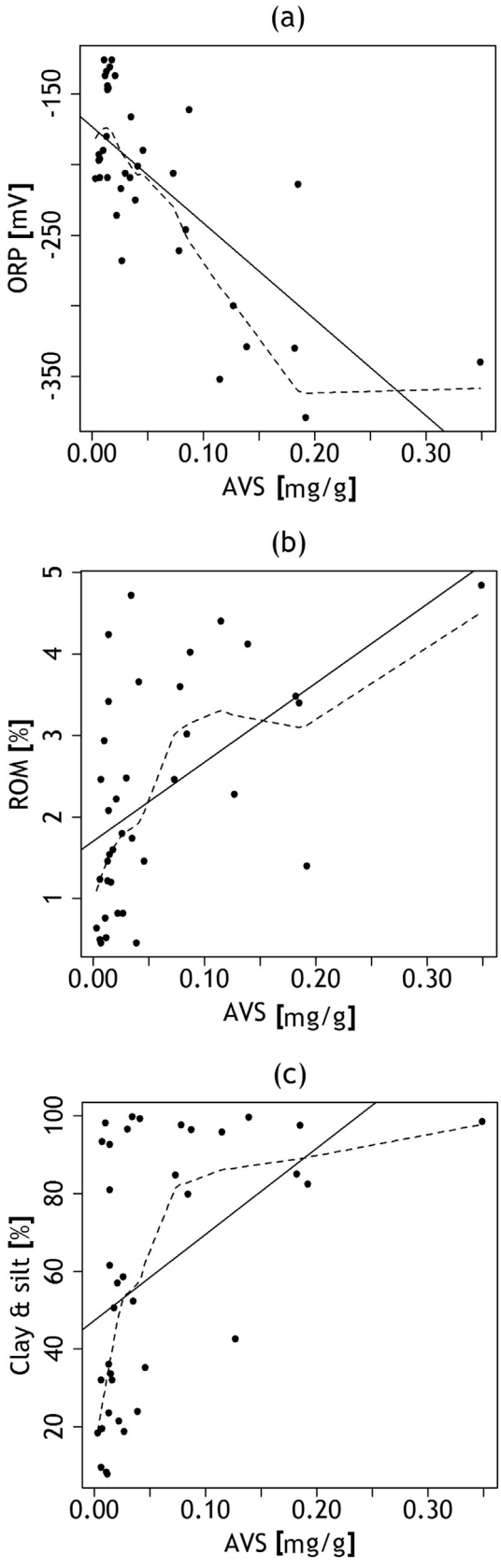

Figure 4 Scatterplots showing the relation of measured values of (a) acid volatile sulphide (AVS) and oxidation–reduction potential (ORP), (b) AVS and readily oxidisable organic matter (ROM), and (c) AVS and clay + silt using linear regression (bold line) and non-linear regression (dotted line).

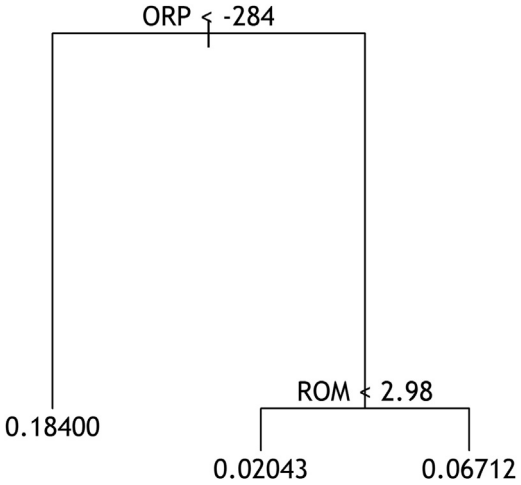

Figure 5 A regression tree model for predicting mean acid volatile sulphide (AVS) based on selected parameters.

smoothness of AVS (Fig. 2). Even though the mean value of AVS from OK, CK, and RK remained nearly constant ($\sim$0.05 mg g^{-1}), the range was small for CK and RK. A good contribution of auxiliary information from correlations > 0.5 was expected to provide prediction strength in CK. Interestingly, CK produced a weaker estimation than OK in this study when the two covariates (ORP and ROM) were included but performed a better estimation than OK when only ORP ($r = -0.73$) was included as a covariate. Even though the moderate to high correlation coefficients show that ORP, ROM, and clay + silt provide more information about AVS, a better prediction is not necessarily generated unless the patterns of spatial continuity were similar (Goovaerts, 1997). Šiljeg et al. (2015) indicated that CK was the best geostatistical method among the 14 deterministic and geostatistical methods (excluding RK) in predicting digital elevation models (DEM) in a bathymetric survey. Their explanation was that precisely-obtained data and more detailed analysis enabled the production of a better continuous surface at micro levels.

In this study, RK, a technique combining a regression tree and OK, is shown to be the most accurate model, rather than CK or OK, based on very small MAE and RMSE results. The RK model was fitted locally based on tree conditions to optimise the data fitting. The findings in this study are consistent with others (Li et al., 2011; Martínez-Cob, 1996; Moral, 2010) which indicated that RK was by far the most accurate method in predicting environmental data. Results of the error metrics from different approaches are shown in Table 3.

5. Conclusions

This study has shown measurements and spatial variability in AVS and selected sediment parameters and their relationships. The average AVS contents of surface sediment ranged from 0.003 to 0.349 mg g^{-1} dry weight sediment with an average value of 0.057 mg g^{-1}. A high amount of AVS was

Table 3 A comparison of error metrics of predicted AVS in mg g^{-1} dry weight unit, calculated on point-by-point data (n = 39).

Geostatistical methods	Min	Max	Mean	SD	MAE	RMSE
OK	0.004	0.249	0.052	0.055	0.005	0.033
CK*	0.010	0.154	0.057	0.040	0.001	0.004
CK**	0.007	0.288	0.050	0.050	−0.016	0.100
RK	0.009	0.142	0.059	0.042	−0.0003	0.002

OK = ordinary kriging; CK = cokriging; RK = regression kriging; SD = standard deviation; MAE = mean absolute error; RMSE = root mean squared error; CK* = ORP included as covariate; CK** = two parameters (ORP and ROM) included as covariates.

found along the east coast. The spatial dependence of ORP and pH was contained in a medium-range pattern. The rest of the sediment parameters appeared to be within a short range. The concentrations of AVS in the sediments of EUGoT were closely related to the ORP and ROM in a linear interaction. The ORP and ROM, therefore, were spatial sediment covariates of AVS in the nonparametric model. When using the CK method, the correlation between parameters of values greater than 0.7 outperformed OK. Overall, RK was the most robust method, over CK and OK, for predicting AVS. It is recommended that nonparametric or nonlinear models be considered as an alternative method in estimating spatial AVS variability to reduce modelling bias.

Acknowledgements

This project was funded by the Ratchadaphiseksomphot Endowment fund (Grant number RGN_2559_003_03_23). It is partially supported by the Sci Super III, Chulalongkorn University, the Research Program of Municipal Solid Waste and Hazardous Waste Management, Center of Excellence on Hazardous Substance Management (HSM), the S&T Postgraduate Education and Research Development Office (PERDO), the Office of Higher Education Commission (OHEC). We thank Miss Pacharamon Sripoonpan for digitising the bathymetry contours and Mr. Ian Fraser for language editing.

References

Allen, H.E., Fu, G., Deng, B., 1993. Analysis of acid-volatile sulfide (AVS) and simultaneously extracted metals (SEM) for the estimation of potential toxicity in aquatic sediments. Environ. Toxicol. Chem. 12, 1441–1453, http://dx.doi.org/10.1002/etc.5620120812.

Barton, L. (Ed.), 1995. Sulfate-reducing Bacteria, Biotechnology Handbooks. Springer Science + Business Media, LLC, New York, 336 pp.

Boonphakdee, T., Sawangwong, P., Fujiwara, T., 1999. Freshwater discharge of Bangpakong River flowing into the inner Gulf of Thailand. La mer 37, 103–109.

Buranapratheprat, A., 2008. Circulation in the Upper Gulf of Thailand: a review. Burapha Sci. J. 13, 75–83.

Burnett, W.C., Wattayakorn, G., Taniguchi, M., Dulaiova, H., Sojisuporn, P., Rungsupa, S., Ishitobi, T., 2007. Groundwater-derived nutrient inputs to the Upper Gulf of Thailand. Cont. Shelf Res. 27 (2), 176–190, http://dx.doi.org/10.1016/j.csr.2006.09.006.

Caetano, M., Madureira, M.-J., Vale, C., 2003. Metal remobilisation during resuspension of anoxic contaminated sediment: short-term laboratory study. Water Air Soil Pollut. 143 (1–4), 23–40, http://dx.doi.org/10.1023/A:1022877120813.

Cambardella, C.A., Moorman, T.B., Parkin, T.B., Karlen, D.L., Novak, J.M., Turco, R.F., Konopka, A.E., 1994. Field-scale variability of soil properties in central Iowa soils. Soil Sci. Soc. Am. J. 58 (5), 1501, http://dx.doi.org/10.2136/sssaj1994.03615995005800050033x.

Carver, R.E., 1971. Procedures in Sedimentary Petrology. John Wiley & Sons Ltd., New York, 653 pp.

Chaikaew, P., Nawatrairat, N., Srithongouthai, S., 2017. Modeling spatio-vertical distribution of sulfate and total sulfide along the mangrove intertidal zone. Environ. Asia 10 (2), 1–8, http://dx.doi.org/10.14456/ea.2017.15.

Emery, K.O., Niino, H., 1963. Sediments of the Gulf of Thailand and adjacent continental shelf. GSA Bull. 74 (5), 541–554, http://dx.doi.org/10.1130/0016-7606(1963)74[541:SOTGOT]2.0.CO;2.

Gastec Corporation, 2017. Gas Detector Tubes (and Some Relevant Industrial Standards).

Goovaerts, P., 1999. Geostatistics in soil science: state-of-the-art and perspectives. Geoderma 89 (1–2), 1–45, http://dx.doi.org/10.1016/S0016-7061(98)00078-0.

Goovaerts, P., 1997. Geostatistics for Natural Resources Evaluation, Applied Geostatistics Series. Oxford University Press, New York, 483 pp.

Grunwald, S. (Ed.), 2006. Environmental Soil-Landscape Modeling – Geographic Information Technologies and Pedometrics. CRC Press, Boca Raton, 504 pp.

Jiwarungrueangkul, T., Dharmavanij, S., Sompongchaiyakul, P., Kornkanitnan, N., 2015. Equilibrium partitioning approach to define sediment quality guideline of some metals in Chao Phraya Estuary, Thailand. Asian J. Water Environ. Pollut. 12 (3), 23–31, http://dx.doi.org/10.3233/AJW-150004.

Johnson, W.S., Allen, D.M., 2012. Zooplankton of the Atlantic and Gulf Coasts: A Guide to Their Identification and Ecology, 2nd ed. The Johns Hopkins University Press, Baltimore, 452 pp.

Kanaya, G., 2014. Recolonization of macrozoobenthos on defaunated sediments in a hypertrophic brackish lagoon: effects of sulfide removal and sediment grain size. Mar. Environ. Res. 95, 81–88, http://dx.doi.org/10.1016/j.marenvres.2013.12.014.

Khaodon, K., Intarachart, A., Joeraket, W., 2011. Some aspects of sediment quality in eastern coast of the Gulf of Thailand. In: Presented at the Kasetsart University Annual Conference, 1–4 February, 2011, Bangkok (Thailand).

Krige, D.G., 1951. A statistical approach to some basic mine valuation problems on the Witwatersrand. J. Chem. Met. Min. Soc. S. Afr. 52, 119–139.

Li, J., Heap, A.D., Potter, A., Daniell, J.J., 2011. Application of machine learning methods to spatial interpolation of environmental variables. Environ. Modell. Softw. 26 (12), 1647–1659, http://dx.doi.org/10.1016/j.envsoft.2011.07.004.

Loring, D.H., Rantala, R.T.T., 1992. Manual for the geochemical analyses of marine sediments and suspended particulate matter. Earth-Sci. Rev. 32 (4), 235–283, http://dx.doi.org/10.1016/0012-8252(92)90001-A.

Martínez-Cob, A., 1996. Multivariate geostatistical analysis of evapotranspiration and precipitation in mountainous terrain. J. Hydrol. 174 (1–2), 19–35, http://dx.doi.org/10.1016/0022-1694(95)02755-6.

Mayer, L.M., 1994. Surface area control of organic carbon accumulation in continental shelf sediments. Geochim. Cosmochim. Acta

58 (4), 1271–1284, http://dx.doi.org/10.1016/0016-7037(94)90381-6.

Mayer, L.M., Jumars, P.A., Taghon, G.L., Macko, S.A., Trumbore, S., 1993. Low-density particles as potential nitrogenous foods for benthos. J. Mar. Res. 51 (2), 373–389, http://dx.doi.org/10.1357/0022240933223738.

McBratney, A.B., Mendonça Santos, M.L., Minasny, B., 2003. On digital soil mapping. Geoderma 117 (1–2), 3–52, http://dx.doi.org/10.1016/S0016-7061(03)00223-4.

Milliman, J.D., Farnsworth, K.L., 2011. River Discharge to the Coastal Ocean: A Global Synthesis. University Press, Cambridge, UK, 394 pp.

Moqsud, M.A., Shigenori, H., 2016. Evaluation of acid volatile sulfide (AVS) distribution in tidal mud of the Ariake Sea, Japan. Int. J. Energy Environ. Res. 4, 1–6.

Moral, F.J., 2010. Comparison of different geostatistical approaches to map climate variables: application to precipitation. Int. J. Climatol. 30 (4), 620–631, http://dx.doi.org/10.1002/joc.1913.

Morimoto, A., 2015. Behavior of anoxic water in the Bangpakong estuary. Mar. Res. Indonesia 37 (2), 109–121, http://dx.doi.org/10.14203/mri.v37i2.29.

Morse, J.W., Cornwell, J.C., 1987. Analysis and distribution of iron sulfide minerals in recent anoxic marine sediments. Mar. Chem. 22 (1), 55–69, http://dx.doi.org/10.1016/0304-4203(87)90048-X.

Morse, J.W., Millero, J.M., Cornwell, J.C., Rickard, D., 1987. The chemistry of the hydrogen sulfide and iron sulfide systems in natural waters. Earth-Sci. Rev. 24, 1–42.

Prasad, A.M., Iverson, L.R., Liaw, A., 2006. Newer classification and regression tree techniques: bagging and random forests for ecological prediction. Ecosystems 9 (2), 181–199, http://dx.doi.org/10.1007/s10021-005-0054-1.

Qiao, S., Shi, X., Fang, X., Liu, S., Kornkanitnan, N., Gao, J., Zhu, A., Hu, L., Yu, Y., 2015. Heavy metal and clay mineral analyses in the sediments of Upper Gulf of Thailand and their implications on sedimentary provenance and dispersion pattern. J. Asian Earth. Sci. 114 (3), 488–496, http://dx.doi.org/10.1016/j.jseaes.2015.04.043.

Simpson, S.L., Ward, D., Strom, D., Jolley, D.F., 2012. Oxidation of acid-volatile sulfide in surface sediments increases the release and toxicity of copper to the benthic amphipod Melita plumulosa. Chemosphere 88, 953–961, http://dx.doi.org/10.1016/j.chemosphere.2012.03.026.

Srisuksawad, K., Porntepkasemsan, B., Nouchpramool, S., Yamkate, P., Carpenter, R., Peterson, M.L., Hamilton, T., 1997. Radionuclide activities, geochemistry, and accumulation rates of sediments in the Gulf of Thailand. Cont. Shelf Res. 17 (8), 925–965, http://dx.doi.org/10.1016/S0278-4343(96)00065-9.

Šiljeg, A., Lozić, S., Šiljeg, S., 2015. A comparison of interpolation methods on the basis of data obtained from a bathymetric survey of Lake Vrana, Croatia. Hydrol. Earth Syst. Sci. 19 (8), 3653–3666, http://dx.doi.org/10.5194/hess-19-3653-2015.

Taghizadeh-Mehrjardi, R., Toomanian, N., Khavaninzadeh, A.R., Triantafilis, J., 2016. Predicting and mapping of soil particle-size fractions with adaptive neuro-fuzzy inference and ant colony optimization in central Iran. Eur. J. Soil Sci. 67, 707–725.

van Griethuysen, C., Meijboom, E.W., Koelmans, A.A., 2003. Spatial variation of metals and acid volatile sulfide in floodplain lake sediment. Environ. Toxicol. Chem. 22, 457–465.

Wattayakorn, G., 2006. Environmental Issues in the Gulf of Thailand. In: The Environment in Asia Pacific Harbours. Springer, Dordrecht, 249–259, http://dx.doi.org/10.1007/1-4020-3655-8_16.

Webster, R., Oliver, M.A., 2001. Geostatistics for Environmental Scientists. John Wiley & Sons Ltd., West Sussex, 330 pp.

Wongsin, T., Boonprab, K., Okamoto, Y., Salaenoi, J., 2015. Hydrogen sulfide distribution in sediments collected from cockle farm at Bandon Bay, Thailand. In: Presented at the International Conference on Plant, Marine and Environmental Sciences (PMES-2015), Kuala Lumpur, Malaysia, 97–99.

Wu, S.S., Tsutsumi, H., Kita-Tsukamoto, K., Kogure, K., Ohwada, K., Wada, M., 2003. Visualization of the respiring bacteria in sediments inhabited by *Capitella* sp. 1. Fish. Sci. 69 (1), 170–175, http://dx.doi.org/10.1046/j.1444-2906.2003.00602.x.

Xing, L., Zhang, H., Yuan, Z., Sun, Y., Zhao, M., 2011. Terrestrial and marine biomarker estimates of organic matter sources and distributions in surface sediments from the East China Sea shelf. Cont. Shelf Res. 31 (10), 1106–1115, http://dx.doi.org/10.1016/j.csr.2011.04.003.

Oceanologia (2018) 60, 488—499

Available online at www.sciencedirect.com

ScienceDirect

journal homepage: www.journals.elsevier.com/oceanologia/

ORIGINAL RESEARCH ARTICLE

Bio-optical trends of seas around Turkey: An assessment of the spatial and temporal variability

Fethi Bengil [a,*], **Sinan Mavruk** [b]

[a] *Marine School — Earth System Science Research Center, Girne American University, Girne, TRNC, Turkey*
[b] *Fisheries Faculty, Department of Marine Biology, Çukurova University, Balcalı, Adana, Turkey*

Received 23 October 2017; accepted 27 March 2018
Available online 13 April 2018

KEYWORDS
Trend analysis;
Chlorophyll-*a*;
Colored dissolved organic matter;
Particulate backscattering;
Ecosystem dynamics

Summary Until present, bio-optical characteristics and their variations in the eastern Mediterranean and Black Sea have rarely been studied. In order to characterize the basic features of bio-optical variables found in the seas surrounding Turkey, remotely sensed data sets covering the period between September 1997 and March 2017 were studied for the purpose of this research. Chlorophyll-*a* concentration (CHL), absorption coefficient by colored dissolved organic matter (CDOM) and particulate backscattering coefficient (BBP) were both evaluated to describe their recent linear and non-linear inter-annual patterns in the sub regions of the northern Levantine Sea (LS), the eastern Aegean Sea (AS), the Marmara Sea (MS) and the southern Black Sea (BS). The results determined a highly significant and decreasing trend of CHL in the Black Sea, whilst most other regions from the seas around Turkey displayed non-significant trends. The analysis indicated that the seas around Turkey can be clustered into two regions based on their bio-optical properties; one being the Black Sea and Marmara Sea, and the second cluster being the Aegean Sea and Levantine Sea.

* Corresponding author at: Girne American University, Marine School-Earth System Science Research Center, University Drive, Karmi Campus, Girne, TRNC, Turkey. Tel.: +90 533 836 08 22; Fax: +90 392 650 20 61.
E-mail address: fethibengil@gau.edu.tr (F. Bengil).
Peer review under the responsibility of Institute of Oceanology of the Polish Academy of Sciences.

ELSEVIER Production and hosting by Elsevier

https://doi.org/10.1016/j.oceano.2018.03.004

1. Introduction

Turkey is surrounded by semi-enclosed seas; the Black Sea at the north, the Marmara Sea in the north west, and two important sectors of the eastern basin of the Mediterranean Sea – the Aegean Sea in the west and the Levantine Sea in the south. Each sea has its own distinctive biogeochemical and hydrographic properties as well as ecosystem dynamics.

The Black Sea is commonly known to be one of the world's most distinct seas, with specific regard to its brackish water and anoxic deep water formation. It is surrounded by land, with the exception of its connection to the Marmara Sea through a narrow and shallow strait, the Istanbul Strait (Fig. 1). With considerable precipitation and the inflow of freshwater from local rivers, the water is dominated by brackish characteristics (Berner and Berner, 2012; Oguz et al., 2004). These inflows carry with them various particulate or dissolved matters (Cauwet et al., 2002; Oguz et al., 2004) which significantly influence the biogeochemical dynamics of the Black Sea. During the last century, the Black Sea revealed remarkable regime shifts in climatic conditions and biological communities (Oguz and Gilbert, 2007). Parallel to these developments, there were significant changes to the food-web structure, caused by invasive planktonic predators such as *Mnemiopsis leidyi* and *Beroe ovata* (Oguz et al., 2012). Changes within the structure of the phytoplankton community were also reported during this same period (Agirbas et al., 2017; Kideys, 1994). Mikaelyan et al. (2013) reported a significant biomass increase in phytoplankton and observed a shift from a Dinoflagellate dominated community to a Coccolithophore dominated community over the same period. These shifts also reflected in higher trophic levels, and caused subsequent changes in both spawning and the recruitment dynamics of small pelagic fishes (Gucu et al., 2016).

The Marmara Sea is another semi-closed sea that connects the Black Sea to the Aegean Sea through the Turkish straits, and is characterized by two stratified water layers. The water of the Black Sea is present throughout the upper layer of the Marmara Sea, whilst water from the Mediterranean fills in the lower layers. The mixing of these water types is limited, and salinity gradually increases westward, toward the Dardanelles (see Fig. 1). Detailed investigations about the circulation patterns as well as the physical (Beşiktepe et al., 1994) and biogeochemical properties (Yalçın et al., 2017; Zeri et al., 2014) of the Marmara Sea have previously been conducted. Yalçın et al. (2017) reported on the nutrient dynamics of the Marmara Sea, and observed a high enrichment level of nutrients caused by anthropogenic impacts; which are often responsible for eutrophication issues.

The physical properties and circulation patterns of the Aegean Sea have been outlined in many studies evaluating both coastal (Eronat and Sayin, 2014; Sayin, 2003) and open (Nittis and Perivoliotis, 2002; Roether et al., 1996; Theocharis et al., 1993; Vervatis et al., 2013) regions (see Fig. 1). Results from studies conducted in the Aegean Sea have shown gradual changes in biogeochemical properties ranging from north to south (Ehrmann et al., 2007; Tzortziou et al., 2015). Nutrient-rich surface waters have been detected to the north of the Aegean Sea due to the inflow of water from the Marmara Sea via the Dardanelles (Fig. 1) and inputs from local rivers (Polat and Tugrul, 1995; Souvermezoglou et al., 2014). The biogeochemical properties of these surface waters have an important impact on the ecological status of the Aegean Sea. Although the Aegean Sea is generally thought to be oligotrophic (Ignatiades, 1998; Ignatiades

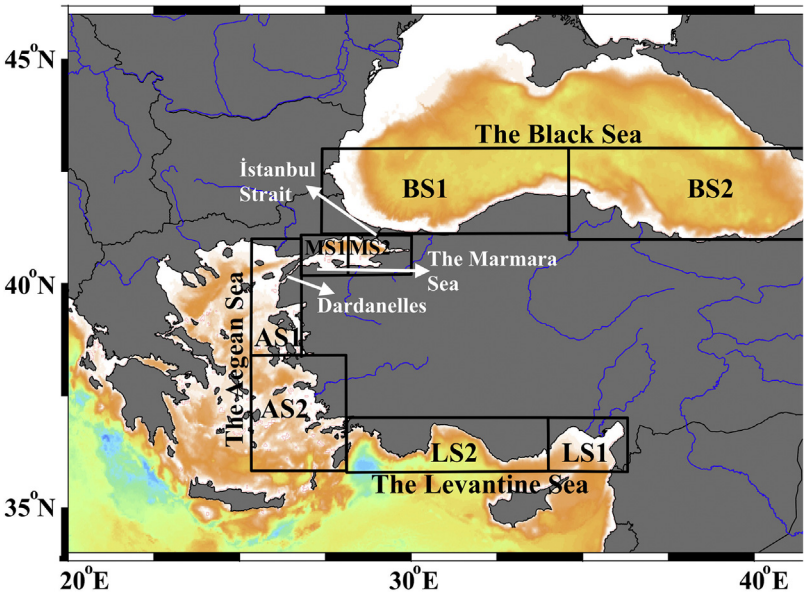

Figure 1 Study area and sub-regions for Seas of Turkey (LS1: the eastern Levantine Sea, LS2: the western Levantine Sea, AS1: the northern Aegean Sea, AS2: the southern Aegean Sea, MS1: the western Marmara Sea, MS2: the eastern Marmara Sea, BS1: the western Black Sea, BS2: the eastern Black Sea).

et al., 2002), a significant decrease in phytoplankton biomass spreading from the northern Aegean Sea toward the southern Aegean Sea, in addition to changes in the food web structure throughout the Aegean Sea, has been formerly presented by Siokou-Frangou et al. (2002).

The Levantine Sea is another important region for water formation in the Mediterranean Sea, and can be divided into two sub-regions based on its bathymetry and habitat characteristics (Fig. 1). The north-western Levantine Sea has a narrow continental shelf, scarce terrestrial inputs and a highly oligotrophic structure. In contrast, the north-eastern Levantine Sea is known to have a wider continental shelf area (Ozsoy et al., 1993) as well as intensive riverine inputs, enriched nutrient concentration and a higher primary production rate (Tuğrul et al., 2016). Driving forces in the areas throughout the southern Turkish coasts also create both permanent and recurrent eddies, gyres and jets. Details on the physical properties of the Levantine Sea are presented by Akpinar et al. (2016) and a hydro-chemical analysis is reviewed by Tuğrul et al. (2016). However, it is important to note that although the bio-optical properties of the northern Levantine Sea have already been described (Orek, 2007), there is currently no information available on the trends of these parameters.

Marine ecosystems are dynamic due to the changes and interactions amongst their living and non-living components over the course of time. Chlorophyll pigments are an important contributor of optically active constituents (OACs) with colored dissolved organic matter (CDOM) and total particulate matter in the seawater column. OACs interact with light based on their inherent optical properties (IOPs) such as absorption or scattering (Garaba et al., 2014). The distribution and composition of OACs in the water column can also contribute to the determination of underwater light fields, which are important for understanding the dynamics of primary production in aquatic environments. From hereinafter OACs and IOPs will be referred to as bio-optical properties due to their optical interactions.

Chlorophyll-*a* concentration (CHL) is a proxy for the estimation of phytoplankton biomass, and is a highly useful indicator in marine studies as it is directly related to primary production in the marine food-web (Kasprzak et al., 2008). Remote sensing enables access to extensive data available in high spatial and temporal resolution. The remotely sensed CHL signal provides a wide range of applications to monitor marine ecosystems, with examples being the Black Sea (Oguz and Gilbert, 2007) and the Mediterranean Sea (Colella et al., 2016).

CDOM represents the colored portion of dissolved organic matter in the sea water and another important bio-optical component to increase understanding of marine ecosystems (Coble et al., 1998; Stedmon and Markager, 2001). Dissolved organic matter (DOM) in marine environments contribute significantly to the organic carbon budget of the earth (Hedges, 1992), and influences the global carbon cycle (Puddu et al., 2000). Although there are many studies on the distribution of dissolved organic carbon, which correlate with CDOM in both the Black Sea and the eastern Mediterranean (Margolin, 2017; Pitta, 2016), CDOM is still an under-researched variable (Margolin, 2017; Pitta, 2016; Tzortziou et al., 2015). Furthermore, the spatial and inter-annual variability of CDOM has not yet been adequately evaluated.

BBP refers to an optical property used for the purpose of estimating different measurements taken from seawater, including suspended particle assemblages, and more specifically, particulate organic carbon (POC) (Loisel et al., 2001; Stramski et al., 2008) and phytoplankton carbon biomass (Siegel et al., 2014). These types of estimations are determined by using either space- or airborne sensors in relation to their refraction properties (Reynolds et al., 2016). Thus, BBP is another important bio-optical property required for understanding the dynamics of primary production. Although previous studies have been conducted via the utilization of optical principles in the Black Sea (Chami et al., 2005; Karageorgis et al., 2014; Orek, 2007), the Aegean Sea (Burenkov et al., 1999; Orek, 2007) and the northern Levantine Sea (Orek, 2007), these efforts focused on either the determination of optical characteristics, the understanding of suspended particulate composition or the circulation patterns of local water masses. To date, no evaluation regarding the temporal trends of BBP in the aforementioned region exists.

Bio-optical properties are responsible for determining the distribution of light in the water column. These properties are also optically relevant components for phytoplankton absorption, which is directly related to primary production. The temporal changes in these properties create a direct impact on biogeochemical cycles, and also influence the dynamics of lower trophic levels. Examples of feedback related to the effects of temporal changes on higher trophic levels observed in Black Sea anchovy have previously been documented by Gucu et al. (2016). Whilst detailed considerations of these properties exist throughout the world (El Hourany et al., 2017; Gregg and Rousseaux, 2014), very few studies describing their trends in the Mediterranean Sea (e.g., Coppini et al., 2013; Colella et al., 2016) are currently available.

The present study investigated a remotely sensed dataset of bio-optical properties, CHL, CDOM and BBP in the seas around Turkey. The study focuses on the northern Levantine Sea, the eastern Aegean Sea, the Marmara Sea and the southern Black Sea, where each region has different climatic and trophic characteristics. The main objective of our study was to characterize the basic features of the bio-optical properties being investigated, and to describe and compare their recent linear and non-linear inter-annual patterns. These properties are all indicators of ecological conditions within any marine system.

2. Material and methods

Inter-annual changes of bio-optical properties were investigated in the seas surrounding Turkey (the southern Black Sea, the Marmara Sea, the eastern Aegean Sea and the northern Levantine Sea). In order to remove any possible source of bias from the wide spatial coverage and the different sub-regional physical and biological properties, each sea was divided into two sub-regions based on statistical considerations (Fig. 1). Sub-regions were chosen in accordance with the oceanographic properties or dynamics of each sea, as presented in previous studies (Akpinar et al., 2016; Beşiktepe et al., 1994; Nittis and Perivoliotis, 2002; Oguz et al., 2004 for the

Levantine Sea, the Marmara Sea, the Aegean Sea and the Black Sea respectively).

3. Data description

Trends of bio-optical properties were evaluated in terms of CHL, CDOM and BBP. In order to analyze these variables, GlobColour data (http://globcolour.info) was used, which has been developed, validated, and distributed by ACRI-ST, France. GlobColour is a project of the European Space Agency Data User Element (ESA DUE) and provides a continuous dataset from merged outputs of Ocean Color products from different sensors (see the GlobColour Product User Guide document in http://www.globcolour.info/CDR_Docs/GlobCOLOUR_PUG.pdf). The data-sets used in this study were produced at full spatial resolution (1 km^2) under the spatial domain of the extended European area. A total of 235 composite products were generated by using different ocean color products during certain time periods between September 1997 and March 2017. Each composite product was composed by utilizing remotely sensed signals from sensors that were available during the aforementioned time period (see the GlobColour Product User Guide for the detailed information). Composite products by Garver, Siegel, Maritorena Model (GSM) were also used for further analysis. The GSM method, which is a semi-analytical model, uses the normalized reflectances at the original sensor wavelengths without inter calibration (see Maritorena and Siegel (2005) for more details). This method is only available for GlobColour products of CHL, BBP and CDOM (see the GLOBCOLOUR Product User Guide document in http://www.globcolour.info/CDR_Docs/GlobCOLOUR_PUG.pdf). Semi-analytical models are more sensitive than standard algorithms (O'Reilly et al., 1998) and GSM showed a generally excellent level of agreement with in situ measurements (Siegel et al., 2005). A seasonal bias of the variables retrieved from ocean color algorithms showed that there was both underestimation and overestimation apparent within the region (Orek, 2007; Sancak et al., 2005). However, the use of an inter-annual approach in trend analysis is expected to overcome any such systematic errors generated from the algorithms.

Regarding regional analysis, the mean of all pixels belonging to a defined region was calculated for all of the variables used in this study. Monthly mean values were calculated between September 1997 and March 2017 for bio-optical properties, and the maximum, minimum, mean and standard deviation were then calculated to present the descriptive characteristics of each region.

4. Time series analyses

In order to analyze inter-annual changes, a time series of each parameter (Y_t) was firstly decomposed to trend (T_t), seasonal (S_t) and remainder (R_t) components by using a locally reweighted regression (loess) based seasonal trend decomposition (stl) procedure (Cleveland et al., 1990) as follows:

$$Y_t = T_t + S_t + R_t.$$

The trend components (T) from this procedure were used to represent the non-linear trends of parameters. To calculate the linear trends, seasonal signals were first removed ($X_t = Y_t - S_t$). The direction and magnitude of trends were then detected with rank-based non-parametric Mann–Kendall correlation (Hipel and McLeod, 1994) using R library "Kendall" (McLeod, 2011). Letting $X_t = x_1, x_2, \ldots, x_n$; the library uses the following equations to calculate the Mann–Kendall test statistic (S) and Mann–Kendall correlation coefficient (τ);

Table 1 Descriptive statistics of investigated variables in each region of Turkish seas; LS1: the eastern Levantine Sea, LS2: the western Levantine Sea, AS1: the northern Aegean Sea, AS2: the southern Aegean Sea, MS1: the western Marmara Sea, MS2: the eastern Marmara Sea, BS1: the western Black Sea, BS2: the eastern Black Sea; sd: standard deviation.

	LS1	LS2	AS1	AS2	MS1	MS2	BS1	BS2
Chlorophyll concentration (mg m^{-3})								
Max	0.32	0.23	0.92	0.22	6.53	7.01	1.88	1.52
Min	0.07	0.04	0.07	0.04	0.42	0.42	0.18	0.23
Mean	0.16	0.09	0.25	0.10	1.62	1.93	0.62	0.51
sd	0.05	0.04	0.14	0.04	1.13	1.10	0.28	0.20
Colored dissolved organic matter absorption coefficient (m^{-1})								
Max	0.04	0.03	0.08	0.03	0.45	0.36	0.16	0.12
Min	0.01	0.01	0.02	0.01	0.06	0.08	0.04	0.04
Mean	0.02	0.02	0.04	0.02	0.14	0.16	0.08	0.08
sd	0.01	0.01	0.01	0.01	0.06	0.06	0.02	0.02
Particulate backscattering coefficient (m^{-1})								
Max	0.0059	0.0037	0.0053	0.0022	0.0439	0.0488	0.0249	0.0323
Min	0.0013	0.0008	0.0011	0.0008	0.0010	0.0014	0.0020	0.0023
Mean	0.0027	0.0016	0.0020	0.0013	0.0056	0.0071	0.0056	0.0058
sd	0.0009	0.0005	0.0007	0.0002	0.0062	0.0062	0.0031	0.0034

$$S = \sum_{k=1}^{n-1} \sum_{j=k+1}^{n} sgn(x_j - x_k),$$

$$sgn(x) = \begin{cases} +1, & x > 0 \\ 0, & x = 0 \\ -1, & x < 0 \end{cases},$$

$$\tau = \frac{S}{\binom{n}{2}}.$$

The intercept and slope of trend lines were estimated by using Theil-Sen's regression method, which models the variation of medians along a time gradient (Sen, 1968). To compare the slopes of trend lines among regions, 95% confidence intervals were calculated. For these calculations we used R library "zyp" (Bronaugh and Werner, 2013). The library uses the following equation to calculate Theil-Sen's slope (b_{sen});

$$d_k = \frac{x_j - x_i}{j - i},$$

$$b_{sen} = \text{median}(d_k),$$

where $i < j < n$ and, j and i are indices of the de-seasonalized time series, X_t.

In general terms, the inter-annual changes of ecological properties are non-linear and the trend curves reveal shifts between the stable states (Oguz and Gilbert, 2007). To detect these change-points in non-linear trends, we used Pettitt's single point change detection test (Pettitt, 1979) with R library "trend" (Pohlert, 2016; R Core Team, 2016). This function transforms the original time series to ranks (r) and uses the following equations to calculate change-point (U):

$$U_k = \sum_{i=1}^{k} r_i - (n+1); \quad k = 1, 2, \ldots, n,$$

$$\hat{U}_k = \max|U_k|.$$

Pearson product moment correlations were also calculated between the de-seasonalized time-series (Zuur et al., 2007) of all parameters within each sub-region. For this purpose, we used the cross correlation function in R (R Core Team, 2016).

5. Results

5.1. Descriptives of the variables

The mean CHL were between 0.09 mg m^{-3} (the western Levantine Sea (LS2)) and 1.93 mg m^{-3} (the eastern Marmara Sea (MS2)). The highest maximum was 7.01 mg m^{-3} in MS2, and the lowest minimum was 0.04 mg m^{-3} in LS2 and the southern Aegean Sea (AS2) (Table 1). The seasonality of CHL varied between regions. The summer months were generally identified as having the lowest CHL values for all regions, whilst the highest concentrations were seen in winter and spring.

The mean absorption values of CDOM ranged between 0.02 m^{-1} (LS1, LS2 and AS2) and 0.16 m^{-1} (MS2). The western Marmara Sea (MS1) had the highest maximum value with 0.45 m^{-1}, with the lowest minimum value being 0.01 m^{-1} in LS1, LS2, AS1 and AS2 (Table 1). Seasonal changes generally followed a unimodal pattern, whereby the minimum values were apparent in summer and the maximum values were recorded during the seasons of winter and spring.

Seasonal patterns of BBP varied among regions. Mean values dispersed from 0.0013 m^{-1} in AS2 to 0.0071 m^{-1} in MS2. The highest annual maximum belonged to MS2 (0.0488 m^{-1}), while the lowest annual minimum was 0.0008 m^{-1}in LS2 and AS2 (Table 1).

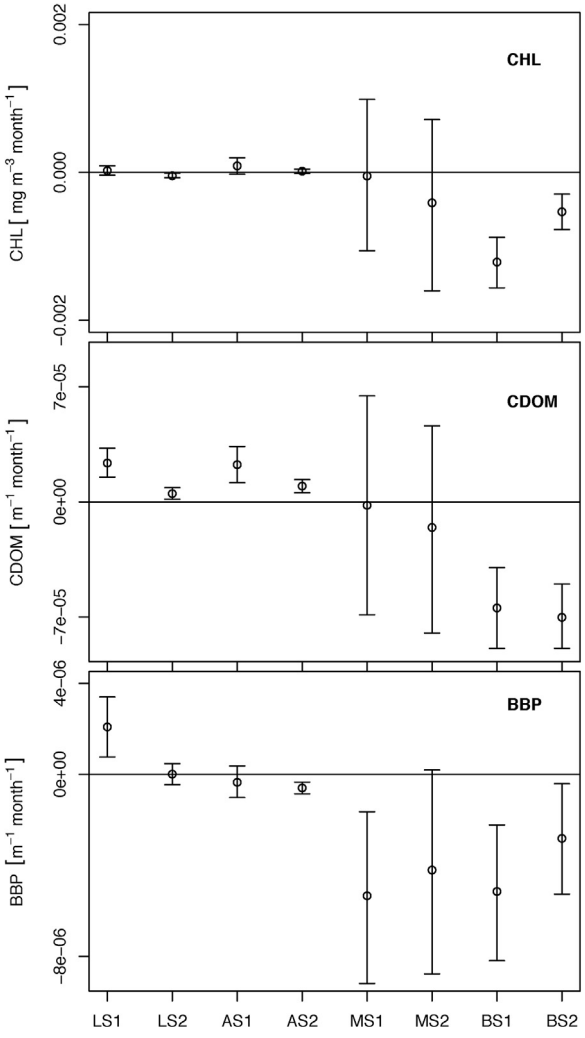

Figure 2 Slope of Theil-Sen regression of time series data (vertical bars indicate 95% confidence intervals). CHL: chlorophyll-*a* concentration, CDOM: colored dissolved organic matter absorption coefficient, BBP: particulate backscattering coefficient.

Table 2 Trends of physical and bio-optical conditions across Turkish Seas. (τ: Mann Kendal Thau, a: intercept, b_{sen}: slope of Theil-Sen's regression, CI: confidence intervals of slope, U: change points derived from Pettitt's test; LS1: the eastern Levantine Sea, LS2: the western Levantine Sea, AS1: the northern Aegean Sea, AS2: the southern Aegean Sea, MS1: the western Marmara Sea, MS2: the eastern Marmara Sea, BS1: the western Black Sea, BS2: the eastern Black Sea).

	LS1	LS2	AS1	AS2	MS1	MS2	BS1	BS2
Chlorophyll concentration								
τ	0.04^{ns}	-0.11^{*}	0.07^{ns}	0.06^{ns}	0.01^{ns}	-0.03^{ns}	-0.29^{***}	-0.19^{***}
a	0.1543	0.0964	0.2292	0.0953	1.5391	1.8937	0.7313	0.5414
b_{sen}	0.00003	−0.00004	0.00009	0.00002	−0.00005	−0.00041	−0.00121	−0.00053
±%95 CI	0.00006	0.00003	0.00011	0.00003	0.00102	0.00116	0.00034	0.00024
U	10/2001	10/2007	9/1999	7/2014	11/2009	6/2006	12/2002	6/2003
Colored dissolved organic matter absorption coefficient								
τ	0.22^{***}	0.12^{**}	0.17^{***}	0.19^{***}	0.00^{ns}	-0.02^{ns}	-0.23^{***}	-0.29^{***}
a	0.0213	0.0161	0.0348	0.0175	0.1318	0.1569	0.0874	0.0852
b_{sen}	0.00002	0.00001	0.00002	0.00001	0.000002	−0.00002	−0.00006	−0.00007
±%95 CI	0.000009	0.000004	0.000011	0.000004	0.000067	0.000063	0.000025	0.000020
U	9/2002	11/2002	2/2003	4/2003	1/2003	8/2014	10/2002	1/2003
Particulate backscattering coefficient								
τ	0.14^{**}	0.00^{ns}	-0.04^{ns}	-0.20^{***}	-0.12^{**}	-0.08^{ns}	-0.15^{***}	-0.10^{*}
a	0.0024	0.0016	0.0020	0.0013	0.0058	0.0070	0.0059	0.0061
b_{sen}	2.1×10^{-6}	1.6×10^{-8}	-3.4×10^{-7}	-5.9×10^{-7}	-5.3×10^{-6}	-4.2×10^{-6}	-5.1×10^{-6}	-2.8×10^{-6}
±%95 CI	1.3×10^{-6}	4.6×10^{-7}	7.0×10^{-7}	2.6×10^{-7}	3.8×10^{-6}	4.5×10^{-6}	3.0×10^{-6}	2.4×10^{-6}
U	6/2002	3/2013	9/2002	1/2008	2/2011	12/2010	2/2003	12/2008

ns: non-significant.
* Significant at 0.05.
** Significant at 0.01.
*** Significant at 0.001.

5.2. Analyses

The trend of CHL was not significant in the LS1, the Aegean Sea or the Marmara Sea, and a slightly decreasing trend was detected in LS2 (Fig. 2). Based on the Pettitt's test, in 2007 the CHL trend in LS2 turned downward. However, there were highly significant and decreasing trends in both the western Black Sea (BS1) and the eastern Black Sea (BS2). The change-points of non-linear trends for the BS1 and BS2 were detected in 2002 and 2003, respectively (Table 2; Fig. 3).

The trends of CDOM were found to be significant in all regions, with the only exception being the Marmara Sea. Generally increasing trends were found in the Levantine Sea and the Aegean Sea. Among these regions, the slopes of LS2 and AS2 were significantly lower than that of the other two regions ($p < 0.05$) (Fig. 2). The Pettitt's test also revealed that for both regions of the Levantine Sea the change point of non-linear trends occurred in 2002, and then in 2003 for both regions of the Aegean Sea. Contrary to the Levantine Sea and the Aegean Sea, CDOM revealed decreasing trends in both regions of the Black Sea, although the slopes were not significantly different to each other. The change-point in the non-linear trend was consistent with the other seas; 2002 for BS1 and then 2003 for BS2 (Table 2; Fig. 4).

The only significant positive trend in BBP was detected in LS1 (Fig. 2). The change point for the non-linear trend was in June 2002. The trends were not found to be significant in the regions of LS2 and AS1, nor were they found to be significant in MS2. In the AS2, MS1 and both regions of the Black Sea, the BBP revealed significantly decreasing trends. The non-linear trend curves showed fluctuating patterns around the linear trend lines, thus Pettitt's method did not detect meaningful change-points in these regions (Table 2; Fig. 5).

However, there were some strong positive correlations between the trends of CHL and BBP values within the regions of study. The strength of correlation was found to be highest in the Levantine Sea (0.65, 0.66 respectively for LS1 and LS2; $p < 0.01$), yet decreasing in both the Aegean Sea (0.65, 0.41 respectively for AS1 and AS1, $p < 0.01$) and the Marmara Sea (0.23, 0.28 respectively for MS1 and MS2, $p < 0.01$), lowest in BS1 (0.11, $p < 0.05$) and was determined as not being significant in BS2 (Table 3).

The trends from CHL and CDOM measurements were significantly correlated within the study domain. The correlations were relatively lower in the Levantine Sea (0.47, 0.28 respectively for LS1 and LS2; $p < 0.01$) and AS2 (0.10; $p < 0.05$) and higher in AS1 (0.67; $p < 0.01$), the Marmara Sea (0.62, 0.58 respectively for M1 and M2; $p < 0.01$) and the Black Sea (0.69, 0.50 respectively for BS1 and BS2; $p < 0.01$) (Table 3).

High positive correlations were observed between the trends of CDOM and BBP in LS1 (0.72; $p < 0.01$), L2 (0.55; $p < 0.01$) and AS1 (0.64; $p < 0.01$). However, the correlation values were found to be lower in the Marmara Sea (0.38, 0.35 respectively for MS1 and MS2; $p < 0.01$) and the western Black Sea (0.21; $p < 0.01$) (Table 3).

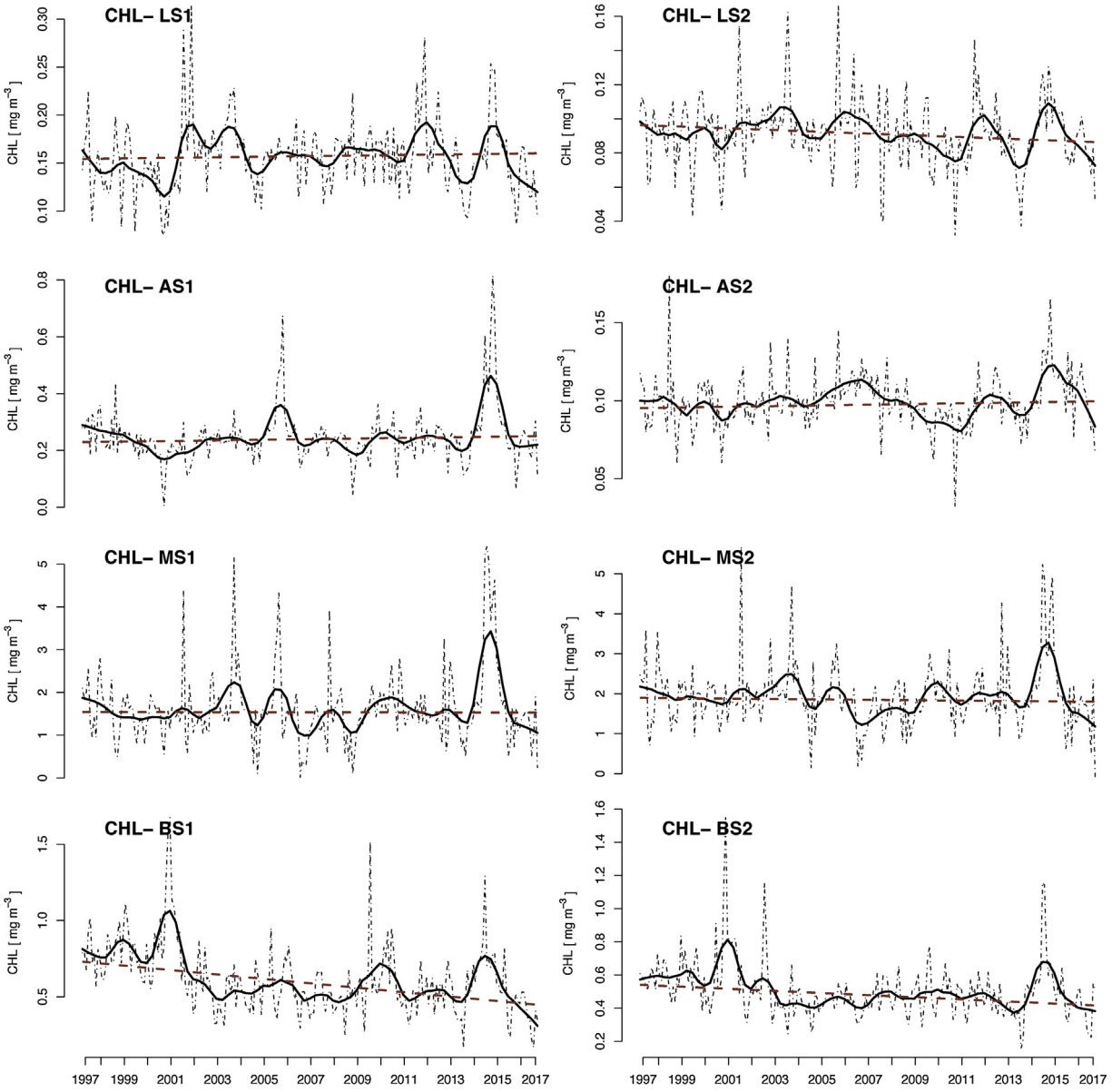

Figure 3 Deseasonalized time series (dash-dot line), non-linear (straight line) and linear (dashed line) trends of chlorophyll in Seas of Turkey (LS1: the eastern Levantine Sea, LS2: the western Levantine Sea, AS1: the northern Aegean Sea, AS2: the southern Aegean Sea, MS1: the western Marmara Sea, MS2: the eastern Marmara Sea, BS1: the western Black Sea, BS2: the eastern Black Sea, CHL: chlorophyll-*a* concentration, CDOM: colored dissolved organic matter absorption coefficient, BBP: particulate backscattering coefficient).

6. Discussion

The phytoplankton community and CHL revealed regime shifts in the Black Sea during the study period (Mikaelyan et al., 2013; Oguz and Gilbert, 2007). From the mid 1970s, the pre-eutrophication regime gradually altered due to the increment of anthropogenic nutrient inputs. The eutrophic phase remained present until the beginning of the 1990s with the contribution of intensified vertical mixings due to the cold SST regime. The Black Sea ecosystem was introduced to the post eutrophication phase after the mid 1990s, and the food web structure was then reorganized after this period. From this point, the phytoplankton biomass turned toward a decreasing trend as a result of several factors, such as diminishing anthropogenic nutrient inputs and the decreasing effect of winter mixing due to increasing SST and changes in the food-web structure (Oguz and Gilbert, 2007). According to our analyses, this decreasing pattern in CHL remained consistent in both parts of the Black Sea during the post-eutrophication phase between the period of 1997 and 2017. Along with other factors, CHL can also be influenced by changes in the phytoplankton community structure (see

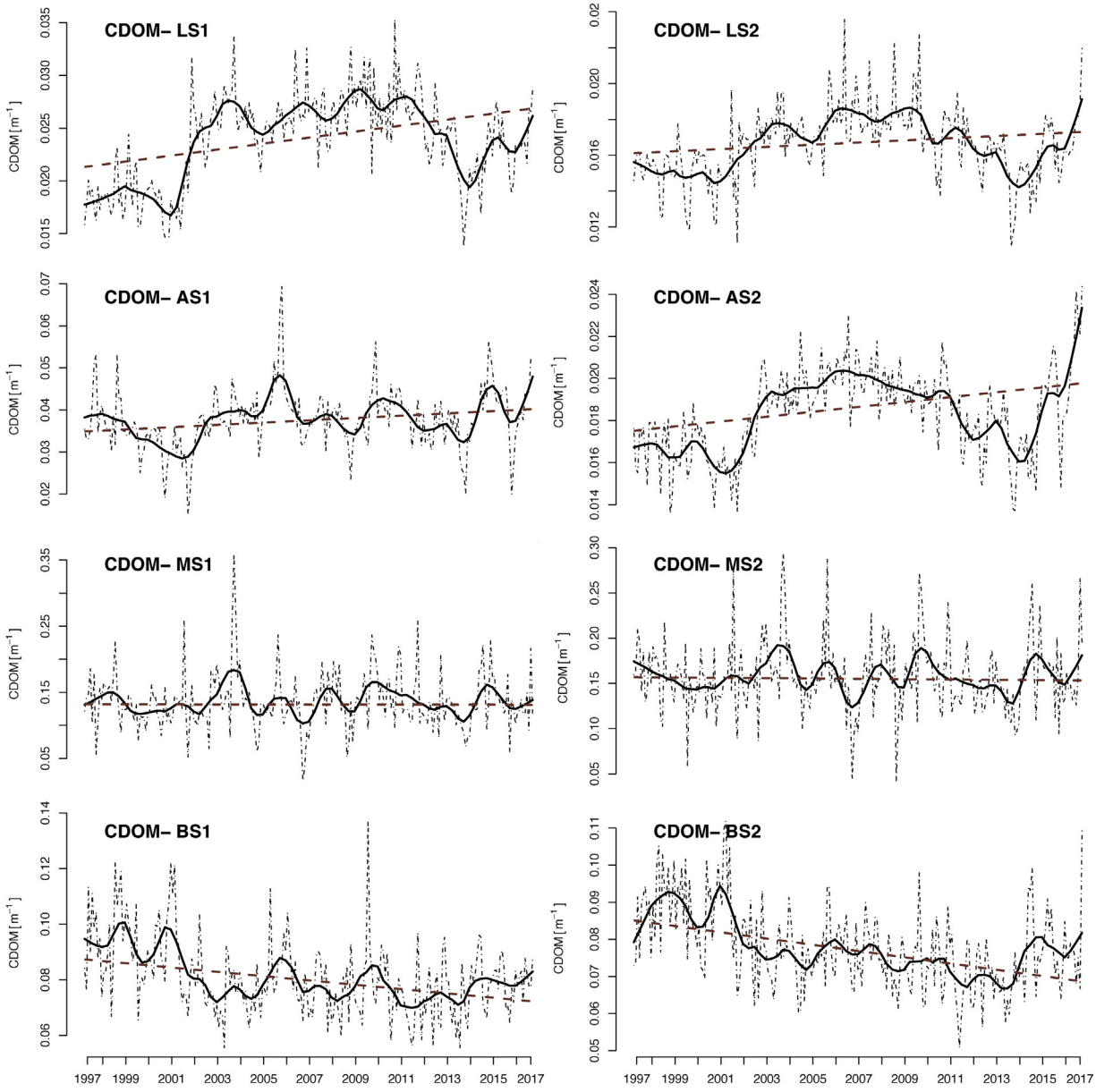

Figure 4 Deseasonalized time series (dash-dot line), non-linear (straight line) and linear (dashed line) trends of CDOM in Seas of Turkey (LS1: the eastern Levantine Sea, LS2: the western Levantine Sea, AS1: the northern Aegean Sea, AS2: the southern Aegean Sea, MS1: the western Marmara Sea, MS2: the eastern Marmara Sea, BS1: the western Black Sea, BS2: the eastern Black Sea, CHL: chlorophyll-*a* concentration, CDOM: colored dissolved organic matter absorption coefficient, BBP: particulate backscattering coefficient).

Orek (2007) for the northeastern Mediterranean), which is a well-documented phenomenon for the Black Sea during the last several decades (Kideys, 1994; Mikaelyan, 1997; Mikaelyan et al., 2013).

Previous studies into CHL throughout the Mediterranean Sea revealed mostly weak and insignificant trends and with the exclusion of some coastal areas the south-western Black Sea showed mostly negative trends (Coppini et al., 2013; Colella et al., 2016). Parallel to previous studies, this study only detected significantly decreasing trends in the Black Sea, with some weak and insignificant fluctuations in other regions (Fig. 3).

The slope of CDOM trends was identified as varying across the different seas of Turkey. These variations may be due to the different compositions of dissolved matter present in the seas as a result of impacts to either terrestrial inputs (Cauwet et al., 2002; Margolin, 2017) or local community differences (Orek, 2007) (Table 2). For example, the CDOM trend was found to be significant in the Black Sea, whereas no significant trend was evident in the Marmara Sea, despite the surface waters originating from the Black Sea (Beşiktepe et al., 1994). This difference may be due to the influences of different terrestrial inputs into the Marmara Sea. Factors such as the chemical structure (humic and fulvic acid ratio) of CDOM together with photo-oxidation properties and salinity levels, may reveal the reason for changes to CDOM in the surface water.

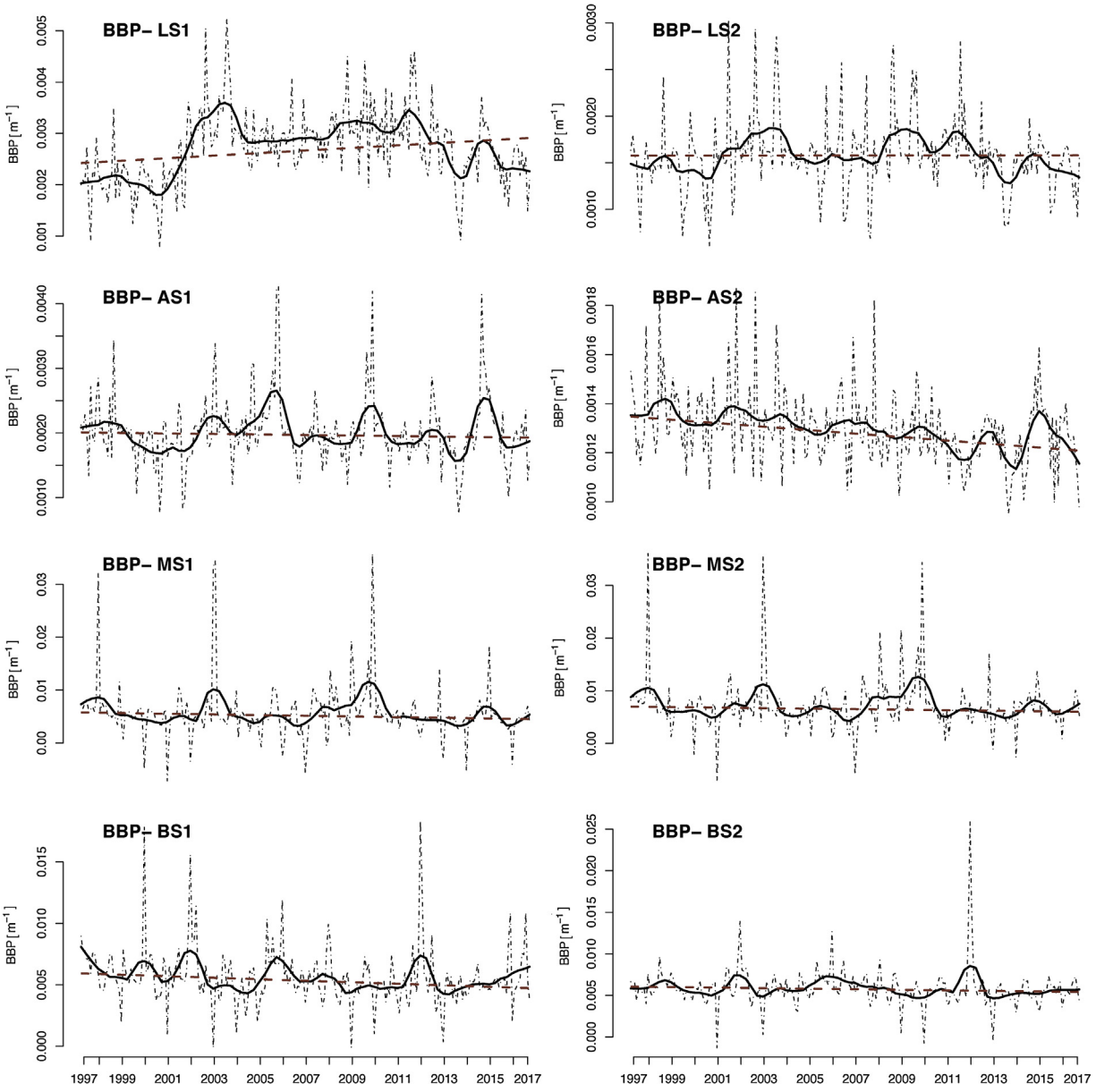

Figure 5 Deseasonalized time series (dash-dot line), non-linear (straight line) and linear (dashed line) trends of BBP in Seas of Turkey (LS1: the eastern Levantine Sea, LS2: the western Levantine Sea, AS1: the northern Aegean Sea, AS2: the southern Aegean Sea, MS1: the western Marmara Sea, MS2: the eastern Marmara Sea, BS1: the western Black Sea, BS2: the eastern Black Sea, CHL: chlorophyll-*a* concentration, CDOM: colored dissolved organic matter absorption coefficient, BBP: particulate backscattering coefficient).

Table 3 Pearson product moment correlation between variables. (CHL: chlorophyll-*a* concentration, CDOM: colored dissolved organic matter absorption coefficient, BBP: particulate backscattering coefficient).

	LS1	LS2	AS1	AS2	MS1	MS2	BS1	BS2
CHL-BBP	0.65**	0.66**	0.65**	0.41**	0.23**	0.28**	0.11*	−0.07
CHL-CDOM	0.47**	0.28**	0.67**	0.10*	0.62**	0.58**	0.69**	0.50**
BBP-CDOM	0.72**	0.55**	0.64**	0.06	0.38**	0.35**	0.21**	0.02

* $p < 0.05$.
** $p < 0.01$; $n = 235$.

Overall, positive CDOM trends were apparent in the waters of both the Levantine and Aegean Seas. Although the increment was lower in the two adjacent regions, LS2 and AS2 in accordance with the results of cross-correlation analyses, the trend dynamics of CDOM did not correlate with CHL. the. The difference in the relationship between these two properties indicates the possible effect that bacterial production can have on the variables. Bacterial production constitutes an important role in the food-web (Siokou-Frangou et al., 2002) and its impact on the dynamics of CHL and CDOM is pointed out by Pitta (2016) in the southern Aegean Sea.

Pitta (2016) highlighted that a lack of correlation between CHL and CDOM is due to the intensity of bacterial production in the summer season being simultaneous to a vertical water column movement in the same region (e.g. Rhodes Gyre).

BBP is calculated by the integration of angular function in the backward direction, thus it is mostly used as an indicator of particle concentration and composition evident in the seawater. Previous studies have discussed the relationship between BBP and different types of particles (Loisel et al., 2001; Stramski et al., 2008) or turbidity (Jafar-Sidik et al., 2017). In this study concept, the trends of BBP did not show any distinctive regional patterns between the seas. LS1 was the region which showed a significantly positive trend, and this region is known to have intensive river inputs (Tuğrul et al., 2016). Changes to the particle load or inflow (Akyurek, 2003) into these rivers from terrestrial sources that contain high humic acids, may be the reason for the increasing trend detected in this study. The Black Sea regions and MS1 both had a significantly negative BBP trend. This negative trend might have been caused by the decreasing terrestrial inputs from rivers, driven by the decreasing trends of precipitation in the region, as stated by Ceribasi and Dogan (2015). Another possible explanation for this trend could be due to changes in the phytoplankton community (Kideys, 1994; Mikaelyan et al., 2013). The relationship between the trends of BBP and CHL are not significant in the Black Sea, and our study also showed a weak correlation in the Marmara Sea. Further biogeochemical, bio-optical and taxonomic investigations will, therefore, be required to fully understand the drivers that determine particle concentration and composition in the regions. Nonetheless, it can be stated that CHL is clearly the main driver in determining the trends of BBP in the Aegean Sea and the Levantine Seas of Turkey.

Our results show that whilst the Black Sea and the Marmara Sea revealed similar patterns, the trends of the Aegean and Levantine Seas were also found to be similar. These spatial differences should, therefore, be further considered and investigated in accordance with the usage of all remotely sensed bio-optical variables involved in monitoring the implications of the seas around Turkey.

7. Conclusion

A descriptive and multi-decadal trend analysis indicated that two main clusters occurred in the seas of Turkey, with regards to bio-optical properties: one cluster being the Black Sea and the Marmara Sea, and the second cluster being the Aegean Sea and the Levantine Sea. The Black Sea and the Marmara Sea both showed different characteristics to the other seas studied, with either higher concentrations of CHL, CDOM or BBP.

This is a descriptive study, aimed at defining recent linear and non-linear inter-annual patterns in bio-optical variables. This study also took an interest in the descriptive features of these variables throughout the different regions of the seas around Turkey. These empirical considerations cannot detect the underlying reasons alone, and should instead be used to develop hypotheses (Daskalov, 1999). Although the results of this study have provided some insight into the dynamical changes found in marine ecosystems, it is not possible to fully comprehend the ecological status of a system unless complementary datasets are utilized. Changes in environmental conditions are usually rather complex and should be investigated with further ecosystem-based approaches (Oguz and Gilbert, 2007). In addition to the purpose and requirement of monitoring, multiyear analyses on datasets that are available for extended time periods provide the baseline required in order to develop key hypotheses for the further understanding of ecosystem dynamics. As pointed out by Zielinski et al. (2009), key aims held by marine scientists include the monitoring and investigation of variables, thus increasing our understanding of all important processes taking place in the oceans. The expansion of spatio-temporal scales of observation, possible through improved satellite technologies, has made possible to proceed toward and reach this aim. However, this technology is limited to surface area observation only, and observations required for calibration or validation purposes.

Acknowledgement

We would like to thank Ayla Yildirim for English proofreading.

References

Agirbas, E., Koca, L., Aytan, U., 2017. Spatio-temporal pattern of phytoplankton and pigment composition in surface waters of south-eastern Black Sea. Oceanologia 59 (3), 283–299, http://dx.doi.org/10.1016/j.oceano.2017.03.004.

Akpinar, A., Yilmaz, E., Fach, B.A., Salihoğlu, B., 2016. Physical oceanography of the Eastern Mediterranean Sea. In: Turan, C., Salihoğlu, B., Özgür Özbek, E., Öztürk, B. (Eds.), The Turkish Part of the Mediterranean Sea; Marine Biodiversity, Fisheries, Conservation and Governance. Turkish Marine Research Foundation (TUDAV), Turkish Marine Foundation, İstanbul, 1–14.

Akyurek, M., 2003. Türkiye yıllık ortalama akımlarının trend analizi. Istanbul Technical University, Istanbul, 105 pp.

Berner, K.A.B., Berner, R.A.C., 2012. Global Environment: Water, Air, and Geochemical Cycles, 2nd ed. Princeton Univ. Press, 444 pp.

Beşiktepe, Ş.T., Sur, H.İ., Özsoy, E., Latif, M.A., Oğuz, T., Ünlüata, Ü., 1994. The circulation and hydrography of the Marmara Sea. Prog. Oceanogr. 34 (4), 285–334, http://dx.doi.org/10.1016/0079-6611(94)90018-3.

Bronaugh, D., Werner, A., 2013. zyp: Zhang + Yue-Pilon trends package.

Burenkov, V.I., Kopelevich, O.V., Sheberstov, S.V., Ershova, S.V., Evdoshenko, M.A., 1999. Bio-optical characteristics of the Aegean Sea retrieved from satellite ocean color data. In: The Eastern Mediterranean as a Laboratory Basin for the Assessment of Contrasting Ecosystems. Springer, Netherlands, Dordrecht, 313–326, http://dx.doi.org/10.1007/978-94-011-4796-5_21.

Cauwet, G., Déliat, G., Krastev, A., Shtereva, G., Becquevort, S., Lancelot, C., Momzikoff, A., Saliot, A., Cociasu, A., Popa, L., 2002. Seasonal DOC accumulation in the Black Sea: a regional explanation for a general mechanism. Mar. Chem. 79 (3–4), 193–205, http://dx.doi.org/10.1016/S0304-4203(02)00064-6.

Ceribasi, G., Dogan, E., 2015. Trend analizi yöntemi kullanılarak batı ve doğu Karadeniz ile Sakarya havzası akım miktarlarının değerlendirilmesi. SDU Int. J. Technol. Sci. 7 (2), 1–12.

Chami, M., Shybanov, E.B., Churilova, T.Y., Khomenko, G.A., Lee, M. E.-G., Martynov, O.V., Berseneva, G.A., Korotaev, G.K., 2005. Optical properties of the particles in the Crimea coastal waters (Black Sea). J. Geophys. Res. 110, C11020, http://dx.doi.org/10.1029/2005JC003008.

Cleveland, R.B., Cleveland, W.S., McRae, J.E., Terpenning, I., 1990. STL: a seasonal-trend decomposition procedure based on loess. J. Off. Stat. 6 (1), 3–73.

Coble, P.G., Del Castillo, C.E., Avril, B., 1998. Distribution and optical properties of CDOM in the Arabian Sea during the 1995 SW monsoon. Deep Res. Pt. II 45, 2195–2223, http://dx.doi.org/10.1016/S0967-0645(98)00068-X.

Colella, S., Falcini, F., Rinaldi, E., Sammartino, M., Santoleri, R., 2016. Mediterranean ocean colour chlorophyll trends. PLOS ONE 11 (6), e0155756, http://dx.doi.org/10.1371/journal.pone.0155756.

Coppini, G., Lyubarstev, V., Pinardi, N., Colella, S., Santoleri, R., Christiansen, T., 2013. The use of ocean-colour data to estimate Chl-*a* trends in European seas. Int. J. Geosci. 4 (6), 927–949, http://dx.doi.org/10.4236/ijg.2013.46087.

Daskalov, G., 1999. Relating fish recruitment to stock biomass and physical environment in the Black Sea using generalized additive models. Fish. Res. 41 (1), 1–23, http://dx.doi.org/10.1016/S0165-7836(99)00006-5.

Ehrmann, W., Schmiedl, G., Hamann, Y., Kuhnt, T., 2007. Distribution of clay minerals in surface sediments of the Aegean Sea: a compilation. Int. J. Earth Sci. 96 (4), 769–780, http://dx.doi.org/10.1007/s00531-006-0119-1.

El Hourany, R., Fadel, A., Gemayel, E., Abboud-Abi Saab, M., Faour, G., 2017. Spatio-temporal variability of the phytoplankton biomass in the Levantine basin between 2002 and 2015 using MODIS products. Oceanologia 59 (2), 153–165, http://dx.doi.org/10.1016/j.oceano.2016.12.002.

Eronat, C., Sayin, E., 2014. Temporal evolution of the water characteristics in the bays along the eastern coast of the Aegean Sea: Saros, İzmir, and Gökova bays. Turk. J. Earth Sci. 23, 53–66, http://dx.doi.org/10.3906/yer-1307-4.

Garaba, S., Voß, D., Zielinski, O., 2014. Physical, bio-optical state and correlations in North–Western European shelf seas. Remote Sens. 6 (6), 5042–5066, http://dx.doi.org/10.3390/rs6065042.

Gregg, W.W., Rousseaux, C.S., 2014. Decadal trends in global pelagic ocean chlorophyll: a new assessment integrating multiple satellites, in situ data, and models. J. Geophys. Res. Ocean. 119 (9), 5921–5933, http://dx.doi.org/10.1002/2014JC010158.

Gucu, A.C., Inanmaz, Ö.E., Ok, M., Sakinan, S., 2016. Recent changes in the spawning grounds of Black Sea anchovy, *Engraulis encrasicolus*. Fish. Oceanogr. 25 (1), 67–84, http://dx.doi.org/10.1111/fog.12135.

Hedges, J.I., 1992. Global biogeochemical cycles: progress and problems. Mar. Chem. 39 (1–3), 67–93, http://dx.doi.org/10.1016/0304-4203(92)90096-S.

Hipel, K.W., McLeod, A.I., 1994. Time Series Modelling of Water Resources and Environmental Systems. Elsevier, Amsterdam, 1013 pp.

Ignatiades, L., 1998. The productive and optical status of the oligotrophic waters of the Southern Aegean Sea (Cretan Sea), Eastern Mediterranean. J. Plankton Res. 20 (5), 985–995, http://dx.doi.org/10.1093/plankt/20.5.985.

Ignatiades, L., Psarra, S., Zervakis, V., Pagou, K., Souvermezoglou, E., Assimakopoulou, G., Gotsis-Skretas, O., 2002. Phytoplankton size-based dynamics in the Aegean Sea (Eastern Mediterranean). J. Mar. Syst. 36 (1–2), 11–28, http://dx.doi.org/10.1016/S0924-7963(02)00132-X.

Jafar-Sidik, M., Gohin, F., Bowers, D., Howarth, J., Hull, T., 2017. The relationship between Suspended Particulate Matter and Turbidity at a mooring station in a coastal environment: consequences for satellite-derived products. Oceanologia 59 (3), 365–378, http://dx.doi.org/10.1016/j.oceano.2017.04.003.

Karageorgis, A.P., Gardner, W.D., Mikkelsen, O.A., Georgopoulos, D., Ogston, A.S., Assimakopoulou, G., Krasakopoulou, E., Oaie, G., Secrieru, D., Kanellopoulos, T.D., Pagou, K., Anagnostou, C., Papathanassiou, E., 2014. Particle sources over the Danube River delta, Black Sea based on distribution, composition and size using optics, imaging and bulk analyses. J. Mar. Syst. 131, 74–90, http://dx.doi.org/10.1016/j.jmarsys.2013.11.013.

Kasprzak, P., Padisák, J., Koschel, R., Krienitz, L., Gervais, F., 2008. Chlorophyll *a* concentration across a trophic gradient of lakes: an estimator of phytoplankton biomass? Limnol. — Ecol. Manag. Inl. Waters 38 (3–4), 327–338, http://dx.doi.org/10.1016/j.limno.2008.07.002.

Kideys, A.E., 1994. Recent dramatic changes in the Black Sea ecosystem: the reason for the sharp decline in Turkish anchovy fisheries. J. Mar. Syst. 5 (2), 171–181, http://dx.doi.org/10.1016/0924-7963(94)90030-2.

Loisel, H., Bosc, E., Stramski, D., Oubelkheir, K., Deschamps, P.-Y., 2001. Seasonal variability of the backscattering coefficient in the Mediterranean Sea based on satellite SeaWiFS imagery. Geophys. Res. Lett. 28 (22), 4203–4206, http://dx.doi.org/10.1029/2001GL013863.

Margolin, A.R., 2017. Environmental Impacts on Carbon Biogeochemistry in Marginal Seas. Unive. Miami, Miami, 137 pp.

Maritorena, S., Siegel, D.A., 2005. Consistent merging of satellite ocean color data sets using a bio-optical model. Remote Sens. Environ. 94 (4), 429–440, http://dx.doi.org/10.1016/j.rse.2004.08.014.

McLeod, A.I., 2011. Kendall: Kendall Rank Correlation and Mann-Kendall Trend Test.

Mikaelyan, A.S., 1997. Long-term variability of phytoplankton communities in open black sea in relation to environmental changes. In: Sensitivity to Change: Black Sea, Baltic Sea and North Sea. Springer Netherlands, Dordrecht, 105–116, http://dx.doi.org/10.1007/978-94-011-5758-2_9.

Mikaelyan, A.S., Zatsepin, A.G., Chasovnikov, V.K., 2013. Long-term changes in nutrient supply of phytoplankton growth in the Black Sea. J. Mar. Syst. 117–118, 53–64, http://dx.doi.org/10.1016/j.jmarsys.2013.02.012.

Nittis, K., Perivoliotis, L., 2002. Circulation and hydrological characteristics of the North Aegean Sea: a contribution from real-time buoy measurements. Mediterr. Mar. Sci. 3 (1), 21, http://dx.doi.org/10.12681/mms.255.

O'Reilly, J.E., Maritorena, S., Mitchell, B.G., Siegel, D.A., Carder, K.L., Garver, S.A., Kahru, M., McClain, C., 1998. Ocean color chlorophyll *a* algorithms for SeaWiFS. J. Geophys. Res. Ocean. 103 (C11), 24937–24953, http://dx.doi.org/10.1029/98JC02160.

Oguz, T., Gilbert, D., 2007. Abrupt transitions of the top-down controlled Black Sea pelagic ecosystem during 1960–2000: evidence for regime-shifts under strong fishery exploitation and nutrient enrichment modulated by climate-induced variations. Deep Res. Pt. I Oceanogr. Res. Pap. 54 (2), 220–242, http://dx.doi.org/10.1016/j.dsr.2006.09.010.

Oguz, T., Salihoglu, B., Moncheva, S., Abaza, V., 2012. Regional peculiarities of community-wide trophic cascades in strongly degraded Black Sea food web. J. Plankton Res. 34 (4), 338–343, http://dx.doi.org/10.1093/plankt/fbs002.

Oguz, T., Tugrul, S., Kideys, A., Ediger, V., Kubilay, N., 2004. Physical and biogeochemical characteristics of the Black Sea. In: Robinson, A.R., Brink, H.K. (Eds.), The Sea. Harvard Univ. Press, 1331–1369.

Örek, H., 2007. Bio-optical Characteristics of Turkish Seas. Middle East Tech. Univ., Ankara, 160 pp.

Özsoy, E., Hecht, A., Ünlüata, Ü., Brenner, S., Sur, H.I., Bishop, J., Latif, M.A., Rozentraub, Z., Oğuz, T., 1993. A synthesis of the Levantine Basin circulation and hydrography, 1985—1990. Deep Res. Pt. II 40 (6), 1075—1119, http://dx.doi.org/10.1016/0967-0645(93)90063-S.

Pettitt, A.N., 1979. A non-parametric approach to the change-point problem. Appl. Stat. 28, 126—135.

Pitta, E., 2016. Properties and Dynamics of Chromophoric Dissolved Organic Matter (CDOM) in Eastern Mediterranean Waters. National and Kapodistrian Univ. Athens, Athens, 175 pp.

Pohlert, T., 2016. Package 'Trend': Non-Parametric Trend Tests and Change-Point Detection. R Packag. 26., http://dx.doi.org/10.13140/RG.2.1.2633.4243.

Polat, C.S., Tugrul, S., 1995. Nutrient and organic carbon exchanges between the Black and Marmara Seas through the Bosphorus Strait. Cont. Shelf Res. 15 (9), 1115—1132, http://dx.doi.org/10.1016/0278-4343(94)00064-T.

Puddu, A., Zoppini, A., Pettine, M., 2000. Dissolved organic matter and microbial food web interactions in the marine environment: the case of the Adriatic Sea. Int. J. Environ. Pollut. 13 (1—6), 473—494, http://dx.doi.org/10.1504/IJEP.2000.002331.

Reynolds, R.A., Stramski, D., Neukermans, G., 2016. Optical backscattering by particles in Arctic seawater and relationships to particle mass concentration, size distribution, and bulk composition. Limnol. Oceanogr. 61 (5), 1869—1890, http://dx.doi.org/10.1002/lno.10341.

Roether, W., Manca, B.B., Klein, B., Bregant, D., Georgopoulos, D., Beitzel, V., Kovacevic, V., Luchetta, A., 1996. Recent changes in eastern Mediterranean deep waters. Science 271 (5247), 333—335, http://dx.doi.org/10.1126/science.271.5247.333.

R Core Team, 2016. R: A Language and Environment for Statistical Computing. R Foundation for Statistical Computing, Vienna, Austria Available from: http://www.R-project.org/ (accessed 15.11.16).

Sancak, S., Besiktepe, S.T., Yilmaz, A., Lee, M., Frouin, R., 2005. Evaluation of SeaWiFS chlorophyll-*a* in the Black and Mediterranean Seas. Int. J. Remote Sens. 26 (10), 2045—2060, http://dx.doi.org/10.1080/01431160512331337853.

Sayin, E., 2003. Physical features of the Izmir Bay. Cont. Shelf Res. 23 (10), 957—970, http://dx.doi.org/10.1016/S0278-4343(03)00083-9.

Sen, P.K., 1968. Estimates of the regression based on Kendall's Tau. J. Am. Stat. Assoc. 63, 1379—1389.

Siegel, D.A., Buesseler, K.O., Doney, S.C., Sailley, S.F., Behrenfeld, M.J., Boyd, P.W., 2014. Global assessment of ocean carbon export by combining satellite observations and food-web models. Global Biogeochem. Cy. 28, 181—196, http://dx.doi.org/10.1002/2013GB004743.

Siegel, D.A., Maritorena, S., Nelson, N.B., Behrenfeld, M.J., 2005. Independence and interdependencies among global ocean color properties: reassessing the bio-optical assumption. J. Geophys. Res. 110, C07011, http://dx.doi.org/10.1029/2004JC002527.

Siokou-Frangou, I., Bianchi, M., Christaki, U., Christou, E.D., Giannakourou, A., Gotsis, O., Ignatiades, L., Pagou, K., Pitta, P., Psarra, S., Souvermezoglou, E., Van Wambeke, F., Zervakis, V., 2002. Carbon flow in the planktonic food web along a gradient of oligotrophy in the Aegean Sea (Mediterranean Sea). J. Mar. Syst. 33—34, 335—353, http://dx.doi.org/10.1016/S0924-7963(02)00065-9.

Souvermezoglou, E., Karasakopoulou, E., Pavlidou, A., 2014. Temporal and spatial variability of nutrients and oxygen in the North Aegean Sea during the last thirty years. Mediterr. Mar. Sci. 15 (4), 18, http://dx.doi.org/10.12681/mms.1017.

Stedmon, C.A., Markager, S., 2001. The optics of chromophoric dissolved organic matter (CDOM) in the Greenland Sea: an algorithm for differentiation between marine and terrestrially derived organic matter. Limnol. Oceanogr. 46 (8), 2087—2093, http://dx.doi.org/10.4319/lo.2001.46.8.2087.

Stramski, D., Reynolds, R.A., Babin, M., Kaczmarek, S., Lewis, M.R., Röttgers, R., Sciandra, A., Stramska, M., Twardowski, M.S., Franz, B.A., Claustre, H., 2008. Relationships between the surface concentration of particulate organic carbon and optical properties in the eastern South Pacific and eastern Atlantic Oceans. Biogeosciences 5 (1), 171—201, http://dx.doi.org/10.5194/bg-5-171-2008.

Theocharis, A., Georgopoulos, D., Lascaratos, A., Nittis, K., 1993. Water masses and circulation in the central region of the Eastern Mediterranean: Eastern Ionian, South Aegean and Northwest Levantine, 1986—1987. Deep Sea Res. Pt. II Top. Stud. Oceanogr. 40 (6), 1121—1142, http://dx.doi.org/10.1016/0967-0645(93)90064-T.

Tuğrul, S., Yücel, N., Akçay, I., 2016. Chemical oceanography of North Eastern Mediterranean. In: Turan, C., Salihoğlu, B., Özgür Özbek, E., Öztürk, B. (Eds.), The Turkish Part of the Mediterranean Sea; Marine Biodiversity, Fisheries, Conservation and Governance. Mar. Res. Foundation, İstanbul, 15—29.

Tzortziou, M., Zeri, C., Dimitriou, E., Ding, Y., Jaffé, R., Anagnostou, E., Pitta, E., Mentzafou, A., 2015. Colored dissolved organic matter dynamics and anthropogenic influences in a major transboundary river and its coastal wetland. Limnol. Oceanogr. 60 (4), 1222—1240, http://dx.doi.org/10.1002/lno.10092.

Vervatis, V.D., Sofianos, S.S., Skliris, N., Somot, S., Lascaratos, A., Rixen, M., 2013. Mechanisms controlling the thermohaline circulation pattern variability in the Aegean-Levantine region. A hindcast simulation (1960—2000) with an eddy resolving model. Deep Res. Pt. I Oceanogr. Res. Pap. 74, 82—97, http://dx.doi.org/10.1016/j.dsr.2012.12.011.

Yalçın, B., Artüz, M.L., Pavlidou, A., Çubuk, S., Dassenakis, M., 2017. Nutrient dynamics and eutrophication in the Sea of Marmara: data from recent oceanographic research. Sci. Total Environ. 601—602, 405—424, http://dx.doi.org/10.1016/j.scitotenv.2017.05.179.

Zeri, C., Beşiktepe, Ş., Giannakourou, A., Krasakopoulou, E., Tzortziou, M., Tsoliakos, D., Pavlidou, A., Mousdis, G., Pitta, E., Scoullos, M., Papathanassiou, E., 2014. Chemical properties and fluorescence of DOM in relation to biodegradation in the interconnected Marmara-North Aegean Seas during August 2008. J. Mar. Syst. 135, 124—136, http://dx.doi.org/10.1016/j.jmarsys.2013.11.019.

Zielinski, O., Busch, J.A., Cembella, A.D., Daly, K.L., Engelbrektsson, J., Hannides, A.K., Schmidt, H., 2009. Detecting marine hazardous substances and organisms: sensors for pollutants, toxins, and pathogens. Ocean Sci. 5 (3), 329—349, http://dx.doi.org/10.5194/os-5-329-2009.

Zuur, A.F., Ieno, E.N., Smith, G.M., 2007. Analysing Ecological Data, Statistics for Biology and Health. Springer New York, p. 672, http://dx.doi.org/10.1007/978-0-387-45972-1.

Oceanologia (2018) 60, 500—512

Available online at www.sciencedirect.com

ScienceDirect

journal homepage: www.journals.elsevier.com/oceanologia/

ORIGINAL RESEARCH ARTICLE

Some characteristic wave energy dissipation patterns along the Polish coast

Grzegorz Różyński *, **Piotr Szmytkiewicz**

Institute of Hydro-Engineering, Polish Academy of Sciences, Gdańsk, Poland

Received 25 October 2017; accepted 10 April 2018
Available online 25 April 2018

KEYWORDS
Coastal morphology;
Wave energy dissipation;
Equilibrium profiles;
Data-driven modelling;
Signal processing

Summary The paper analyses cross-shore bathymetric profiles between Władysławowo (km 125 of the national coastal chainage) and Lake Sarbsko (km 174) commissioned in 2005 and 2011 by coastal authorities for monitoring purposes. The profiles, spaced every 500 m, cover beach topography from dune/cliff tops through the emerged beach to a seabed depth of about 15 m. They were decomposed by signal processing techniques to extract their monotonic components containing all major modes of the variability of beach topography. They are termed empirical equilibrium profiles and can be used for straightforward assessment of wave energy dissipation rates. Three characteristic patterns of wave energy dissipation were thus identified: one associated with large nearshore bars and several zones of wave breaking; a second, to which the equilibrium beach profile concept can be applied; and a third, characterized by mixed behaviour. Interestingly, most profiles showed significant seabed variations beyond the nearshore depth of closure — this phenomenon requires comprehensive studies in future.

* Corresponding author at: Institute of Hydro-Engineering, Polish Academy of Sciences, Kościerska 7, 80-328 Gdańsk, Poland. Tel.: +48 58 5222907; fax: +48 58 5524211.
E-mail addresses: grzegorz@ibwpan.gda.pl (G. Różyński), P.Szmytkiewicz@ibwpan.gda.pl (P. Szmytkiewicz).
Peer review under the responsibility of Institute of Oceanology of the Polish Academy of Sciences.

ELSEVIER Production and hosting by Elsevier

https://doi.org/10.1016/j.oceano.2018.04.001

1. Introduction

The first concepts of beach equilibrium profiles were developed empirically by Bruun (1954), who assumed that cross-shore beach topography is basically a function of wave energy E supplied to the shore at a shallow-water group wave velocity c_g. Bruun then concluded that nearshore seabed configurations are best described by monotonic power functions:

$$h(x) = Ax^n. \tag{1}$$

In Eq. (1) h is the seabed depth at the offshore distance x from the shoreline, and the parameters A and n are empirical quantities.

The theoretical background of the equilibrium beach configuration in constant hydrodynamic regimes was developed by Dean (1976), who assumed a constant wave energy dissipation rate E_r across the entire surf zone. Other assumptions included sediment homogeneity along the profile (D_{50} = const), monochromatic waves, linear wave theory and a constant wave breaking index $\gamma = H\,h^{-1} = const$. As a result, the wave energy dissipation rate could be calculated by:

$$E_r = \frac{5}{16}\rho g^{3/2}\gamma^2 h^{1/2}\frac{dh}{dx}. \tag{2}$$

Wave energy dissipation disappears at the shoreline for $h(x = 0) = 0$, and the well-known Dean monotonic beach equilibrium power function emerges for E_r = const:

$$h(x) = Ax^{2/3}. \tag{3}$$

The coefficient A has a dimension of $[m^{1/3}]$ and is directly related to E_r:

$$A = \left(\frac{24E_r}{5\rho g^{3/2}\gamma^2}\right)^{2/3}. \tag{4}$$

In Eq. (4), g = 9.81 m s^{-2} is the acceleration of gravity, and ρ = 1000 kg m^{-3} is the specific gravity of water. The situation of constant wave energy dissipation is known as the saturated wave breaking regime. It reflects the situation in which constant hydrodynamic forcing produces an equilibrium seabed configuration.

The relationships between the coefficient A and physical parameters of beach sediment were first investigated by Moore (1982). Next, Dean (1987) related this coefficient to the sediment fall velocity w_s with the formula $A = 0.067\,(w_s)^{0.44}$. A similar contribution by Kriebel et al. (1991) produced another fairly straightforward relationship:

$$A \approx 2.25\left(\frac{w_s^2}{g}\right)^{1/3}. \tag{5}$$

A temporal dependence of beach equilibrium profiles was proposed by Pruszak (1993), who introduced a time-varying A in the form of a sum of components oscillating over time:

$$A(t) = \overline{A} + A_1 + A_2 + A'. \tag{6}$$

In this expression, $\overline{A}$ is the time-invariant component expressed through e.g. Eq. (5), A_1 represents long-term variations due to the migration of large bed forms or changes in sediment supply driven by long-term variations in the hydrodynamic background, A_2 accounts for seasonal variability, and A' corresponds to short individual events, such as storms. Periodic changes in the parameter describing the equilibrium profile can be presented as:

$$A(t) = \sum_{k=1}^{2} a_k \cos\left(2\pi\frac{t}{T_k} + \theta_k\right) + A'. \tag{7}$$

The periods T_k correspond to long (k = 1) and medium (seasonal) time scales (k = 2); the period T_1 was found to be approximately 27 years for the Polish coast.

A different refinement of the beach equilibrium theory was proposed by Inman et al. (1993), who assumed a model in which the offshore portion of the profile was treated independently of the inner bar-berm portion, and both portions were matched at the breakpoint bar. Such partitioning was justified by different forcing modes on either side of the breakpoint. Both portions were fitted well by Eq. (1), with $n \approx 0.4$ being nearly the same for the bar-berm portion and the outer portion, irrespectively of seasonal changes. In this way, changes in seasonal equilibriums could be manifested by self-similar displacements of the bar-berm and outer curves, driven by seasonal surf zone variations.

Bodge (1992) addressed two major shortcomings of previous formulations, namely the physically unrealistic offshore-infinite range of beach equilibrium profiles and the infinite slope at the shoreline. He proposed an exponential curve, asymptotically converging to the closure depth to describe the beach equilibrium profiles. This effort was further improved by Komar and McDougal (1994), who replaced the closure depth with a ratio of the shoreline beach slope S_0 to the empirical parameter k [m^{-1}] accounting for profile concavity:

$$h(x) = \frac{S_0}{k}\left(1 - e^{-kx}\right). \tag{8}$$

This model predicts asymptotic convergence to a depth of S_0/k metres for the shoreline beach slope of S_0, which can be established as a function of sediment grain size and wave parameters, or evaluated directly from profile measurements, so only the concavity parameter k should be least-square fitted to profile measurements.

Several alternative approaches have been proposed to tackle shoreline singularity. Larson and Kraus (1989) suggested a form that superimposed a planar shallow water component with an offshore Dean form. Özkan-Haller and Brundidge (2007) introduced a further modification to limit the influence of the planar component to shallow water. Perhaps the most advanced model was presented by Holman et al. (2014), who developed an equilibrium beach profile concept capable of accounting for (a) a finite shoreline slope, (b) a concave-up form in wave-dominated shallow waters and (c) an asymptotic planar slope in the far field:

$$h(x) = \alpha\left(1 - e^{-kx}\right) + \beta x. \tag{9}$$

This model requires three parameters: (a) the far-field slope β can be obtained directly from available bathymetric charts, (b) the shoreline slope can also be easily established using the expression $d(h = 0)/d(x = 0) = S_o + \alpha k + \beta$, and (c) the depth h should be known at some location x', which can be anywhere in the profile, but should be representative of the background, average profile depth, so it should best be a

point seaward of the active bar zone. This last parameter is therefore subjective to some extent, but is necessary to establish the second equation relating α and k: $h(x') = \alpha(1 - e^{-kx'}) + \beta x'$.

The conceptual simplicity and modelling robustness of monotonic beach equilibrium profiles resulted in their wide acceptance. In particular, the equilibrium profiles are used extensively in beach fill design studies and projects, see e.g. CEM (2008) Part III-3, or CEM (2008) Part V-4. The major underlying reason is that the complicated and nonlinear phenomena of wave energy dissipation are often intractable by most physical models, particularly in systems with multiple bars. It can be briefly explained as follows:

1) When waves are mild, the surf zone is narrow, and they break only over the innermost bar.
2) Higher waves begin to break over the 2nd bar; the surf zone now includes two bars, and the breakers can include a spilling or a plunging mode or both.
3) During heavy storms, the outer bars contribute to wave energy dissipation as well — the surf zone now includes 4 bars or more and is several hundred metres wide. Various combinations of spilling and plunging modes are then possible, resulting in very complicated longshore and cross-shore sediment transport patterns.
4) Variations of wave set-up and wind-driven storm surges (in a range of 1 m) further modify the breaking regimes during the build-up, peak and recession of storms.

The insufficient robustness of physical models to successfully deal with complex surf zone morphodynamic processes necessitates other types of instruments that can provide some insight into the evolution of complicated coastal bathymetries. One such solution was proposed by Różyński and Lin (2015), who developed the concept of empirical equilibrium profiles. These profiles originate from actual bathymetric measurements and are derived by extraction of their monotonic components, which usually contain more than 90% of overall profile variability. Empirical equilibrium profiles relax the core assumption of theoretical Dean-type equilibrium profiles, namely the constant wave energy dissipation rate in the entire surf zone. In addition, if an empirical equilibrium profile closely resembles the shape of a Dean function, it demonstrates that saturated wave breaking regimes can be encountered in reality, at least along some portion of the surf zone, usually closer to the shoreline.

The extraction of empirical equilibrium profiles from measured cross-shore seabed configurations can be done by two methods of intensive signal processing: Empirical Mode Decomposition (EMD), see Różyński and Lin (2015), or Singular Spectrum Analysis (SSA), see Różyński et al. (2001). The only constraint is the monotonicity of empirical equilibrium profiles. It is needed to secure the applicability of Eq. (2), in which changes in wave energy dissipation intensity are governed primarily by the 1st derivative of the empirical equilibrium profile and secondarily by the square root of that profile. The positive sign of the derivative is needed to sustain wave energy dissipation. This equation is very useful because the resulting rates of energy dissipation are continuous, smooth and can be easily computed. Moreover, departures from actual dissipation rates are not very significant, because the empirical equilibrium profiles usually contain more that 90% of profile variability.

The primary goal of the paper was to identify wave energy dissipation patterns along a fairly long coastal segment in Poland, stretching between the western breakwater of the Władysławowo harbour (km 125 of the national coastal chainage) and a beach east of Lake Sarbsko (km 174). Wave energy dissipation patterns were identified using the empirical equilibrium profile concept for two sets of geodetically fixed bathymetric profiles commissioned in 2005 and 2011 by coastal authorities for monitoring purposes. Special attention was given to evaluation of the resemblance between empirical and theoretical Dean profiles in areas where saturated wave breaking regimes are encountered. The second goal was to identify the offshore range of application of the wave energy dissipation concept. This was done upon the assessment of the nearshore closure depth, based on the reconstruction of past wave climates (1958–2001) and the comparison of the offshore convergence of the two bathymetries of 2005 and 2011 at the offshore limit of the littoral zone. An unplanned by-product of the study was the identification of significant seabed variations beyond the nearshore depth of closure. This phenomenon consisted in significant changes in recorded bathymetries after profile convergence along their fairly long section, located at depths greater than 10 m. Some mechanisms regarding the driving force of those variations were hypothesized, providing grounds for follow-up studies.

2. Data and methodology

Fig. 1 presents the Polish coast and shows both ends of the national coastal chainage at km 0 (border with Russia) and km 428 (border with Germany). It also presents the limits of the study area at km 125 and 174. The profile lines, surveyed in the study area in 2005 and 2011, are geodetically fixed and spaced every 500 m, providing a rich data base with almost 100 profiles sampled twice. Their cross-shore range covers the area from the dune/cliff crest down to a depth of 15 m or more; it normally measures more than 2000 m. The surveys were commissioned by coastal authorities for monitoring purposes, in compliance with the Coastal Protection Act of Parliament of 2003.

A significant onshore and offshore extension of the profile lines provides a perfect opportunity for the extraction of their key modes of variability with much greater precision, as the extensive coverage substantially reduces the so-called end effects that can distort the modes of variability near the onshore and offshore profile extremities. One of data-driven techniques used for the extraction of the modes of variability, well tested in coastal applications, is the Singular Spectrum Analysis (SSA), see Appendix. Extensive background information on this method and its application to beach surveys can also be found, e.g. in Różyński et al. (2001). In brief, it consists in evaluation of the covariance structure of each profile and the computation of the associated modes of variability, known as the reconstructed components. If the number of points in a profile is n, then the number of modes of variability should not exceed $\frac{1}{3}n$ to eliminate imprecise estimation of higher modes. The modes are ranked according to the portion of total signal (profile)

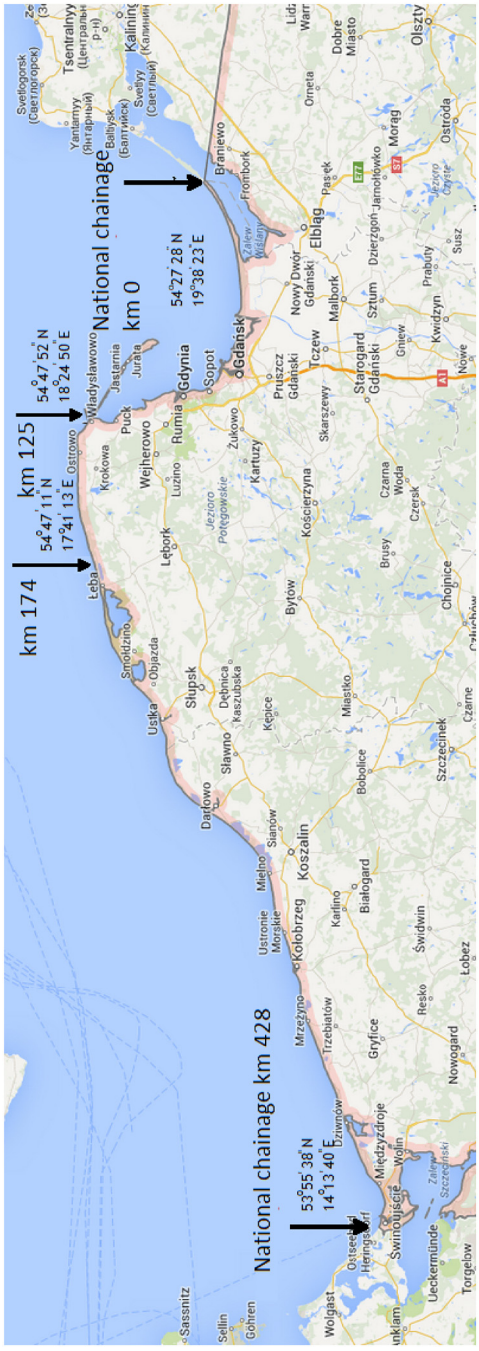

Figure 1 General map of Polish coastline.

variance each of them contains, starting from the one with the largest contribution. Being additive, they are summed, starting from the most significant one down to a mode whose inclusion destroys the monotonicity of the empirical equilibrium line. This summation is described in more detail for each profile line studied. The profiles studied usually contained 210—220 elements, so the maximum number of modes was set at $m = 70$. However, the number of modes that contribute to empirical equilibrium profiles was found to be much less, usually no more than 5.

3. Results

Fig. 2 shows fractions of profile variances explained by empirical equilibrium profiles for the survey of 2005. They were calculated for $N = 50$ profiles, so the span between the profiles was 1 km. The reason for that was twofold: (1) for a span of 500 m the profiles are often very similar, (2) computations of empirical equilibrium profiles for very similar profiles are usually redundant and do not add valuable information to the analysis. The average variance fraction explained by empirical equilibrium profiles was 92%, the related median 94.9%, the minimum 66.5% and the maximum 99.3%. On the basis of Fig. 2 we decided to scrutinize in detail 6 representative profiles whose explained variance is near the average value (km 130, 149 and 156) or significantly departs from that value (km 125, 139 and 161). These 6 profiles are marked in Fig. 2.

Fig. 3 presents the results of analysis for km 125. We can see that in both surveys the morphology is very similar and is dominated by two very large nearshore bars. Owing to the resemblance between the two surveys, SSA decomposition was done for the 2005 seabed configuration only. The empirical equilibrium profile contains only one mode of variability; the inclusion of another immediately destroys profile monotonicity. As a result, it significantly departs from the measured seabed configuration (see Fig. 2), as it contains only 73.7% of the original profile variability. This result demonstrates that the concept of one surf zone with wave breaking processes distributed continuously across its entire cross-shore range cannot be accepted, because the prominence of bars forms a beach system with intensive wave breaking processes along the offshore bar slopes and zones of no dissipation of wave energy inside the troughs. It was schematized by plotting three systems of coordinates, fixed at the shoreline and bar crests, for which separate Dean curves, representing disjoint subzones of wave energy dissipation, could be postulated. No saturated wave energy dissipation can be expected, though, and the monotonic profile cannot describe wave energy dissipation with sufficient precision.

Fig. 4 represents the analysis done for km 130 near Chłapowo, at the eastern end of a soft cliff running from Chłapowo to Jastrzębia Góra. Both surveys show one dominant bar with a crest situated about 400 m from the shoreline, which is preceded by a distinct trough with the greatest depth some 280 m offshore. The comparison of the two seabed configurations reveals substantial shoreline advance between 2011 and 2005 and much shallower depths onshore of the trough. The trough and the bar do not show important changes, and at a depth of some 7.5 m both profiles converge to the nearshore depth of closure.

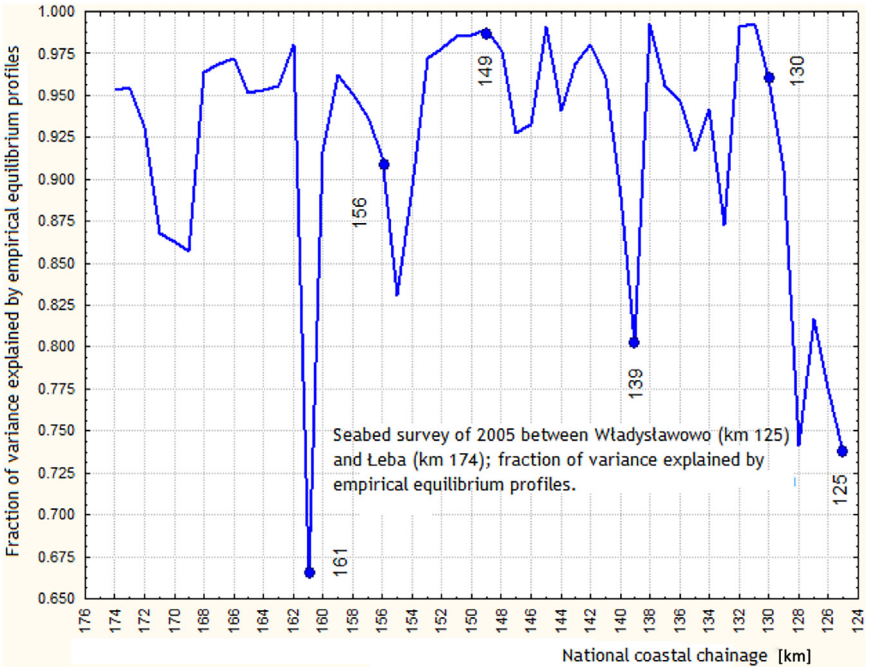

Figure 2 Fraction of profile variance explained by empirical equilibrium profiles.

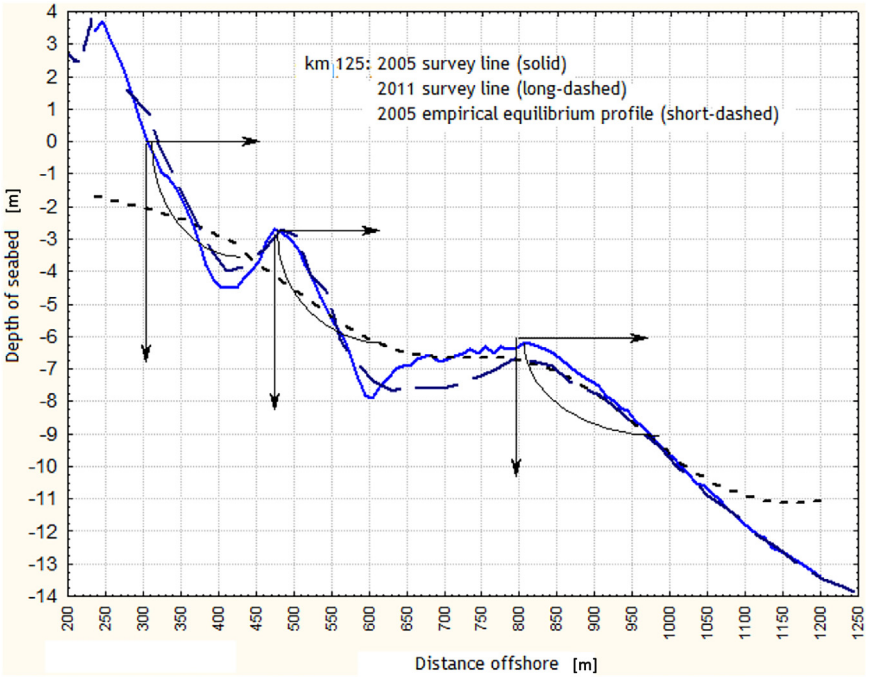

Figure 3 Empirical equilibrium profile at km 125.

The resemblance between the two surveys with respect to key morphologic features (locations and magnitudes of the bar and the trough) justified the computation of the empirical equilibrium profile for the seabed configuration of 2005 only. It consists of three modes of variability, which contain 96.1% of total survey variance. Thus, the empirical equilibrium profile reproduced the actual seabed configuration with high accuracy, highlighting the versatility of SSA decomposition. Its most important characteristic is the inflection point some 330 m offshore at a depth of about 3.5 m. The shape of the empirical equilibrium profile above that depth is akin to that of the Dean curve to a certain extent. Therefore, it can be assumed that the saturated wave breaking regime can develop there. The least-square fit of the Dean function to the empirical equilibrium profile yielded $A = 0.085\ \mathrm{m}^{1/3}$, and, using Eq. (4), the saturated rate of wave

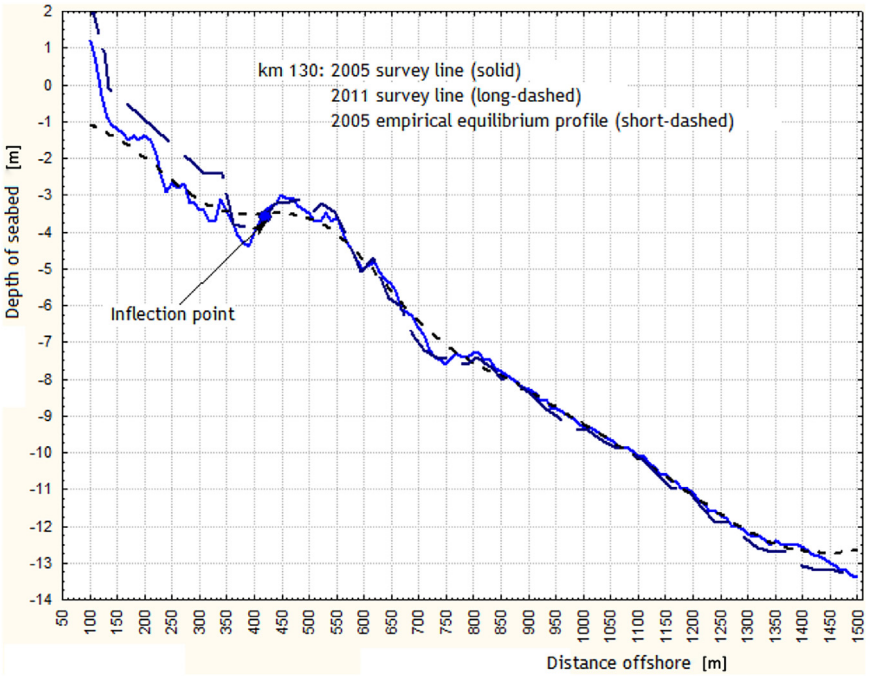

Figure 4 Empirical equilibrium profile at km 130.

energy dissipation was evaluated at E_r = 96.5 W m^{-2}. Offshore of that inflection point, seabed changes are not prominent and converge at about 7.5 m. Wave energy dissipation beyond the nearshore closure depth is negligible; it is initiated at that depth (7.5 m) and becomes saturated at 3.5 m. In all, the concept of saturated wave energy dissipation in the form of the beach equilibrium profile is fully applicable at km 130.

The next profile analyzed in detail is situated at km 139. Both surveys are plotted in Fig. 5. We can see that general morphological characteristics of the two surveys are the same, although in 2011 the bars and the shoreline moved onshore, so the beach underwent some erosion. Fig. 5 also shows the results of analysis. The profile at km 139 is located at Ostrowo, west of Jastrzębia Góra and east of Karwia. We can discern 5 nearshore bars, starting from the small innermost one, whose tiny crest is located at a depth of 1 m. The crests of the remaining 4 bars are located at 1.5, 2.1, 5 and 8 m. The empirical equilibrium profile consists of two modes of variability that embrace only 80.2% of the variance of the profile configuration of 2005. However, except for the offshore region of the outermost bar, absolute departures from the original seabed configuration are reasonable, so the empirical equilibrium profile is acceptable for multiple bars of moderate magnitude. Interestingly, the inflection point, similar to the one found at km 130, can be identified at a depth of 8 m. Moreover, its offshore distance is also the same as the offshore distance to the outermost bar, so they are both co-located. The remote location of the inflection point suggests that the entire surf zone morphology is close to the Dean-type regime of saturated wave breaking. The least-square fit of the Dean parameter to the empirical equilibrium profile yielded A = 0.089 and E_r = 103.4 W m^{-2}. The latter value closely resembles the saturated dissipation of wave energy at km 130 (96.5 W m^{-2}). Interestingly, the region of the outermost bar underwent the smallest seabed change, so it was justified to determine the depth of (nearshore) closure there. However, offshore of the rather flat and long crest of that bar, the two surveys diverged significantly on the offshore slope of the outermost bar at depths visibly greater than 8 m. This phenomenon was also found in other profiles and will be discussed later.

The next profile investigated in the current study is situated at km 149, just east of the mouth of the river Piaśnica, see Fig. 6. In 2005, it exhibited 3 shallow nearshore bars with crests at 0.5, 2 and 3.8 m. The related empirical equilibrium profile was composed of 4 modes of variability and matched very closely the 2005 survey line, capturing 98.9% of its variability There was also an inflection point at 4 m depth, just offshore of the 3rd bar (crest at 3.8 m). The fitted Dean parameter up to the inflection point was estimated as A = 0.086, and the related E_r = 98.2 W m^{-2}. In 2011, the two innermost bars merged into one quasi-bar structure. The smaller bar remained close to the location of bar 3 from 2005, with its crest at 3.8 m depth, located a bit onshore of the inflection point of the empirical equilibrium profile of 2005. The major difference between the surveys of 2005 and 2011 is a large trough found in the 2011 seabed morphology with a maximum depth of about 7.3 m, located about 450 m offshore. Further offshore, the seabed of 2011 exhibits a large outermost bar with the crest at 5.7 m depth and 650 m offshore. The related attempted empirical equilibrium profile retained 98.6% of total seabed variance, but lost monotonicity in the vicinity of the large trough. Thus, the profile at km 149 in 2011 exhibits two types of behaviour: one with the inflection point that delimits the zone of saturated wave breaking and a second, similar to km 125, where a large bar produces two subzones of wave breaking regimes. Consequently, this profile line demonstrates mixed behaviour: at times it generates conditions of saturated wave breaking and wave energy dissipation, whereas at other times it forms two separate zones of wave breaking and energy release.

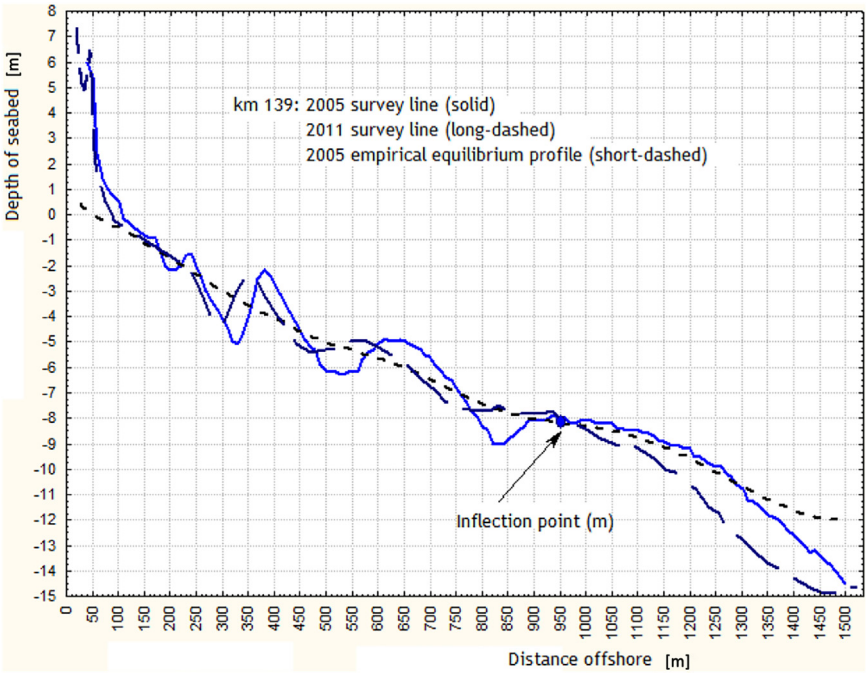

Figure 5 Empirical equilibrium profile at km 139.

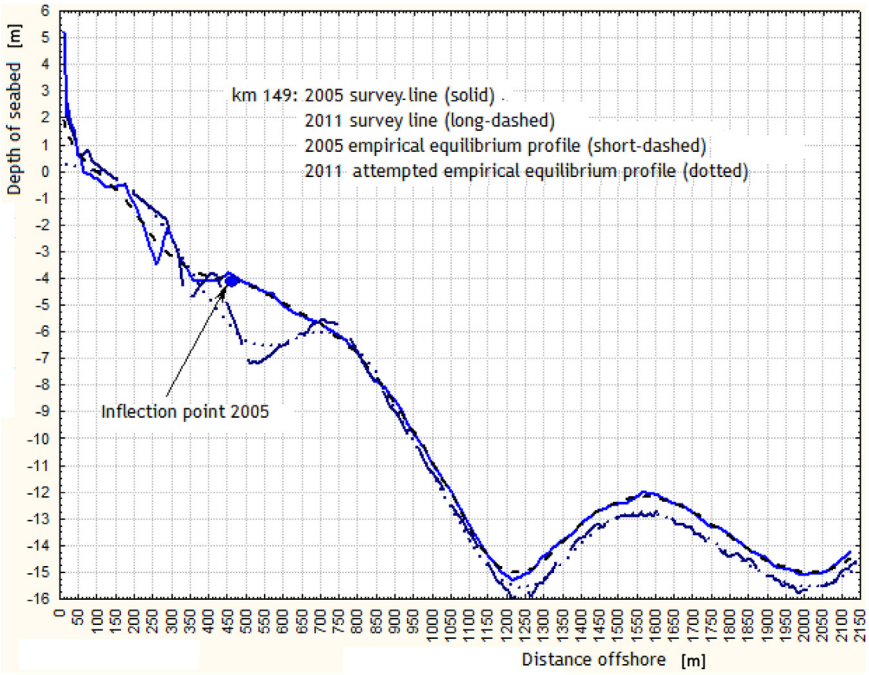

Figure 6 Empirical equilibrium profile at km 149.

Identification of mixed behaviour is a very strong point of SSA decomposition applied in the context of empirical equilibrium profiles. Interestingly, both profiles converge just offshore of the crest of the large bar at about 7 m depth, some 750 m offshore. This spot defines the (local) nearshore closure depth. The profiles remain close until some 1050 m offshore and 14 m depth. Then, they diverge, and the difference between the depths of the two surveys can reach 1 m.

The next profile is located at km 156 near Białogóra, see Fig. 7. In 2005, 3 tiny shallow bars were found at seabed depths of 2, 3 and 3.8 m. The associated empirical equilibrium profile has an inflection point in this region, at a depth of about 3 m and embraces 91.4% of the seabed variance of 2005 in 4 most significant modes of variability. The least-square fitted Dean parameter for this region was found to be $A = 0.069$, which corresponds to $E_r = 70.6\ \mathrm{W\ m^{-2}}$. This value points to a lower wave energy dissipation compared with the

previously analyzed configurations. The seabed in 2011 had some similarities to the profile from 2005, with bar crests at 1.9, 3 and 5.1 m. The main difference were three deep troughs found in 2011 at 3.5, 5.3 and 5.7 m. As previously, the two profiles converged at about 650 m offshore and opened up again at 900 m with depth discrepancies of over 1 m; the former location corresponds to the nearshore closure depth of 5.5 m. The empirical equilibrium profile for 2011 is plotted as the dotted line in Fig. 7. It contains 93.3% of seabed variance in 4 primary modes of variability. It also has an inflection point at a depth of 5 m, but the zone of saturated wave breaking is wider; the corresponding Dean parameter is $A = 0.083$, and E_r W m^{-2}. We can see that the zone of saturated wave energy dissipation can persist between measurements separated by as long as 6 years, but energy dissipation itself and the width of saturated energy dissipation can vary. However, it can be tentatively concluded that saturated wave energy dissipation decreases to 70—100 W m^{-2}. These results again underline the versatility of the empirical equilibrium concept and show variations of wave energy dissipation rates at the same site over semi-decadal scales.

Perhaps the most peculiar seabed configuration was discovered at km 161, see Fig. 8. This profile line runs through the submerged region of the Białogóra dune, whose onshore part was stabilized by forestation in the early 20th century. It is characterized by an enormous, remotely located bar, with the crest at some 900 m offshore at a depth of only 4.9 m. By contrast, the trough, located onshore, had a very large maximum depth of almost 11 m at some 600 m offshore. Closer to the shoreline, three typical smaller bars were discovered with crests at depths of 1, 2 and 3.5 m. The empirical equilibrium profile contained only one mode of variability that captured just 61% of signal variations. The line plotted in Fig. 8 has two modes of variability embracing 91.7% of total variability, but it significantly departs from monotonicity. This attempted empirical equilibrium profile points to behaviour similar to that found at km 125. The concept of saturated wave breaking is not applicable to this seabed configuration; there are definitely two zones of wave energy dissipation and saturation.

In 2011, the seabed configuration at km 161 was somewhat more typical. The huge bar moved offshore, so its crest shifted to 1100 m offshore and sank to a depth of 7 m, whereas the deep trough remained in place, but its depth decreased to 9 m. The other onshore bars remained more or less stable, the only difference being the shoreline retreat of about 50 m, which was not dangerous, because of the very wide beach. The attempted empirical equilibrium profile for 2011 turned out to be similar to that for 2005, except that it was generally much steeper. This was the result of the offshore translation and sinking of the huge outermost bar. In general, though, both seabed configurations represent a site in which a single zone of saturated wave breaking (and energy dissipation) is not possible. A relatively large time span between the two measurements (6 years) indicates that this situation is stable. Regarding the closure depth, both seabed configurations converged at a depth of 9.5 m, designating the offshore limit of the nearshore region, but diverged again at 13 m. This is another indication of a hydrodynamic forcing that is strong enough to trigger significant sediment motion at greater depths, beyond the nearshore region.

The above morphological findings require verification based on the available hydrodynamic data. One such dataset is the wave climate of the Baltic Sea reconstructed in the FP5 HIPOCAS project for the period of 1958—2001. A point near Lubiatowo located just offshore of the study area, for which such reconstructions were made, was therefore chosen to

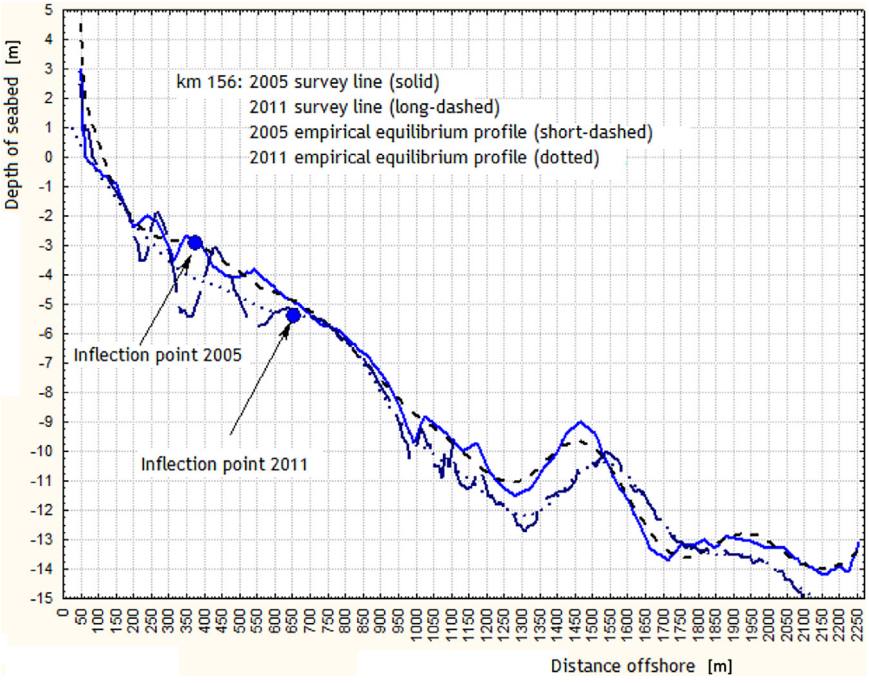

Figure 7 Empirical equilibrium profile at km 156.

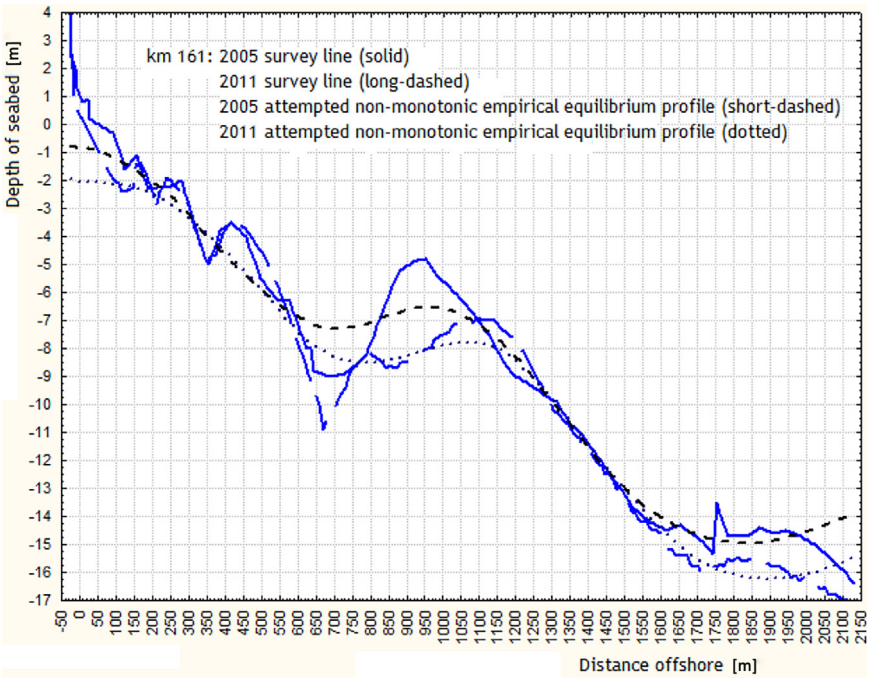

Figure 8 Empirical equilibrium profile at km 161.

Table 1 Statistical parameters of closure depth for 1958–2001 period (44 years).

Depth of closure parameters				
Mean [m]	Median [m]	Min [m]	Max [m]	St. Dev. [m]
8.4	8.2	5.9	10.7	1.15

calculate annual nearshore closure depths valid for all study area. Hallermeier's well-known formula was used, see Hallermeier (1981):

$$h_c = 2.28H_s - 68.5\left(\frac{H_s^2}{gT_s^2}\right). \tag{10}$$

In Eq. (10), H_s is a significant wave height exceeded for 12 h in the year preceding the seabed survey, and T_s is the associated wave period. The results are presented in Table 1. They were compared with the nearshore depths of closure of individual profiles between 2005 and 2011, put together in Table 2. We can see that the means and medians are very similar and range from 8 to 8.5 m. Thus, this value can be assumed as a fairly accurate estimate of the nearshore closure depth despite the fact that Hallermeier's estimates describe annual closure depths, whereas the investigations of seabed surveys span a period of 6 years. Both methods of estimating the nearshore closure depth also yield fairly low standard deviations, although the value obtained from comparisons of the two morphologies is roughly twice as high. The range between the minima and maxima is also greater for morphological observations. This cannot be surprising, because morphological considerations are based on very local profile characteristics, which vary significantly from site to site, whereas hydrodynamic data reflect wave climates valid for the entire study area.

Table 2 Statistical parameters of closure depths of individual profiles between 2005 and 2011.

Mean [m]	Median [m]	Min [m]	Max [m]	St. Dev. [m]
8.5	8.0	4	15	2.3

The relatively precise determination of the nearshore closure depth and identification of saturated wave breaking regimes at most beaches in Poland makes it possible to develop formulas for surf zone wave energy dissipation. We can assume that it is initiated at the nearshore closure depth and achieves saturation at the inflection point of empirical equilibrium profiles. In the most simplistic approach, wave energy dissipation outside the saturation sub-zone can be evaluated as:

$$E_r = E_{r_{dean}}\left[\frac{h_c - h}{h_c - h_{infl}}\right]^m \approx 100\left[\frac{h_c - h}{h_c - h_{infl}}\right]^m. \tag{11a}$$

In this equation, E_r represents wave energy dissipation between the locations of closure depth and inflection point. In other words, the saturation of wave energy dissipation develops between the nearshore closure depth h_c, where the expression in brackets is equal to zero, and the depth of inflection point h_{infl}, where it is equal to 1. Within the

Table 3 Descriptive statistical parameters of offshoremost bar and inflection point of empirical equilibrium profiles.

	Mean [m]	Median [m]	Min [m]	Max [m]	St. Dev. [m]
X_{infl}	472.9	425	100	925	212.7
X_{offb}	530	475	225	1050	240.7
h_{infl}	4.7	4.5	2.4	8.5	1.34
h_{offb}	4.4	4.3	2.1	8.5	1.37

sub-zone of saturated wave breaking, the formula reduces to $E_r = E_{r_{Dean}} \approx 100$ W m^{-2}. The cross-shore width of the zone with unsaturated wave energy dissipation is delimited by offshore locations of the nearshore closure depth X_c and inflection point X_{infl}. Eq. (11a) can be refined to include the actual profile configuration in the zone of unsaturated wave energy dissipation:

$$E = \frac{5}{16}\rho g^{3/2}\gamma^2 h^{1/2}\frac{dh}{dx}\left[\frac{h_c - h}{h_c - h_{infl}}\right]^m. \quad (11b)$$

The exponent m is normally set to 1. It can be further modified empirically if hydro-, litho- and morphodynamic observations and measurements provide sufficient justification. This estimation however is usually time-consuming.

One interesting aspect related to the locations of inflection points, determined by X_{infl} and h_{infl}, is their very high correlation with the corresponding locations of the outermost bar, given by X_{offb} and h_{offb}. The correlation between X_{infl} and X_{offb} is equal to 0.95, whereas for h_{infl} and h_{offb} the correlation is even greater and equals 0.97. This close relationship is further evidenced in Table 3, where basic statistical parameters of these four quantities are presented. We can see that inflection points should be located slightly deeper than the depth of the crest of the outermost bar and somewhat onshore of that crest. Thus, the location of the outermost bar may serve as a crude estimate of the location of the inflection points of empirical equilibrium profiles.

The last issue to discuss is the offshore divergence of profile surveys beyond their convergence at the nearshore closure depth. This phenomenon is not entirely unknown. It is widely accepted by offshore engineers that seabed evolution beyond the nearshore region can be significant. Hallermeier (1983) came up with the following formula:

$$h_{out} = 0.018 H_m T_m \sqrt{\frac{g}{D_{50}(s-1)}}. \quad (12)$$

In Eq. (12), H_m and T_m are the median wave height and period, respectively, D_{50} is the median sediment diameter, and s is the ratio of the specific gravity of sand to that of water (about 2.65). Formations of the offshore seabed can be attributed to earlier coastal and geologic processes, but not to the offshore movement of sediment from the present beach. The convergence of the profile envelope landward of those seabed formations indicates that sediment movement there is not directly related to sediment exchange in the nearshore profile.

Eq. (12) relates the mean wave conditions with D_{50}, a key sediment characteristic. Therefore, the average parameters of waves occurring over long periods of relatively calm weather are held responsible for seabed evolution beyond the littoral zone. This assumption can be realistic for the conditions of the United States, situated on two oceans, where wave lengths and periods are much longer than those recorded on the Baltic Sea. Nevertheless, the identification of significant seabed variations beyond the nearshore zone, after the apparent closure of seabed surveys at the nearshore closure depth h_c, demonstrates that the divergence of seabed surveys is also a common phenomenon in the Baltic Sea. For this reason, both components of Eq. (12) need to be verified for the Baltic Sea conditions. With regard to wave parameters, the available data can provide inputs for such analyses. However, energy fluxes related to mean waves in the Baltic Sea seem to be hardly sufficient to drive significant sediment movements beyond the nearshore zone for ordinary sands. Therefore, sediment samples from depths greater than about 14 m should be taken to obtain their granulometric curves, including D_{50}. Sufficiently small grains could justify the observed variations. However, it appears advisable to co-locate a current metre (or, better, an array of at least several current metres) in an area of sediment collection to obtain a full deepwater hydrodynamic background. The primary goal is to determine whether sufficiently strong oscillatory flows exist beyond the nearshore region. If they do, then Eq. (12) will be validated for the Baltic Sea conditions. However, if the oscillatory component is absent or insignificant, then the presently unidentified currents of other origin should be detected. Such currents can generate favourable conditions for non-trivial deepwater sediment motion, and Eq. (12) will have to be modified to include the current effect. This, however, is justified only when the hypothesized currents are actually detected.

One issue not discussed in this paper is the comparison of Dean coefficients obtained from least-square fits with those predicted by Hanson and Kraus (1989), who elaborated the relationships between A and D_{50} upon hydraulic experiments. Solution to this problem requires vast granulometric analyses of sediment samples from characteristic cross-shore locations in the surveyed profiles for a credible assessment of D_{50}. This is definitely a subject for follow-up research, which, however, requires an extensive field campaign.

4. Discussion

In general, the identified wave energy dissipation patterns are highly varied. For beaches with very large bars, whether natural or altered by anthropogenic activities, the concept of the equilibrium profile is not valid. In such instances, the surf zone consists of sub-zones, where energy dissipation occurs. Such zones are associated with offshore bar slopes that culminate at the crest. In troughs, often very deep, energy dissipation does not take place. Some assessment of energy dissipation intensity can be given by Eq. (2). Most profiles, though, exhibit zones of saturated wave breaking and energy dissipation, which can be identified when the empirical equilibrium profile is similar to the shape of the Dean function. Usually, such a zone starts at the shoreline and extends up to the inflection point. Interestingly, the evaluated maximum dissipation rates are in a range of about 100 W m^{-2}. The length of a segment where the saturated wave breaking regime and energy dissipation can develop and the associated dissipation intensity, are valuable pieces of information that can be used in beach fill design studies and procedures. Importantly, equilibrium conditions were reproduced from empirical measurements in areas where bars are not very large, and such systems can often exhibit erosive tendencies, particularly under changing climatic conditions. Therefore, they are usually subjected to beach fills, which are routinely designed on the basis of the equilibrium profile theory. On the other hand, the study results show that sediment-rich systems that usually develop isolated subzones of energy dissipation between very large bars, serving

as sediment buffers, are not usually prone to erosion and therefore are not subjected to beach fill operations.

With regard to individual profiles, the study revealed that the concept of monotonic empirical beach equilibrium profiles cannot be recommended for coastal segments in which distinct, very large bars occur. Such systems can have either natural (km 161) or anthropogenic origin (km 125). For example, the region of Białogóra (km 161) is known for its enormous natural dune system, located in both the emerged and submerged parts of the coastal zone. The emerged part was stabilized by humans with a forest, whereas the submerged part became a huge natural sand reservoir. In contrast, the construction of the western breakwater of the Władysławowo harbour (km 125) resulted in the obstruction of the predominant west-to-east littoral drift. In such instances, the empirical equilibrium profile significantly departs from the measured seabed configuration. The empirical equilibrium profile typically includes only the basic deepening seabed trend, usually contained in the first reconstructed component. The addition of another immediately destroys the monotonicity of the empirical equilibrium profile, so wave energy dissipation cannot be evaluated with Eq. (2): application of this equation to the empirical profile flawed by substantial departures from the original seabed configuration will certainly produce unrealistic assessments of actual wave energy dissipation rates. In sum, this observation indicates a possible line of follow-up research aimed at the identification of parameters limiting the applicability of the empirical equilibrium profile theory. Such parameters should be sought first in the geometry of barred profiles and then in sedimentary characteristics of coastal segments under study and their hydro- and lithodynamic background. The determination of these characteristics requires full-scale field experiments focused on seawater level changes, wave transformation, wave driven currents and seabed variations during storms and post-storm recovery periods.

The seabed configurations near soft cliffs (km 130) regularly develop steeper profiles without bars or with only one bar. The equilibrium zone is narrow, but the empirical equilibrium profile is usually monotonic. Also, its departures from the measured seabed configurations are usually small, so empirical equilibrium profiles can be used for the assessment of wave energy dissipation. The saturation of dissipation processes is possible in the narrow sub-zone, where the empirical equilibrium profile resembles the Dean function. In general, the presence of one bar reflects general erosive tendencies of soft cliffs on open sea coasts, where wave energy fluxes are only gently reduced over a bar and shoaling seabed and then attack the cliff foot directly, particularly during storms.

In general, most beaches with multiple bars of ordinary magnitude demonstrate equilibrium properties over the entire system of bars. The bars cannot be very large, so the empirical equilibrium profiles reproduce well over 90% of profile variability. These results show that the empirical equilibrium profile theory is fully applicable to most coastal segments in Poland.

The equilibrium conditions are identified at locations where the shape of empirical equilibrium profiles closely resembles the theoretical Dean curve. Such profiles usually extend from the shoreline up to the inflection point, beyond which they become concave. The locations of the outermost bar can serve as a fairly accurate proxy for the locations of the inflection points of empirical equilibrium profiles. The close resemblance between theoretical and empirical equilibrium profiles confirms the correctness of beach fill design principles, which are based on the Dean-type equilibrium profile theory and applied where the natural bars cannot sufficiently suppress wave energy during storms and prevent local erosion. The results of computations of wave energy dissipation show that this dissipation is in the range of 100 $W\,m^{-3}$ (per unit volume of water) or 100 $W\,m^{-2}$ (per longshore distance of 1 m). Also, the study of nearshore closure depths found a close resemblance between the estimates of closure depths from wave parameters and beach surveys. This led to a modification of wave energy dissipation formulas to include the zone where dissipation is initiated from zero up to saturation, associated with the inflection point of the empirical equilibrium profile. Onshore of that point, the saturated (constant) energy dissipation regime can be assumed. Finally, significant profile variations were identified beyond the nearshore region. Research on the nature of nearbed hydrodynamic regimes in that area should be conducted in order to determine whether oscillatory flow regimes of wave origin can drive noteworthy seabed variations, or whether other hydrodynamic phenomena (currents?) should be sought. Elimination of wave action as the agent of morphodynamic evolution outside the nearshore region will immediately trigger the question about the drivers of those hypothetical currents. The possible processes might include events of intensive water exchange between the Baltic and the North Sea, affecting the entire Baltic region, wind set-up during extreme events and the associated changes in the water table due to rapid passages of low-pressure air masses from (south) west to (north) east, or up- and down-welling events. Combinations of these processes are also possible. Parallel granulometric studies of sediments sampled beyond the nearshore region should provide additional information on minimum nearbed water velocities needed to mobilize the sediment there.

Overall, the analysis demonstrated that the coastline exhibits highly variable morphologies in the longshore direction, resulting in the corresponding longshore variations of wave energy dissipation rates. The monotonic empirical equilibrium profiles, made up of the sum of the modes of variability of SSA decomposition proved to be remarkably versatile and allowed us to determine highly variable wave energy dissipation rates. They can be divided into three basic classes: (1) this class includes the areas where wave breaking is relatively cross-shore uniform (km 130, 139 and 156), (2) locations where two or three sub-zones of intensive breaking exist (km 125 and 161), separated by deeper calm areas, in which broken waves can reform, and (3) locations of mixed behaviour (km 149), where sometimes predominantly cross-shore uniform wave energy dissipation rates can be observed and at some other times two distinct sub-zones of more intensive breaking can be encountered. This classification was achieved by the relaxation of the rigid assumption of constant energy dissipation, encapsulated in the Dean coefficient.

Acknowledgements

The research presented in this paper was financed and conducted under the H2020 project HYDRALAB+, contract number 654110 — HYDRALAB-PLUS — H2020-INFRAIA-2014—2015

and mission-related activities of IBW PAN, financed by the Polish Academy of Sciences.

Appendix. Singular spectrum analysis (SSA)

SSA is based on the Karhunen-Loéve expansion theorem, applied to the lagged covariance matrix of a time series x_i for $1 \le i \le N$. It has constant diagonals corresponding to equal lags:

$$T_x = \begin{bmatrix} c(0) & c(1) & \dots & c(M-1) \\ c(1) & c(0) & c(1) & . \\ . & c(1) & c(0) & . \\ c(M-1) & \dots & c(1) & c(0) \end{bmatrix}, \quad \text{(A1)}$$

where

$$c(j) = \frac{1}{N-j}\sum_{i=1}^{N-j}(x_i-\overline{x})(x_{i+j}-\overline{x}) \quad \text{(A2)}$$

and $\overline{x}$ is the mean value of the series. M is the user-defined *window length* or *embedding dimension:* the larger M is, the better the spectral resolution of oscillatory components in the time series. However, to reduce statistical errors in $c(j)$ for large lags j, it is recommended that M should not exceed $\frac{1}{3}N$.

The auto-covariance matrix is symmetric and positive definite for natural data, so the eigenvalues λ_k are positive, the eigenvectors E^k are orthogonal, and the scalar product of the (column) eigenvectors E^j and $E^l$is equal to the Kronecker delta:

$$\sum_{k=1}^{M} E_k^j E_k^l = \delta_{jl}, \quad 1 \le j \le M, 1 \le l \le M. \quad \text{(A3)}$$

The same is true for the scalar products of the jth and lth rows:

$$\sum_{k=1}^{M} E_j^k E_l^k = \delta_{jl}, \quad 1 \le j \le M, 1 \le l \le M. \quad \text{(A4)}$$

The eigenvectors are the invariant part of SSA decomposition and the variability is contained in *principal components* (PCs). The kth PC is a projection coefficient of the original signal onto the kth eigenvector:

$$a_i^k = \sum_{j=1}^{M} x_{i+j-1} E_j^k, \quad 1 \le i \le N-M+1. \quad \text{(A5)}$$

This equation states that we have to take M elements of the series x from the ith to $i + M$th element, compute their products with the corresponding elements of the kth (column) eigenvector and sum them up to obtain the ith element of the kth PC. Hence, the PCs are time series of the length $N-M$. Also, M consecutive elements of the series x are needed to compute one term of every PC, so there are k common elements of this series for the ith term of the rth PC a_i^r and the jth term of the sth PC a_j^s, such that $k = M-|j-i| > 0$ (lag $|j-i|$). Therefore, the correlation structure of the original series must be imprinted in the sequence of PC terms, producing non-zero correlations for non-zero lags.

The PCs do not provide a unique expansion of the signal: using the PCs, it can be expanded as:

$$x_{i+j} = \sum_{k=1}^{M} a_i^k E_k^j, \quad 1 \le j \le M. \quad \text{(A6)}$$

There may be up to M subsets of the original series containing the specific element x_{i+j}. Thus, there are up to M different ways of reconstructing the components of the signal with Eq. (A6), and a series having $N - M + 1$ elements is obtained. However, we can construct a least-square optimum series for a given subset of eigenelements by minimizing the following expression:

$$H_\Psi(y) = \sum_{i=1}^{N-M+1}\sum_{j=1}^{M}\left(y_{i+j} - \sum_{k\in\Psi} a_i^k E_j^k\right)^2, \quad \text{(A7)}$$

where y is the desired series, and Ψ is the subset of eigenelements. The solution is given by:

$$(R_\Psi x)_i = \frac{1}{M}\sum_{j=1}^{M}\sum_{k\in\Psi} a_{i-j+1}^k E_j^k \quad \text{for } M \le i \le N-M+1, \quad \text{(A8a)}$$

$$(R_\Psi x)_i = \frac{1}{i}\sum_{j=1}^{i}\sum_{k\in\Psi} a_{i-j+1}^k E_j^k \quad \text{for } 1 \le i \le M-1, \quad \text{(A8b)}$$

$$(R_\Psi x)_i = \frac{1}{N-i+1}\sum_{j=i-N+M}^{M}\sum_{k\in\Psi} a_{i-j+1}^k E_j^k \quad \text{for } N-M+2 \le i \le N. \quad \text{(A8c)}$$

If Ψ contains a single index k, the resulting series is the *k-th reconstructed component* (RC) x^k. The RCs are additive, so the series x can be *uniquely* expanded as the sum of its RCs:

$$x = \sum_{k=1}^{M} x^k. \quad \text{(A9)}$$

The RCs are then analyzed individually in terms of their magnitudes, trends, oscillatory behaviour and/or spells of chaotic behaviour with traditional signal processing tools. This process is the core of the SSA analysis. Usually, the whole useful information is contained in a few most significant RCs associated with the largest eigenvalues λ_k. They can be correlated, so the structure of correlations between the key RCs is frequently analyzed.

References

Bodge, K., 1992. Representing equilibrium beach profiles with an exponential expression. J. Coast. Res. 8 (1), 47–55.

Bruun, P., 1954. Coastal Erosion and Development of Beach Profiles. Tech. Memo. (Beach Erosion Board) No. 44, Washington, 1–79.

Coastal Engineering Manual (CEM) III-3, 2008. US Army Corps of Engineers, http://www.publications.usace.army.mil/Portals/76/Publications/EngineerManuals/EM_1110-2-1100_Part-03.pdf?ver=2014-03-10-134006-163.

Coastal Engineering Manual (CEM) V-4, 2008. US Army Corps of Engineers, http://www.publications.usace.army.mil/Portals/

76/Publications/EngineerManuals/EM_1110-2-1100_Part-05.pdf?ver=2014-03-10-135016-380.

Dean, R.G., 1976. Beach erosion: causes, processes and remedial measures. CRC Crit. Rev. Environ. Control 6 (3), 259—296.

Dean, R.G., 1987. Coastal sediment processes: toward engineering solutions. In: Proc. Coastal Sediments '87 Conf., American Soc. Civil Eng., New Orleans, LA, 1. 1—24.

Hallermeier, R.J., 1981. A profile zonation for seasonal sand beaches from wave climate. Coast. Eng. 4, 253—277, http://dx.doi.org/10.1016/0378-3839(80)90022-8.

Hallermeier, R.J., 1983. Sand transport limits in coastal structure design. In: Proc. Coastal Structures '83 Conf., American Soc. Civil Eng. 703—716.

Hanson, H., Kraus, N., 1989. GENESIS, Generalized model for simulating shoreline change. In: Technical Rep. CERC 89-19, Washington, USA, 1—185.

Holman, R.A., Lalejini, D.M., Edwards, K., Veeramony, J., 2014. A parametric model for barred equilibrium beach profiles. Coast. Eng. 90, 85—94, http://dx.doi.org/10.1016/j.coastaleng.2014.03.005.

Inman, D.L., Elwany, M.H.S., Jenkins, S.A., 1993. Shorerise and bar-berm profiles on ocean beaches. J. Geophys. Res. 98 (C 10), 18181—18199.

Komar, P.D., McDougal, W.G., 1994. The analysis of exponential beach profiles. J. Coast. Res. 10 (1), 59—69.

Kriebel, D., Kraus, N.C., Larson, M., 1991. Engineering methods for predicting beach profile response. In: Proc. Coastal Sediments '91 Conf., ASCE, Seattle, 557—571.

Larson, M., Kraus, N.C., 1989. SBEACH: numerical model to simulate storm-induced beach change. Tech. Re CERC-899, 115 pp.

Moore, B.D., 1982. Beach Profile Evolution in Response to Changes in Water Level and Wave Height. University of Delaware, Newark, USA, (MSc Thesis).

Özkan-Haller, H.T., Brundidge, S., 2007. Equilibrium beach profile concept for Delaware Beaches. J. Waterw. Port C Div. 133 (2), 147—160, http://dx.doi.org/10.1061/(ASCE)0733-950X.

Pruszak, Z., 1993. The analysis of beach profile changes using Dean's method and empirical orthogonal functions. Coast. Eng. 19 (3—4), 245—261.

Różyński, G., Larson, M., Pruszak, Z., 2001. Forced and self-organized shoreline response for a beach in the southern baltic sea determined through singular spectrum analysis. Coast. Eng. 43 (1), 41—58.

Różyński, G., Lin, J.G., 2015. Data-driven and theoretical beach equilibrium profiles: implications and consequences. J. Waterw. Port C Div. 141 (5), 04015002, http://dx.doi.org/10.1061/(ASCE)WW.1943-5460.0000304.

Oceanologia (2018) 60, 513—526

Available online at www.sciencedirect.com

ScienceDirect

journal homepage: www.journals.elsevier.com/oceanologia/

ORIGINAL RESEARCH ARTICLE

Ecological assessment of heavy metals in the grey mangrove (*Avicennia marina*) and associated sediments along the Red Sea coast of Saudi Arabia

Dhafer A. Alzahrani [a], **El-Metwally M. Selim** [b], **Mohsen M. El-Sherbiny** [c,d,*]

[a] *Department of Biological Sciences, Faculty of Science, King Abdulaziz University, Jeddah, Saudi Arabia*
[b] *Department of Soil Sciences, Faculty of Agriculture, Damietta University, Damietta, Egypt*
[c] *Marine Biology Department, Faculty of Marine Sciences, King Abdulaziz University, Jeddah, Saudi Arabia*
[d] *Marine Biology Department, Faculty of Science, Suez Canal University, Ismailia, Egypt*

Received 6 September 2017; accepted 12 April 2018
Available online 30 April 2018

KEYWORDS
Mangrove;
Avicennia marina;
Heavy metals;
Pollution indices;
Sediment quality;
Red Sea

Summary Mangroves play an integral role as a metal accumulator in tropical and subtropical marine ecosystems. Twenty-one sets of sediment samples and portions of mangroves were collected along the Saudi Arabian coast of the Red Sea to assess the accumulation and ecological risks of heavy metals. Results showed that the following mean concentrations of heavy metals in sediments: Cr ($46.14\ \mu g\ g^{-1} \pm 18.48$) > Cu ($22.87\ \mu g\ g^{-1} \pm 13.60$) > Ni ($21.11\ \mu g\ g^{-1} \pm 3.2$) > Pb ($3.82\ \mu g\ g^{-1} \pm 2.46$) > Cd ($0.75\ \mu g\ g^{-1} \pm 0.87$). The maximum concentrations of the studied metals were above the threshold effect level, indicating a limited impact on the respective ecosystems. The maximum concentration of Cd exceeded its toxic effect threshold, revealing a harmful risk to biota in the sediments. Based on metallo-phytoremedation, biological concentration factors were >1, suggesting that *Avicennia marina* can accumulate heavy metals, especially Cr and Pb. The translocation factor was above the known worldwide average. The geo-accumulation index revealed that sediments in mangrove areas ranged from moderately to heavily contaminated with Cd at Al-Haridhah and moderately contaminated at South Jeddah, Rabigh, Duba, and the wastewater treatment station near Jazan. The ecological risk index revealed that Cd could pose a relatively very high risk to the mangrove ecosystem. The present study emphasized the possibility of establishing a framework for the management of the coastal aquatic ecosystems along the Red Sea coast of Saudi Arabia.

* Corresponding author at: Marine Biology Department, Faculty of Marine Sciences, King Abdulaziz University, Abdalla Al-Sulayman Street, Jeddah 21589, Saudi Arabia. Fax: +966-012-6401747.
E-mail address: ooomar@kau.edu.sa (M.M. El-Sherbiny).
Peer review under the responsibility of Institute of Oceanology of the Polish Academy of Sciences.

https://doi.org/10.1016/j.oceano.2018.04.002

1. Introduction

Human activities such as transportation, construction and manufacturing not only diminish natural resources but also create large quantities of waste materials that cause soil, water and air pollution. These waste further results in global warming, acid rain and ocean contamination (Saenger et al., 1983). Mangrove ecosystems are highly influenced by anthropogenic activities including urbanization, pollutants from urban runoff, oil spills, industrial wastes, harmful waste disposal and wastewater treatment plants and are highly susceptible to the accumulation of heavy metals from all of these sources (Bodin et al., 2013; Marchand et al., 2006). Throughout tropical and subtropical tidal marshes, mangrove ecosystems are located mainly in intertidal and subtidal estuarine wetlands (Lee et al., 2014; Qiu et al., 2011; Wang et al., 2013). These regions are further characterized by mangrove plants, including shrubs and trees (monocots and dicots), that provide unique ecological benefits (Fernández-Cadena et al., 2014; Lewis et al., 2011). Mangrove plants act as a large source of organic carbon for the associated sediments and have a direct impact on the food web of the marine ecosystem (Alongi, 2002; Asaeda and Kalibbala, 2009; Wang and Sousa, 2009). In addition, they provide nursery shelter for many marine organisms (MacFarlane et al., 2007; Walters et al., 2008) and are used by human beings in many ways, such as food, fodder for animals, house construction, fishing boat construction and warming/cooking of food (FAO, 2007; PERSGA, 2004). Mangrove plants further represent a refuge for many migratory birds (Abohassan et al., 2012; Kumar et al., 2010).

Generally, mangroves are known to adapt well to different environmental conditions such as low oxygenated sediments, intermittent flooding, sustaining osmotic balance and metal pollutants (Buajan and Pumijumnong, 2010; Greger, 2004; Li et al., 2016; MacFarlane et al., 2007). Several studies have been carried out on heavy metal pollution within mangrove environments worldwide (e.g., Bodin et al., 2013; Defew et al., 2005; Fernandes et al., 2012; Fernández-Cadena et al., 2014; Li et al., 2016; Usman et al., 2013). These studies have proven the capability of mangroves to eliminate or control the absorption of various heavy metals next to the root media and transport them to the shoot (MacFarlane et al., 2003). Heavy metals are considered to be hazardous pollutants when they have a specific density greater than 5 g cm^{-3}, and they may change the structure of the environment and living organisms (Järup, 2003; Yan et al., 2017). High concentrations of heavy metals in sediments can also result in reduced density and diversity of organisms by affecting the balance of the food chain. They can also alter survival, metabolism, growth and reproduction of organisms (Wright and Welbourn, 2002). Numerous studies have pointed out that metal pollutants (Pb, Mn, Cu, Zn, Fe and Cd) accumulate mainly in the root tissue as compared to the shoots in various mangrove taxa such as *Rhizophora* spp., *Avicennia* spp. and *Kandelia* spp. (Chiu et al., 1995; MacFarlane and Burchett, 2002; Peters et al., 1997; Tam and Wong, 2000; Thomas and Fernandez, 1997). Globally, many indices can be used to assess the status of heavy metals in the surrounding environment and their potential risks. These indices include contamination factor (CF), pollution load index (PLI), potential ecological risk, ecological risk index (E_r^i) and geo-accumulation index (I_{geo}) (Li et al., 2016; Nath et al., 2014; Sakan et al., 2015; Sekabira et al., 2010; Udechukwu et al., 2015).

As a part of urbanization, the Red Sea coast is continuously subjected to changes that result in the loss of many intertidal and near shore subtidal habitats (Chiffings, 1989). Petrochemical industries and the associated ship traffic can also cause pollution in coastal water bodies of the Red Sea (Badr et al., 2009; Fahmy and Saad, 1996). However, it has also been reported that mangrove plants in the Red Sea environment of Saudi Arabia are exposed to severe growth conditions such as extreme salinity, low soil fertility and poor textures (Mandura et al., 1988) as well as anthropogenic activities that contribute various pollutants, particularly trace elements (Badr et al., 2009). Current information about the interactions between heavy metals in the sediments and mangrove plants is inadequate, especially as pertains to the Red Sea coastal area of Saudi Arabia (Badr et al., 2009; Usman et al., 2013). Accordingly, this work was designed to assess the status of heavy metals and their potential risk to the grey mangrove, *Avicennia marina* (Forsk.) Vierh, and associated sediments along the Red Sea coast of Saudi Arabia.

2. Material and methods

2.1. Study area

The length of the Saudi Arabian coastline is approximately 1840 km, which comprises 79% of the eastern Red Sea coastline (MEPA/IUCN, 1987). The present study area extended along the entire Saudi Arabian coast of the Red Sea (between 36°10′–42°20′E, 16°30′–25°30′N). The study was conducted during February–March 2014. Sediment and mangrove samples (aerial roots and leaves) were collected from twenty-one mangrove stands distributed along the coastlines of several cities (Fig. 1 and Table 1). These stations, arranged from south to north, are as follows: Jazan (5 stations), Sabya (1 station), Wadi Baish (1 station), Al-Haridhah (1 station), Al-Qahma (1 station), Al-Birk (1 station), Al-Shaqqah (1 station), Al-Lith (2 stations), Jeddah (3 stations), Rabigh (3 stations), Al-Wajh (1 station) and Duba (1 station). The Jazan region comprised a total of 5 stations in which JI was characterized by the presence of dead mangrove trees, JII lies near a fish farm effluent, JIII was located in front of a sewage water treatment plant, JIV was 2 km away from a sewage treatment plant, and JV was situated near a shelter area for fishing boats. Stations such as Sabya (VI), Wadi Baish (VII), Al-Haridhah (VIII), Al-Qahma (IX), Al-Birk (X), Al-Shaqqah (XI) and Al-Lith (XII) represented the typical type of mangrove stands (back reef) located at the end of wadis. The Al-Haridhah station (VIII) was located near a fish farm effluent. Of the three stations studied in the Jeddah region, one station (XV) was located near the effluent of a municipal sewage treatment plant. The Rabigh area contained two stations (one located at the end of the Al-Kharrar lagoon and the other in the central part of the lagoon), while Al-Wajh and Duba consisted of one station each that can be considered as unaffected by human interference.

2.2. Physico-chemical properties and heavy metals determination in sediments

Composite surface sediment (0–10 cm) samples were randomly collected from all the studied stations from

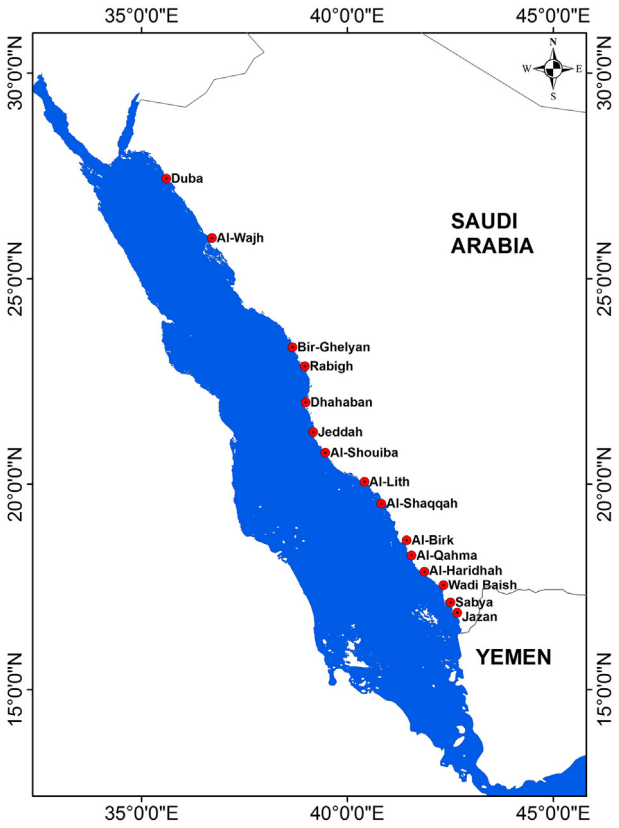

Figure 1 Sampling stations along the Saudi Arabian coast of the Red Sea.

underneath/or adjacent to the mangrove trees. All the sediment samples were dried at 50 ± 5°C, sieved through a 63 μm stainless steel sieve and stored for subsequent analysis. To determine the physico-chemical properties of the sediments, particle size distributions were examined using the pipette method as described by Dewis and Fertias (1970). Total carbonates were estimated gasometrically using a Collins calcimeter and calculated following Hesse (1971). Total soluble salts were determined by measuring electrical conductivity (dS m^{-1}) in 1:3 soil:water extract and soil pH (in saturated soil paste), while total organic matter (TOM) was measured according to Walkley and Black (1934). The concentrations of Cr, Cu, Ni, Pb and Cd were measured according to the direct aqua regia method. A total of 1000 mg of normalized sediment sample was weighed and digested using a 4:1 mix of nitric acid (HNO_3 AnalaR grade, BDH 69%) and perchloric acid ($HClO_4$, AnalaR grade 60%) (Yap et al., 2002). The digested samples were then filtered and diluted with deionized water to a total volume of 50 ml and kept for further analysis. The total content of Cr, Cu, Ni, Pb and Cd in the sediment samples were analysed using ICP-OES.

2.3. Sediment quality guidelines

In this study, sediment quality guidelines (SQGs) were applied as described by Bakan and Özkoç (2007), Luo et al. (2010) and MacDonald et al. (2000). These guidelines include the lowest effect level (LEL), threshold effect level (TEL), probable effect level (PEL), effect range low (ERL), probable effect

Table 1 Coordinates of the studied mangrove stations along the Saudi Arabian coast of the Red Sea.

Station name	Station no.	Latitude	Longitude
Jazan	JI	16°41′38.18″N	42°43′3.57″E
	JII	16°43′50.49″N	42°42′22.91″E
	JIII	16°47′5.84″N	42°40′22.43″E
	JIV	16°46′32.57″N	42°40′24.37″E
	JV	16°49′39.37″N	42°36′36.09″E
Sabya	VI	17°3′3.74″N	42°27′8.99″E
Wadi Baish	VII	17°10′43.76″N	42°21′57.12″E
Al-Haridhah	VIII	17°48′4.32″N	41°53′21.38″E
Al-Qahma	IX	17°57′13.99″N	41°41′2.28″E
Al-Birk	X	18°7′11.99″N	41°34′51.97″E
Al-Shaqqah	XI	19°47′32.84″N	40°37′50.29″E
Al-Lith			
Al-Lith 1	XII	20°3′11.06″N	40°25′0.06″E
Al-Lith 2	XIII	20°32′49.87″N	39°36′40.36″E
Jeddah			
Al-Shouiba	XIV	20°45′46.94″N	39°27′59.26″E
South Jeddah	XV	21°16′8.27″N	39°7′33.13″E
Dhahaban	XVI	21°59′24.84″N	38°59′15.84″E
Rabigh			
Rabigh I	XVII	22°51′50.75″N	38°58′12.43″E
Rabigh II	XVIII	22°54′7.61″N	38°55′13.38″E
Bir-Ghelyan	XIX	23°19′45.49″N	38°41′15.70″E
Al-Wajh	XX	25°59′27.67″N	36°42′39.29″E
Duba	XXI	27°25′52.30″N	35°36′9.54″E

level (PEL), effect range median (ERM), severe effect level (SEL), and toxic effect threshold (TET).

2.4. Heavy metals determination in leaves and pneumatophores (aerial roots) of mangroves

Leaves of *A. marina* were collected from 5 to 10 trees of similar health status (>3 m in height and >20 cm in diameter at breast height) from the studied stations. Three leaves of the second whorl from each tree were collected from each of three facing branches at 1 m in height. In addition, aerial roots were sampled from what were considered to be nutritive roots for absorption; larger anchoring roots were avoided. The samples (leaves and aerial roots) were washed several times with distilled water to remove the adhering fine sediments and homogenized after drying at 60°C. One gram (with three replicates) of the ground leaf material was placed into 125 ml digestion tubes. Five ml of concentrated perchlorate acid was added to each tube in a block digester, then heated for 3 h at 120°C, and finally diluted to a final volume of 50 ml upon analysis (Cottenie et al., 1982). Heavy metal (Cr, Cu, Ni, Pb and Cd) concentrations, as $\mu g\ g^{-1}$, were determined using an Inductively Coupled Plasma Optical Emission Spectrometer (Optima 5300 DV with an autosampler Model AS 93 Plus/S10, Perkin Elmer, USA). Standards were prepared to detect the concentrations of the digested samples. To ensure the accuracy of the analysis, a certified reference material from the National Institute of Standards and Technology Standard (CRM 1570) was used. The certified reference material was analysed (in triplicate) with the measured samples for quality control of the analytical procedures. The results showed that all of the heavy metals were analysed with a 99.5% recovery rate.

2.5. Biological concentration (BCF) and translocation factors (TFs)

In the present study, three relative measures of metal uptake were used to differentiate the uptake of each heavy metal. The biological concentration factor (BCF) of aerial roots and leaves was calculated to evaluate the sensitivity of different tissue types under varying environmental loadings. In addition, the translocation factor (TF) was calculated as the ratio between the concentrations of heavy metals in the leaves and the aerial roots. This parameter indicates the ability to transport heavy metals from the roots to the leaves. BCF and TF values for aerial roots and leaves were expressed as original data averages. For the heavy metals (Cr, Cu, Ni, Pb and Cd), the bio-concentration factors were calculated based on the equation described by Cui et al. (2007) and Yoon et al. (2006):

$$\mathrm{BCF_{leaf}} = \frac{C_{\mathrm{leaf}}}{C_{\mathrm{sediment}}}, \quad \mathrm{BCF_{root}} = \frac{C_{\mathrm{root}}}{C_{\mathrm{sediment}}}, \tag{1}$$

where C_{leaf} and C_{root} are the heavy metal concentrations in the leaf and aerial root, respectively, and C_{sediment} is the heavy metal concentration in the sediment. The translocation factor (TF) was calculated using the following equation:

$$\mathrm{TF_{leaf}} = \frac{C_{\mathrm{leaf}}}{C_{\mathrm{root}}}, \tag{2}$$

where C_{leaf} and C_{root} are the heavy metal concentrations in the leaves and roots, respectively.

2.6. Risk assessment model

For environmental pollution assessment, the geochemical and physiochemical characteristics of sediments are very crucial to identify the contamination sources. Geo-accumulation index (I_{geo}) was calculated to assess the changes of heavy metal concentrations by associating the heavy metal concentrations in aquatic sediments with the geochemical background. It is calculated according to Müller (1969) based on the following equation:

$$I_{geo} = \log_2\left(\frac{C_n}{1.5B_n}\right), \tag{3}$$

where C_n is the concentration of metal measured in mangrove sedimentary and B_n is the geochemical background value in the earth's crust (Taylor and McLennan, 1985). A constant of 1.5 was applied to account for the potential variability in the reference value due to the influence of lithogenic processes. In this regard, seven classes of I_{geo} were categorized as follows: uncontaminated (UC) when $I_{geo} \leq 0$; uncontaminated to moderately contaminated (UMC) when $0 < I_{geo} < 1$; moderately contaminated (MC) when $1 < I_{geo} < 2$; moderately to heavily contaminated (MHC) when $2 < I_{geo} < 3$; heavily contaminated (HC) when $3 < I_{geo} < 4$; heavily to extremely contaminated (HEC) when $4 < I_{geo} < 5$; and extremely contaminated (EC) when $5 < I_{geo}$. The probable ecological risk coefficient (E_r^i) was calculated using the formula by Hakanson (1980) as follows:

$$E_r^i = T_r^i * C_r^i = T_r^i * \frac{C_s^i}{C_n^i}, \tag{4}$$

where T_r^i values for measured heavy metals are as follows: Cr = 2, Cu = 5, Ni = 5, Pb = 5 and Cd = 30; C_r^i is the contamination factor; C_s^i is the concentration of heavy metals in the sediment; C_n^i a background value for heavy metals and T_r^i is the metal toxic response factor. The degree of E_r^i can be categorized as follows: if $E_r^i < 40$: low risk (LR), $40 \leq E_r^i < 80$: moderate risk (MR), $80 \leq E_r^i < 160$, considerable risk (CR), $160 \leq E_r^i < 320$: high-risk (HR) and $E_r^i \leq 320$: very high risk (VHR).

2.7. Statistical analysis

Descriptive statistics for each of the studied heavy metals in sediments were obtained using the Statistical Package for the Social Sciences (SPSS) (version 23.0). The possible relationship between measured heavy metals and the other physico-chemical properties was determined by calculating Pearson's correlation coefficient (r). A principal component analysis (PCA) was performed on the logarithmic transformed data using factor extraction. The Eigenvalue remained greater than 1 after varimax rotation.

Table 2 Physico-chemical properties of the investigated mangrove sediments along the Saudi Arabian coast of the Red Sea (EC = electrical conductivity, %$CaCO_3$ = percent of calcium carbonate, %OM = percent of organic matter).

Characters	Range	Mean	Std. error	Std. deviation	Variance	Skewness	Kurtosis
Sand%	90.0–99.8	96.56	0.60	2.75	7.55	−1.07	0.28
Mud%	0.2–10.0	3.45	0.56	2.74	7.56	1.06	0.26
Soil pH	4.3–8.1	7.45	0.18	0.84	0.71	−2.94	10.27
EC [dS m^{-1}]	2.3–37.5	12.47	2.01	9.20	84.58	1.50	1.62
%$CaCO_3$	1.3–71.4	14.83	3.99	18.26	333.48	1.89	3.67
%OM	0.3–5.0	2.54	0.31	1.44	2.08	0.21	−0.96

3. Results and discussions

3.1. Sediment characteristics and quality

The properties of the studied sediment samples (conductivity, acidity and organic matter content) are presented in Table 2. Based on the grain size analysis, the results revealed that sand is the highly dominant fraction at all of the study stations (90% to 99.8%). According to the soil texture of the studied stations, which was predominantly sandy, the soils were then classified as "sandy, siliceous, hyperthermic, and *aquic Torripsamments*". Soil pH values fluctuated within a wide range, from 4.28 at JII and 8.08 at Al-Wajh area (XX), with a mean value of 7.45. The lower pH values were observed at the same stations that displayed higher concentrations of organic matter. Electrical conductivity (EC) ranged from 2.31 to 37.50 dS m^{-1} at Rabigh 1 (XVII) and JI, respectively (average: 12.47 dS m^{-1}). This high variation can be explained by the fact that Red Sea mangroves usually grow in coastal areas that receive seasonal floods, which in turn reduce the salinity of those regions (Usman et al., 2013). The higher salt concentrations observed at station JI can also be due to the construction of a road, which eventually separated the mangrove swamp from the sea. This unexpected increase in salt concentration can adversely affect the growth of mangrove trees, which further leads to their death and decay (Lambs et al., 2015). Calcium carbonate concentration in sediment samples varied from 1.30% to 71.40%, with a mean value of 14.83%. Organic matter content was relatively low and ranged from 0.27% to 5.00% (average: 2.54%). The highest values of 5.00%, 4.46%, 4.46% and 4.94% were observed at stations JI, JII, JIV and XIX, respectively. This can be mainly due to the accumulation of mangrove litter in the associated sediments at these stations. This phenomenon can be further connected to the higher salinities observed at these stations, which, as mentioned above, will reduce the growth of the mangrove trees and have an inhibitory effect on the decomposition of organic substances in sediments within the mangrove ecosystem (Van de Broek et al., 2016).

The concentrations of the different heavy metals in the sediment samples varied from 10.19 to 76.79 μg g^{-1} for Cr, from 3.27 to 51.46 μg g^{-1} for Cu, from 7.00 to 59.19 μg g^{-1} for Ni, from 0.80 to 10.07 μg g^{-1} for Pb and from 0.10 to 3.10 μg g^{-1} for Cd (Table 3). These heavy metals are arranged as following order according to their mean value and standard deviation: Cr (46.14 μg g^{-1} ± 18.48) > Cu (22.87 μg g^{-1} ± 13.60) > Ni (21.11 μg g^{-1} ± 3.2) > Pb (3.82 μg g^{-1} ± 2.46) > Cd (0.75 μg g^{-1} ± 0.86). The highest value of Cr (76.79 μg g^{-1}) was observed at station XVI. The highest concentrations of Cu and Ni were detected at stations JII, XVI and XVII, and the highest value of Pb (10.07 μg g^{-1}) was recorded at station XIX. The concentrations of Cd were relatively high at stations III, IV, XIV, XVI and XVII, with the maximum value (3.10 μg g^{-1}) observed at station IV. Interestingly, the highest concentrations of most of the heavy metals were observed at stations that were positioned near various anthropogenic influences, such as sewage effluents, refineries, aquaculture facilities and commercial ports. These findings are in agreement with those reported by Badr et al. (2009), who emphasized that the upper 15 cm of sediments contained higher concentrations of pollutants (Cr, Ni, Mn and Zn) along the Red Sea coastal areas of Saudi Arabia. The average concentration of Cu was 22.87 μg g^{-1} and is lower than the values obtained from previous studies in the Red Sea area, except for the Farasan Island region (Table 3). We assume that the major reason for this difference is the presence of many fishing boats that use antifouling paints containing $CuSO_4$ as a major ingredient, as proposed by Usman et al. (2013). The mean concentration of Ni (21.11 μg g^{-1}) was lower than its value in previous studies in the Red Sea except for Farasan Island (Saudi Arabia) and the Yemeni coast (Table 3). Moreover, the mean concentration of Pb was higher than recorded by Abohassan (2013) at both the Al-Shouiba and Yanbou sites (Table 3). Except for Jeddah and Rabigh, the mean concentration of Cd was typically higher in the current study than values recorded in previous studies carried out along the Red Sea (Table 3). From a global perspective, many investigators have discussed the possibility of anthropogenic influences being responsible for the increase of heavy metals in mangrove sediments (e.g., Cuong et al., 2005; Defew et al., 2005; El-Said and Youssef, 2013; Harikumar and Jisha, 2010; Li et al., 2016; Qiu et al., 2011; Tam and Wong, 2000). Both the maximum (3.10 μg g^{-1}) and the average (0.75 μg g^{-1}) concentrations of Cd in the investigated area surpassed the averages in shale around the world (Turekian and Wedepohl, 1961). The maximum concentration observed for Cu (51.46 μg g^{-1}) was also above the world average concentration in shale (45 μg g^{-1}) and is comparable to the findings of Lindsay (1979). The results of this study revealed that the maximum concentrations of Cu, Ni, Pb and Cd exceeded the minimum and average of the common ranges (30, 40, 10 and 0.10 μg g^{-1} respectively). This indicates the possible lithogenic origin of all of these heavy metals (Cu, Ni, Pb and Cd). It is known that heavy metals can be introduced into coastal environments from different sources, including natural weathering processes and anthropogenic activities (Badr

Table 3 Comparison of total heavy metals [$\mu g\ g^{-1}$] in mangrove sediment at different stations along the coastal areas from Saudi Arabia and around the world.

Locations	Cr	Cu	Ni	Pb	Cd	References
Minimum (Min.)	10.19	3.27	7.00	0.80	0.10	
Maximum (Max.)	76.79	51.46	59.19	10.07	3.10	
Average	46.11	22.87	21.11	3.82	0.75	Current study
Std. deviation (SD)	18.48	13.60	13.85	2.46	0.86	
Average shale	90	45	68	20	0.30	Turekian and Wedepohl (1961)
Common range						
Max.	1000	100	500	200	0.70	
Min.	1	2	5	2	0.01	Lindsay (1979)
Av.	100	30	40	10	0.06	
The coastal areas of Red Sea						
Saudi Arabia						
Farasan Island	9.6	112.0	8.50	45.2	1.23	Usman et al. (2013)
Al-Shouiba	8.8	4.10	27.40	0.5	0.02	Abohassan (2013)
Yanbou	11.5	13.90	–	3.8	0.20	Abohassan (2013)
Jeddah	17.9	20.60	76.60	89.5	4.84	Badr et al. (2009)
Rabigh	19.4	21.30	80.10	87.2	3.51	Badr et al. (2009)
Egypt	ND	108	22	25	1.8	El-Said and Youssef (2013)
Yemen	20.2	32.10	12.00	6.90	–	Hassan and Nadia (2000)
Around the world						
Kottuli, India	ND–0.71	0.8–224	0.03–1.9	2.3–23.6	ND–0.08	Harikumar and Jisha (2010)
Punta Portete, Costa Rica	22.60	8.40	102.00	34.50	7.30	Guzmán and Jiménez (1992)
Queensland, Australia	72.00	1–12	9.00	36.0	0.60	Preda and Cox (2002)
Mai Po, Hong Kong	39.20	78.50	–	79.2	2.62	Tam and Wong (2000)
Guanabara Bay, Brazil	42.40	98.60	–	160.8	1.32	Kehrig et al. (2003)
Punta Mala Bay, Panama	23.30	56.30	27.3	78.2	<10	Defew et al. (2005)
Shenzhen Bay, China	75.70	79.72	40.40	–	0.83	Li et al. (2016)
South Port Klang, Malaysia	60.19	24.89	13.9	96.02	1.46	Udechukwu et al. (2015)
Threshold effect concentration (TEC) SQGs						
Threshold effect level (TEL)	26	16	16	31	0.596	
Lowest effect level (LEL)	37.3	35.7	18	35	0.6	MacDonald et al. (2000)
Effect range low (ERL)	80	70	30	35	5	
Canadian sediment quality guidelines (TEL)	–	18.7	–	30.2	0.7	Canadian Council of Ministers of Environment (2002)
Probable effect concentration (PEC) SQGs						
Probable effect level (PEL)	90	149	36	91.3	3.53	
Severe effect level (SEL)	110	110	75	250	10	
Toxic effect threshold (TET)	100	86	61	170	3	MacDonald et al. (2000)
Effective range median (ERM)	145	390	50	110	9	
Canadian sediment quality guidelines (PEL)	–	108	–	112	112	Canadian Council of Ministers of Environment (2002)

et al., 2009; Sadiq and Zaidi, 1994). Several previous studies have recorded high concentrations of heavy metals in mangrove sediments and have concluded that anthropogenic activities are a long-term pollution source (e.g., Defew et al., 2005; Tam and Wong, 2000). This study revealed that the measured concentrations of Cd, Cr, Cu, Ni and Pb were above the optimum levels in some of the mangrove sediments from the Red Sea as well as other mangrove ecosystems worldwide (Table 3). The average concentration of Cr was also higher than the average concentrations within the Red Sea coastal area but was lower than other studies, especially in China and Australia (Li et al., 2016; Udechukwu et al., 2015).

3.2. Sediment quality guidelines (SQGs)

In terms of TEC, the results obtained here revealed that the maximum concentrations of Cr and Cu were 76.79 and 51.46 $\mu g\ g^{-1}$, respectively. These values were higher than the LEL, but below the TEL and the ERL, as illustrated in Table 3. The maximum concentration of Ni (59.19 $\mu g\ g^{-1}$) was above the TEC, EL, TEL and ERL. On the other hand, the maximum concentration of Pb (10.07 $\mu g\ g^{-1}$) was below the LEL, TEL and ERL. The maximum concentration of Cd (3.10 $\mu g\ g^{-1}$) exceeded its LEL and TEL limits, revealing its extreme impact on different biological processes (MacDonald et al., 2000). Regarding the PEL, the maximum

Table 4 Average concentrations of measured heavy metals [μg g^{-1} dw] in mangrove tissue along Saudi Arabian coast of the Red Sea and around the world.

Locations	Tissue type	Cr	Cu	Ni	Pb	Cd	References
Saudi Arabian coastal areas, Red Sea	Leaves	14.96	13.24	7.56	3.79	0.18	Current study
	Pneumatophores	17.46	9.82	7.58	3.67	0.07	
Excessive or toxic levels		5–30	20–100	10–100	30–300	5–30	Kabata-Pendias and Pendias (1992)
Farasan Island, Saudi Arabia	Leaves	9.30	356.6	2.30	–	1.04	Usman et al. (2013)
	Pneumatophores	14.9	270.5	4.02	–	NC	
Al-Shouiba, Saudi Arabia	Leaves	4.53	4.17	6.70	0.57	0.01	Abohassan (2013)
	Pneumatophores	4.35	3.37	4.07	–	0.33	
Yanbou, Saudi Arabia	Leaves	2.37	6.38	21.10	–	–	Abohassan (2013)
	Pneumatophores	11.94	6.79	3.64	0.46	0.32	
Around the world							
Shenzhen, China	Leaves	–	5.20	–	1.90	–	Li et al. (2016)
	Pneumatophores	–	13.00	–	3.50	–	
Punta Mala Bay, Panama	Leaves	–	3.70	–	6.20	–	Guzmán and Jiménez (1992)
	Pneumatophores	–	–	–	–	–	
FAO (2007)	Leaves	5.00	40.00	1.50	5.00	0.20	FAO (2007)
	Pneumatophores	–	–	–	–	–	
Sydney Estuary, Australia	Leaves	–	–	–	–	–	Nath et al. (2014)
	Pneumatophores	1.40	20.00	2.00	5.80	0.60	
Port Jackson, Australia	Leaves	–	3.2	–	1.7	–	MacFarlane and Burchett (2002)
	Pneumatophores	–	–	–	–	–	

concentration of Ni (59.19 μg g^{-1}) was above the PEL and ERM levels, but it was below the SEL and TEL. This can be considered as an occasional threat to benthic organisms (MacDonald et al., 2000). In the case of Cr, Cu and Pb, their maximum concentrations were lower than the PEL, ERM, SEL and TET, which in turn reveals an adverse biological impact. The maximum concentration of Cd also exceeded its TET and can be considered as harmful to benthic organisms (MacDonald et al., 2000; Vane et al., 2009). By comparing the mean concentrations of Cu, Cd, and Pb with those of Canadian sediment quality guidelines, it was observed that the concentrations of Cu and Cd were above the TEL. This indicates that adverse biological effects may occur frequently (Canadian Council of Ministers of the Environment, 2002). On the other hand, the concentrations of Cu, Pb and Cd were below the PEL, which shows that these metals are not known to have any negative impact on living organisms.

3.3. Accumulation of heavy metals in mangrove compartments

The results obtained here indicated wide variations in the content of heavy metals within the leaves and aerial roots of *A. marina*. The concentrations of heavy metals were in the following order: Cr > Cu > Ni > Pb > Cd and are shown in Table 4. The levels of measured heavy metals, especially Cr, in mangrove tissues were considered to be relatively high when compared with respective global concentrations. This may be due to the presence of those metals in higher concentrations in the surrounding sediments. This study showed that the concentrations of Cr in the root tissues of mangrove plants were relatively higher than the concentrations in the leaves. Chromium can be highly toxic to plants, seriously affecting their growth; however, the exact mechanism of Cr translocation in plants remains uncertain (Hajar et al., 2014; Shanker et al., 2005). In the current study, the concentrations of Ni and Pb observed in the leaves were comparable with those observed in the aerial roots of the same mangroves. Generally, most of the absorbed trace elements are restricted to the outer cortex of the root (MacFarlane et al., 2003; Peng et al., 1997). The present study clearly showed that the concentrations of most accumulated heavy metals in mangrove tissues were higher than their respective concentrations in mangroves worldwide (Guzmán and Jiménez, 1992; Li et al., 2016; MacFarlane and Burchett, 2002; MacFarlane et al., 2003; Peng et al., 1997; Qiu et al., 2011; Usman et al., 2013) (Table 4). One of the most important findings of the current study was the higher concentrations of Cr in both the leaves and aerial roots of *A. marina*, which were considerably above toxic levels (Kabata-Pendias and Pendias, 1992). Moreover, it was also clear from the present study that the accumulation of Cr in the sediments was higher than that in the aerial roots and leaves (Fig. 2), which further indicates the passive absorption of Cr by *A. marina* compared to the other heavy metals. Except for Pb and Cd, the present study found much

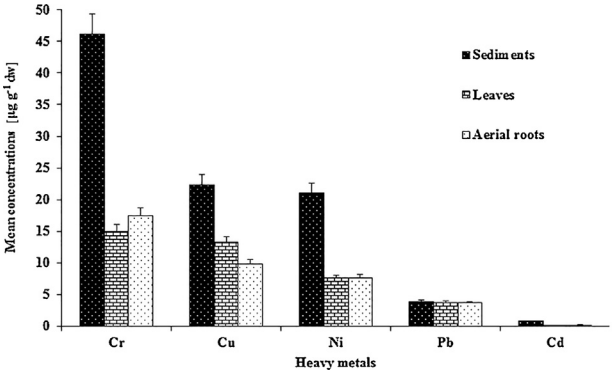

Figure 2 Average concentrations (± standard error) of heavy metals in sediment, mangrove leaves and aerial roots.

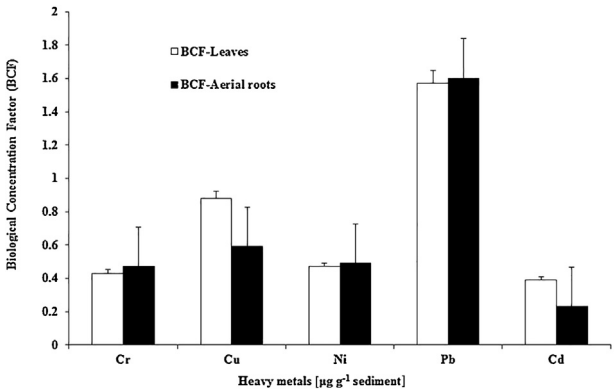

Figure 3 Average of biological concentration factors (± standard error) of heavy metals in mangrove leaves and aerial roots.

higher values for the other heavy metal concentrations in the sediments than in the aerial roots and leaves of *A. marina*.

3.4. Biological concentration factors (BCFs) and translocation factors (TFs)

The mean BCFs values obtained for Cr, Cu, Ni, Pb and Cd in the mangrove leaves were 0.43, 0.88, 0.47, 1.57 and 0.39, respectively (Table 5). Moreover, the mean BCFs values in aerial roots were 0.47 for Cr, 0.59 for Cu, 0.49 for Ni, 1.60 for Pb and 0.23 for Cd. In general, the highest BCF average among the different investigated stations was obtained for Pb in both the leaves and aerial roots. This is a clear reflection of the bioavailability of Pb in the sediments as compared to other heavy metals (Fig. 3). The lowest BCF values in the highly contaminated sediments (station XIII) can be due to the low bioavailability of these heavy metals in the respective sediments. This can be explained by the binding of heavy metals to form immovable compounds as a result of chelation with organic molecules (Li et al., 2016; MacFarlane et al., 2003; Nath et al., 2014). Future studies regarding the bioavailable fractions and toxicity of heavy metals should take speciation into consideration (Li et al., 2016; Luo et al., 2017; MacFarlane et al., 2007). Generally, plants with TF values greater than 1 are classified as having a greater potential for metal accumulation in polluted sites (Usman et al., 2012). These plants can effectively translocate metals

Table 5 Comparison between the biological concentrations factors (BCFs), translocation factors (TFs) of heavy metals in the Red Sea coastal areas and around the world.

Locations	Tissue type		Cr	Cu	Ni	Pb	Cd	Reference
Red Sea coastal areas, Saudi Arabia	BCF	Leaves	0.43	0.88	0.47	1.57	0.39	Current study
		Pneumatophores	0.47	0.59	0.49	1.60	0.23	
		TF	0.90	1.74	1.29	1.42	2.72	
Farasan Island, Saudi Arabia	BCF	Leaves	0.23	1.25	1.06	–	1.50	Usman et al. (2013)
		Pneumatophores	4.23	9.08	3.01	0.01	0.03	
		TF	0.42	1.30	0.35	0.00	00	
Al-Shouiba, Saudi Arabia	BCF	Leaves	0.34	1.00	0.46	1.07	0.50	Abohassan (2013)
		Pneumatophores	3.43	9.23	1.21	9.45	16.50	
		TF	0.25	0.10	0.20	0.11	0.03	
Futian Mangrove, South China Sea	BCF	Leaves	–	–	–	–	–	Li et al. (2016)
		Pneumatophores	0.36	0.10	0.27	–	0.06	
		TF	0.22	2.27	0.38	–	0.58	
Shenzen, China	BCF	Leaves	–	0.15	–	0.06	–	Peng et al. (1997)
		Pneumatophores	–	0.37	–	0.10	–	
		TF	–		–	0.54		
Ting Kok, Hong Kong	BCF	Leaves	–	1.26	–	0.24	–	Chen et al. (2003)
		Pneumatophores	–	1.02	–	0.44	–	
		TF	–	1.23	–	0.53		
SE, Australia	BCF	Leaves	–	0.15	–	0.05	–	MacFarlane et al. (2003)
		Pneumatophores	–	1.66	–	1.64	–	
		TF	–	0.09	–	0.03	–	

Table 6 Averages of geo-accumulation index (I_{geo}) and potential ecological risk index (E_r^i) of the measured heavy metals in mangrove sediments for all studied stations.

Stations	Geo-accumulation index (I_{geo})					Potential ecological risk index (E_r^i)				
	Cr	Cu	Ni	Pb	Cd	Cr	Cu	Ni	Pb	Cd
J I	−1.87UC	−1.95UC	−2.68UC	−3.22UC	−0.49UC	0.89/LR	1.94/LR	1.81/LR	0.80/LR	42.67/MR
J II	−1.02UC	−0.46UC	−1.55UC	−1.92UC	0.83UMC	1.48/LR	5.45/LR	3.97/LR	1.98/LR	106.67/CR
J III	−1.04UC	−2.20UC	−2.73UC	−2.58UC	2.55MHC	1.46/LR	1.63/LR	1.74/LR	1.26/LR	352.00/VHR
J IV	−1.77UC	−1.41UC	−2.59UC	−2.16UC	2.78MHC	0.88/LR	2.82/LR	1.93/LR	1.68/LR	413.33/VHR
J V	−2.40UC	−2.98UC	−3.58UC	−3.75UC	−1.17UC	0.57/LR	0.95/LR	0.97/LR	0.56/LR	26.67/LR
Sabya	−1.10UC	−1.34UC	−2.13UC	−2.49UC	−2.17UC	1.40/LR	2.96/LR	2.65/LR	1.34/LR	13.33/LR
Wadi Baish	−2.32UC	−3.07UC	−3.34UC	−3.67UC	−1.79UC	0.60/LR	0.89/LR	1.14/LR	0.59/LR	17.33/LR
Al-Haridhah	−2.30UC	−2.13UC	−3.04UC	−3.91UC	−1.79UC	0.61/LR	1.71/LR	1.41/LR	0.50/LR	17.33/LR
Al-Qahma	−1.12UC	−1.29UC	−2.22UC	−2.78UC	0.00UC	1.38/LR	3.07/LR	2.49/LR	1.09/LR	60.00/MR
Al-Birk	−1.60UC	−1.77UC	−2.08UC	−4.69UC	0.49UMC	0.99/LR	2.20/LR	2.74/LR	0.29/LR	84.00/CR
Al-Shaqqah	−1.23UC	−1.42UC	−2.16UC	−2.33UC	−1.91UC	1.28/LR	2.80/LR	2.59/LR	1.49/LR	16.00/LR
Al-Lith 1	−1.36UC	−1.24UC	−2.19UC	−1.58UC	−2.17UC	1.17/LR	3.18/LR	2.54/LR	2.51/LR	13.33/LR
Al-Lith 2	−2.55UC	−2.77UC	−3.43UC	−4.99UC	0.53UMC	0.51/LR	1.10/LR	1.08/LR	0.24/LR	86.67/CR
Al-Shouiba	−2.01UC	−1.59UC	−2.52UC	−3.20UC	−1.91UC	0.75/LR	2.48/LR	2.02/LR	0.81/LR	16.00/LR
South Jeddah	−1.43UC	−2.68UC	−3.87UC	−4.09UC	1.45MC	1.11/LR	1.17/LR	0.80/LR	0.44/LR	164.00/HR
Dhahaban	−0.81UC	−0.50UC	−0.87UC	−2.43UC	1.64MC	1.71/LR	5.29/LR	6.35/LR	1.39/LR	186.67/HR
Rabigh I	−3.73UC	−4.37UC	−3.59UC	−4.67UC	2.15MHC	0.23/LR	0.36/LR	0.96/LR	0.29/LR	266.67/HR
Rabigh II	−0.86UC	−0.39UC	−0.79UC	−2.64UC	0.32UMC	1.65/LR	5.72/LR	6.73/LR	1.20/LR	74.67/MR
Bir-Ghelyan	−1.94UC	−2.28UC	−2.62UC	−1.34UC	−0.58UC	0.78/LR	1.54/LR	1.89/LR	2.96/LR	40.00/MR
Al-Wajh	−1.21UC	−0.99UC	−2.30UC	−2.88UC	0.83UMC	1.30/LR	3.78/LR	2.36/LR	1.02/LR	40.00/MR
Duba	−1.80UC	−1.70UC	−2.39UC	−2.69UC	−0.49UC	0.86/LR	2.30/LR	2.21/LR	1.16/LR	74.67/MR

from roots to other tissues. The mean values of TF for the studied metals in aerial roots displayed the following order: Cd (2.72) > Cu (1.74) > Ni (1.42) > Pb (1.29) > Cr (0.90) (Table 5). These results indicate that all of the TF means were greater than 1, except in the case of Cr, and further reveal that the mangrove plants can accumulate Cu, Ni, Pb and Cd in considerable amounts. This finding is also supported by the higher concentrations obtained for Cu, Ni, Pb and Cd in the leaves (13.24, 7.56, 3.79 and 0.18 $\mu g\ g^{-1}$ dw, respectively), which are in accordance with TF values >1 (1.74, 1.42, 1.29 and 2.72, respectively). In addition, as shown in Table 5, it can be seen that the leaf BCF of Pb observed here was higher than those reported by many previous studies (i.e., Abohassan, 2013; Chen et al., 2003; MacFarlane et al., 2003; Usman et al., 2013). To the contrary, the root BCF of Cu, Pb and Ni were higher than that reported by Li et al. (2016).

3.5. Risk assessment indices

Müller classification (Müller, 1981) was used for assessing pollution levels among the studied mangrove sediments (Table 6). The I_{geo} index revealed that Cd exhibited moderate to heavy contamination in the sediments (MHC), with values ranging from 2.15 at station XVII (Rabigh I) and 2.78 at station JIV, compared to the I_{geo} range in that class ($2 < I_{geo} < 3$). Stations XV (I_{geo} = 1.45) and XVI (I_{geo} = 1.64) showed moderately contaminated (MC) sediments ($1 < I_{geo} < 2$). Furthermore, only five stations (JII, X, XIII, XVII and XX) showed uncontaminated to moderately polluted sediments ($0 < I_{geo} < 1$). Generally, all stations revealed uncontaminated sediment types with respect to Cr, Cu, Ni and Pb, with moderate to heavy contamination of Cd. The ecological risk assessment index, E_r^i, revealed that the studied heavy metals in mangrove sediments showed almost the same pattern as the I_{geo} index. The concentration of Cr, Cu, Ni and Pb in sediments of the studied stations showed low ecological risk (E_r^i values lower than 40). On the other hand, Cd showed a moderate risk (E_r^i values of $40 \leq E_r^i < 80$) at stations JI, IX, XVII, XIX and XX. In addition, Cd exhibited considerable risk (E_r^i values of $80 \leq E_r^i < 160$) at stations JII, X, XIII, XVIII and XXI, while it showed high risk (E_r^i values of $160 \leq E_r^i < 320$) at stations XV, XVI and XVII. Moreover, a very high ecological risk (HVR) (E_r^i values ≥ 320) was observed at stations JIII and JIV. These results could be attributed to the huge inputs of wastes coming from anthropogenic sources at these stations, including discharge of refining wastes and untreated sewage effluents (Usman et al., 2013). Further, this finding is in agreement with those of Badr et al. (2009) who reported that urbanization activities (electrical power and desalination plants, the Aramco refinery plant and commercial harbours) may be responsible for augmenting trace metals concentrations in mangrove sediments near the city of Rabigh, in the central Red Sea.

3.6. Correlation analyses

Pearson's correlation coefficient (r) was performed to study the relation between heavy metals and physico-chemical properties (Garcia and Millan, 1998). The results, presented in Table 7, show that the EC values were positively correlated with organic matter (OM) content (r = 0.56, $P < 0.01$). It is noteworthy that microbiological decomposition of soil organic matter is mainly initiated by the enzymatic hydro-

Table 7 Pearson's correlation coefficient (r) between physico-chemical properties and total concentration of heavy metals in sediment of the study area (values in bold indicate the statistically significant ones).

	%Sand	%Mud	pH	EC	%OM	%$CaCO_3$	Cr	Cu	Ni	Pb
%Mud	**−1.000****									
	0.000									
pH	0.124	−0.133								
	0.591	0.566								
EC	−0.279	0.291	**0.647****							
	0.221	0.201	**0.002**							
%OC	−0.371	0.383	**−0.577****	**0.560****						
	0.098	0.086	**0.006**	**0.008**						
%$CaCO_3$	0.143	−0.143	0.051	0.129	−0.280					
	0.536	0.537	0.825	0.577	0.219					
Cr	−0.348	0.343	−0.305	0.076	0.184	0.052				
	0.122	0.127	0.179	0.744	0.425	0.822				
Cu	−0.330	0.327	**−0.449***	0.178	0.272	−0.294	**0.818****			
	0.144	0.148	**0.041**	0.441	0.234	0.196	**0.000**			
Ni	−0.332	0.330	−0.234	0.092	0.167	−0.330	**0.754****	**0.907****		
	0.142	0.144	0.306	0.691	0.470	0.144	**0.000**	**0.000**		
Pb	−0.077	0.092	**−0.480***	0.316	**0.605****	−0.063	0.415	0.431	0.323	
	0.739	0.693	**0.027**	0.162	**0.004**	0.786	0.062	0.051	0.153	
Cd	−0.188	0.193	−0.074	−0.135	−0.047	0.262	0.054	−0.051	−0.016	−0.008
	0.415	0.402	0.749	0.560	0.839	0.252	0.815	0.827	0.944	0.973

* Correlation is significant at the 0.05 level ($P < 0.05$).
** Correlation is significant at the 0.01 level ($P < 0.01$).

Table 8 Varimax rotated principal component analysis (PCA) of measured heavy metals in sediment samples (bold loadings are statistically significant).

Studied variables	Factor 1	Factor 2	Factor 3	Factor 4
Cu [μ g^{-1}]	**0.922**			
Ni [μ g^{-1}]	**0.909**			
Cr [μ g^{-1}]	**0.896**			
pH		−0.829		
EC [dS m^{-1}]		**0.826**		
OM%		**0.803**	0.307	
Pb [μ g^{-1}]	0.407	**0.666**		
%Sand			−0.962	
%Mud			**0.960**	
%$CaCO_3$				**0.848**
Cd [μ g^{-1}]				**0.713**
Eigenvalue	4.11	1.83	1.69	1.31
Variance %	37.32	16.66	15.36	11.92
Cumulative %	37.32	53.97	69.34	81.25

lysis of miscellaneous extracellular macromolecules and plant debris converted to monomeric and oligomeric molecules (Shi, 2011). This leads to the recycling of organic materials and the return of nutrient content to sediments and plants in tidal wetlands (Morrissey et al., 2014). However, elevated salinity reduces the activity of microorganisms (Wichern et al., 2006) by inhibiting amino acid capture and protein synthesis (Gennari et al., 2007) and altering the C N^{-1} ratio in the soil (Wichern et al., 2006). Soil pH showed negative correlations with EC ($r = -0.647$, $P < 0.01$), OM ($r = -0.577$, $P < 0.01$), Cu ($r = -0.449$, $P < 0.01$) and Pb ($r = -0.480$, $P < 0.01$) (Table 8). Lower pH values were associated with the highest levels of organic decomposition in the studied area, which is in accordance with Matsui et al. (2015). Based on the negative relationship between soil pH and both Cu and Pb under the alkaline conditions, the solubility and availability of Cu and Pb to plants were decreased (Fijałkowski et al., 2012). A significant positive correlation was observed between Pb and organic matter in sediments ($r = 0.605$, $P < 0.01$), implying that anaerobic conditions and enrichment of sediments with organic matter result in greater retention of heavy metals (Li et al., 2016;

Tam and Wong, 2000). Significant correlations were also observed between Cr and both Cu and Ni ($r = 0.818$, 0.754, $P < 0.01$, respectively). In addition, Cu had a significant positive correlation with Ni ($r = 0.907$, $P < 0.01$). These correlations among heavy metals in sediments might be due to the changes in physico-chemical properties, biological processes and discharging of contaminants into the aquatic ecosystem (Kumar et al., 2010; MacFarlane et al., 2007).

3.7. Principal component analysis (PCA)

In this study, principal component analysis (PCA) and computed Eigenvalues had a substantial role in identifying and understanding the associations of heavy metals with metallo-organic compounds (chelation) and the conditions of sediment change. Furthermore, the Varimax method was carried out to perform the rotation of the PCA. Loadings greater than 0.60 are statistically significant and are marked in bold in Table 8. The factor analysis included four factors that described 81.25% of total data variability in the mangrove sediments. The first dominant factor accounted for 37.32% of the total variance with an Eigenvalue of 4.11. This describes the accumulation of heavy metals such as Cu, Ni and Cr. These results are in agreement with those of Badr et al. (2009) and Usman et al. (2013), based on work conducted along the coast of the Red Sea. These studies reported that Cu, Pb, Zn, Ni and Cr were primarily introduced as a result of human activities (sewage treatment plant at JIII, the Aramco refinery, commercial harbours and sewage discharge at Jeddah and Rabigh areas). Similar results were reported by Mao et al. (2013), who identified the source of heavy metals in the upper layers of sediments. This study found that Co, Cr, Cu, Cd and Pb originated from human activities, but Ni came from lithogenic origin. The second factor (16.66% of the total variance with Eigenvalue = 1.83) revealed significant loading on the sediment properties, such as EC and organic matter, as well as Pb. This finding could be attributed to anthropogenic activities, such as bridge construction, which separated most of the mangrove areas from the open sea. The third component amounted to 15.36% of the total variance (Eigenvalue = 1.69). This factor gave significant load to only the mud fraction. Finally, the fourth factor accounted for only 10.97% of total variance, with an Eigenvalue of 1.21 and gave load to $CaCO_3$ content and Cd. This suggests that $CaCO_3$ content and Cd that originate due to weathering of lithogenous sources have a greater contribution than water and urban development, including industrial activities found in some areas. In conclusion, our results imply that activities associated with urbanization have significant influences on the contamination of the biotic community in the mangrove ecosystem along the coastal areas of the Red Sea, Saudi Arabia.

4. Conclusions

The concentrations of various heavy metals in the areas along the Saudi Arabian coast of the Red Sea were higher than their respective world average shale concentrations. These concentrations were above the threshold effect level, indicating a very limited biological impact on the marine environment. The concentration of Cd was higher than its toxic effect threshold level, which revealed a harmful risk to marine ecosystems. The higher concentrations of heavy metals in both the leaves and aerial roots of mangroves indicated that *A. marina* accumulates heavy metals, particularly Cr and Pb. Based on the I_{geo} index, sediments ranged between moderately and heavily contaminated with Cd, in Al-Haridhah (station VIII), but were moderately contaminated in South Jeddah, Rabigh, Duba and the wastewater treatment station in Jazan. The translocation factor was above the known worldwide average. The ecological risk index also revealed that Cd could have a considerable potential risk to the mangrove ecosystem. Principal component analysis indicated that industrial activities represent the main sources of heavy metal contamination at the studied locations. In terms of future investigations, the bioavailability fractions and toxicity of heavy metals should take molecular speciation into account. Finally, the results obtained from this study can contribute to establishing a decision-making framework for the future management of natural aquatic ecosystems of the Red Sea in Saudi Arabia.

Acknowledgements

This project was funded by the Deanship of Scientific Research (DSR) at King Abdulaziz University, Jeddah, under grant no. G-281-130-36. The authors, therefore, acknowledge with thanks DSR for technical and financial support. We are grateful to Dr. Abdelhamid A. Elnaggar, Dr. Gamal Al-Masry for their critical reading and suggestions that improved the quality of the manuscript. We further extend our gratitude towards the three anonymous referees for critically evaluating the manuscript and providing valuable suggestions.

References

Abohassan, R.A., 2013. Heavy metal pollution in *Avicennia marina* mangrove systems on the Red Sea coast of Saudi Arabia. JKAU: Meteorol. Environ. Arid Land Agric. Sci. 24 (1), 35–53.

Abohassan, R.A., Okia, C.A., Agea, J.G., Kimondo, J.M., McDonald, M.M., 2012. Perennial biomass production in arid mangrove systems on the Red Sea coast of Saudi Arabia. Environ. Res. J. 6 (1), 22–31.

Alongi, D.M., 2002. Present state and future of the world's mangrove forests. Environ. Conserv. 29 (3), 331–349, http://dx.doi.org/10.1017/S0376892902000231.

Asaeda, T., Kalibbala, M., 2009. Modelling growth and primary production of the marine mangrove (*Rhizophora apiculata* BL): a dynamic approach. J. Exp. Mar. Biol. Ecol. 371 (2), 103–111, http://dx.doi.org/10.1016/j.jembe.2009.01.009.

Badr, N.B.E., El-Fiky, A.A., Mostafa, A.R., Al-Mur, B.A., 2009. Metal pollution records in core sediments of some Red Sea coastal areas, Kingdom of Saudi Arabia. Environ. Monit. Assess. 155 (1), 509–526, http://dx.doi.org/10.1007/s10661-008-0452-x.

Bakan, G., Özkoç, H.B., 2007. An ecological risk assessment of the impact of heavy metals in surface sediments on biota from the mid-Black Sea coast of Turkey. Int. J. Environ. Stud. 64 (1), 45–57, http://dx.doi.org/10.1080/00207230601125069.

Bodin, N., N'Gom-Kâ, R., Kâ, S., Thiaw, O.T., De Morais, L.T., Le Loc'h, F., Rozuel-Chartier, E., Auger, D., Chiffoleau, J.F., 2013. Assessment of trace metal contamination in mangrove ecosystems from Senegal, West Africa. Chemosphere 90 (2), 150–157, http://dx.doi.org/10.1016/j.chemosphere.2012.06.019.

Buajan, S., Pumijumnong, N., 2010. Distribution of heavy metals in mangrove sediment at the Tha China estuary, Samut Sakhon province, Thailand. Appl. Environ. Res. 32 (2), 61—77.

Canadian Council of Ministers of the Environment (CCME), 2002. Canadian sediment quality guidelines for the protection of aquatic life: summary tables. In: Canadian Environmental Quality Guidelines, 1999. Canadian Council of Ministers of Environment, Winnipeg, 1—5, (updated).

Chen, X.Y., Tsang, E.P.K., Chan, A.L.W., 2003. Heavy metal contents in sediments, mangroves and bivalves from Ting Kok, Hong Kong, China. Environ. Sci. 23 (5), 480—484.

Chiffings, A.W., 1989. A draft marine protection area system plan for the Kingdom of Saudi Arabia. IUCN/NCWCD Specialist Report, Riyadh, KSA, 289 pp.

Chiu, C.Y., Hsiu, F.S., Chen, S.S., Chou, C.H., 1995. Reduced toxicity of Cu and Zn to mangrove seedlings (*Kandelia candel* (L.) Druce.) in saline environments. Bot. Bull. Acad. Sin. 36 (1), 19—24.

Cottenie, A., Verloo, M., Velghe, G., Camerlynch, R., 1982. Chemical Analysis of Plants and Soil. Laboratory of Analytical and Chemistry, State of Univ. Gent, Belgium, 63 pp.

Cui, S., Zhou, Q., Chao, L., 2007. Potential hyperaccumulation of Pb, Zn, Cu and Cd in endurant plants distributed in an old smeltery, northeast China. Environ. Geol. 51 (6), 1043—1048, http://dx.doi.org/10.1007/s00254-006-0373-3.

Cuong, D.T., Bayen, S., Wurl, O., Subramanian, K., Wong, K.K.S., Sivasothi, N., Obbard, J.P., 2005. Heavy metal contamination in mangrove habitats of Singapore. Mar. Pollut. Bull. 50 (12), 1732—1738.

Defew, L.H., Mair, J.M., Guzman, H.M., 2005. An assessment of metal contamination in mangrove sediments and leaves from Punta Mala Bay, Pacific Panama. Mar. Pollut. Bull. 50 (5), 547—552, http://dx.doi.org/10.1016/j.marpolbul.2004.11.047.

Dewis, J., Fertias, F., 1970. Physical and Chemical Methods of Soil and Water Analysis. FAO, Rome, Italy, Soils Bulletin No. 10.

El-Said, G.F., Youssef, D.H., 2013. Ecotoxicological impact assessment of some heavy metals and their distribution in some fractions of mangrove sediments from Red Sea, Egypt. Environ. Monit. Assess. 185 (1), 393—404, http://dx.doi.org/10.1007/s10661-012-2561-9.

Fahmy, M.A.F., Saad, M.A.S., 1996. Temporal and spatial distribution of heavy metals in Obhur Creek, a coastal Red Sea water body north of Jeddah. Mar. Sci. 7 (Spec. Iss.), 75—83.

FAO (Food and Agriculture Organization of the United Nations), 2007. The world's mangroves 1980—2005. FAO Forestry Paper 153. Food and Agricultural Organization, Rome, Italy, 77 pp.

Fernandes, L., Nayak, G.N., Ilangovan, D., 2012. Geochemical assessment of metal concentrations in mangrove sediments along Mumbai Coast, India. World Acad. Sci. Eng. Technol. 61 (1), 258—263.

Fernández-Cadena, J.C., Andrade, S., Silva-Coello, C.L., De la Iglesia, R., 2014. Heavy metal concentration in mangrove surface sediments from the north-west coast of South America. Mar. Pollut. Bull. 82 (1), 221—226, http://dx.doi.org/10.1016/j.marpolbul.2014.03.016.

Fijałkowski, K., Kacprzak, M., Grobelak, M., Placek, A., 2012. The influence of selected soil parameters on the mobility of heavy metals in soils. Inż. Ochr. Śr. 15, 81—92.

Garcia, R., Millan, E., 1998. Assessment of Cd, Pb and Zn contamination in roadside soils and grasses from Gipuzkoa (Spain). Chemosphere 37 (8), 1615—1625, http://dx.doi.org/10.1016/S0045-6535(98)00152-0.

Gennari, M., Abbate, C., Porta, V.L., Baglieri, A., Cignetti, A., 2007. Microbial response to Na_2SO_4 additions in a volcanic soil. Arid Land Res. Manag. 21 (3), 211—227, http://dx.doi.org/10.1080/15324980701428732.

Greger, M., 2004. Metal availability, uptake, transport and accumulation in plants. In: Prasad, M.N.V. (Ed.), Heavy Metal Stress in Plants: From Biomolecules to Ecosystems. Springer, Berlin, 1—27.

Guzmán, H.M., Jiménez, C.E., 1992. Contamination of coral reefs by heavy metals along the Caribbean coast of Central America (Costa Rica and Panama). Mar. Pollut. Bull. 24 (11), 554—561, http://dx.doi.org/10.1016/0025-326X(92)90708-E.

Hajar, E.W.I., Sulaiman, A.Z.B., Sakinah, A.M., 2014. Assessment of heavy metals tolerance in leaves, stems and flowers of *Stevia rebaudiana* plant. Procedia Environ. Sci. 20, 386—393, http://dx.doi.org/10.1016/j.proenv.2014.03.049.

Hakanson, L., 1980. Ecological risk index for aquatic pollution control. A sedimentological approach. Water Res. 14 (8), 975—1001, http://dx.doi.org/10.1016/0043-1354(80)90143-8.

Harikumar, P.S., Jisha, T.S., 2010. Distribution pattern of trace metal pollutants in the sediments of an urban wetland in the southwest coast of India. Int. J. Eng. Sci. Technol. 2 (5), 840—850.

Hassan, M.A.H., Nadia, A.A., 2000. Trace metals in fish, mussels, shrimp and sediment from Red Sea coast of Yemen. Bull. Inst. Oceanogr. Fish. 26, 339—353.

Hesse, P.R., 1971. A Textbook of Soil Chemical Analysis. John Murray, London, 250 pp.

Järup, L., 2003. Hazards of heavy metal contamination. Br. Med. Bull. 68 (1), 167—182, http://dx.doi.org/10.1093/bmb/ldg032.

Kabata-Pendias, A., Pendias, H., 1992. Trace Elements in Soils and Plants, second ed. CRC Press Inc., Boca Raton, FL, 365 pp.

Kehrig, H.A., Pinto, F.N., Moreira, I., Malm, O., 2003. Heavy metals and methyl mercury in a tropical coastal estuary and a mangrove in Brazil. Org. Geochem. 34 (5), 661—669, http://dx.doi.org/10.1016/S0146-6380(03)00021-4.

Kumar, A., Khan, M.A., Muqtadir, A., 2010. Distribution of mangroves along the Red Sea coast of the Arabian Peninsula: Part 1. The northern coast of western Saudi Arabia. Earth Sci. India 3 (1), 28—42.

Lambs, L., Bompy, F., Imbert, D., Corenblit, D., Dulormne, M., 2015. Seawater and freshwater circulations through coastal forested wetlands on a Caribbean Island. Water 7 (8), 4108—4128, http://dx.doi.org/10.3390/w7084108.

Lee, S.Y., Primavera, J.H., Dahdouh-Guebas, F., McKee, K., Bosire, J.O., Cannicci, S., Diele, K., Fromard, F., Koedam, N., Marchand, C., Mendelssohn, I., 2014. Ecological role and services of tropical mangrove ecosystems: a reassessment. Glob. Ecol. Biogeogr. 23 (7), 726—743, http://dx.doi.org/10.1111/geb.12155.

Lewis, M., Pryor, R., Wilking, L., 2011. Fate and effects of anthropogenic chemicals in mangrove ecosystems: a review. Environ. Pollut. 159 (10), 2328—2346, http://dx.doi.org/10.1016/j.envpol.2011.04.027.

Li, R., Chai, M., Qiu, G.Y., 2016. Distribution, fraction, and ecological assessment of heavy metals in sediment—plant system in Mangrove Forest, South China Sea. PLOS ONE 11 (1), e0147308, http://dx.doi.org/10.1371/journal.pone.0147308.

Lindsay, W., 1979. Chemical Equilibria in Soils, first ed. John Wiley and Sons Ltd., New York, 448 pp.

Luo, W., Lu, Y., Wang, T., Hu, W., Jiao, W., Naile, J.E., Khim, J.S., Giesy, J.P., 2010. Ecological risk assessment of arsenic and metals in sediments of coastal areas of northern Bohai and Yellow Seas, China. AMBIO 39 (5—6), 367—375, http://dx.doi.org/10.1007/s13280-010-0077-5.

Luo, X., Yu, L., Wang, C., Yin, X., Mosa, A., Lv, J., Sun, H., 2017. Sorption of vanadium (V) onto natural soil colloids under various solution pH and ionic strength conditions. Chemosphere 169, 609—617, http://dx.doi.org/10.1016/j.chemosphere.2016.11.105.

MacDonald, D.D., Ingersoll, C.G., Berger, T.A., 2000. Development and evaluation of consensus-based sediment quality guidelines for fresh water ecosystems. Arch. Environ. Contam. Toxicol. 39 (1), 20—31, http://dx.doi.org/10.1002/etc.5620190524.

MacFarlane, G.R., Burchett, M.D., 2002. Toxicity, growth and accumulation relationships of copper, lead and zinc in the grey mangrove *Avicennia marina* (Forsk.) Vierh. Mar. Environ. Res. 54 (1), 65—84, http://dx.doi.org/10.1016/S0141-1136(02)00095-8.

MacFarlane, G.R., Koller, C.E., Blomberg, S.P., 2007. Accumulation and partitioning of heavy metals in mangroves: a synthesis of field studies. Chemosphere 69 (9), 1454–1464, http://dx.doi.org/10.1016/j.chemosphere.2007.04.059.

MacFarlane, G.R., Pulkownik, A., Burchett, M.D., 2003. Accumulation and distribution of heavy metals in the grey mangrove, *Avicennia marina* (Forsk.) Vierh.: biological indication potential. Environ. Pollut. 123 (1), 139–151, http://dx.doi.org/10.1016/S0269-7491(02)00342-1.

Mandura, A.S., Khafaji, A.K., Saifullah, S.M., 1988. Ecology of a mangrove stand of a central Red Sea coast area: Ras Hatiba (Saudi Arabia). Proc. Saudi Biol. Soc. 11, 85–112.

Mao, L., Mo, D., Guo, Y., Fu, Q., Yang, J., Jia, Y., 2013. Multivariate analysis of heavy metals in surface sediments from lower reaches of the Xiangjiang River, southern China. Environ. Earth Sci. 69 (3), 765–771, http://dx.doi.org/10.1007/s12665-012-1959-6.

Marchand, C., Lallier-Verges, E., Baltzer, F., Albéric, P., Cossa, D., Baillif, P., 2006. Heavy metals distribution in mangrove sediments along the mobile coastline of French Guiana. Mar. Chem. 98 (1), 1–17, http://dx.doi.org/10.1016/j.marchem.2005.06.001.

Matsui, N., Meepol, W., Chukwamdee, J., 2015. Soil organic carbon in mangrove ecosystems with different vegetation and sedimentological conditions. J. Mar. Sci. Eng. 3 (4), 1404–1424, http://dx.doi.org/10.3390/jmse3041404.

MEPA/IUCN (Meteorological and Environmental Protection Administration/International Union for Conservation of Nature), 1987. Saudi Arabia Assessment of Coastal Zone Management Requirements. Meteorology and Environmental Protection, Jeddah, Saudi Arabia, (7 volumes).

Morrissey, E.M., Gillespie, J.L., Morina, J.C., Franklin, R.B., 2014. Salinity affects microbial activity and soil organic matter content in tidal wetlands. Glob. Change Biol. 20 (4), 1351–1362, http://dx.doi.org/10.1111/gcb.12431.

Müller, G., 1969. Index of geoaccumulation in sediments of the Rhine River. Geo J. 2 (3), 108–118.

Müller, G., 1981. Schwermetallbelastung der sedimente des Neckars und seiner Nebenflusse: eine Estandsaufnahmedie. Chem. Ztg. 105, 157–164.

Nath, B., Birch, G., Chaudhuri, P., 2014. Assessment of sediment quality in *Avicennia* marina-dominated embayments of Sydney Estuary: the potential use of pneumatophores (aerial roots) as a bio-indicator of trace metal contamination. Sci. Total Environ. 472, 1010–1022, http://dx.doi.org/10.1016/j.scitotenv.2013.11.096.

Peng, L., Wenjian, Z., Zhenji, L., 1997. Distribution and accumulation of heavy metals in *Avicenna marina* community in Shenzhen, China. J. Environ. Sci. 9 (4), 472–479.

PERSGA (The regional organization for the conservation of the environment of the Red Sea and Gulf of Aden), 2004. Status of Mangroves in the Red Sea and Gulf of Aden. PERSGA Technical Series No. 11, 68 pp.

Peters, E.C., Gassman, N.J., Firman, J.C., Richmond, R.H., Power, E.A., 1997. Ecotoxicology of tropical marine ecosystems. Environ. Toxicol. Chem. 16 (1), 12–40, http://dx.doi.org/10.1002/etc.5620160103.

Preda, M., Cox, M.E., 2002. Trace metal occurrence and distribution in sediments and mangroves, Pumicestone region, southeast Queensland, Australia. Environ. Int. 28 (5), 433–449, http://dx.doi.org/10.1016/S0160-4120(02)00074-0.

Qiu, Y.W., Yu, K.F., Zhang, G., Wang, W.X., 2011. Accumulation and partitioning of seven trace metals in mangroves and sediment cores from three estuarine wetlands of Hainan Island, China. J. Hazard. Mater. 190 (1–3), 631–638, http://dx.doi.org/10.1016/j.jhazmat.2011.03.091.

Sadiq, M., Zaidi, T.H., 1994. Sediment composition and metal concentrations in Mangrove leaves from the Saudi coast of the Arabian Gulf. Sci. Total Environ. 155 (1), 1–8, http://dx.doi.org/10.1016/0048-9697(94)90356-5.

Saenger, P., Hegerl, E.J., Davie, J.D., 1983. Global status of mangrove ecosystems. International Union for Conservation of Nature and Natural Resources Gland, Switzerland. Environmentalist (3) 88 pp.

Sakan, S., Dević, G., Relić, D., Anđelković, I., Sakan, N., ãorđević, D., 2015. Risk assessment of trace element contamination in river sediments in Serbia using pollution indices and statistical methods: a pilot study. Environ. Earth Sci. 73 (10), 6625–6638, http://dx.doi.org/10.1007/s12665-014-3886-1.

Sekabira, K., Origa, H.O., Basamba, T.A., Mutumba, G., Kakudidi, E., 2010. Assessment of heavy metal pollution in the urban stream sediments and its tributaries. Int. J. Environ. Sci. Technol. 7 (3), 435–446, http://dx.doi.org/10.1007/BF03326153.

Shanker, A.K., Ravichandran, V., Pathmanabhan, G., 2005. Phytoaccumulation of chromium by some multipurpose-tree seedlings. Agrofor. Syst. 64 (1), 83–87, http://dx.doi.org/10.1007/s10457-005-2477-2.

Shi, W., 2011. Agriculture and ecological significance of soil enzymes: soil carbon sequestration and nutrient cycling. In: Varma, A., Shukla, G. (Eds.), Soil Enzymology. Springer, Verlag-Berlin-Heidelberg, 43–60, http://dx.doi.org/10.1007/978-3642-14225-3_3.

Tam, N.F.Y., Wong, Y.S., 2000. Spatial variation of heavy metals in surface sediments of Hong Kong mangrove swamps. Environ. Pollut. 110 (2), 195–205, http://dx.doi.org/10.1016/S0269-7491(99)00310-3.

Taylor, S.R., McLennan, S.M., 1985. The Continental Crust: Its Composition and Evolution. Blackwell Scientific Publ., Carlton, 312 pp.

Thomas, G., Fernandez, T.V., 1997. Incidence of heavy metals in the mangrove flora and sediments in Kerala, India. In: Wong, Y.S., Tam, N.F.Y. (Eds.), Asia-Pacific Conference on Science and Management of Coastal Environment, Developments in Hydrobiology, vol. 123. Springer, Dordrecht, 77–87, http://dx.doi.org/10.1007/978-94-011-5234-1_9.

Turekian, K.K., Wedepohl, K.H., 1961. Distribution of the elements in some major units of the earth's crust. Geol. Soc. Am. Bull. 72 (2), 175–192, http://dx.doi.org/10.1130/0016-7606(1961)72[175:DOTEIS]2.0.CO;2.

Udechukwu, B.E., Ismail, A., Zulkifli, S.Z., Omar, H., 2015. Distribution, mobility, and pollution assessment of Cd, Cu, Ni, Pb, Zn, and Fe in intertidal surface sediments of Sg. Puloh mangrove estuary, Malaysia. Environ. Sci. Pollut. Res. 22 (6), 4242–4255, http://dx.doi.org/10.1007/s11356-014-3663-4.

Usman, A.R., Alkredaa, R.S., Al-Wabel, M.I., 2013. Heavy metal contamination in sediments and mangroves from the coast of Red Sea: *Avicennia marina* as potential metal bioaccumulator. Ecotoxicol. Environ. Saf. 97, 263–270, http://dx.doi.org/10.1016/j.ecoenv.2013.08.009.

Usman, A.R., Lee, S.S., Awad, Y.M., Lim, K.J., Yang, J.E., Ok, Y.S., 2012. Soil pollution assessment and identification of hyperaccumulating plants in chromated copper arsenate (CCA) contaminated locations, Korea. Chemosphere 87 (8), 872–878, http://dx.doi.org/10.1016/j.chemosphere.2012.01.028.

Van de Broek, M., Temmerman, S., Merckx, R., Govers, G., 2016. The importance of an estuarine salinity gradient on soil organic carbon stocks of tidal marshes. Biogeosci. Discuss., http://dx.doi.org/10.5194/bg-2016-285.

Vane, C.H., Harrison, I., Kim, A.W., Moss-Hayes, V., Vickers, B.P., Hong, K., 2009. Organic and metal contamination in surface mangrove sediments of South China. Mar. Pollut. Bull. 85 (1), 134–144.

Walkley, A., Black, I.A., 1934. An examination of the Degtareff method for determining soil organic matter, and a proposed modification of the chromic acid titration method. Soil Sci. 37 (1), 29–38.

Walters, B.B., Rönnbäck, P., Kovacs, J.M., Crona, B., Hussain, S.A., Badola, R., Primavera, J.H., Barbier, E., Dahdouh-Guebas, F.,

2008. Ethnobiology, socio-economic and management of mangrove forests: a review. Aquat. Bot. 89 (2), 220—236, http://dx.doi.org/10.1016/j.aquabot.2008.02.009.

Wang, L.E., Sousa, W.P., 2009. Distinguishing mangrove species with laboratory measurements of hyperspectral leaf reflectance. Int. J. Remote Sens. 30 (5), 1267—1281.

Wang, Y., Qiu, Q., Xin, G., Yang, Z., Zheng, J., Ye, Z., Li, S., 2013. Heavy metal contamination in a vulnerable mangrove swamp in South China. Environ. Monit. Assess. 185 (7), 5775—5787, http://dx.doi.org/10.1007/s10661-012-2983-4.

Wichern, J., Wichern, F., Joergensen, R.G., 2006. Impact of salinity on soil microbial communities and the decomposition of maize in acidic soils. Geoderma 137 (1—2), 100—108, http://dx.doi.org/10.1016/j.geoderma.2006.08.001.

Wright, D.A., Welbourn, P., 2002. Environmental Toxicology, vol. 11. Cambridge University Press, 656 pp.

Yan, Z., Sun, X., Xu, Y., Zhang, Q., Li, X., 2017. Accumulation and tolerance of mangroves to heavy metals: a review. Curr. Pollut. Rep. 3 (4), 302—317, http://dx.doi.org/10.1007/s40726-017-0066-4.

Yap, C., Ismail, A., Tan, S., Omar, H., 2002. Concentrations of Cu and Pb in the offshore and intertidal sediments of the west coast of Peninsular Malaysia. Environ. Int. 28 (6), 467—479, http://dx.doi.org/10.1016/S0160-4120(02)00073-9.

Yoon, J., Cao, X.D., Zhou, Q.X., Ma, L.Q., 2006. Accumulation of Pb, Cu, and Zn in native plants growing on a contaminated Florida site. Sci. Total Environ. 368 (2—3), 456—464, http://dx.doi.org/10.1016/j.scitotenv.2006.01.016.

Oceanologia (2018) 60, 527—543

Available online at www.sciencedirect.com

ScienceDirect

journal homepage: www.journals.elsevier.com/oceanologia/

ORIGINAL RESEARCH ARTICLE

Narrowband shortwave minima of multispectral reflectance as indication of algal blooms associated with the mesoscale variability in the Brazil-Malvinas Confluence☆

Genrik S. Karabashev*, **Marina A. Evdoshenko**

Laboratory of Ocean Optics, Shirshov Institute of Oceanology RAS, Moscow, Russia

Received 5 February 2018; accepted 13 April 2018
Available online 30 April 2018

KEYWORDS
Algae;
Bloom;
Pigments;
Reflectance spectrum;
MODIS;
Brazil-Malvinas Confluence

Summary We examine the narrowband shortwave minima (NSM) of multispectral reflectance as indication of mesoscale algal blooms. They are frequent in the Brazil-Malvinas confluence zone (BMCZ) where our testing site (TS) belongs. Its MODIS A images of December 2008 and 2014 were the source of initial data. Classification of reflectance spectra in these images revealed that the TS look from space was determined by the most populated cluster of pixels having the only NSM at 443 nm. We divided this cluster into sub-clusters by maximum wavelengths λ_{max} from 412 to 555 nm and retrieved the estimates of λ_{max} (proxy for abundance of colored dissolved organic matter (CDOM)), chl_a (MODIS chlorophyll), R_{rs} (555) (turbidity proxy), and C_{ALH} (NSM-based chlorophyll) on a pixel-by-pixel basis. This allowed us to demonstrate: (1) the NSM magnitude at 443 nm peaked in mesoscale structures, (2) C_{ALH} was consistent with chlorophyll in the BMCZ waters samples, (3) positive linear correlation of R_{rs} (555) and C_{ALH} was characteristic of the TS waters at any λ_{max}, (4) the MODIS *chl_a* was overestimated when $\lambda_{max} > 488$ nm, (5) localization and outlines of mesoscale structures agreed well in the fields of pairs $R_{rs}(555) - C_{ALH}$ and $\lambda_{max} - chl\_a$, but not in the $C_{ALH} - chl\_a$ pair. The NSM-based chlorophyll C_{ALH} outperformed the

☆ Part of the paper was presented at the 9th International Conference "Current Problems in the Optics of Natural Waters", St. Petersburg, Russia, 20—22 September 2017.

* Corresponding author at: Laboratory of Ocean Optics, Shirshov Institute of Oceanology RAS, 36, Nahimovskiy prospekt, 117997 Moscow, Russia. Tel. +79672134331.
E-mail address: genkar@mail.ru (G.S. Karabashev).

Peer review under the responsibility of Institute of Oceanology of the Polish Academy of Sciences.

ELSEVIER Production and hosting by Elsevier

https://doi.org/10.1016/j.oceano.2018.04.003

standard *chl_a* determinations in exactness because the C_{ALH} is insensitive to CDOM. This is advantageous when studying the Case 1 waters of intensive mesoscale variability where chlorophyll co-exists with the CDOM from eddy-induced blooms.

1. Introduction

In terms of semi-analytical approach (Morel et al., 2007), reflectance R_{rs} of a water body is a function of backscattering coefficient b_b and absorption coefficient a

$$R_{rs} = f[b_b/(a + b_b)]. \quad (1)$$

In Eq. (1), dimensionless factor f accounts for characteristics of incident radiance field and all members of Eq. (1) depend on wavelength λ. Every coefficient involves components that correspond to backscattering or absorption of solar radiation by different constituents of seawater. Therefore, we can write $b_b = b_{bp} + b_{bw}$ having in mind suspended particles of any origination (b_{bp}) and water proper (b_{bw}) as contributors into backscattering. Similarly, $a = a_{CDOM} + a_{ph} + a_m + a_w$ where a_{CDOM} is the absorption coefficients of CDOM (Colored Dissolved Organic Matter (Jerlov, 1976; Kalle, 1963)), a_{ph} represents the absorption of phytoplankton pigments in particles of biological origin, a_m characterizes absorption of mineralized particles of different nature, and a_w is the absorption coefficient of water proper. Hence, according to Eq. (1), the reflectance spectrum of water surface has to exhibit the maximums at wavelengths of maximal backscattering by particles and/or the minimums at wavelengths of maximal absorption by colored admixtures. In the context of remote sensing of water bodies, these relations are of interest exclusively in the visible because water severely attenuates UV and IR radiation.

Among the items of total absorption coefficient a, the pigment absorption a_{ph} is the only component whose wavelength dependence exhibits spectral bands much narrower than the visible range. High spectral selectivity of pigment absorption is advantageous in terms of analytical applications. This is the more so that the absorption of light by pigments directly depends on their content in water (Wozniak and Dera, 2007). Thus, it is reasonable to use a reflectance minimum at wavelength of maximal pigment absorption for retrieving the content of pigments from reflectance spectra of water surface.

Earlier studies (Jerlov, 1976) and current research (Stramski et al., 2004) provide no evidence that backscattering water constituents of any origination are able to mask the minimums of pigment absorption in seawater. The universal exponential growth of a_{CDOM} with diminishing wavelength of light (Jerlov, 1976; Nelson et al., 2010) does not preclude discrimination of a narrow-band reflectance pigment minimum. No fine structure of reflectance components due to mineral particles (a_{sm}) has been reported in Wozniak and Stramski (2004). Absorption spectrum of water proper is free of fine structure extremums too (Pope and Fry, 1997).

Based on the data of an airborne spectroradiometer, it has been found that the Sargasso Sea reflectance spectra are deprived of reflectance minima caused by pigment absorption (Clarke et al., 1970) which contradicts to what one might expect proceeding from the expression Eq. (1). The authors had noted that the shape of reflectance spectra was changing with the chlorophyll content and proposed to use this dependence for remote determination of chlorophyll.

The proposition was taken up and transformed into the concept of Case 1/Case 2 waters (Mobley et al., 2004; Morel, 1988, 2009). The latter implies that chlorophyll content in seawater is retrievable from the shape of reflectance spectra of water bodies whose optics depends exclusively on local phytoplankton abundance (Case 1 waters, mainly high seas) otherwise additional information is needed (Case 2 waters). This approach has been embodied in band-ratio algorithms. Since late 1970s to the present, this was the main avenue of remote sensing the chlorophyll in seas and oceans by means of multispectral ocean color scanners (Blondeau-Patissier et al., 2014; McClain, 2001).

The shipborne hyperspectral radiometers were widely used for groundtruthing the data of these instruments. Two outcomes of this activity are relevant to the present study. First, the content of chlorophyll in water retrieved with the help of band-ratio algorithms from multispectral reflectance tends to be over- or underestimated as compared to the ground truth data (Blondeau-Patissier et al., 2014; d'Ortenzio et al., 2002; Garcia et al., 2005). Second, the shortwave reflectance minima at wavelengths of maximal pigment absorption sometimes occurred in the open seawaters when measured with a hyperspectral shipborne radiometers (Kopelevich et al., 2005; Lubac and Loisel, 2007).

The first item is at least partially attributable to the fact that a band ratio algorithm is based on empirical dependence of ratio of reflectances loosely related to optical properties of chlorophyll. The second item hints to take advantage of absorption bands of chlorophyll and accessory pigments. According to expression Eq. (1), the presence of pigments in water manifests itself in minima of reflectance at wavelengths of absorption band maximums (reflectance deficit due to absorption). These bands peak mainly at $\lambda < 550$ nm (Wozniak and Dera, 2007). We named respective reflectance deficits as Narrowband Shortwave Minima (NSM) to highlight basic difference of our approach from band-ratio algorithms relying on reflectances of much wider spectral range.

Remote sensing at $\lambda < 550$ nm secures the deepest penetration of solar radiation in ocean water of high and moderate transparency (see Table XXVI in Jerlov, 1976). It is advantageous that the amplitude of the absorption bands of algal chlorophyll and respective NMS are directly proportional to the content of a pigment in algal cells in the absence of packaging and other secondary effects. These prospects are quite feasible in the case of an orbiting hyperspectral sensor. Yet, there are no indications that sensors of this kind are able

to become comparable to the multispectral ones in global coverage, revisit time, and availability of data collected.

When studying the cyanobacterial blooms in the Baltic Sea (Stal et al., 2003) from the data of multispectral sensor MODIS-Aqua, we have found numerous manifestations of NMS at 443 nm in the area of intensive blooming (Karabashev and Evdoshenko, 2015a). Based on the same approach, we observed similar NMS in transparent waters of the Southwest Tropical Pacific (Karabashev and Evdoshenko, 2015b) where cyanobacterial blooms were documented by conventional means (Dupouy et al., 2011). The same reflectance minima at different $\lambda < 550$ nm were observable in waters of the Patagonian shelf (Karabashev and Evdoshenko, 2016) noted for the diversity of algal species (Moreno et al., 2012), in the Caspian Sea (Karabashev and Evdoshenko, 2017a) and the Kerguelen Plateau in the Indian Ocean (Karabashev and Evdoshenko, 2017b) where water dynamics stimulates the protista bloom (Georges et al., 2014; Park et al., 2008).

The above blooms in the Baltic and Caspian Seas and at the Southwest Tropical Pacific Ocean were due to species of cyanobacteria. They are able to control their buoyancy and to accumulate near the air-water interface. The Kerguelen Plateau locates at latitude of the Circumpolar Current. It has been shown that internal tides promote here local vertical mixing and upward transfer of iron while general ocean circulation may foster the annual recurrence of blooms observed over the plateau (Park et al., 2008). Thus, different mechanisms support the surfacing of phytoplankton and make it visible as the NMS inherent to chlorophyll.

This inference prompted us to search for another mechanism of chlorophyll surfacing because none of the above ones is appropriate in the cases of reflectance deficit at 443 nm found in MODIS imagery east of the Patagonian shelf-break (Karabashev and Evdoshenko, 2016). This is the Brazil-Malvinas confluence zone (BMCZ) known for considerable variability of water surface reflectance (Acha et al., 2004; Garcia et al., 2008; Matano et al., 2010; Telesca et al., 2018) and characteristics of algal abundance and species diversity (d'Ovidio et al., 2010; Ferreira et al., 2013; Garcia et al., 2008). "The collision of the Brazil and Malvinas currents spawns one of the most spectacular eddy fields of the global ocean. The generation of warm- and cold-core eddies at either side of the front have led to mesoscale variability only matched by the offshore extensions of the Gulf Stream, the Kuroshio, and the Agulhas Current" (Piola and Matano, 2001).

The area of such oceanological intricacy is the most appropriate place for attaining our aim: to reveal the potential of narrowband shortwave minima (NSM) of multispectral satellite reflectance as indication of chlorophyll abundance related to the mesoscale variability in Case 1 waters.

2. Background, methods, and materials

2.1. Testing site

Fig. 1 gives an idea of basic features of the BMCZ and positioning of the testing site (TS) relative expectable sources of mesoscale variability.

(a) Potential temperature θ of the Malvinas Current grows from 4°C at ~56°S to 16°C at ~40°S (Fig. 1) where it turns back under the action of warmer Brazil Current ($\theta > 20$°C) according to Piola and Matano (2001). This promises intensive mesoscale between-currents water exchange observable in remotely sensed fields of optical characteristics and SST.

(b) Interaction of the Malvinas Current and continental slope is hypothetically one of potential triggers of mesoscale variability of water properties along the route of the Malvinas Current.

(c) The Malvinas Current flows around the Malvinas Archipelago, which may trigger the mesoscale island wakes to the north of the latter. The island-generated eddies are characteristic of deep ocean islands in the paths of currents (Barton, 2001).

(d) A shelfbreak upwelling is a permanent feature of the study area (Matano and Palma, 2008). The upwelling is visible in satellite distributions of SST and reflectance as a narrow stripe where isobaths 150–1000 m in Fig. 1 come closer together. To all appearance, the upwelling and northbound general transport of shelf waters prevents intrusion of the latter to the east of the shelfbreak.

To summarize, the testing site area to the east of the shelfbreak (Fig. 1) is a natural model of Case 1 water

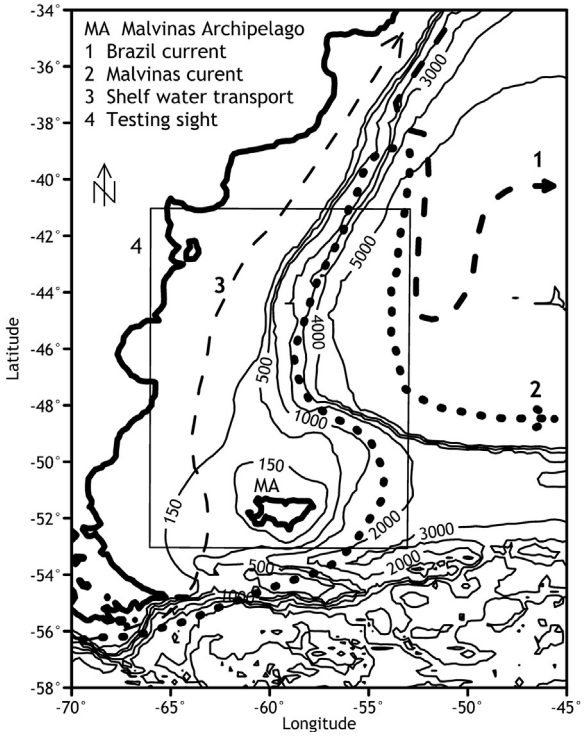

Figure 1 Study area, its bottom relief, and quasi-permanent water flows 1–3 in the BMCZ reproduced from patterns in (d'Ovidio et al., 2010; Loder et al., 1998; Matano et al., 2010; Piola and Matano, 2001). The bold lines indicate the land-water interface. Testing site 4 designates the limits of satellite images used as a source of initial data on reflectance and SST. Here and in the following figures, the isobaths are plotted from the bathymetry gridded with the help of GEBCO Grid Demonstrator (https://www.bodc.ac.uk/).

body were intensive mesoscale variability is a common phenomenon.

2.2. Approach

2.2.1. Sensor

The mesoscale inhomogeneities, being anything from 10^1 to 10^2 km in size and from a few days to a few weeks in time, are considered as fluid dynamical niches of phytoplankton types in the ocean (d'Ovidio et al., 2010). These scales and periods match the specifications of any multispectral orbiting sensor. However, the Moderate Resolution Imaging Spectroradiometer (MODIS) is the most advantageous one for our goals.

MODIS is the only sensor whose set of spectral channels at λ = 412, 443, 469, 488, 531, 547, 555, 645, 667, and 678 nm permits, to an extent, to discriminate reflectance deficit due to shortwave absorption bands of chlorophyll and accessory pigments in phytoplankton cells. The 443 nm channel is tuned to the absorption peak of chlorophyll *a* (Soret band). Hence, reflectance minimum at 443 points to chlorophyll in water regardless of spectrum shape. Reflectance minimum at 488 nm is attributable to the same band of other chlorophylls and/or accessory pigments of phytoplankton (Wozniak and Dera, 2007), while broader reflectance minimum from 412 to 555 nm is probable when diversity of pigments in local phytoplankton is at its maximum. The study area is known as a region of widely varying species composition of phytoplankton population (d'Ovidio et al., 2010; Garcia et al., 2008). It is advantageous that the archive of MODIS global imagery covers the period from 2002 to the present and MODIS images provide global coverage at GSD = 1 km.

2.2.2. Absorption line of chlorophyll as an indication of its content in water

Index D1 = $R_{rs}(412) - R_{rs}(443)$ has been proposed as a simplest quantitative measure of chlorophyll content in water based on reflectances deficit at 443 nm (Karabashev and Evdoshenko, 2015b). In inland seas, reflectance spectra peak at $\lambda_{max} > 469$ nm and D1 < 0. Linear dependence of D1 upon chlorophyll content has been established from the Caspian Sea data (Karabashev and Evdoshenko, 2016). However, the index D1 becomes positive in transparent ocean waters where λ_{max} = 412 nm. Now we eliminate this inconvenience and propose a new universal chlorophyll index. It is designated the Absorption Line Height of chlorophyll (ALH) by analogy with the Fluorescence Line Height (FLH) of the same pigment (Letelier and Abbott, 1996). We calculate ALH pixel-by-pixel through the linear interpolation

$$\mathrm{ALH} = R_{rs}(412) + 0.54 \times [R_{rs}(469 - R_{rs}(412)] - R_{rs}(443). \quad (2)$$

Additional goal of the present study is to examine the diagnostic potential of the ALH index.

2.3. Optical characteristics of phytoplankton blooming

In the context of ALH examination, characteristic no. 1 should be the satellite concentration of chlorophyll *chl_a*. It is retrieved with the help of the OCI algorithm for Case 1 waters (Hu et al., 2012) and available as a level L2 standard product of MODIS sensors along with the estimates of chlorophyll *chl_ocx* based on the OCX algorithm. According to Hu et al. (2012), *chl_ocx* is inferior to *chl_a* in accuracy of retrieval of chlorophyll concentration in ocean waters.

Proportionality of absorption of chlorophyll to its content in water justifies the use of a simple formula for converting ALH into chlorophyll concentration C_{ALH} as a trial solution:

$$C_{ALH} = 12 \times \mathrm{ALH} + 0.106. \quad (3)$$

Expression (3) is based on the data of MODIS-A image of anticyclonic eddy at the Southern Caspian Sea (September 1, 2005). The regional algorithm (Kopelevich et al., 2013) for chlorophyll retrieving and expression (2) for ALH determination were used to obtain regression (3) at R^2 = 0.92.

Having regard to the fact that reflectance $R_{rs}(555)$ belongs to the spectral range of minimal absorption of light by CDOM and water proper (Jerlov, 1976), we use $R_{rs}(555)$ as an index of relative abundance of suspended light-scattering particles in a layer of origination of water-leaving radiance. The scattering coefficient b_b is more appropriate here, but it is hardly possible to calculate it from reflectance at satisfactory accuracy in waters widely varying in size, density, composition, and vertical distribution of suspended particles.

The MODIS spectral channels allow one to discriminate the ocean waters in relative abundance of CDOM: the higher is CDOM content in water, the closer is λ_{max} to 555 nm because of expression (1) and exponential growth of a_{CDOM} with diminishing λ (Jerlov, 1976). This dependence is helpful for typifying the ocean waters from λ_{max}. The latter is higher in areas where CDOM attenuates the shortwave reflectance stronger than it is contributed by backscattering of suspended matter. The advantage of λ_{max} is in the fact, that it is defined by MODIS design without relying on questionable assumptions and is universally applicable in ocean waters of low and moderate biological productivity.

2.4. Initial data

The season of maximum insolation of ocean surface and lowest losses of data due to cloudiness, Sun glint, and other inferences — these were the main criteria for selecting the images of the testing site. These conditions turned out to be too severe to compose series of images of the testing site for assessing seasonal changes in distributions of characteristics involved. However, tolerance to data gaps hampers identification of mesoscale events in individual images of the testing site. This is of primary importance for the present work.

Use has been made of the browser at http://oceancolor.gsfc.nasa.gov/ (NASA) to select and download the data of level L2 of MODIS Aqua in more than 20 images of the testing site obtained in December–January from 2004 to 2016. Final selection of images was performed with the help of SMCS browser (Sheberstov, 2015). The latter supports batch processing and visualization of data of many orbital sensors, allows to eliminate pixels corrupted by cloudiness, Sun glint, and other inferences and to export the pre-processed data for further treatment. In the present study, we exported reflectance R_{rs} at 412, 443, 469, 488, 531, 547, 555, 620, 645 and 678 nm and estimates of chlorophyll concentration *chl_a*, found with the

standard MODIS algorithm OCI (Hu et al., 2012). Error-free distributions of SST, obtained by MODIS sensor concurrently with optical information, were also exported from the SMCS browser. Finally, we restricted our choice to scenes A2014336182000.L2_LAC_OC.nc, A2014336182000.L2_LAC_SST.nc, A2008341184000.L2_LAC_OC.nc, A2008341184000.L2_LAC_SST.nc, A2008345181500.L2_LAC_OC.nc, and A2008345181500.L2_LAC_SST.nc. They were downloaded on July 5, 2017, from the US NASA OBPG (http://oceancolor.gsfc.nasa.gov/) using reprocessing R2014.0, at GSD = 1 km.

2.5. Data processing

According to earlier experience (Karabashev and Evdoshenko, 2016), reflectance spectra of pixels in images of testing site widely vary in shape over the BMCZ. Therefore, we restricted our consideration to the specific type of reflectance spectrum having the only chlorophyll-inherent minimum at 443 nm. More complicated spectral shapes at $\lambda < 550$ nm should be attributed to co-occurrence of different pigments in water but scarcity of relevant information gives no way of identifying their nature at present.

The MATLAB scripts were the main tool for data treatment. It started from eliminating the pixels corrupted by cloudiness, Sun glint, outliers, and the like from files of every scene. Next was the stage of pixels classification by shape of reflectance spectrum. The logical sums of inequalities of adjacent R_{rs}, describing the shape of pixel's spectrum at $\lambda \leq 555$ nm, were applied to discriminate four clusters of pixels' spectra. For example, the sum $[(R_{rs}(412) > R_{rs}(443)) + (R_{rs}(469) > R_{rs}(443)) = 2]$ identified the pixels whose reflectance spectra exhibited the sole minimum at 443 nm.

The sum tuned to distinguish spectra of broad minimum at 469 nm from 412 to 531 nm identified the pixels of cluster no. 1. They were removed from the set of remaining pixels. Cluster no. 2 was recognized based on the sum tuned to spectral minima at 488 nm (obligatory) and 443 nm (optionally) and removed from the rest of pixels. The pixels of cluster no. 3 were identified using the sum tuned to the only minimum at 443 nm inherent to the chlorophyll. Cluster no. 4 involves remaining unidentified pixels. This operating sequence secures the absence of "foreign" pixels in spectra of cluster no. 3 and the absence of any shortwave minima in spectra of cluster no. 4. Now we subdivide the pixels of clusters no. 3 and no. 4 into respective sub-clusters by maximal wavelength of pixels' spectra at 412, 443, 469, 488, 531, 547, 555 nm. Finally, the attributes of every pixel in cluster no. 3 were added with the estimates of λ_{max}, ALH, and C_{ALH}, calculated from pixel's reflectances according to above considerations and expressions. In this way, we have

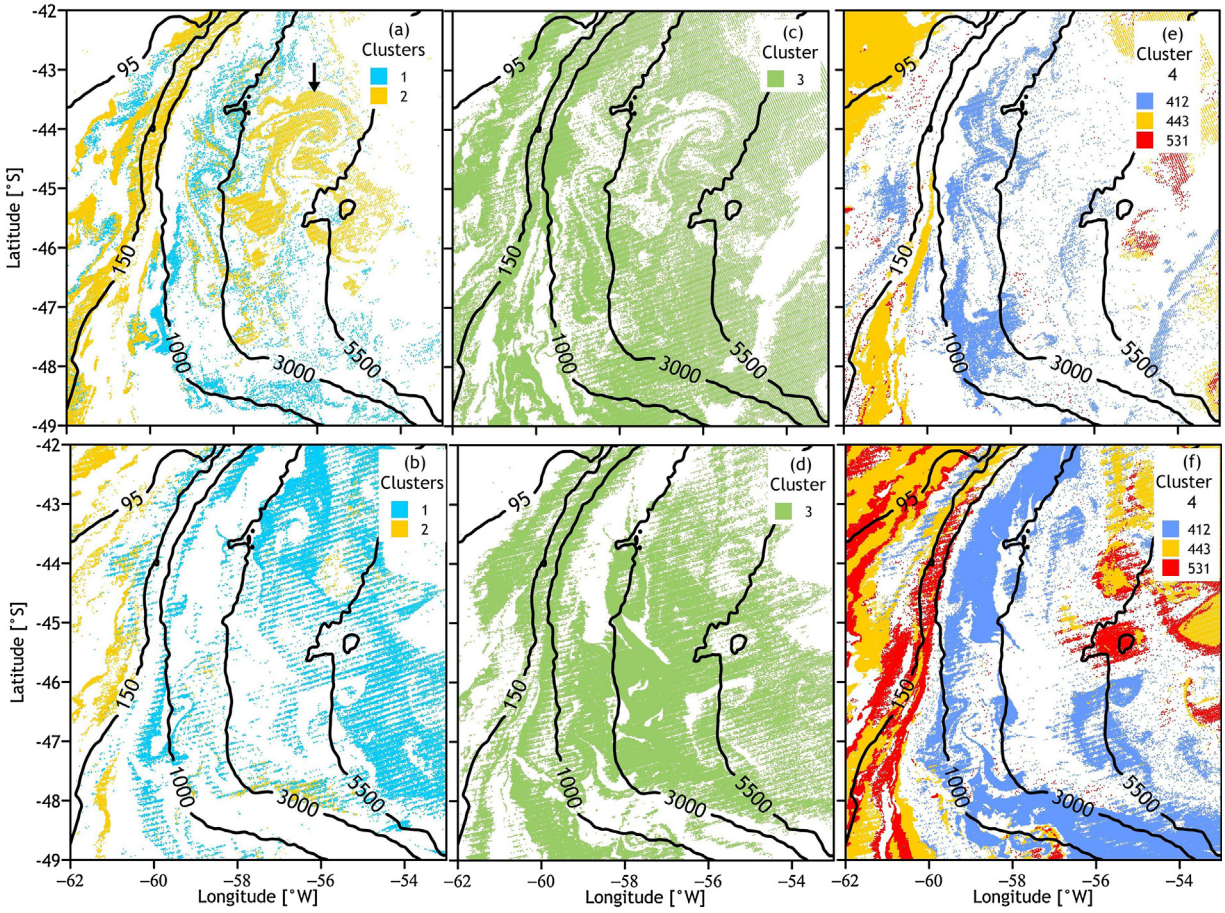

Figure 2 Distributions of pixels' clusters in testing sight images taken with the MODIS Aqua sensor on 2008-12-06 (panels (a), (c), (e)) and 2014-12-02 (panels (b), (d), (f)). Cluster 4 is divided into three sub-clusters by λ_{max} from 412 to 547 nm. For details see text.

prepared tables of reflectance data and derived quantities for dates 2008-12-06, 2008-12-10, and 2014-12-02 along with the SST tables for the same dates.

These tables were used for visualizing the distributions of quantities in question and for estimating their statistical characteristics. The visual perception of spatial patterns was particularly important because extensions of testing site allow us to observe the co-occurrence of different mesoscale events and their relation to the satellite SST distribution and the TS bottom relief.

3. Results

3.1. Distribution of spectral clusters

Fig. 2 shows the distributions of members of above spectral clusters over the TS fragment mapped from MODIS images of 2008-12-06 and 2014-12-02. The maps in Fig. 2 demonstrate spatial intermittency of spectrally different pixels at scales close to MODIS GSD = 1 km (submesoscale range). Nevertheless, there were spectrally uniform mesoscale structures. They are (i) the shelf to the west of 95 m isobath, where pixels of cluster no. 4 outnumber the spectra of other clusters, (ii) spaces between the 1000 and 3000 m isobaths, that are empty in maps (b) and (d) but filled with pixels of sub-cluster 412 of cluster no. 4 in map (f), (iii) in map (a) (arrow), the pixels of cluster no. 2 fill the empty places in outlines of an eddy dipole visible in map (c) between the 3000 m and 5000 m isobaths from 46.0°S to 43.5°S.

The population of cluster no. 3 is comparable to the total population of other clusters (Fig. 2). We focused on analyzing the data of cluster no. 3 for two reasons. First, being the most populated, it plays a leading role in shaping the patterns observable from space in testing site images. Second, it is a good probability that the NSMs in spectra of this cluster are uniquely determined by chlorophyll in water whereas the broad or multiple NSMs are due to pigments whose composition is difficult to establish without ground truthing information.

We divided the spectra of the cluster no. 3 into sub-clusters by λ_{max} (sc412, sc469, sc488, sc531, sc547, and sc555). Fig. 3 displays the average spectra of these sub-clusters calculated from the data that underlie the respective distributions of 2008-12-06 and 2014-12-02 in Fig. 2. In both cases, sub-cluster sc412 significantly surpassed the rest of sub-clusters in population, and sc531 was the second largest sub-cluster. Fig. 3 gives the idea of the NSM shape and shows significant inter-annual changes of spectral shapes in sub-clusters at the same λ_{max} and season.

3.2. Distributions of optical characteristics

The maps (a) and (b) in Fig. 4 demonstrate coincidence of localization and outlines of patches of higher λ_{max} and larger *chl_a* north of the Malvinas Archipelago and the X-shaped structure occurrence at 47°S east of the 4000 m isobath. These patchy structures are absent in maps (c) and (d). Here the areas of maximum estimates of $R_{rs}(555)$ and C_{ALH} coincide in part. The similarity of distributions in pairs λ_{max} — *chl_a* and $R_{rs}(555)$ — C_{ALH} survived in images of the same water area recorded a few days later (Fig. 5, panels (a),(b) and (c),(d)).

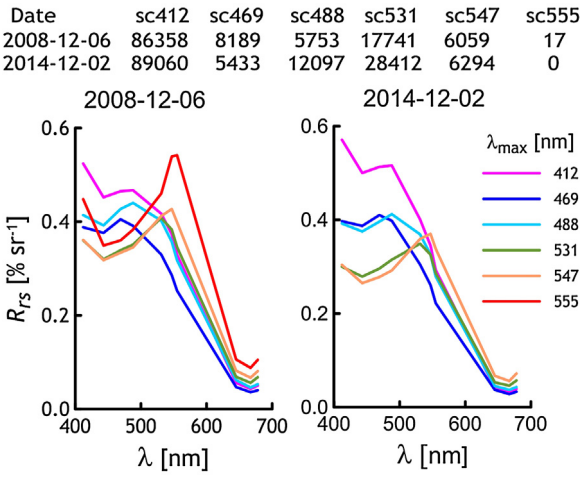

Figure 3 Population of sub-clusters sc412-sc555 of cluster no. 3 distinguished by wavelength λ_{max} from 412 to 555 nm (top) and average spectra of these sub-clusters (bottom) calculated from data underlying the maps of 2008-12-06 and 2014-12-02 in Fig. 2.

Figs. 6 and 7 show more radical interannual changes in the distributions of λ_{max}, *chl_a*, R_{rs} (555), and C_{ALH}. However, the similarity in paired distributions of λ_{max} — *chl_a* and R_{rs} (555) — C_{ALH} as well as the differences between the pairs took place too. The following facts came to our attention.

1. The highest levels of $R_{rs}(555)$ and C_{ALH} visualize compact eddy-like structures 1—3 in maps (c) and (d) of Fig. 6, but they are difficult to distinguish in panels (a) (λ_{max}) and (b) (*chl_a*) in the same maps.
2. In Fig. 6, the stripes of $\lambda_{max} \geq 531$ nm and moderate *chl_a* occur between the isobaths 500 and 1000 m (maps (a) and (b)) while elevated $R_{rs}(555)$ (c) and C_{ALH} (d) located between the 1000 and 2000 m isobaths.
3. In maps (a) and (b), Fig. 7, a distinctive structure *1* of intricate shape stands out against a background of 2000 m isobath between 47°S and 45°S. This structure is difficult to distinguish in maps (c) and (d).
4. A mesoscale circular structure *2* in maps (c) and (d) in Fig. 7 is easy to recognize thanks to maximal $R_{rs}(555)$ and NSM-chlorophyll, but the same places in maps (a) and (b) are occupied by the lowest estimates of λ_{max} and *chl_a*.

In order to clarify this facts, we have turned to MODIS-determinations of the SST in the testing site for the same date and time (scene A2014336182000.L2_LAC_SST.nc), and compared the outlines of inhomogeneities of SST and optical characteristics (Fig. 8). Here the pathway of the Malvinas Current is traced by the lowest SST. A loop-like structure L is a distinctive feature of distributions of SST (a), λ_{max} (b), and *chl_a* (c) to the south of 46°S. This structure is visualized by SST > 9.4°C and higher λ_{max} and *chl_a* (same maps). The highest contrast exhibits the distribution of λ_{max} where λ_{max} = 547 nm traces the loop itself against a background of pixels whose λ_{max} = 412 nm. This loop is traceable in the field of $R_{rs}(555)$ (e) and almost disappears in C_{ALH} distribution (f). The maps (d)—(f) demonstrate an eddy-like structure E marked by the highest $R_{rs}(555)$ and C_{ALH} and medium level SST.

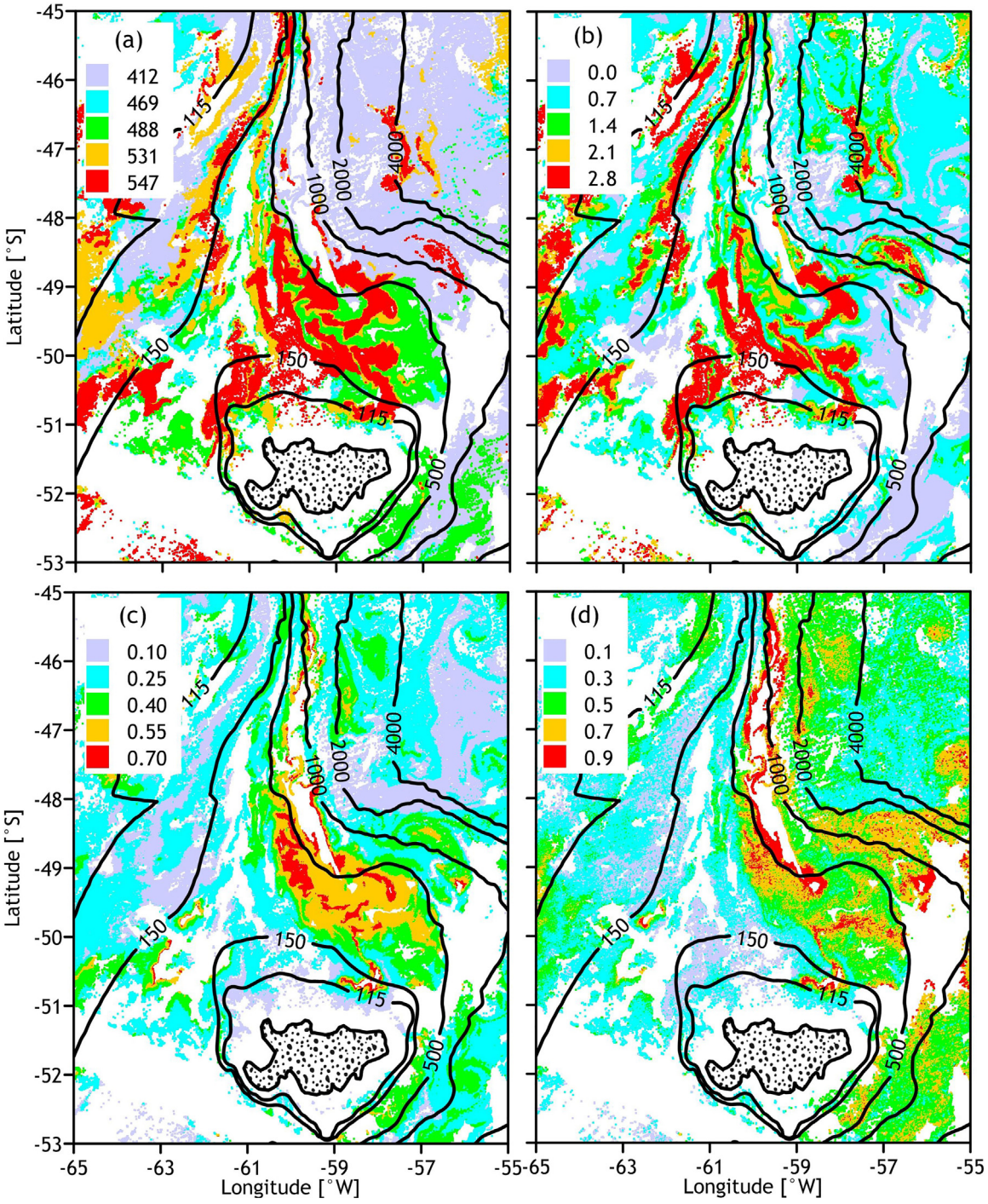

Figure 4 Pixel-by-pixel distributions of (a) wavelength of reflectance spectral maximum λ_{max} [nm], (b) MODIS chlorophyll *chl-a* [mg m^{-3}], (c) reflectance $R_{rs}(555)$ [% sr^{-1}], and (d) NSM-based chlorophyll C_{ALH} [mg m^{-3}]. They were plotted from pixels' attributes of the TS image of 2008-12-06.

3.3. Relationships of characteristics associated with suspended matter

The scatter of *chl_a* and C_{ALH} relative to the $R_{rs}(555)$ determinations (Fig. 9) provides impartial idea of inconsistency of chlorophyll concentrations retrieved from reflectance spectra of individual pixels' by means of MODIS algorithm or based on determinations of C_{ALH}. The graphs in Fig. 9 were plotted from the data of 2008-12-06 and 2014-12-02 and show that the changes in C_{ALH} and $R_{rs}(555)$ positively co-varied in both cases. Except for the subsample at λ_{max} = 469 nm, the estimates of *chl_a* changed chaotically relative to variations in $R_{rs}(555)$ under the same conditions.

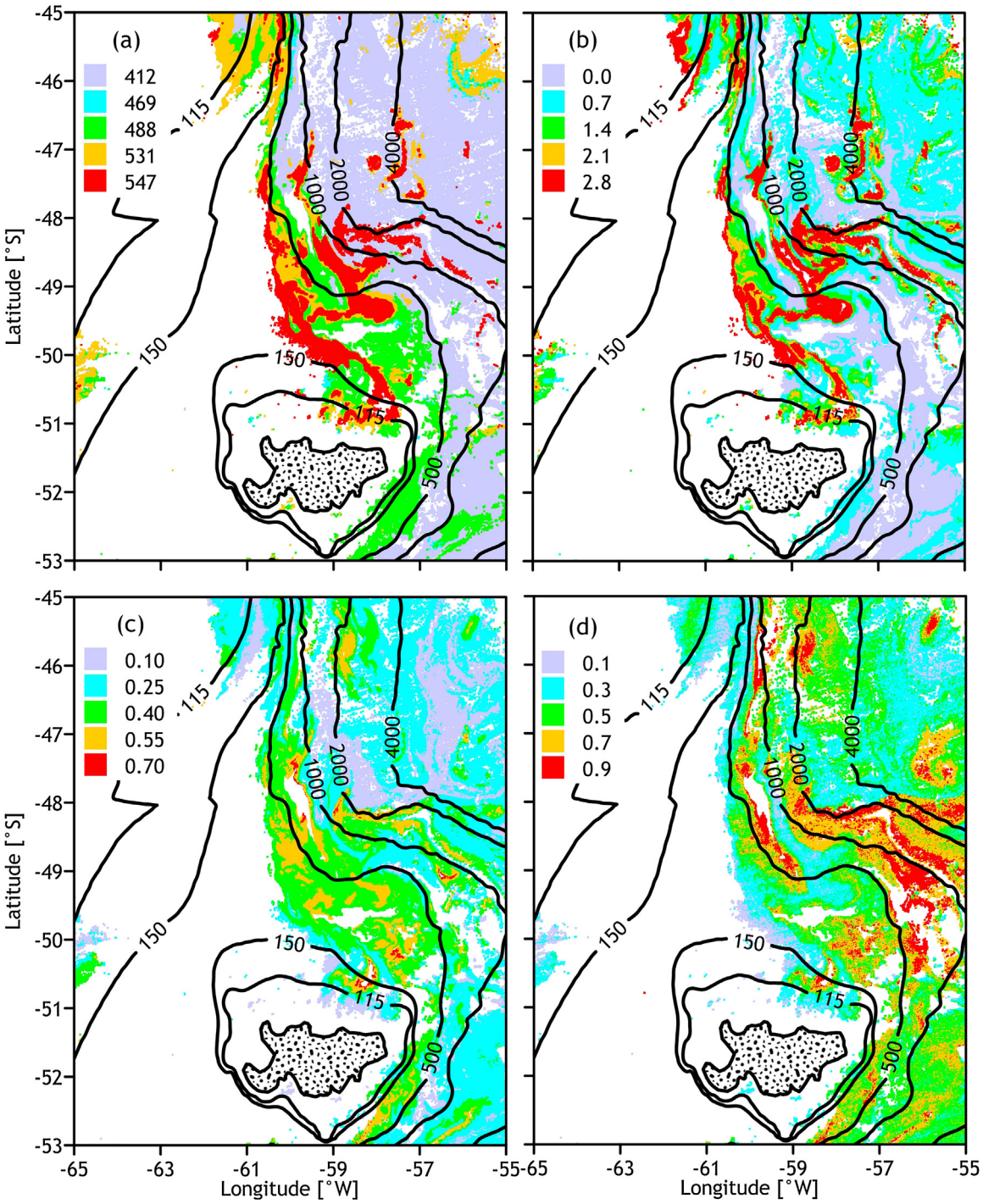

Figure 5 The same as in Fig. 4 but from the TS image of 2008-12-10. White spaces represent areas of missing data.

The histograms in Fig. 10 demonstrate the distributions of C_{ALH}, $R_{rs}(555)$, and *chl_a* in the sub-clusters of cluster no. 3 classed by λ_{max} and calculated from data of 2008-12-06 and 2014-12. The distributions of C_{ALH} belong to the common range of C_{ALH} estimates regardless of λ_{max}. The same behavior is evident in distributions of $R_{rs}(555)$. On the contrary, the histograms of *chl-a* tend to displace to higher *chl_a* subsequent to λ_{max} of pixel's spectrum.

4. Discussion

4.1. Surprising results in distribution and shape of reflectance spectra

The outcomes of clustering procedure seem acceptable with the exception of two results: spatial intermittency of spec-

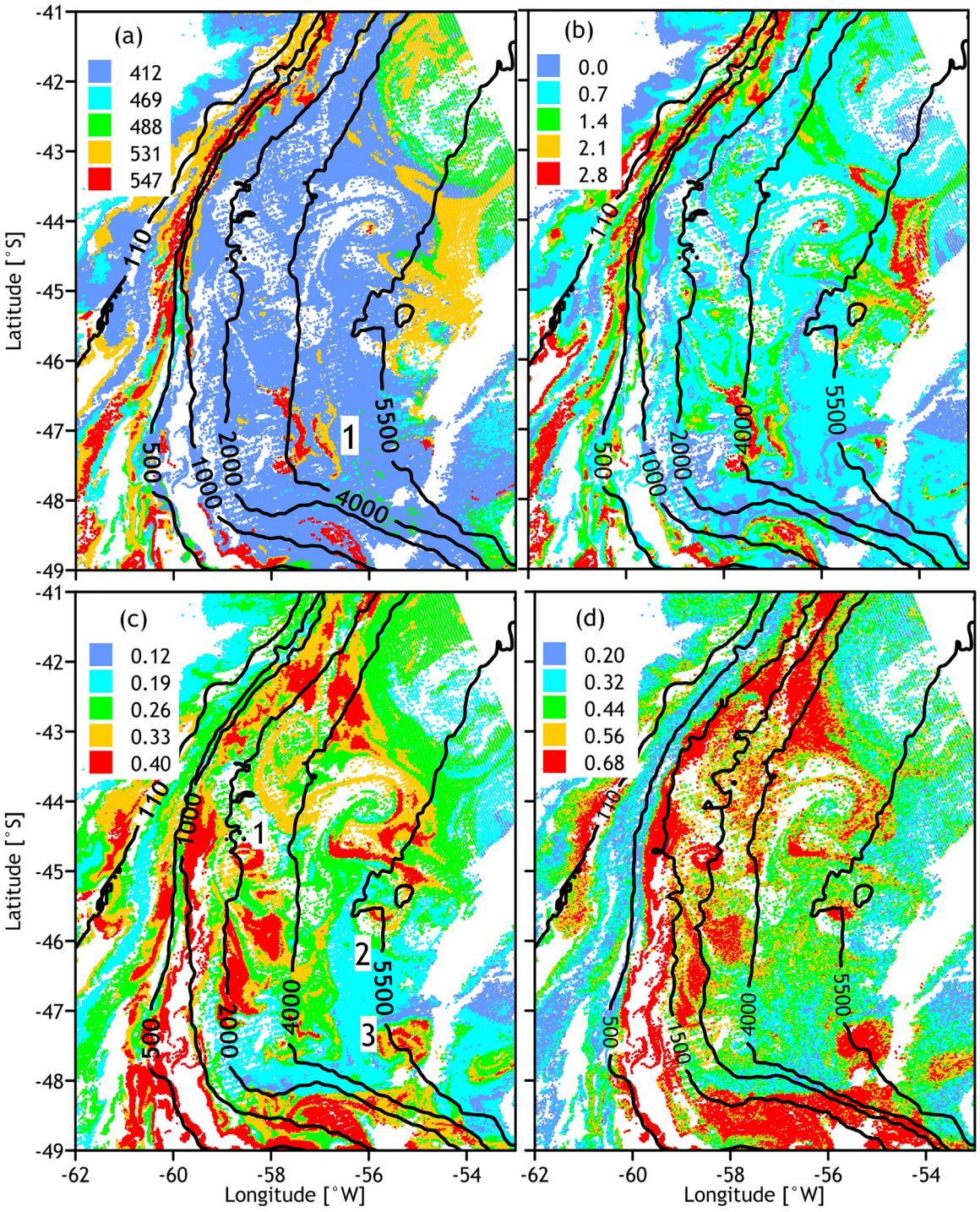

Figure 6 Pixel-by-pixel distributions of (a) wavelength of reflectance spectral maximum λ_{max} [nm], (b) MODIS chlorophyll *chl-a* [mg m^{-3}], (c) reflectance $R_{rs}(555)$ [% sr^{-1}], and (d) NSM-based chlorophyll C_{ALH} [mg m^{-3}] plotted from TS image of 2008-12-06. The distributions characterize the TS fragment shifted 4° to the north relative the TS fragment in Fig. 4. Figure-of-one in panel (a) indicates the X-like structure in panels (a) and (b). Figs. 1–3 in panel (c) mark circular structures similarly located in panels (c) and (d).

trally different pixels (Fig. 2) and widening of the shortwave minimum in spectra of sub-clusters of cluster no. 3 at $\lambda_{max} > 488$ nm (Fig. 3).

The intermittency of members of different spectral clusters is not a universal feature of the study area because large mesoscale structures comprise the pixels of the same spectral type (see Section 3.1). Supposedly, an illusory intermittency arises at places where NSM amplitude of pixels is close to zero. However, intermittency of reflectance spectra at scales below 10 km may be due to submesoscale forcings: "Submesoscale dynamics contribute to phytoplankton production by enhancing the supply of nutrients in regions that are nutrient limited and by generating density stratification in the surface layer to increase light exposure

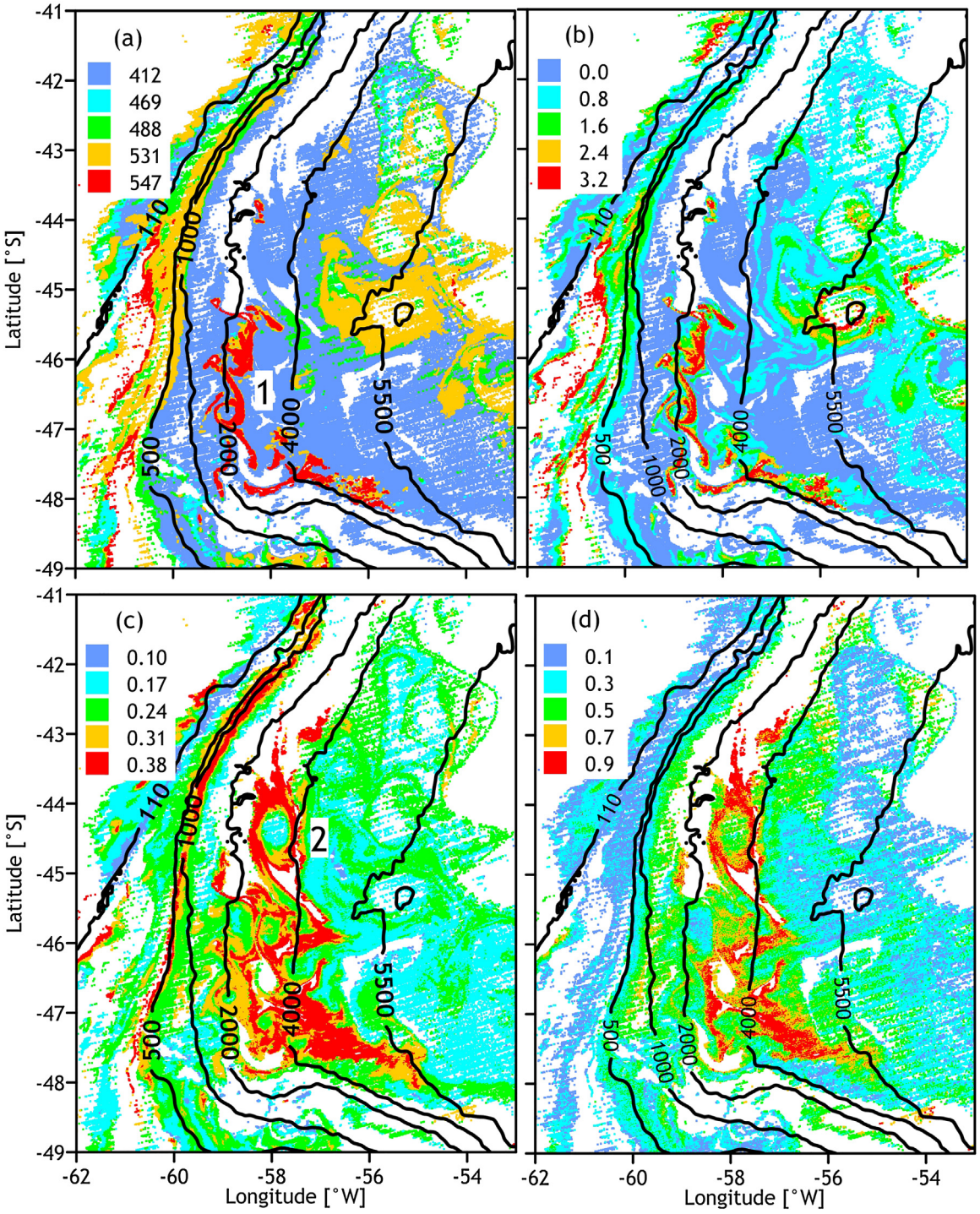

Figure 7 The same as in Fig. 6 but the maps were plotted from the TS image of 2014-12-02. The figure-of-one points to the similar mesoscale structures in panels (a) and (b) and figure-of-two indicates the eddy-like structure in panels (c) and (d).

for phytoplankton that are light limited. These effects occur locally at scales of 0.1–10 km and over a few days and result in the heterogeneous supply and distribution of nutrients, stratification, and mixed-layer depth, which generate patches of high productivity that are thought to contribute substantially to oceanic ecosystems, their structure and phenology, and the ensuing trophic cascades." (Mahadevan, 2016). The issue of spectral intermittency deserves a targeted study before it may be write off for experimental errors.

As for the widening of the NSM, it is evidently due to algal cells containing large quantities of accessory pigments along

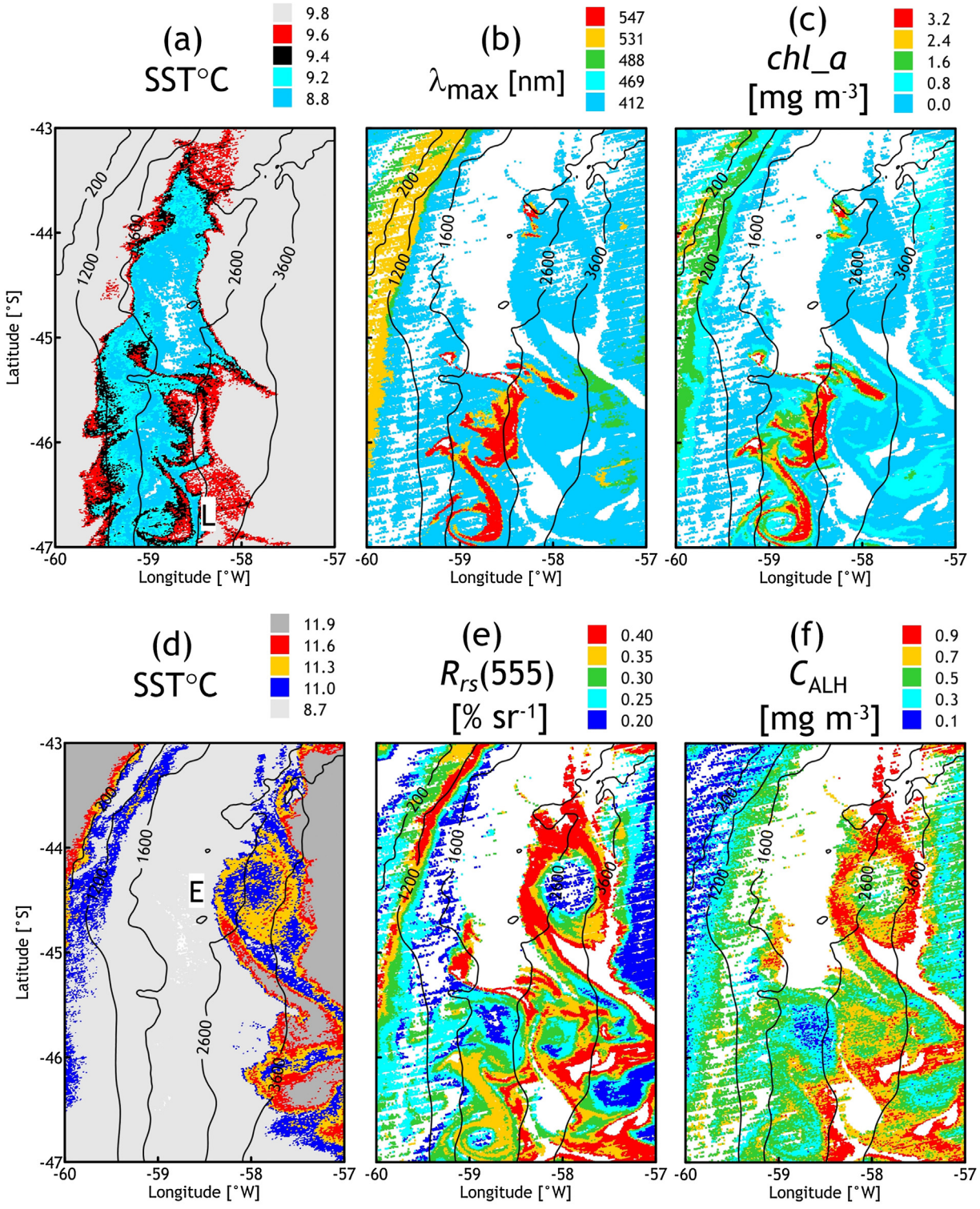

Figure 8 Distribution of SST ((a) and (d)) and bio-optical characteristics λ_{max} (b), *chl_a* (c), $R_{rs}(555)$ (e), and C_{ALH} (f) retrieved from attributes of pixels of cluster no. 3 in a fragment of testing site image of 2014-12-02. White spaces in maps (b), (c), (e), and (d) indicate missing data or pixels of clusters other than cluster no. 3.

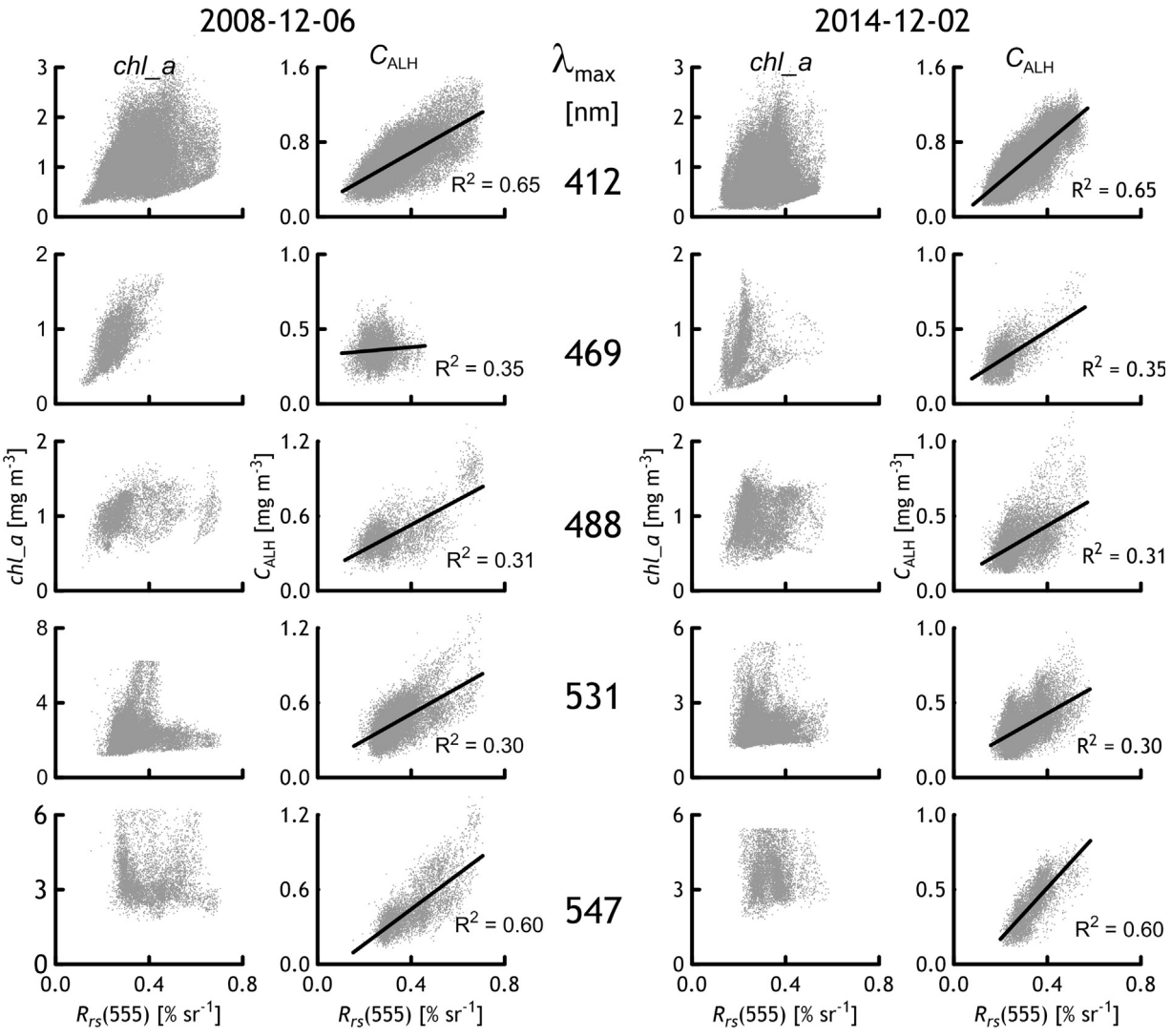

Figure 9 Plots of *chl_a* and C_{ALH} scatter relative to $R_{rs}(555)$. They are based on cluster no. 3 data divided into sub-clusters by wavelength of spectral maximums λ_{max} of pixels in images of 2008-12-06 (Fig. 6) and 2014-12-02 (Fig. 7). R^2 is the coefficient of determination.

with the chlorophyll *a*. Inability to resolve the combined reflectance spectrum of pigment mixture is a limitation inherent to the multispectral sensors.

4.2. Relation of C_{ALH} to bio-optical characteristics derivable from spectral reflectance

In a large natural water basin, unpredictable occurrence and relatively short residence time of mesoscale structures hamper the analysis of satellite data obtainable concurrently with a ship-borne and orbiting instruments. This sends us to a comparative qualitative analysis of C_{ALH} and well-understood quantities. To a first approximation, reflectance $R_{rs}(555)$ is a quantity determined by content of particles in water and independent of CDOM and phytoplankton pigments (Jerlov, 1976; Stramski et al., 2004). Therefore, $R_{rs}(555)$ may be regarded as an index of the water turbidity caused by suspended matter while C_{ALH} indicates the living particles. They are the main source of suspended matter of local origin in the shelf-break and adjacent waters and qualified as nanoplankton (Ferreira et al., 2013). Being larger than the wavelength of light (2 μm and more against $\lambda < 0.7$ μm), they non-selectively backscatter the solar radiation (Jerlov, 1976). Consequently, the CDOM and phytoplankton pigments are the main agents that dictate the shape of reflectance spectrum in the TS.

The linear relationship of C_{ALH} and $R_{rs}(555)$ in Fig. 9 agrees well with these considerations and the idea of ALH as a remote index of chlorophyll content in water. The coefficient of determination ranges from 0.30 to 0.65, points to moderately strong linear correlation of C_{ALH} with $R_{rs}(555)$, and appears quite expectable for genetically related but physically different substances. The graphs in Fig. 9 show that MODIS chlorophyll *chl_a* is unrelated to $R_{rs}(555)$ and to C_{ALH}. Chaotic scatter of *chl_a* relative to $R_{rs}(555)$ estimates is incompatible with the Case 1 water concept. The latter regards the algal mass as a sole source of suspended matter in water bodies free of sources of allochthonous optically

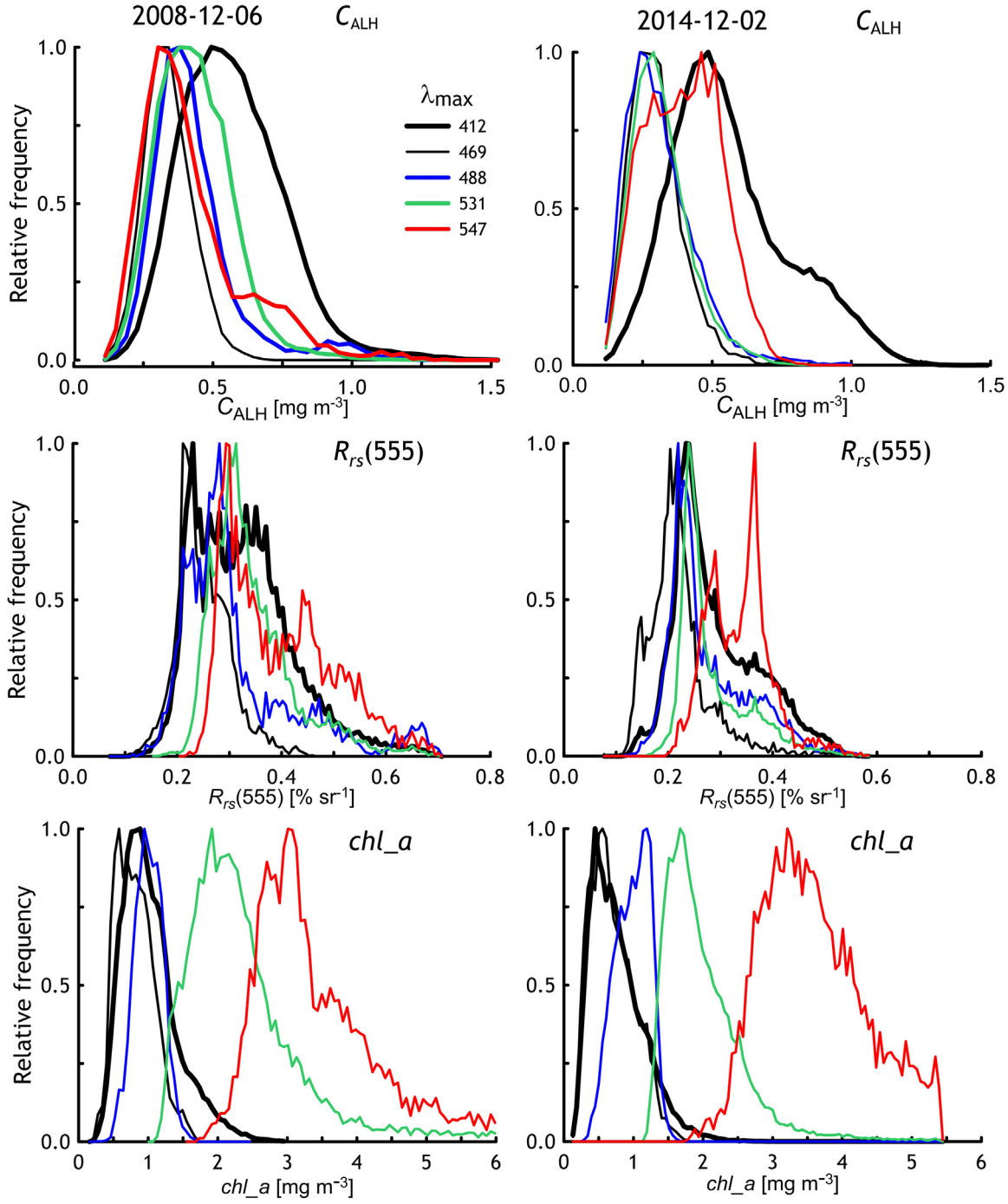

Figure 10 Relative frequencies of the estimates of NSM-chlorophyll C_{ALH}, reflectance R_{rs} (555), and MODIS chlorophyll *chl_a*. They rely on data of TS images taken by MODIS sensor for dates 2008-12-06 (Fig. 6) and 2014-12-02 (Fig. 7) and pertain to cluster no. 3 divided into sub-clusters by λ_{max} of reflectance spectra of individual pixels.

significant admixtures and is perfectly applicable to the BMCZ waters.

4.3. λ_{max} as an index of local relative abundance of CDOM

This quantity varies with the ratio of suspended matter to the CDOM: according to (1), at constant b_b, λ_{max} shifts to the red with the content of CDOM in water because absorption coefficient of the latter exponentially grows with diminishing wavelength. Suspended matter in waters of our testing site is dominated by relatively large particles because of their biological origination (Ferreira et al., 2013; Stramski et al., 2004). In this case, b_b is virtually independent of λ and CDOM abundance becomes the only cause of λ_{max} variability in the visible.

The concept of Case 1/Case 2 waters disregards two facts: (1) living algal cells release dissolved organic carbon (DOC) in

measurable quantities during log-phase growth (Chen and Wangersky, 1996a) and (2) this DOC might be highly labile to bacterial utilization and could be degraded significantly within hours (Chen and Wangersky, 1996b). The CDOM is a fraction of dissolved degradation products that absorbs light and emits fluorescence. The time scales of evolution of refractory CDOM considerably exceed the residence time of algal blooms induced by mesoscale dynamical events (from days up to 2–3 weeks). Thus, a bloom of algae is always accompanied by evolution of optically significant CDOM of algal origination.

This matters for remote determination of chlorophyll by means of band-ratio and band-difference algorithms. However, the first one relies on reflectances spaced in a wavelength scale by a hundred of nanometers while the band-difference algorithm for ALH determination involves violet-blue reflectances on each side of chlorophyll absorption peak at 443 nm. Hence, the ALH algorithm is tuned to the algae specific property while the band-ratio algorithms use much wider part of reflectance spectrum influenced by a number of natural admixtures in seawater, the products of algae degradation inclusive. These circumstances explain the similarity of patches of longer λ_{max} and higher *chl_a* in Figs. 4–8 and the dependence of *chl_a* distributions upon the λ_{max} in Fig. 10. Thus, the similarity of λ_{max} and *chl_a* in spatial distribution goes beyond the cases of mesoscale patches but is characteristic of the entire area of frequent occurrence of these inhomogeneities.

The products of degradation of a substance lag behind the evolution of substance itself by definition. It is reasonable to admit that co-existence of elevated λ_{max} with low C_{ALH} are indicative of senescent or extinct mesoscale algal blooms.

4.4. Origination of shortwave reflectance deficit

The absorption and backscattering spectra of non-pigment natural seawater admixtures in the visible appear as monotonous wavelength functions. Superposition of the latter results at best in a unimodal distribution of reflectance whose maximum shifts to the red with the content of CDOM in water (Jerlov, 1976). Undeniably, the chlorophyll and accessory phytoplankton pigments are the only seawater admixtures responsible for the shortwave reflectance minima because, firstly, they fall into the spectral range of absorption peaks of these pigments (Wozniak and Dera, 2007) and, secondly, their absorption considerably exceeds absorption of non-pigment natural admixtures in spectral selectivity.

It has been shown in the above Introduction that every instance of shortwave reflectance deficit in MODIS spectra took place at sites where algal cells accumulated near the water surface owing to various forcings. First, this is cell buoyancy tuning for surfacing in the case of cyanobacterial blooms. Second, the internal tide served as a driver of bloom in the Kerguelen area (Park et al., 2008) where the Circumpolar Current branch attacks the slope of the underwater plateau and, hypothetically, gives rise to an orographic upwelling that enhances the tide effect. Third, a quasi-permanent upwelling over the shelfbreak triggers the phytoplankton bloom hundreds of miles long and visible as a frequent feature in satellite images off the Patagonian shelf (Garcia et al., 2008; Matano and Palma, 2008).

Fig. 8 shows the TS part where NSMs occurred against a background of water exchange between the local waters and the Malvinas Current (low SST in map (a)). The latter comes from higher latitudes, where waters are colder and richer in CDOM (Nelson et al., 2010) relative to the BMCZ waters of moderate latitudes. Thus, the lower SST marks the outcroppings of Malvinas Current waters or their mixture with local waters because the SST signal originates in the skin layer of a water body. The shapes in Fig. 8 demonstrate various mesoscale patterns resulting from interaction of intruding and local waters. Loop L in map (a) coincides in space with well discriminable loops in the fields of λ_{max} (map (b)) and *chl_a* (map (c)). The same loop L is traced by medium level estimates of R_{rs} (555) (map(e)) but vanishes in the field of C_{ALH} (map (f)). In contrast, the shape of eddy-like structure E is reproduced by higher estimates of R_{rs}(555) (map (e)) and C_{ALH} (map (f)). To all appearance, this is a consequence of algal bloom induced by eddy E in the zone of horizontal water exchange between the northwards flowing Malvinas Current and warmer offshore waters. These patterns point to meso- and sub-mesoscale scale water dynamics near the air-water interface as the fourth ubiquitous cause of non-zero ALH estimates in Case 1 waters. Our interpretation is consistent with recent findings concerning the impact of mesoscale water dynamics on the primary production of the open ocean (Mahadevan, 2016; McGillicuddy et al., 2007).

4.5. C_{ALH} versus *chl_a* and FLH

Chlorophyll content in water retrieved from the sea surface reflectance is open to inacceptable bias if concentration of chlorophyll peaks below the layer of reflectance origination. The tentative thickness of this layer $Z = 1/K_d$ where K_d is the diffuse attenuation coefficient of solar radiation (Gordon and McCluney, 1975). According to Jerlov (1976), $Z \approx 55$ M in the clearest ocean water at $\lambda = 475$ nm. However, it has long been known that the chlorophyll maxima happen to be as deep as 100 m and deeper (Karabashev, 1987; McGillicuddy, 2001). In this respect, the ALH index offers no advantage over the multitude of algorithms appeared since late 1970s and based on the band-ratio approach (Blondeau-Patissier et al., 2014). However, the latter relies on empirical relation of reflectances that depend on a number of water constituents of elusive nature. In contrast, the ALH is obtainable from measured intensity of a physical phenomenon inherent to the substance to be determined. This approach corresponds to the principles of optical chemical analysis widely used in science and industry. The basic disadvantage of ALH-approach is higher scatter of chlorophyll determinations because the ALH is calculable as a difference of reflectances close in amplitude. To summaries, band-ratio methods are advantageous in lower output scatter while the ALH approach promises lower bias.

The ALH index is akin to the FLH index in that they are attributable to the chlorophyll as a water admixture. However, the former depends upon the absorption of light by chlorophyll while the latter is dependent on the same absorption plus the energy dissipation processes, the act of emitting fluorescence inclusive (Aiken, 2001). In the case of aquatic applications, at least three circumstances downgrade the

diagnostic potential of chlorophyll fluorescence as compared to the chlorophyll absorption of solar radiation.

(1) The chlorophyll fluorescence spectrum peaks at $\lambda \approx 678$ nm where water proper is the main contributor in seawater light absorption: in ocean waters at $\lambda = 675$ nm we have $0.42 < K_d < 0.52$ m^{-1} (Jerlov, 1976). Thus, $Z < 2.5$ m represents the thickness of origination layer of red reflectance round the ocean. In contrast, absorption bands of chlorophyll and accessory pigments of algae belong to the blue-green spectral range where remotely sensed reflectance originates from layers tens of meters thick in waters of high and moderate transparency (see above). As a result, the chlorophyll fluorescence from algal cells excited by shortwave solar radiation below 2.5 m depth level cannot be detected by ship-borne and satellite sensors throughout the World Ocean.
(2) The spectral resolution of multispectral sensors is too low to reliably avoid absorption features in the atmosphere and to resolve absorption and fluorescence bands of chlorophyll in the red (Letelier and Abbott, 1996).
(3) "The in vivo fluorescence (IVF) yield of chlorophyll has been reported to vary with species composition, size category, and time of day (IVF yields may be greater by a factor of 5 at night). Near-surface phytoplankton, in high light and with high photosynthetic activity, have reduced (quenched) IVF yield" (Aiken, 2001). This inconvenience is difficult to eliminate without resorting to ground truthing.

5. Conclusions

Analytical treatment of MODIS images of testing site in the Brazil-Malvinas Confluence Zone allowed us to:

(1) establish occurrence of reflectance NSM (reflectance deficit due to chlorophyll absorption) in the Brazil-Malvinas Confluence during austral summer,
(2) demonstrate association of reflectance NSM with the mesoscale dynamical structures and suitability of the NSM for indication of chlorophyll abundance in water,
(3) propose a new satellite indicator of chlorophyll abundance ALH (Absorption Line Height) based on reflectance minimum at 443 nm and calculable as linear interpolant of $R_{rs}(412)$ and $R_{rs}(469)$ to $\lambda = 443$ nm minus $R_{rs}(443)$,
(4) find the qualitative conformity of chlorophyll determinations in the BMCZ based on water sampling (Balch et al., 2014) with those based on linear dependence of the ALH upon chlorophyll concentration derived from the Caspian Sea ground truth data,
(5) reveal the informativeness of the multispectral λ_{max} as a measurable objective index of the CDOM impact on the reflectance spectrum of optically complex waters,
(6) propose a two-stage procedure for physical clustering the reflectance spectra of pixels of MODIS images based on evaluation of λ_{max} and the NSM characteristics.
(7) to demonstrate that the mesoscale structures in Case 1 waters are often accompanied by CDOM manifestations, which have no effect on ALH as index of chlorophyll abundance but are damaging for band-ratio algorithms for chlorophyll retrieving from multispectral reflectance of water surface.

Most likely, the index ALH will find use as a remote index of chlorophyll abundance in aquatic areas where phytoplankton accumulates just below the air-water interface due to adaptive behavior of algae, permanent water upwellings, and mesoscale water dynamics. The meso- and sub-mesoscale eddies are accepted as significant suppliers of nutrients into the photic layer of the ocean (McGillicuddy et al., 1998). It is felt that the ALH-based algorithm is advantageous in studies of eddy-driven blooms in Case 1 waters because it more adequately differentiates between the chlorophyll and by-products of algal life cycle. Hence, validation of trial solution (3) under the most diverse natural conditions is of crucial importance for implementing the results of the present paper.

The intermittency of spectral clusters within the testing site, the attribution of complex spectral shapes, and other previously mentioned phenomena deserve special consideration in parallel with efforts to squeeze out the maximum informativeness of the ALH index. This is particularly challenging in the case of blooms caused by the meso- and sub-mesoscale dynamical events because they are short-lived, sliding, and unpredictable. Our results can be useful for a qualitative analysis of the oceanological situation when preparing and supporting scientific biological-ecological expeditions and for exploration of oceanic fishing areas distinguished by considerable mesoscale variability.

Acknowledgments

The estimates of R_{rs}, chl_a, C_{ALH} and λ_{max} were retrieved from the L2 product of the MODIS Aqua available at the ocean color website (http://oceancolor.gsfc.nasa.gov/), NASA Goddard Space Flight Center, Ocean Ecology Laboratory, Ocean Biology Processing Group (Moderate-resolution Imaging Spectroradiometer (MODIS) Aqua Ocean Color Data; 2014).

This research was performed in the framework of the state assignment of FASO Russia (theme no. 0149-2018-0002).

References

Acha, E.A., Mianzan, H.W., Guerrero, R.A., Favero, M., Bava, J., 2004. Marine fronts at the continental shelves of austral South America. J. Mar. Syst. 44 (1–2), 83–105, http://dx.doi.org/10.1016/j.jmarsys.2003.09.005.

Aiken, J., 2001. Fluorometry for biological sensing. In: Steele, J.H., Turekian, K.K., Thorpe, S.A. (Eds.), Encyclopedia of Ocean Sciences. Acad. Press, London, 1695–1945, http://dx.doi.org/10.1006/rwos.2001.0338.

Balch, W.M., Drapeau, D.T., Bowler, B.C., Lyczkowski, E.R., Lubelczyk, L.C., Painter, S.C., Poulton, A.J., 2014. Surface biological, chemical, and optical properties of the Patagonian Shelf coccolithophore bloom, the brightest waters of the Great Calcite Belt. Limnol. Oceanogr. 59 (5), 1715–1732, http://dx.doi.org/10.4319/lo.2014.59.5.1715.

Barton, E.D., 2001. Island wakes. In: Steele, J.H., Turekian, K.K., Thorpe, S.A. (Eds.), Encyclopedia of Ocean Sciences. Acad. Press, London, 1397–1403, http://dx.doi.org/10.1006/rwos.2001.0338.

Blondeau-Patissier, D., Gower, J.F.R., Dekker, A.G., Phinn, S.R., Brando, V.E., 2014. A review of ocean color remote sensing methods and statistical techniques for the detection, mapping and analysis of phytoplankton blooms in coastal and open oceans. Progr. Oceanogr. 123, 123–144.

Chen, W., Wangersky, P.J., 1996a. Production of dissolved organic carbon in phytoplankton cultures as measured by high-temperature catalytic oxidation and ultraviolet photo-oxidation methods. J. Plankton Res. 18, 1201–1211, http://dx.doi.org/10.1093/plankt/18.7.1201.

Chen, W., Wangersky, P.J., 1996b. Rates of microbial degradation of dissolved organic carbon from phytoplankton cultures. J. Plankton Res. 18, 1521–1533, http://dx.doi.org/10.1093/plankt/18.9.1521.

Clarke, G.L., Ewing, G.C., Lorenzen, C.J., 1970. Spectra of backscattered light from the sea obtained from aircraft as a measure of chlorophyll concentration. Science 167 (3921), 1119–1121, http://dx.doi.org/10.1126/science.167.3921.1119.

d'Ortenzio, F., Marullo, S., Ragni, M., d'Alcalà, M.R., Santoleri, R., 2002. Validation of empirical SeaWiFS algorithms for chlorophyll-*a* retrieval in the Mediterranean Sea: A case study for oligotrophic seas. Remote Sens. Environ. 82 (1), 79–94, http://dx.doi.org/10.1016/S0034-4257(02)00026-3.

d'Ovidio, F., De Monte, S., Alvain, S., Dandonneau, Y., Levy, M., 2010. Fluid dynamical niches of phytoplankton types. PNAS 107 (43), 18366–18370.

Dupouy, C., Benielli-Gary, D., Neveux, J., Dandonneautelesc, Y., Westberry, T.K., 2011. An algorithm for detecting Trichodesmium surface blooms in the South Western Tropical Pacific. Biogeosciences 8, 3631–3647.

Ferreira, A., Stramski, D., Garcia, C.A.E., Garcia, V.M.T., Ciotti, A. M., Mendes, C.R.B., 2013. Variability in light absorption and scattering of phytoplankton in Patagonian waters: role of community size structure and pigment composition. J. Geophys. Res. Oceans 118 (2), 698–714, http://dx.doi.org/10.1002/jgrC.20082.

Garcia, C.A.E., Garcia, V.M.T., McClain, C.R., 2005. Evaluation of SeaWiFS chlorophyll algorithms in the Southwestern Atlantic and Southern Oceans. Remote Sens. Environ. 95, 125–137, http://dx.doi.org/10.1016/j.rse.2004.12.006.

Garcia, V.M.T., Garcia, C.A.E., Mata, M.M., Pollery, R.C., Piola, A.R., Signorini, S.R., McClain, C.R., Iglesias-Rodriguez, M.D., 2008. Environmental factors controlling the phytoplankton blooms at the Patagonia shelf-break in spring. Deep-Sea Res. Pt. I 55, 1150–1166, http://dx.doi.org/10.10l6/j.dsr.2008.04.011.

Georges, C., Monchy, S., Genitsaris, S., Christaki, U., 2014. Protist community composition during early phytoplankton blooms in the naturally iron-fertilized Kerguelen area (Southern Ocean). Biogeosciences 11, 5847–5863, http://dx.doi.org/10.5194/bg-11-5847-2014.

Gordon, H.R., McCluney, W.R., 1975. Estimation of the depth of sunlight penetration in the sea for remote sensing. Appl. Optics 14, 413–416.

Hu, C., Lee, Z., Franz, B., 2012. Chlorophyll *a* algorithms for oligotrophic oceans: a novel approach based on three-band reflectance difference. J. Geophys. Res. 117, C01011, http://dx.doi.org/10.1029/2011JC007395.

Jerlov, N.G., 1976. Marine Optics. Elsevier, Amsterdam, 233 pp.

Kalle, K., 1963. Über das Verhalten und die Herkunft der in den Gewässern und in der Atmosphäre vorhandenen himmelblauen Fluoreszenz. Deutsche Hydrografische Zeitschrift 16, 153–166.

Karabashev, G.S., 1987. Fluorescence in the Ocean. Gidrometeoizdat, Leningrad, http://dx.doi.org/10.13140/2.1.3439.7128, 200 pp., (in Russian).

Karabashev, G.S., Evdoshenko, M.A., 2015a. Spectral features of cyanobacterial bloom in the Baltic Sea from MODIS data. Sovremennye Problemy Distantsionnogo Zondirovaniya Zemli iz Kosmosa 12 (3), 158–170, (in Russian).

Karabashev, G.S., Evdoshenko, M.A., 2015b. On spectral indications of cyanobacteria blooms at ecologically different aquatic areas from satellite data. In: Proc. VIII Int. Conf. "Current Problems in Optics of Natural Waters" (ONW'2015), Saint-Petersburg, 171–176, http://dx.doi.org/10.13140/RG.2.1.2812.6161.

Karabashev, G.S., Evdoshenko, M.A., 2016. Narrowband shortwave minima in spectra of backscattered light from the sea obtained from ocean color scanners as a remote indication of algal blooms. Oceanologia 58 (5), 279–291, http://dx.doi.org/10.1016/j.oceano.2016.05.001.

Karabashev, G.S., Evdoshenko, M.A., 2017a. Shortwave minimums of reflectance of water surface as a remote indication of blooms of *Nodularia spumigena* in the southern Caspian Sea, 2017. Sovremennye Problemy Distantsionnogo Zondirovaniya Zemli iz Kosmosa 14 (1), 159–174, http://dx.doi.org/10.21046/2070-7401-2017-14-1-159-174 (in Russian).

Karabashev, G.S., Evdoshenko, M.A., 2017b. A new approach to satellite diagnostics of phytoplankton blooms from reflectance spectra of ocean surface. In: Proc. IX Int. Conf. "Current Problems in Optics of Natural Waters" (ONW'2017), Saint-Petersburg, 123–126.

Kopelevich, O.V., Burenkov, V.I., Goldin, Yu.A., Sheberstov, S.V., 2005. Bio-optical studies in the Atlantic ocean combining satellite and ship measured data. In: Proc. III Int. Conf. "Current Problems in Optics of Natural Waters" (ONW'20005), Saint-Petersburg, 193–198.

Kopelevich, O.V., Sheberstov, S.V., Sahling, I.V., Vazyulya, S.V., Burenkov, V.I., 2013. Bio-optical Characteristics of the Barents, White, Black, and Caspian Seas from Data of Satellite Ocean Color Scanners, http://optics.ocean.ru.

Letelier, R., Abbott, M., 1996. An analysis of chlorophyll fluorescence algorithms for the Moderate Resolution Imaging Spectrometer (MODIS). Remote Sens. Environ. 58, 215–223, http://dx.doi.org/10.1016/50034-4257(96)00073-9.

Loder, J.W., Boicourt, W.C., Simpson, J.H., 1998. Western ocean boundary shelves coastal segment (W). In: Robinson, A.R., Brink, K.H. (Eds.), The Sea, vol. 11. Wiley, New York, 3–27.

Lubac, B., Loisel, H., 2007. Variability and classification of remote sensing reflectance spectra in the Eastern English Channel and Southern North Sea. Remote Sens. Environ. 110, 45–58.

Mahadevan, A., 2016. The impact of submesoscale physics on primary productivity of plankton. Annu. Rev. Mar. Sci. 8, 161–184, http://dx.doi.org/10.1146/annurev-marine-010814-015912.

Matano, R.P., Palma, E.D., 2008. On the upwelling of downwelling currents. J. Phys. Oceanogr. 38, 2482–2500, http://dx.doi.org/10.1175/2008JPO3783.1.

Matano, R.P., Palma, A.R., Piola, A., 2010. The influence of the Brazil and Malvinas Currents on the Southwestern Atlantic Shelf circulation. Ocean Sci. 6, 983–995, http://dx.doi.org/10.5194/os-6-983-2010.

McClain, C., 2001. Ocean color from satellites. In: Steele, J.H., Turekian, K.K., Thorpe, S.A. (Eds.), Encyclopedia of Ocean Sciences. Acad. Press, London, 1695–1945, http://dx.doi.org/10.1006/rwos.2001.0338.

McGillicuddy Jr., D.J., 2001. Small-scale patchiness, models of. In: Steele, J.H., Turekian, K.K., Thorpe, S.A. (Eds.), Encyclopedia of Ocean Sciences. Acad. Press, London, 2820–2833, http://dx.doi.org/10.1006/rwos.2001.0405.

McGillicuddy Jr., D.J., Anderson, L.A., Bates, N.R., Bibb, T., Buesseler, K.O., Carlson, C.A., Davis, C.S., Ewart, C., Falkowski, P.G., Goldthwait, S.A., Hansell, D.A., Jenkins, W.J., Johnson, R., Kosnyrev, V.K., Ledwell, J.R., Qian, P. Li, Siegel, D.A., Steinberg, D.K., 2007. Eddy/wind interactions stimulate extraordinary mid-ocean plankton blooms. Science 316 (5827), 1021–1026, http://dx.doi.org/10.1126/science.1136256.

McGillicuddy Jr., D.J., Robinson, A.R., Siegel, D.A., Jannasch, H.W., Johnson, R., Dickey, T.D., McNeil, J., Michaels, A.F., Knap, A.H., 1998. Influence of mesoscale eddies on new production in the

Sargasso Sea. Nature 394 (6690), 263—266, http://dx.doi.org/10.1038/28367.

Mobley, C.D., Stramski, D., Bisset, W.P., Boss, E., 2004. Optical modeling of ocean water. Is the Case 1—Case 2 classification still useful? Oceanography 17 (2), 60—67.

Morel, A., 1988. Optical modeling of the upper ocean in relation to its biogenous matter content. J. Geophys. Res. 93 (10), 749—768, http://dx.doi.org/10.1029/JC093iC09p10749.

Morel, A., 2009. Are the empirical relationships describing the bio-optical properties of case 1 waters consistent and internally compatible? J. Geophys. Res. 114, C01016, http://dx.doi.org/10.1029/2008JC004803.

Morel, A., Huot, Y., Gentili, B., Werdell, P.J., Hooker, S.B., Franz, B. A., 2007. Examining the consistency of products derived from various ocean sensors in open ocean (Case 1) waters in the perspective of a multi-sensor approach. Remote Sens. Environ. 111, 69—88, http://dx.doi.org/10.1016/j.rse.2007.03.012.

Moreno, D.V., Pérez Marrero, J., Morales, J., Llerandi García, C., Villagarcía Úbeda, M.G., Rueda, M.J., Llinás, V., 2012. Phytoplankton functional community structure in Argentinian continental shelf determined by HPLC pigment signatures. Estuar. Coast. Shelf Sci. 100, 72—81.

Nelson, N.B., Siegel, D.A., Carlson, C.A., Swan, C.M., 2010. Tracing global biogeochemical cycles and meridional overturning circulation using chromophoric dissolved organic matter. Geophys. Res. Lett. 37, L03610, http://dx.doi.org/10.1029/2009GL042325.

Park, Y.-H., Fuda, J.-L., Durand, I., Garabato, S.C.N., 2008. Internal tides and vertical mixing over the Kerguelen Plateau. Deep-Sea Res. Pt. II 55, 582—593.

Piola, A.R., Matano, R., 2001. Brazil and Falklad (Malvinas) currents. In: Steele, J.H., Turekian, K.K., Thorpe, S.A. (Eds.), Encyclopedia of Ocean Sciences. Acad. Press, London, 340—349, http://dx.doi.org/10.1006/rwos.2001.0358.

Pope, R.M., Fry, E.S., 1997. Absorption spectrum (380—700 nm) of pure water. II. Integrating cavity measurements. Appl. Optics 36 (33), 8710—8723.

Sheberstov, S.V., 2015. System for batch processing of oceanographic satellite data. Sovremennye Problemy Distantsionnogo Zondirovaniya Zemli iz Kosmosa 12 (6), 154—161, (in Russian).

Stal, L.J., Albertano, P., Bergman, B., von Broeckel, K., Gallon, J.R., Hayes, P.K., Sivonen, K., Walsby, A.E., 2003. BASIC: Baltic Sea cyanobacteria. An investigation of the structure and dynamics of water blooms of cyanobacteria in the Baltic Sea—responses to a changing environment. Cont. Shelf Res. 23 (17—19), 1695—1714.

Stramski, D., Boss, E., Bogucki, D., Voss, K.J., 2004. The role of seawater constituents in light backscattering in the ocean. Prog. Oceanogr. (61), 27—56, http://dx.doi.org/10.1016/j.pocean.2004.07.001.

Telesca, L., Pierini, J.O., Lovallo, M., Santamaría-del-Angel, E., 2018. Spatio-temporal variability in the Brazil-Malvinas Confluence Zone (BMCZ), based on spectroradiometric MODIS-AQUA chlorophyll-*a* observations. Oceanologia 60 (1), 76—85, http://dx.doi.org/10.1016/j.oceano.2017.08.002.

Wozniak, B., Dera, J., 2007. Light Absorption in Sea Water. Springer Science, Business Media, New York, 463 pp.

Wozniak, S.B., Stramski, D., 2004. Modeling the optical properties of mineral particles suspended in seawater and their influence on ocean reflectance and chlorophyll estimation from remote sensing algorithms. Appl. Optics 43 (17), 3489—3503.

Oceanologia (2018) 60, 544—552

Available online at www.sciencedirect.com

ScienceDirect

journal homepage: www.journals.elsevier.com/oceanologia/

ORIGINAL RESEARCH ARTICLE

Primary productivity in the Gulf of Riga (Baltic Sea) in relation to phytoplankton species and nutrient variability

Ingrida Purina *, **Atis Labucis, Ieva Barda, Iveta Jurgensone, Juris Aigars**

Latvian Institute of Aquatic Ecology, Riga, Latvia

Received 8 January 2018; accepted 23 April 2018
Available online 8 May 2018

KEYWORDS
Primary production;
New production;
Mesodinium rubrum;
Aphanizomenon flosaquae;
Gulf of Riga;
Baltic Sea

Summary The seasonal patterns of primary production, phytoplankton biomass, chlorophyll *a*, and nutrients were investigated in the central part of the Gulf of Riga (Baltic Sea) during 2011 and 2012. Annual primary productivity in the gulf was in the range of 353.4—376.2 gC m^{-2}. Maximum carbon fixation rates occurred during the phytoplankton spring bloom from April to May when the winter nutrient pool was rapidly exhausted, suggesting the use of regenerated nutrients already in spring. The new production calculated on the draw-down of nitrates amounted to 51.80% of spring net community production. The production rates during summer were considerably lower owing to the availability of only regenerated nutrients and limited nitrogen fixation. Autumn was established as the least productive season. In autumn despite the elevated nutrient concentrations, the increasingly limited light hindered photosynthetic activity. Species governing the nutrient fluxes and the productivity of the Gulf of Riga are the diatom species responsible for new production in spring. The photosynthetic ciliate *Mesodinium rubrum* ((Lohmann) Hamburger & Buddenbrock 1911) prevailed in all seasons and significantly correlated with elevated productivity, while diazotrophic cyanobacteria *Aphanizomenon flosaquae* (Ralfs ex Bornet & Flahault 1886) contributed to new production in the summer nutrient regenerating system.

* Corresponding author at: Latvian Institute of Aquatic Ecology, Voleru Str. 4, LV-1007 Riga, Latvia. Tel.: +371 26186367.
E-mail address: ingrida.purina@lhei.lv (I. Purina).
Peer review under the responsibility of Institute of Oceanology of the Polish Academy of Sciences.

Production and hosting by Elsevier

https://doi.org/10.1016/j.oceano.2018.04.005

1. Introduction

Primary production in an aquatic ecosystem depends on the photosynthetic process carried out by autotrophic organisms such as phytoplankton, phytobenthos, and macroalgae, where phytoplankton is the main primary producer. The taxonomical composition of the microalgae, the physiological and ecological characteristics of individual species, and the availability and optimal use of essential resources such as light and nutrients are the major factors controlling growth processes and phytoplankton production (Smayda and Reynolds, 2001).

The primary production in the Gulf of Riga, considered one of the most eutrophic areas of the Baltic Sea, thus far has only been measured from 1989 to 1997. Earlier researchers used the C^{14} method (Andrushaitis et al., 1992) but later, during the project investigating the Gulf of Riga ecosystem from 1993—1995, the oxygen method was used (Olesen et al., 1999; Wassman and Tamminen, 1999). Andrushaitis et al. (1992) calculated an annual production of 250 gC m^{-2}, while Olesen et al. (1999) suggested that annual production could exceed 350 gC m^{-2}. The discrepancy was attributed to an underestimation of the gross primary production by the C^{14} method in systems with high growth rates and respiratory losses (Olesen et al., 1999). Simultaneously, during a comparative assessment of the coastal and open areas of the south-eastern Baltic Sea from 1993 to 1997, Wasmund et al. (2001) concluded that annual primary productivity in the Gulf of Riga reaches 250—255 gC m^{-2}, attributing the eutrophic status to the Gulf of Riga. Boreal environment determines the scenario of phytoplankton development in the gulf (Jurgensone et al., 2011; Olli and Heiskanen, 1999; Yurkovskis et al., 1999). Diatoms *Pauliella taeniata* ((Grunow) F.E. Round & P. W. Basson 1997) and *Thalassiosira baltica* ((Grunow) Ostenfeld 1901) dominate the spring blooms after ice melt from April to May. *Chaetoceros* spp. becomes dominant towards the end of the bloom accompanied by dinoflagellates *Peridiniella catenata* ((Levander) Balech 1977), and ciliate *Mesodinium rubrum*. With the development of thermal stratification and the depletion of nutrients, the spring bloom phytoplankton species are sedimenting. Blooms of cyanobacteria can be observed in July—August with dominating species *Aphanizomenon flosaquae*. Chlorophytes and cryptophytes are often accompanying cyanobacterial blooms. The second bloom of diatoms terminates the phytoplankton succession in September—October after the disruption of the thermocline and convective mixing of water column (Jurgensone et al., 2011; Yurkovskis et al., 1999 and the references therein). In autumn and winter, wind-induced mixing of the water column brings up nutrients from the bottom to the surface, supporting the growth of phytoplankton (Rydberg et al., 1990). But the significant shortening of daylight and low light intensity (Vihma and Haapala, 2009) hinders photosynthetic activity.

Although the phytoplankton and nutrient dynamic is well described in the Gulf of Riga, the linkage between phytoplankton production and nutrients to date is insufficiently described. This, in turn, does not allow proper characterization of the eutrophication process in the Gulf of Riga. Even less attention was paid to phytoplankton species involved in the primary production. Therefore the aim of this study was to examine the seasonal variation of primary production with a focus on the controlling nutrient fluxes as well as the species composition involved in the production.

2. Material and method

2.1. Study area

The Gulf of Riga (Baltic Sea) is a shallow water body with an average depth of 26.2 m. Its surface area is 16,330 km^2, however, its drainage area covers 135,700 km^2. The south-eastern part of the gulf receives 86.0% of the total river runoff from the main rivers, the Daugava, Lielupe, Gauja, and Salaca (Yurkovskis et al., 1993). The salinity is low (5—7 PSU) due to weak water exchange with the Baltic Sea and the large freshwater impact (Berzinsh, 1995). During winter, the water column of the gulf is well-mixed to the bottom due to convective and wind-induced mixing. During the productive season the stratification restricts vertical water exchange and promotes nutrient accumulation in the bottom layer (Yurkovskis, 2004).

Nutrient limitation is the most important factor governing the phytoplankton community. Most of the earlier nutrient limitation studies in the Gulf of Riga showed that the spring phytoplankton blooms are mainly nitrogen-limited in the central part while the coastal areas can be phosphate-limited (Tamminen and Seppälä, 1999). In contrast, recent studies of long-term phytoplankton data indicated that the spring blooms are mainly phosphorus limited, but could shift to nitrogen or silicate limitation for diatoms in the later stages of the bloom due to the faster regeneration of phosphate relative to the other nutrients (Jurgensone et al., 2011). During the summer period, the system is nitrogen limited in terms of phytoplankton (Balode et al., 1998; Põder et al., 2003; Tamminen and Seppälä, 1999) when both DIN and DIP are depleted in the upper mixed layer, whereas silicates are always present excluding silica limitation as a structuring factor for the summer community.

2.2. Sampling

Sampling was performed by ships A-90 “Varonis” and r/v “Salme”. Samples were collected at 5 regular monitoring stations in the central part of the Gulf of Riga (Fig. 1), 15 times each, over a period from April 2011 to October 2012 (Table 1) covering the full seasonal spectrum. Samples for the physical and chemical variables were taken simultaneously with biological variables. Water temperature and salinity was measured using a water probe (SBE 19plus SeaCat, USA). Water transparency was measured with Secchi disc. The water for physicochemical variables, phytoplankton, chlorophyll *a* concentrations, and primary production was sampled as an integrated sample from the euphotic upper layer (0—10 m).

2.3. Analytic analysis

Nutrient concentrations were determined according to Grasshoff et al. (1983), e.g. ammonium (NH_4^+) and phosphate (PO_4^{3-}) were measured by the indophenol blue and molybdenum blue methods, respectively. The sum of nitrate and

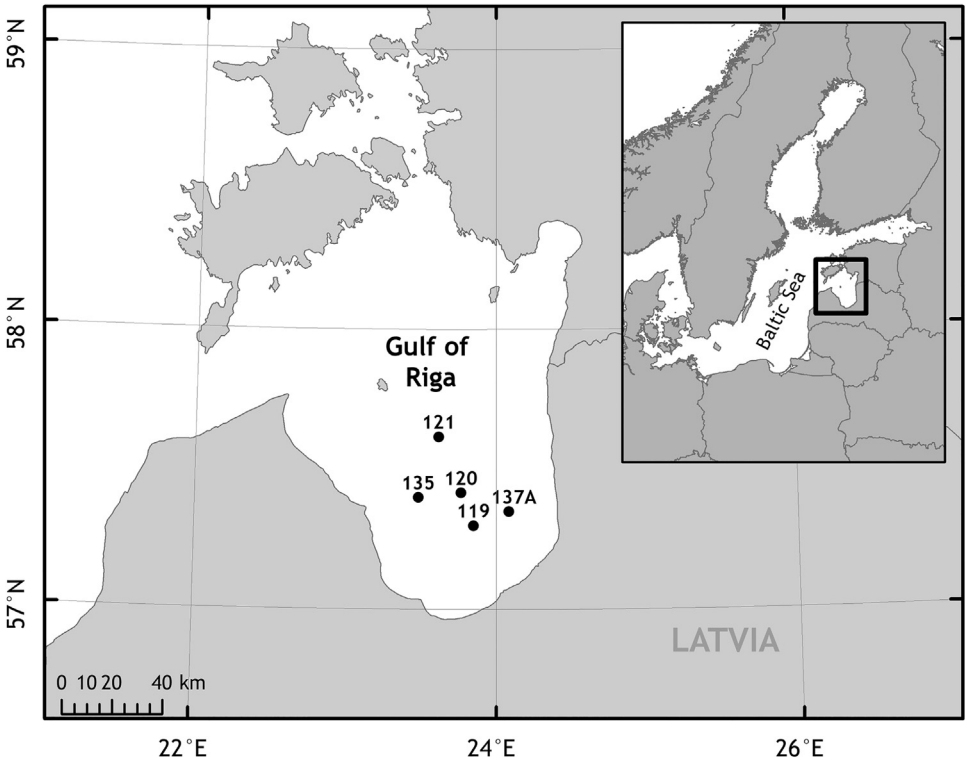

Figure 1 The location of the sampling stations in the Gulf of Riga.

Table 1 Average temperature, Secchi depth, hydrological and hydrochemical data in the central part of the Gulf of Riga during 2011 and 2012.

		Temp. [°C]	PAR [mol photons m^{-2} d^{-1}]	Secchi depth [m]	Photic zone depth [m]	PO_4^{-3} [μmol l^{-1}]	P_{tot} [μmol l^{-1}]	SiO_4 [μmol l^{-1}]	NO_{2+3}^{-} [μmol l^{-1}]	NH_4^{+} [μmol l^{-1}]	N_{tot} [μmol l^{-1}]	DIN/DIP ratio
2011	Apr	2.27	50.29	2.3	6.10	0.28	1.25	25.83	20.05	0.47	53.38	76.26
	May	6.24	45.85	2.8	7.50	0.03	1.00	5.23	4.17	0.10	37.32	128.38
	Jun	17.99	56.37	2.5	6.80	0.08	0.95	2.75	0.22	0.00	39.50	2.97
	Aug	19.71	48.95	4.0	10.70	0.02	0.65	4.99	0.17	0.29	33.36	23.44
	Oct	14.30	9.39	5.1	13.80	0.04	0.53	10.04	1.22	1.31	31.80	68.63
	Nov	9.33	11.63	3.9	10.40	0.41	0.76	20.26	5.95	0.04	28.26	14.79
2012	Jan	3.57	15.54	3.0	8.10	1.10	1.56	31.34	12.77	0.09	36.91	11.69
	Mar	0.18	20.65	4.1	11.00	1.00	1.40	33.44	15.63	0.07	39.25	15.83
	Apr	1.00	39.92	3.5	9.40	0.97	1.46	30.51	15.30	0.07	39.16	16.32
	May	8.08	41.81	2.1	5.60	0.04	1.45	2.05	2.87	0.07	44.94	39.89
	Jun	10.61	51.69	3.2	8.50	0.04	0.76	2.72	0.69	0.41	31.72	27.08
	Jul	15.30	49.54	3.8	10.20	0.01	0.67	3.25	0.40	1.47	36.84	132.13
	Aug	19.02	58.44	3.3	8.80	0.04	0.66	6.10	0.09	0.64	33.15	22.60
	Sep	16.30	34.57	4.5	12.30	0.10	0.58	8.61	0.40	1.24	31.90	17.44
	Oct	12.95	10.77	4.3	11.70	0.26	0.69	13.69	2.59	1.49	28.10	16.23

nitrite (NO_{2+3}^{-}) was determined by nitrite reaction with an azo dye after the reduction of nitrate to nitrite in a copper-coated cadmium column. The nitrite was determined by reaction with an azo dye and nitrate was determined as the difference between nitrite and the sum of nitrate and nitrite. Dissolved silicate (SiO_4) was determined colorimetrically according to the procedure described by Grasshoff et al. (1983). The total nitrogen (N_{tot}) and total phosphorus (P_{tot}) were analyzed as nitrate and phosphate after wet digestion with persulfate. Dissolved inorganic nitrogen (DIN) is the sum of NO_{2+3}^{-} and NH_4^{+}. All laboratory analyses were performed in an accredited laboratory (ISO/IEC 17025).

2.4. Chlorophyll *a* and phytoplankton analysis

Concentrations of chlorophyll *a* (Chl *a*, mg m^3) were measured according to the standard method of the Manual for Marine Monitoring in the COMBINE Programme of HELCOM (HELCOM, 2006).

Phytoplankton samples (300 ml) were fixed with acid Lugol's solution. Subsamples of 10 and 25 ml of fixed samples were settled in a sedimentation chamber for 12 h and counted according to the Uthermöl technique with an inverted microscope at 200× and 400× magnification. The number of counted cells in all subsamples exceeded 500 (Edler, 1979; HELCOM, 2006; Olenina et al., 2006; Utermöhl, 1958). The biomass was expressed as mg m^3 of wet weight. *M. rubrum* was included in phytoplankton counts as the only representative of division Ciliophora.

2.5. Primary production measurements

The light and dark bottle oxygen technique (Olesen et al., 1999) was used in order to evaluate the productivity of the study area. Water was filled in 15 transparent, calibrated glass bottles for oxygen measurements. Bottles were divided into 5 groups (with 3 replicates in each group) to imitate the light conditions at specific depths of the euphotic layer: Start, 100%, 66%, 23% and 0% light transmittance. Specific light transmittance to each group was provided by wrapping the bottles in the plastic optical filters produced by GAM-PRODUCTS, Inc.: no filter for 100% transparency, 1514 GAM for 66% transparency, 1516 GAM for 23% transparency and aluminium folium for 0% transparency. Initial oxygen concentrations were fixed with Winkler reagents (1 ml manganese chloride and 1 ml alkaline iodide) before incubation. All vials were mounted on a rotating wheel and submerged in the onboard incubator with a continuous flow of outboard seawater to ensure ambient water temperature and *in situ* illumination during the 24 h incubation. Photosynthetically active radiation (PAR) was measured on board using the LI-1400 Data Logger and the LI-190 Quantum Sensor during experimental incubation. At the end of incubation, samples were fixed with Winkler reagents. Oxygen concentrations were determined by titration with sodium thiosulphate.

Oxygen consumption in the dark bottles was used as a proxy for community respiration (CR), while the other three groups were used to evaluate daily, water column, primary production rates. Measured oxygen concentrations were converted to carbon units according to the stoichiometry of photosynthesis equation. The approximate attenuation coefficient (k) was calculated for each sampling from the simultaneously measured Secchi depth according to the equation $k = 1.7/D_s$, where D_s is Secchi depth. The depth of specific light conditions (z) was calculated from $z = -\ln I_z/I_o/k$, where I_z is light intensity at a specific depth (66% or 23%) and I_o is the light intensity below the surface (100%). Daily water column net community production (NCP, gC m^{-2} d^{-1}) rates were estimated by trapezoidal integration of the data from various light conditions. Gross primary production (GPP, gC m^{-2} d^{-1}) was calculated summing up the NCP and CR. GPP, NCP, and CR values from 5 stations were averaged to get the monthly average. Annual primary production was calculated as the GPP monthly averages multiplied by the number of days and summed up for 365 days.

2.6. New production calculation from nutrient concentrations

Since primary production rates have low representativeness in time and space, there have been attempts to use other parameters to calculate them, such as nutrient depletion (Rahm et al., 2000; Wasmund et al., 2005), increase in particulate organic carbon (Wasmund et al., 2005), and changes in CO_2 concentrations (Schneider et al., 2003). In our study, we applied the nutrient depletion method described in detail by Wasmund et al. (2005). We used data obtained during 2012, because the sampling frequency was higher this year, and calculated primary production, assuming that carbon, nitrogen, and phosphorus are assimilated in a stable molar ratio of 106:16:1 (Redfield et al., 1963). In April, what we consider the starting month of the spring bloom, the DIN:DIP ratio was 16.3 (Table 1), we assumed that the PO_4^{3-} excess production as described by Rahm et al. (2000) was not relevant for our calculations. The nutrient concentration decrease pattern suggests that the new production period lasts until June. We used concentration change (ΔDIN) in the upper mixed layer (0–20 m) to calculate new production for the period from April to May (1st period, 37 days) and for the period from May to June (2nd period, 23 days). We also considered air depositions of nitrogen in our calculations. Since there was no published information on air deposition for 2012, values calculated for 2010 were used instead. The air deposition over the whole surface area of the Gulf of Riga was 9973 t of nitrogen in 2010 (HELCOM, 2013). Averaging the deposited amount over the surface area of the Gulf of Riga (16,330 km^2), we estimated that nitrogen air deposition is 0.12 mmol m^{-2} day^{-1}. Since the Gulf of Riga is much more significantly impacted by river runoff than air deposition, we also considered the amount of DIN delivered by the four largest rivers, the Daugava, Gauja, Lielupe, and Salaca, which constitute close to 90% of freshwater input to the Gulf of Riga (Yurkovskis et al., 1993), over the respective period. The monitoring frequency was not sufficient for our purposes, so we used the linear regression method (Hirsch et al., 2010) to estimate missing values. The method employs the use of weighted regressions of concentrations on time, discharge, and season. This weighting results in a set of weights on every observation in the dataset, based on the selected values of time and discharge. So, we used known values of specific time and discharge to estimate the expected value of concentration. Data from national monitoring (e.g., flowrate and nutrient concentrations), stored in the database of Latvian Environment, Geology and Meteorology Centre, were used as input data. Estimated nitrogen loads were averaged over the whole area of the Gulf of Riga. Furthermore, from April to May, depletion of DIN could be observed in water layer 20–30 m. We used this concentration change to calculate an additional primary production for the 1st period.

Diatom biomass production was estimated from the silicate consumption by using N:Si = 1.25 mol mol^{-1} constant conversion factor (Sarthou et al., 2005). The nitrogen units thereafter were converted into carbon units by the Redfield ratio of C:N = 6.625 (Redfield et al., 1963).

3. Results

3.1. Environmental factors

The seasonal variation in water temperature, Secchi depth, PAR and nutrient concentrations are summarized in Table 1.

3.2. Phytoplankton and chlorophyll *a*

The highest phytoplankton biomass and Chl *a* were observed in spring — April 2011 and May 2012 (5715, 5411 mg m^{-3} and 18.5, 29.1 mg m^{-3}, respectively) (Fig. 2). However, the typical spring bloom of phytoplankton with high biomass and more than 90.0% dominance of diatoms, consisting mainly of *P. taeniata*, *Chaetoceros wighamii* (Brightwell 1856), and *T. baltica*, was observed only in April 2011. The succession of phytoplankton in May 2011 and 2012 was formed mainly from three taxonomical groups where single species composed up to 72.2—93.4% of the corresponding phytoplankton group — diatoms (*T. baltica*), dinoflagellates (*P. catenata*), and ciliophora (*M. rubrum*).

The summer (June—September) phytoplankton was characterized by relatively low Chl *a* and total phytoplankton biomass (Fig. 2). In this period, cyanobacteria (mostly N_2-fixing *A. flosaquae*) in both years constituted 15.2—57.8% of total phytoplankton biomass with the highest value in July 2012. The dominance of photosynthetic ciliate *M. rubrum* (56.3% of total biomass) was recorded in June 2012 (Fig. 2).

The autumn (October, November) phytoplankton consisted of cyanobacteria, diatoms, and *M. rubrum* (28.2%, 18.4% and 19.8%, respectively) in 2011, whereas in 2012 autumn was dominated by diatoms (>50.3%). The Chl *a* values were slightly higher in 2011 than in 2012 (Fig. 2). In the winter, total phytoplankton biomass (143.6—268.5 mg m^{-3}), as well as Chl *a* concentrations (1.62—1.71 mg m^{-3}), were low. The relative abundance of *M. rubrum* in the phytoplankton community increased during winter, reaching 34.2% of the total biomass in January. The next two most abundant groups, cyanobacteria (mainly *A. flosaquae*) and diatoms, composed 23.3 and 17.4%, respectively. The beginning of the increase in phytoplankton biomass was detected in March when *M. rubrum* composed, on average, 48.4% of total biomass.

3.3. Primary production and respiration

The data of primary production obtained from 5 stations were averaged for each month due to low variability in hydrological and hydrochemical conditions at the individual stations. Therefore, the patchiness of biological communities is the main source of measurement uncertainties. On average, the GPP was highest during the spring. Thereafter, it gradually decreased over summer and reached minimum values during the autumn—winter period (Fig. 3). Multiple regression analyses with dominant species as explanatory values showed the significant importance of *P. catenata* and *M. rubrum* in the formation of GPP in springtime in both years ($r^2 = 0.59$, $p = 0.009$, $n = 9$). The carbon biomass variance of both species explains 59.2% of GPP variance in spring. However, during summer, when similar dominance of *M. rubrum* and *A. flosaquae* was observed, no significant correlation could be established.

Plankton CR varied between 0.01—3.12 gC m^{-2} d^{-1} (average 1.01 gC m^{-2} d^{-1} of both years), accounting to 40.4% of GPP in 2011 and 68.5% in 2012. The rate of respiration mostly followed the pattern of GPP (Fig. 3), except in April 2012 when respiration exceeded GPP. NCP is also highest during the spring bloom and decreased over summer, except for in April 2012, when negative values of NCP were observed.

3.4. New production calculation from nutrient concentrations

The change of DIN concentrations in water from 15.3 μmol l^{-1} to 2.87 μmol l^{-1} (ΔDIN = 12.4 μmol l^{-1}) in the upper mixed layer (0—20 m) amounted to the new production of 1647 mmol C m^{-2} for the period from April to May (1st period) and ΔDIN = 2.18 μmol l^{-1} resulted in new production of 289 mmol C m^{-2} for the period from May to June (2nd period). The depletion of DIN from April to May in water layer 20—30 m (ΔDIN = 5.04 μmol l^{-1}) amounted to an additional primary production of 331 mmol C m^{-2} in the 1st period. The new production, estimated from average nitrogen air deposition rate (0.12 mmol m^{-2} day^{-1}), was 29.0 and 18.0 mmol C m^{-2} for the 1st and 2nd periods, respectively. The calculated average supply of riverine DIN was 289 t day^{-1} in April, 87 t day^{-1} in May and 38 t day^{-1} in June. Averaging received nitrogen over the area of the Gulf of Riga, we estimated an additional supply of 31.2 and 6.45 mmol N m^{-2} in the 1st and 2nd periods, respectively. This resulted in the new production of 205 and 40.1 mmol C m^{-2} in the 1st and 2nd periods, respectively.

The total new production estimated from DIN consumption summed to 2212 and 347 mmol C m^{-2} (26.6 and

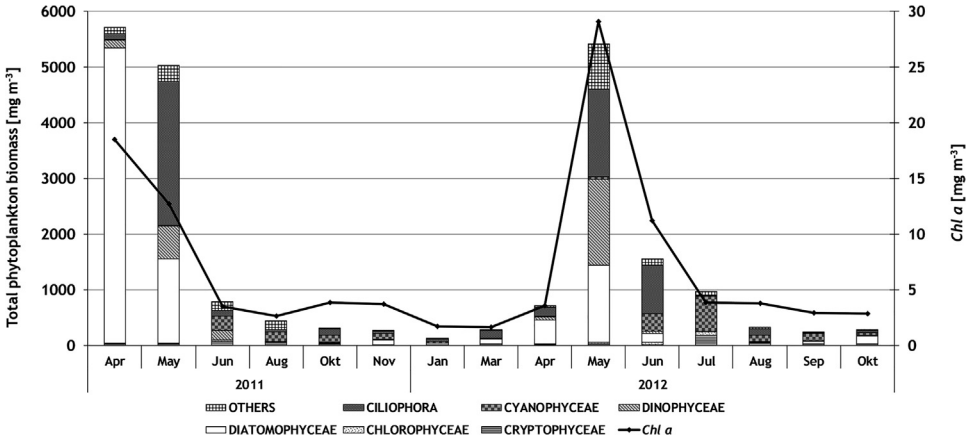

Figure 2 Total phytoplankton biomass and Chl *a* concentrations in the central part of the Gulf of Riga during 2011 and 2012.

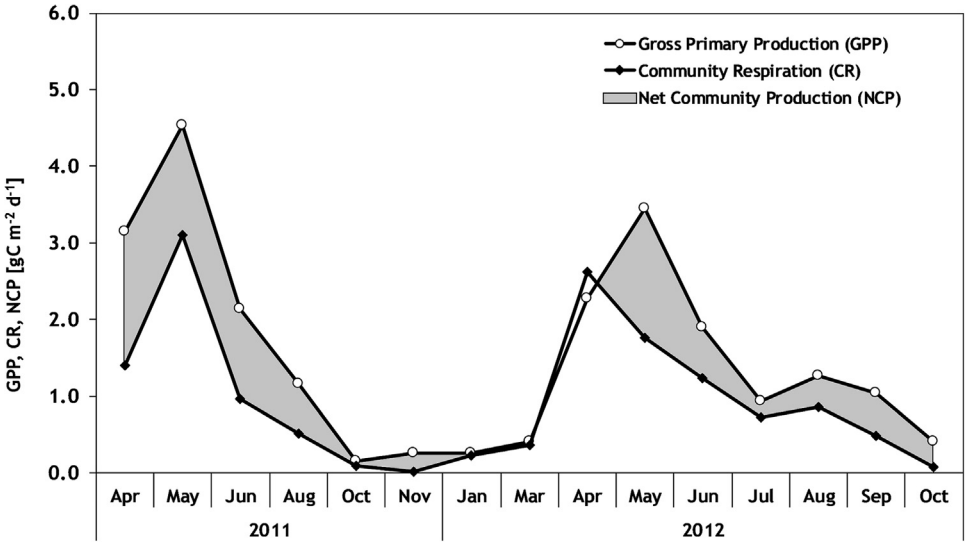

Figure 3 Average daily production (GPP and NCP) and CR in the central part of the Gulf of Riga during 2011 and 2012.

4.23 gC m^{-2}) for the 1st and 2nd period, respectively. The average new primary production rates estimated from the available DIN pool in the upper mixed layer and loads from atmosphere and rivers are 0.72 and 0.17 gC m^{-2} d^{-1} in May and June, respectively.

The change of silicate concentration in the upper mixed layer from April to May 2012 (Table 1) gave an estimate of ΔSi = 569 mmol m^{-2} for the 1st period. The concentration changes from 30.5 μmol l^{-1} to 15.3 μmol l^{-1} in the 20—30 m water layer, which gives an additional 155 mmol m^{-2} of silicate accessible for diatom growth. By applying conversion factors we estimated that new production of diatoms was 5997 mmol C m^{-2} in the 1st period, corresponding to a new production rate of 1.95 gC m^{-2} d^{-1}.

4. Discussion

4.1. Annual and seasonal primary productivity

In the northern temperate and boreal seas, including the Baltic Sea, the spring bloom, sustained by the nutrient winter pool, lasts approximately one month, but typically dominates the annual phytoplankton productivity cycle, contributing 40.0—60.0% of the annual carbon fixation (Heiskanen, 1998). The autumn bloom, sustained by the delivery of nutrients from deeper water layers upon the breakdown of seasonal stratification, is considered second most important period for annual phytoplankton productivity cycle. The summer production and biomass are considered to be low in comparison to the spring bloom period, while winter production is usually neglected as important. This has been somewhat challenged in the past (Platt et al., 1989; Stigebrandt and Djurfeldt, 1996) especially in the case of summer productivity (Sahlsten et al., 1988). In our study, the spring bloom (April—May) comprised 46.3% while summer productivity made another 44.5% of annual productivity. The autumn-winter productivity (October—March) comprised the remaining 10.2% of the annual productivity. Moreover, in our study we established that the least productive period is during October—November despite the water temperature still remaining rather high (13.4°C) and nutrient concentrations substantially increasing due to the breakdown of thermal stratification and resuspension of re-mineralized nutrients from deeper layers. The autumn is characterized by strong, westerly winds that bring mild and moist Atlantic air to northern Europe (Vihma and Haapala, 2009), resulting in dense cloud cover and frequent rain. At the same time the shortening of daylight hours (from 10 h 50 min in October to 6 h 40 min in December) can be observed. Therefore, we can hypothesize, that meteorological conditions in autumn lead to strong light limitation of GPP despite rather good water transparency conditions measured as Secchi depth (Table 1). Later, the onset of colder winter air temperatures results in clear skies and higher light intensity. As a result, relatively low but still comparable primary production was also measured during winter months that previously were considered unproductive.

The annual primary productivity in the Gulf of Riga reached values as high as 353—376 gC m^{-2} in our study, while in the previous studies (Andrushaitis et al., 1992; Wasmund et al., 2001) the estimated annual primary productivity of the Gulf was only 250—255 gC m^{-2} for the period of 1993—1995. However, this estimate was based on measurements that had not included the most productive period of phytoplankton succession from the end of March until the end of April when the biomass of spring diatoms can reach even 20.3 g m^{-3} (Yurkovskis et al., 1999). This allowed the Olesen et al. (1999) to hypothesize that primary productivity in the Gulf of Riga can exceed 350 gC m^{-2}. So, our values of annual production were similar to estimations of Olesen et al. (1999). At the same time, we cannot exclude the possibility that the productivity values in our study were still underestimated since sampling frequency was still too low to fully capture spring phytoplankton bloom development. For example, phytoplankton biomass and composition from April to May 2012 could not explain the depleted pool of SiO_4, suggesting that diatom bloom between these sampling events was unregistered by our study at least at the level of that observed in April 2011.

4.2. New production

The values of new production calculated from nutrient concentrations (0.70 and 0.17 gC m^{-2} d^{-1}, in May and June, respectively) were substantially lower than measured NCP rates, e.g., 1.68 and 0.72 gC m^{-2} d^{-1}, in May and June, respectively. The total new production, calculated from the nitrate consumption, was equivalent to 51.8% of spring NCP. Smetacek et al. (1984) divided the spring bloom into two stages. Stage 1 was characterized by a rapid bloom of diatoms exhausting the winter-accumulated nutrient pool where production is strictly "new" in the sense of Dugdale and Goering (1967). Stage 2 was characterized by the dominance of dinoflagellates and an increase of protozooplankton. Loss rates of this planktonic system were amongst the lowest of the year, indicating a great retention capacity (Smetacek et al., 1984). The new production during stage 1 was >75.0% of NCP, but during stage 2 it was approximately 50%. These data were consistent with our calculations where new production, based on nutrient consumption, composed 51.8% of NCP during both stages of spring bloom. At steady state, there should be a balance between the input of nitrogen and the export of carbon, implying that on a longer time scale, sedimentary loss from the pelagic system approaches new production (Eppley et al., 1983). This could be the case in the Gulf of Riga as the bloom of diatoms, that used most of nitrates and predominantly contributed to the new production and sedimentation fluxes, was largely unobserved in 2012. However, if new production is calculated from the consumption of SiO_4 according to Wasmund et al. (2013), it alone gives an average estimate of 1.95 gC m^{-2} d^{-1} for the first period. As no other algae, except diatoms, can use SiO_4, the bloom maxima of diatoms should be assumed between the sampling occasions in April and May 2012 followed by rapid sedimentation as diatoms composed only 25.2% of total phytoplankton biomass in May. The excess consumption of silica can be explained either by different silicification of diatom species (Olli et al., 2008) or by diatom resting spore formation as this process requires plenty of silicate. It has been reported that the resting spores generally have higher sinking rates than vegetative cells (Alldredge et al., 1995). The spore formation in the deeper water layers could explain the SiO_4 consumption in the 20–30 m (data not shown) layer of the Gulf of Riga.

4.3. Influence of dominant species on the nutrient fluxes and productivity

The species which exert a dominant role in the planktonic ecosystem are often those that govern the fluxes of organic matter and nutrients in the pelagic system (Heiskanen, 1998). To understand the functioning of the aquatic ecosystem it is necessary to understand the role, regulation, and species-specific properties of the "key" species (Verity and Smetacek, 1996).

The main "key" planktonic species dominating almost all seasons was photosynthetic ciliate *M. rubrum*. Leppänen and Bruun (1986) reported that *M. rubrum* contributed about 10.0% of the primary production during spring in the open northern Baltic. Similar values of 6.00–9.00% of phytoplankton biomass and production have also been shown for *M. rubrum* in the Gdańsk Basin of the southern Baltic Sea (Witek, 1998). It appears that in the Gulf of Riga, *M. rubrum* plays an even more important role in the primary production than in other regions of the Baltic Sea, since its biomass composed 18.2–73.9% of the total phytoplankton biomass during the spring bloom period in May, 6.22–41.4% during summer, 14.9–22.2% during autumn, and 40.1–61.3% during winter. Significant positive correlation was detected between the biomass of *M. rubrum* and GPP ($r = 0.650$, $p > 0.001$, $n = 42$). The importance of *M. rubrum* in the Gulf of Riga was observed during periods when nutrient recycling was the most important (spring–summer) as well as during periods when nutrients were freely available, but the light limited the phytoplankton development (autumn–winter). It has been observed that *M. rubrum* demonstrates an ability to accumulate near the sea surface and to photosynthesize at high light intensities (Esteban et al., 2010). At the same time, it has been noted that *M. rubrum* can also tolerate the low-light conditions, composing the main phytoplankton biomass also during winter period (Moeller et al., 2011). In addition, its rapid swimming behaviour appears to reduce its susceptibility to grazing (Jonsson and Tiselius, 1990) and may increase its ability to utilize nutrient micropatches (Stoecker et al., 1991). Our study confirms that the *M. rubrum* is a highly competitive and opportunistic specie that substantially contributes to the productivity of the Gulf of Riga.

Another "key" species substantially contributing to productivity and internal nutrient fluxes of the Gulf of Riga is *A. flosaquae*. Filamentous, N_2-fixing cyanobacteria are well known for bloom formation during August–September in the Baltic Sea (Kahru et al., 1994). In our study, the relative dominance of *A. flosaquae* (18.7–37.4% of total phytoplankton biomass) begun in June when inorganic nutrients (both, N and P) were exhausted, reached a maximum in July (59.4–65.2%) and continued until September (21.3–42.1%). The blooms of *A. flosaquae* are usually associated with calm weather, high surface temperatures, availability of phosphates, and a low DIN:DIP ratio (Kononen et al., 1996). However, according to the results of this study, the phosphates were exhausted already during the spring bloom creating the apparent phosphorus limitation in May (Table 1). This suggested that N_2 fixation was not likely to occur during the summer. Furthermore, the increase of *A. flosaquae* biomass from 309 mg m^{-3} (in June 2012) to 543 mg m^{-3} (in July 2012) was observed simultaneously with the fast increase of the DIN:DIP ratio as well as increase of total N (Table 1). The river runoff and atmospheric deposition was of the secondary importance, since both these nutrient pathways are relatively small during the summer and unlikely to sustain, or let alone increase, the observed population. At the same time, Ploug et al. (2010) showed that *A. flosaquae* was highly productive in the Baltic Sea with high rates of C and N assimilation and the capacity to release a large fraction (35.5%) of newly assimilated N to the surrounding water. This allowed us to create a hypothesis that the population of *A. flosaquae* sustains the observed population level by rapid recirculation of phosphorus upon the death of phytoplankton cells and the assimilation of nitrogen via N_2 fixation to compensate nitrogen loss in the sedimentation pathway.

The importance of *M. rubrum* and *A. flosaquae* was also observed during the autumn and winter seasons. However, more observations were needed to understand their roles

during those seasons as well as regulatory factors of these species under conditions of limited light and replenished nutrients.

5. Conclusions

The annual primary productivity in the Gulf of Riga reached values 353—376 gC m^{-2} in our study. It showed no significant increase of productivity since 1992—1998. Spring bloom (April—May) comprised 46.2% of annual production with maximal carbon fixation rates and draw-down of winter nutrient pool. The new production calculated from consumption of nitrates amounted to 51.8% of spring NCP. Detailed examination of phytoplankton species along with measurements of productivity revealed key species governing the nutrient fluxes and the productivity of the Gulf of Riga. The autotrophic ciliate *M. rubrum* prevailed in all seasons and significantly correlated with elevated productivity, while diazotrophic cyanobacteria *A. flosaquae* contributed to "new production" in the summer nutrient-regenerating system.

Acknowledgements

This study was supported by the project "Development of a mechanistic model of the Gulf of Riga ecosystem in support of efficient national policy to ensure the protection of the Baltic Sea and to promote the sustainable use of its ecosystem (LIMOD)" (Nr.2010/0287/2DP/2.1.1.1.0/10/APIA/VIAA/040) funded by European Regional Development Fund and State research programme EVIDEnT.

We would like to warmly thank our colleagues Ilva Vasmane for phytoplankton analysis, Ņina Sunelika, Alla Ivakina, Elvita Eglīte, Miķelis Mazmačs and Mintauts Jansons for nutrient analysis and work on-board, as well as crews of r/v "Salme" and A-90 "Varonis". We would like to warmly thank Ilona Staprans and Nicole Zviedrite for English corrections. The research leading to these results has also received funding from the European Union Seventh Framework Programme (FP7/2007—2013) under grant agreement n° [228344], [EUROFLEETS].

References

Alldredge, A.L., Gotschalk, C., Passow, U., Riebesell, U., 1995. Mass aggregation of diatom blooms: insights from a mesocosm study. Deep-Sea Res. 42, 9—27.

Andrushaitis, G., Andrushaitis, A., Bitenieks, Y., Priede, S., Lenshs, E., 1992. Organic carbon balance of the Gulf of Riga. In: Swed. Hydrol. Meteor. Inst. Rep., Proc. 17th CBO Conf., Norrköping, p. 1009.

Balode, M., Purina, I., Bechemin, C., Maestrini, S., 1998. Effects of nutrient enrichment on the growth rates and community structure of summer phytoplankton from the Gulf of Riga, Baltic Sea. J. Plankton Res. 20, 2251—2272.

Berzinsh, V., 1995. Hydrology. In: Ojaveer, E. (Ed.), Ecosystem of the Gulf of Riga Between 1920 and 1990. Estonian Acad. Publ., Tallin, 7—31.

Dugdale, R.C., Goering, J.J., 1967. Uptake of new and regenerated forms of nitrogen in primary productivity. Limnol. Oceanogr. 12, 196—206.

Edler, L., 1979. Recommendations on Methods for Marine Biological Studies in the Baltic Sea. Phytoplankton and Chlorophyll, vol. 5. Baltic Marine Biol. Publ., 38 pp.

Eppley, R.W., Renger, E.H., Betzer, P.R., 1983. The residence time of particulate organic carbon in the surface layer of the ocean. Deep-Sea Res. 30, 311—323.

Esteban, G.F., Fenchel, T., Finlay, B.J., 2010. Mixotrophy in ciliates. Protist 161 (5), 621—641, http://dx.doi.org/10.1016/j.protis.2010.08.002.

Grasshoff, K., Ehrhardt, M., Kremling, K., 1983. Methods of Seawater Analysis, 2nd ed. Verlag Chemie, Weinheim, 600 pp.

Heiskanen, A.-S., 1998. Factors Governing Sedimentation and Pelagic Nutrient Cycles in the Northern Baltic Sea. Monographs Boreal Environ. Res. 8. Finnish Environ. Inst., Helsinki, 80 pp.

HELCOM, 2006. Manual of Marine Monitoring Programme in the COMBINE Programme of HELCOM, Part C, Retrieved from: http://www.helcom.fi/Documents/Action%20areas/Monitoring%20and%20assessment/Manuals%20and%20Guidelines/Manual%20for%20Marine%20Monitoring%20in%20the%20COMBINE%20Programme%20of%20HELCOM.pdf (accessed 04 2018).

HELCOM, 2013. Review of the Fifth Baltic Sea Pollution Load Compilation for the 2013 HELCOM Ministerial Meeting. Balt. Sea Environ. Proc. No. 141 Retrieved from: http://www.helcom.fi/Lists/Publications/BSEP141.pdf (accessed 04 2018).

Hirsch, R.M., Moyer, D.L., Archfield, S.A., 2010. Weighted regressions on time, discharge, and season (WRTDS), with an application to Chesapeake Bay river inputs. J. Am. Water Res. Assoc. 46 (5), 857—880, http://dx.doi.org/10.1111/j.1752-1688.2010.00482.x.

Jonsson, P.R., Tiselius, P., 1990. Feeding behavior, prey detection and capture efficiency of the copepod *Acartia tonsa* feeding on planktonic ciliates. Mar. Ecol. Prog. Ser. 60, 35—44.

Jurgensone, I., Carstensen, J., Ikauniece, A., Kalveka, B., 2011. Long-term changes and controlling factors of phytoplankton community in the Gulf of Riga (Baltic Sea). Estuar. Coast. 34 (6), 1205—1219, http://dx.doi.org/10.1007/s12237-011-9402-x.

Kahru, M., Horstmann, U., Rud, O., 1994. Satellite detection of increased cyanobacteria blooms in the Baltic Sea: natural fluctuation or ecosystem change? Ambio 23 (8), 469—472.

Kononen, K., Kuparinen, J., Mäkelä, K., Laanemts, J., Pavelson, J., Nommann, S., 1996. Initiation of cyanobacterial blooms in a frontal region at the entrance to the Gulf of Finland, Baltic Sea. Limnol. Oceanogr. 41, 98—112.

Leppänen, J.M., Bruun, J.E., 1986. The role of pelagic ciliates including the autotrophic *Mesodinium rubrum* during the spring bloom of 1982 in the open northern Baltic proper. Ophelia 4, 147—157.

Moeller, H.V., Johnson, M.D., Falkowski, P.G., 2011. Photoacclimation in the phototrophic marine ciliate *Mesodinium rubrum* (Ciliophora). J. Phycol. 47 (2), 324—332, http://dx.doi.org/10.1111/j.1529-8817.2010.00954.x.

Olenina, I., Hajdu, S., Andersson, A., Edler, L., Wasmund, N., Busch, S., Göbel, J., Gromisz, S., Huseby, S., Huttunen, M., Jaanus, A., Kokkonen, P., Ledaine, I., Niemkiewicz, E., 2006. Biovolumes and size-classes of phytoplankton in the Baltic Sea. BSEP 106, 1—144.

Olesen, M., Lundsgaard, C., Andrushaitis, A., 1999. Influence of nutrients and mixing on the primary production and community respiration in the Gulf of Riga. J. Mar. Syst. 23, 127—143.

Olli, K., Clarke, A., Danielsson, Å., Aigars, J., Conley, D.J., Tamminen, T., 2008. Diatom stratigraphy and long-term silica concentrations in the Baltic Sea. J. Mar. Syst. 73 (3—4), 284—299, http://dx.doi.org/10.1016/j.jmarsys.2007.04.009.

Olli, K., Heiskanen, A.-S., 1999. Seasonal stages of phytoplankton community structure and sinking loss in the Gulf of Riga. J. Mar. Syst. 23, 165—184.

Platt, T., Harrison, W.G., Lewis, M.R., Li, W.K.W., Sathyendranath, S., Smith, R.E., Vezina, A.F., 1989. Biological production of the oceans: the case of consensus. Mar. Ecol. Prog. Ser. 52, 77—88.

Ploug, H., Musat, N., Adam, B., Moraru, C.M., Lavik, G., Vagner, T., Bergman, B., Kuypers, M.M.M., 2010. Carbon and nitrogen fluxes associated with the cyanobacterium *Aphanizomenon* sp. in the Baltic Sea. ISME J. 4, 1215–1223, http://dx.doi.org/10.1038/ismej.2010.53.

Põder, T., Maestrini, S.Y., Balode, M., Lips, U., Bèchemin, C., Andrushaitis, A., Purina, I., 2003. The role of inorganic and organic nutrients on the development of phytoplankton along the transect from Daugava River mouth to the Open Baltic in spring and summer 1999. ICES J. Mar. Sci. 60 (4), 827–835, http://dx.doi.org/10.1016/S1054-3139(03)00069-9.

Rahm, L., Jönsson, A., Wulff, F., 2000. Nitrogen fixation in the Baltic Proper: an empirical study. J. Mar. Syst. 25 (3–4), 239–248, http://dx.doi.org/10.1016/S0924-7963(00)00018-X.

Redfield, A.C., Ketchum, B.H., Richards, F.A., 1963. The influence of organisms on the composition of seawater. In: Hill, M.N. (Ed.), The Sea, vol. 2. Intersci. Publish. John Wiley & Sons, New York, 26–77.

Rydberg, L., Edler, L., Floderus, S., Graneli, W., 1990. Interaction between supply of nutrients, primary production, sedimentation and oxygen consumption in SE Kattegatt. Ambio 19, 134–141.

Sahlsten, E., Sörensen, F., Pettersson, K., 1988. Planktonic nitrogen uptake in the south-eastern Kattegat. J. Exp. Mar. Biol. Ecol. 121, 227–246.

Sarthou, G., Timmermans, K.R., Blain, S., Treguer, P., 2005. Growth physiology and fate of diatoms in the ocean: a review. J. Sea Res. 53 (1–2), 25–42, http://dx.doi.org/10.1016/j.seares.2004.01.007.

Schneider, B., Nausch, G., Nagel, K., Wasmund, N., 2003. The surface water CO_2 budget for the Baltic Proper: a new way to determine nitrogen fixation. J. Mar. Syst. 42 (1–2), 53–64, http://dx.doi.org/10.1016/S0924-7963(03)00064-2.

Smayda, T.S., Reynolds, C.S., 2001. Community assembly in marine phytoplankton: application of recent models to harmful dinoflagellate blooms. J. Plankton Res. 23 (5), 447–461, http://dx.doi.org/10.1093/plankt/23.5.447.

Smetacek, V., Bodungen, B.V., Knoppers, B., Peinert, R., Pollehne, F., Stegmann, P., Zeitzsehel, B., 1984. Seasonal stages in characterizing the annual cycle of an inshore pelagic system. Rapp. P-v. Rdun. Cons. mt. Explor. Mer 183, 126–135.

Stigebrandt, A., Djurfeldt, L., 1996. Control of production of organic matter in the ocean on short and long terms by stratification and remineralisation. Deep-Sea Res. Pt. II 43 (1), 23–35.

Stoecker, D.K., Putt, M., Davis, L.H., Michaels, A.E., 1991. Photosynthesis in *Mesodinium rubrum:* species specific measurements and comparison to community rates. Mar. Ecol. Prog. Ser. 73, 245–252.

Tamminen, T., Seppälä, J., 1999. Nutrient pools, transformations, ratios, and limitation in the Gulf of Riga, the Baltic Sea, during four successional stages. J. Mar. Syst. 23, 83–106.

Utermöhl, H., 1958. Zur Vervollkommnung der quantitativen Phytoplankton-Methodik. Mitt int. Verein. Theor. Angew. Limnol. 9, 1–38.

Verity, P., Smetacek, V., 1996. Organism life cycles, predation, and the structure of marine pelagic ecosystems. Mar. Ecol. Prog. Ser. 130, 277–293.

Vihma, T., Haapala, J., 2009. Geophysics of sea ice in the Baltic Sea: a review. Progr. Oceanogr. 80 (3–4), 129–148, http://dx.doi.org/10.1016/j.pocean.2009.02.002.

Wasmund, N., Andrushaitis, A., Łsiak-Pastuszak, E., Müller-Karulis, B., Nausch, G., Neumann, T., Ojaveer, H., Olenina, I., Postel, L., Witek, Z., 2001. Trophic status of the south-eastern Baltic sea: a comparison of coastal and open areas. Estuar. Coast. Shelf Sci. 53 (6), 1–16, http://dx.doi.org/10.1006/ecss.2001.0828.

Wasmund, N., Nausch, G., Feistel, R., 2013. Silicate consumption: an indicator for long-term trends in spring diatom development in the Baltic Sea. J. Plankton Res. 35 (2), 393–406, http://dx.doi.org/10.1093/plankt/fbs101.

Wasmund, N., Nausch, G., Schneider, B., 2005. Primary production rates calculated by different concepts – an opportunity to study the complex production system in the Baltic Proper. J. Sea Res. 54 (4), 244–255, http://dx.doi.org/10.1016/j.seares.2005.07.004.

Wassman, P., Tamminen, T., 1999. Pelagic eutrophication and sedimentation in the Gulf of Riga: a synthesis. J. Mar. Syst. 23, 269–283.

Witek, M., 1998. Annual changes of abundance and biomass of planktonic ciliates in the Gdańsk Basin, southern Baltic. Int. Rev. Hydrobiol. 83, 163–182.

Yurkovskis, A., 2004. Long-term land-based and internal forcing of the nutrient state of the Gulf of Riga (Baltic Sea). J. Mar. Syst. 50 (3–4), 181–197, http://dx.doi.org/10.1016/j.jmarsys.2004.01.004.

Yurkovskis, A., Kostrichkina, E., Ikauniece, A., 1999. Seasonal succession and growth in the plankton communities of the Gulf of Riga in relation to long-term nutrient dynamics. Hydrobiologia 393, 83–94.

Yurkovskis, A., Wulff, F., Rahm, L., Andrushaitis, A., Rodriguez-Medina, M., 1993. A nutrient budget of the Gulf of Riga, Baltic Sea. Estuar. Coast. Shelf Sci. 37, 113–127.

Oceanologia (2018) 60, 553—559

Available online at www.sciencedirect.com

ScienceDirect

journal homepage: www.journals.elsevier.com/oceanologia/

SHORT COMMUNICATION

The structure of macrozoobenthic communities as an environmental status indicator in the Gulf of Gdańsk (the Outer Puck Bay)☆

Jan Warzocha*, **Sławomira Gromisz, Tycjan Wodzinowski, Lena Szymanek**

Department of Fisheries Oceanography and Marine Ecology, National Marine Fisheries Research Institute, Gdynia, Poland

Received 13 March 2017; accepted 7 May 2018
Available online 18 May 2018

KEYWORDS
Macrozoobenthos;
Long-term changes;
Hypoxia

Summary An attempt is made to use long-term (1979—2014) macrobenthos data series to derive insights on changes in abiotic conditions and on potential effects of long-term macrobenthos variability on food availability for fish and wintering waterfowl. The data were collected from a small embayment, protected as a NATURA 2000 area, functioning as a fishing ground important for the local community and as a site of diverse commercial developments. The analysis showed a drastic reduction of the macrobenthos abundance and biomass, which could have been related to oxygen deficiency; on the other hand, recolonisation processes have also been observed.

The western part of the Gulf of Gdańsk, called the Puck Bay, sheltered by the Hel Peninsula, has been for ages important for local communities as a fishing ground where both freshwater, marine, and migrating species have been harvested. According to the data reported by the fishermen and uploaded to the official data base held by Fisheries Monitoring Centre in Gdynia, the catches are at present dominated by the flounder, a species that feeds mainly on benthic

☆ The study was financed by the Ministry of Science and Higher Education, Republic of Poland.
* Corresponding author at: Department of Fisheries Oceanography and Marine Ecology, National Marine Fisheries Research Institute, Kołłątaja 1, PL-81-332 Gdynia, Poland. Tel.: +48 587356232; fax: +48 587356110.
E-mail address: janw@mir.gdynia.pl (J. Warzocha).
Peer review under the responsibility of Institute of Oceanology of the Polish Academy of Sciences.

ELSEVIER Production and hosting by Elsevier

https://doi.org/10.1016/j.oceano.2018.05.002

invertebrates. The Puck Bay is also an important feeding ground for the wintering waterfowl. In addition, the Bay is protected as a NATURA 2000 area (PLH220032). At the same time, it is affected by intensive human activities and therefore aquatic organisms themselves as well as their contribution to food resources of fish (particularly the flounder) and the wintering waterfowl may be affected by local anthropogenic factors (e.g. effects of a brine-containing sewage discharge, the brine being produced as a result of inland salt deposit leaching to form caverns). The fishermen operating in the Puck Bay suggest that the decline in flounder catches is due to the impoverishment of the food resources consisting of benthic invertebrates. Some opinions hold that the brine produced during salt deposit leaching with treated sewage from the local treatment plant, in progress since 2009, whereby ultimately the brine-containing sewage is released into the Bay, may have resulted in salinity changes and the water column salinity stratification leading to oxygen deficiency in the near-bottom layer. As stipulated by the preconditions of the brine-enriched sewage discharge operation, the salinity of the discharged brine should be equal to that prevalent in the Puck Bay. The area near the brine-containing sewage discharge site has been subjected to monitoring.

This study is not aimed at providing an additional environmental impact assessment, but is an attempt to use the data on macrobenthos assemblages as an indicator of potential environmental changes in the Puck Bay over a large spatio-temporal scale. The motivation lies in a possible synergy created by various anthropogenic and natural factors acting in synchrony, the long-term pressures resulting in a cumulative effect. This in turn may mask the effect of an actual impact of a concrete anthropogenic pressure. In addition, the macrobenthos in the Baltic Sea is an important food source for demersal fish and birds, for which reason long-term studies on the macrobenthic biomass/productivity may aid in addressing the question whether food is a limiting factor for top consumers, e.g. demersal fish and birds.

The macrozoobenthos (alternatively termed the macrobenthos or the macrofauna) is defined as benthic invertebrates retained on a 1 mm mesh size sieve. Compared to, for example, the plankton, the macrobenthos is stable in time and space, as it is composed of long-lived organisms, mostly sessile or with a limited mobility, and inhabiting relatively small areas. Because of this, macrobenthic organisms are exposed, for a relatively long time, to various (also unfavourable) environmental effects prevalent at a given site. For this reason, the macrobenthos is regarded as a good indicator of environmental status, and is particularly useful for the detection of short-term fluctuations of abiotic factors (e.g. oxygen content or salinity) which, on account of their high variability, are difficult to be measured directly.

The Outer Puck Bay is defined as an area which, by convention, is bordered from the west by an emergent shallow known as the Ryf Mew (the Seagull Sandbar), a hypothetical line connecting the Hel Peninsula terminus with Gdynia constituting the eastern border of the Outer Puck Bay (e.g. Demel, 1935; Słomianko, 1974) (Fig. 1). The maximum water depth is about 56 m and the salinity ranges within 7.2—8.0. The bottom in the inshore zone, down to a depth of several to about 30 m, is covered by sandy and mixed (sand and mud) sediments, muddy sediments prevailing at larger depths. As determined by the loss on ignition (LoI), the organic content in the muddy sediments is up to 17%. The relatively scarce data on the near-bottom dissolved oxygen

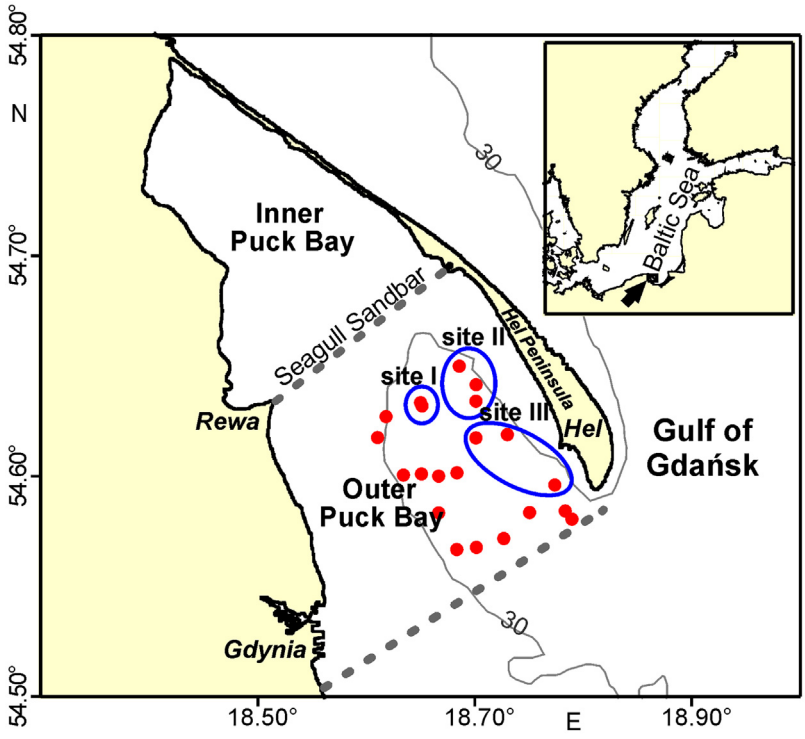

Figure 1 Area of study and distribution of sampling stations in the Outer Puck Bay in 1979—2014. Depth ranges: site I — 30—35 m, site II — 36—40 m, site III — 41—51 m.

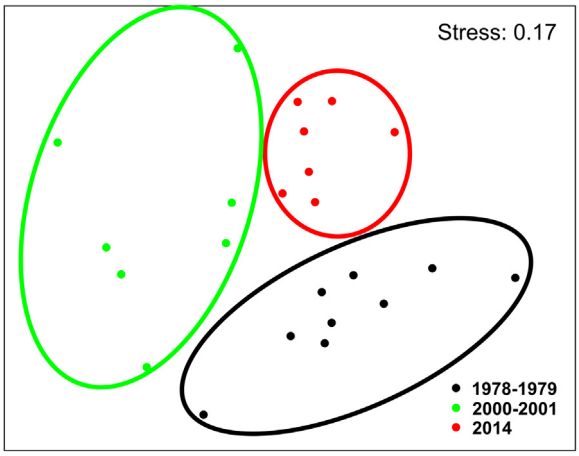

Figure 2 Results of abundance-based non-metric multidimensional scaling.

content indicate hypoxia (e.g. NMFRI database), but are not fully representative due to the lack of systematic long-term measurement series.

Macrobenthos data were collected in 1978–2014 by the National Marine Fisheries Research Institute (NMFRI) within the framework of projects addressing the structure and changes in the macrobenthos within the Polish part of the southern Baltic Sea. The sandy bottom of the Outer Puck Bay showed no changes which could have substantially affected food resources available to the fish or the waterfowl, or which would have been indicative of unfavourable environmental effects (Warzocha et al., unpubl.). Therefore, this study is limited to the muddy bottom of the Outer Puck Bay (Fig. 1). In 1979, 2000 and 2014, samples were collected from several, each time the same, stations distributed so as to cover the entire muddy bottom of the area. In addition, in 2002–2005 and 2007 three sites (marked in Fig. 1 as Sites 1–3), differing in the depth and degree of exposure to waves, were sampled to analyse potential short-term changes. Most samples were collected in summer (June–September); it was only in 1979 that some samples were collected in spring (April) and autumn (October). Therefore, changes in the macrobenthos assemblage are assessed based primarily on the biomass, as its seasonal fluctuations are narrower than those of the abundance. Samples were collected with an 0.1 m^2 Van Veen grab (33 kg weight), a standard gear used in the HELCOM monitoring (e.g. HELCOM, 2014).

The sediment sample retrieved was sieved on a 1 mm mesh size sieve and the sieving residue was preserved in 4% formaldehyde. Water salinity and temperature was measured during each sampling event; the dissolved oxygen

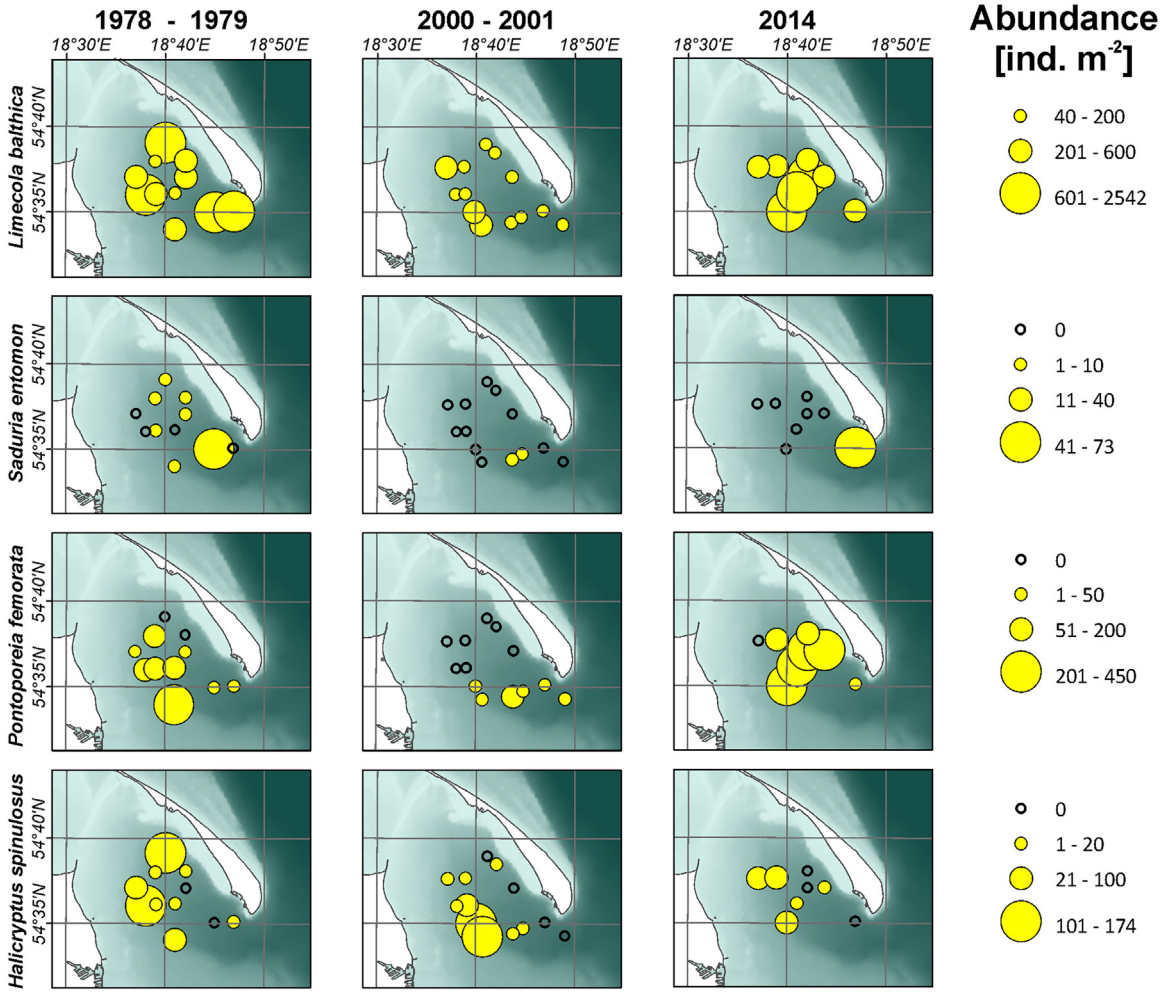

Figure 3 Changes in abundance of the four dominant species occurring in all the periods analysed.

content in the near-bottom water was determined during few cruises on board a larger craft. The analyses presented make also use of long-term oxygen data available in the NMFRI data base. The salinity and temperature did not change substantially during the period of study, hence their potential effects were disregarded in this study. The sediment organic matter content (LoI) was determined by combusting a sediment sample at 500°C. The macrobenthos was sorted under a stereomicroscope, identified to the lowest taxon possible, and dried on a blotting paper. Individuals belonging to the same taxon/species were weighed together. The Bivalvia were weighed with shells, without water in the mantle cavity. The abundance is expressed as the number of individuals per m^2, the biomass being expressed as formalin wet weight per m^2.

Numerical data treatment (MDS) was carried out using the PRIMER software package.

The taxonomic composition of the macrozoobenthos on the muddy bottom of the Outer Puck Bay in 1979 was typical of this bottom type in the Gulf of Gdańsk above the halocline (e.g. Mulicki, 1937; Warzocha, 1995). Characteristic of the community is the relatively low number of species and a strong dominance, particularly in the biomass, of the bivalve *Limecola balthica*. The remaining species typical of the community included *Saduria entomon*, *Pontoporeia femorata* and *Diastylis rathkei* as well as the priapulid *Halicryptus spinulosus*. Within 1979—2014, no species was observed to disappear, while in 2000, the presence of a new taxon, the polychaete *Marenzelleria* was recorded. Nonetheless, because of the strong domination of the Baltic tellinid *L. balthica*, no substantial effect of the new polychaete immigrant on the total macrozoobenthic biomass could be observed. No information has been so far provided on the importance of *Marenzelleria* as a food item for organisms at higher trophic levels in the Gulf of Gdańsk. However, according to observations in other areas (e.g. Šiaulys et al., 2012; Winkler, 1996), a potential role of this species in the food of demersal fish in the Puck Bay, cannot be ruled out.

Results of abundance-based non-metric multidimensional scaling (MDS) are shown in Fig. 2. Samples from 1979, 2000 and 2014 were separated into three distinct groups, which points to substantial differences in the macrobenthic community structure between the periods compared. Figs. 3 and 4 illustrate this differences in the community structure by showing distribution, abundance and biomass of dominant species in the three time periods compared.

Whereas in 1979 all the species were present throughout the entire muddy bottom of the outer Puck Bay, drastic changes in distribution, abundance and biomass (Figs. 3 and 4) were observed in 2000. A new assemblage on the deeper (depth exceeding 30 m) muddy bottom appeared, totally lacking the crustaceans *S. entomon*, *P. femorata* and *D.*

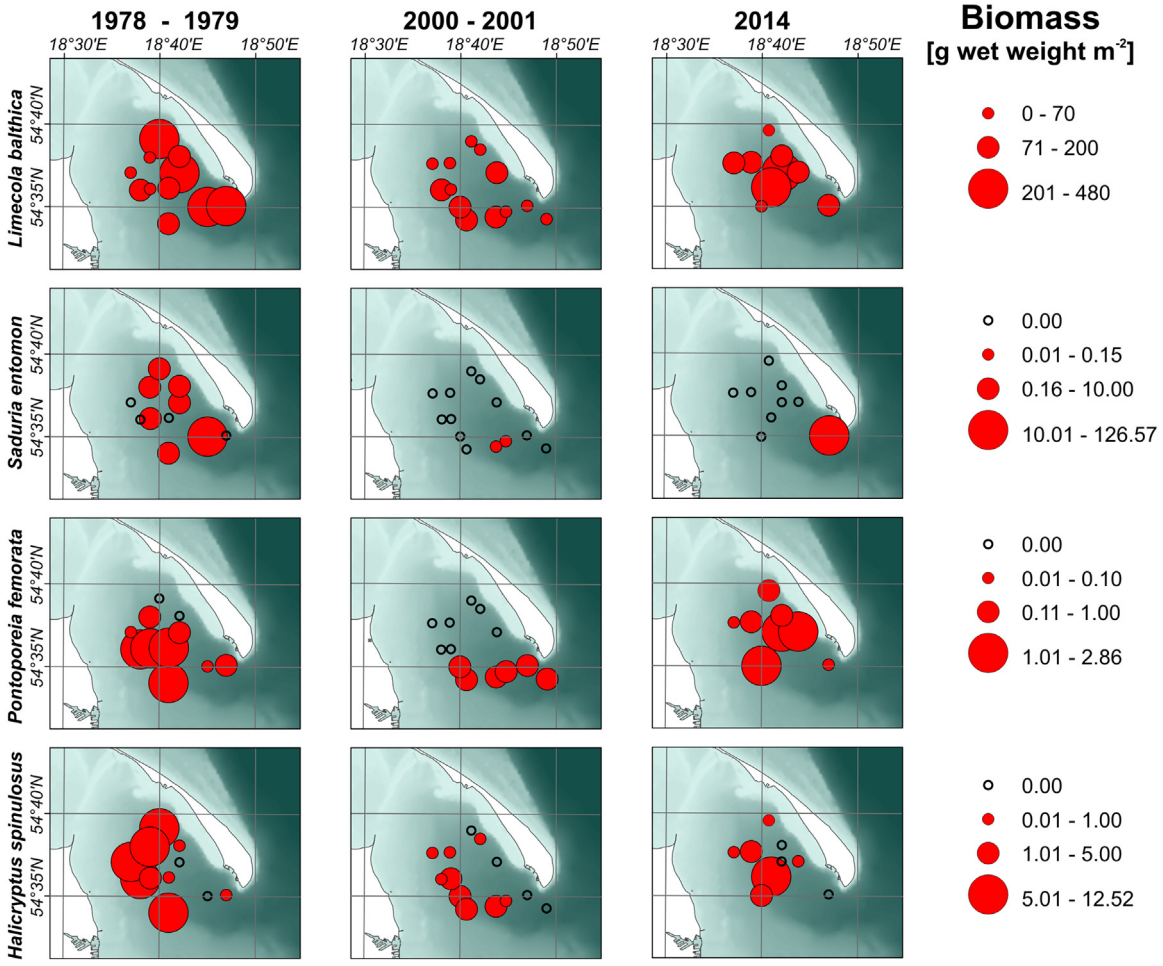

Figure 4 Changes in biomass of the four dominant species occurring in all the periods analysed.

rathkei, and including the sparsely occurring bivalve *L. balthica* only (Figs. 3 and 4). The most drastic reduction in the abundance and biomass of the macrofauna was observed in the deeper and sheltered regions (Figs. 1 and 5; sites II and III).

Subsequent years witnessed recolonisation of the muddy bottom; the data demonstrate gradual re-appearance of the key species (except *S. entomon*) as well as an increase in the macrozoobenthic abundance and biomass (Figs. 3–5). However, the structure of the recovering community changed. From among the species occurring in the area in 1979, it was only the bivalve *L. balthica* and the crustacean *P. femorata* that recovered or exceeded their former abundance and biomass throughout the entire area of study. The contribution of polychaetes (mainly *Marenzelleria* but also *Hediste diversicolor*) to the total abundance increased compared to 1979 (Fig. 5).

A considerable increase in the crustacean contribution to the macrobenthic abundance was due to the numerous individuals of *P. femorata* appearing on the bottom. However, the crustacean contribution to the total macrobenthic biomass did not reach the values recorded in 1979, because the bottom had not been recolonised by *S. entomon*, formerly a substantial contributor to the total macrozoobenthic biomass (Fig. 4). In 2014, the species was recorded only at the easternmost sampling station, basically beyond the border of the area adjacent to the Hel Peninsula (Figs. 3 and 4). Of the crustaceans, *P. femorata* was abundant in 2014, but only in the eastern, deepest part of the area. Only single individuals of another crustacean, *D. rathkei*, were recorded. On the other hand, no clear differences in the distribution of *H. spinulosus* were observed within the period of study. However, as the species occurs at low abundances anyway, the

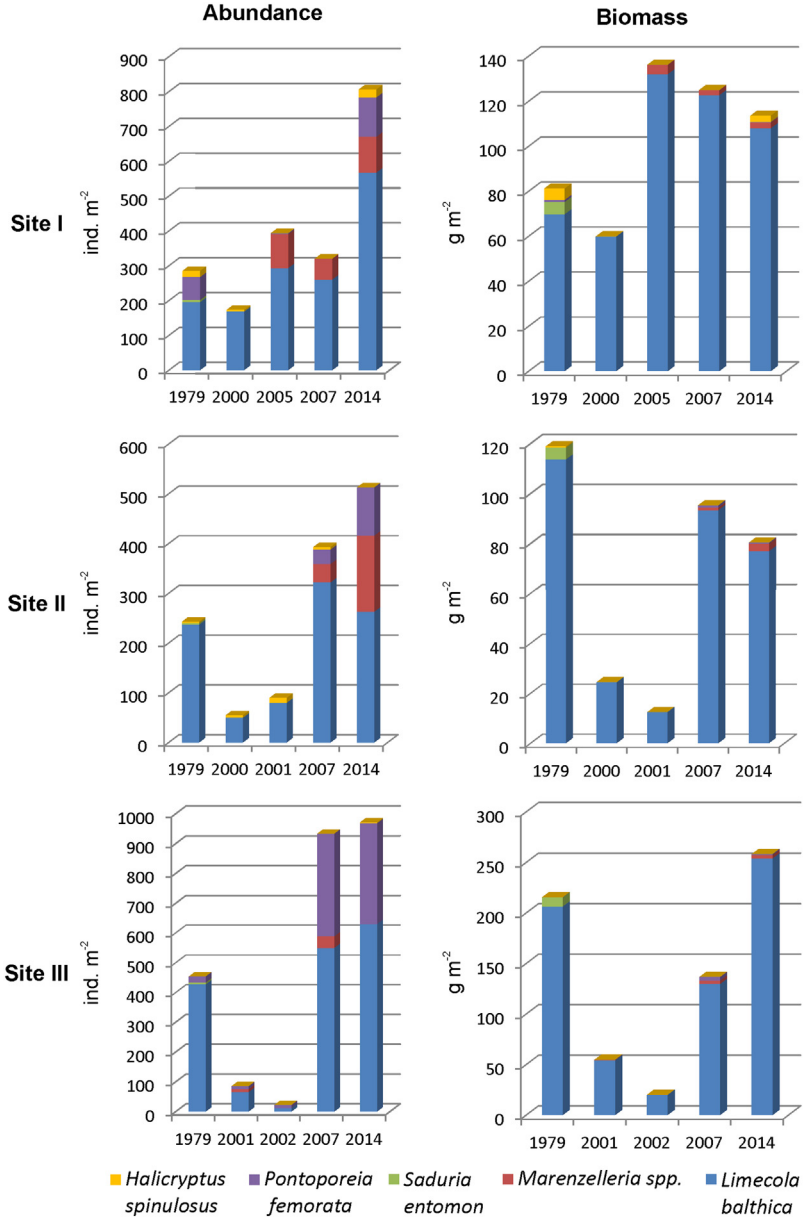

Figure 5 Changes in total macrobenthic abundance and biomass, and in abundance and biomass of individual taxa, at three sites differing in depth and exposure to wave action. Depth ranges: site I — 30–35 m, site II — 36–40 m, site III — 41–51 m.

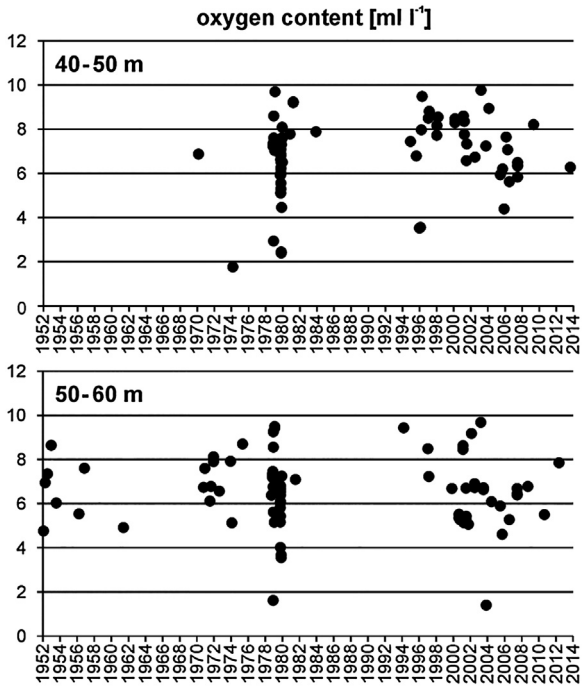

Figure 6 Dissolved oxygen contents in the near-bottom water layer in 1952—2014.

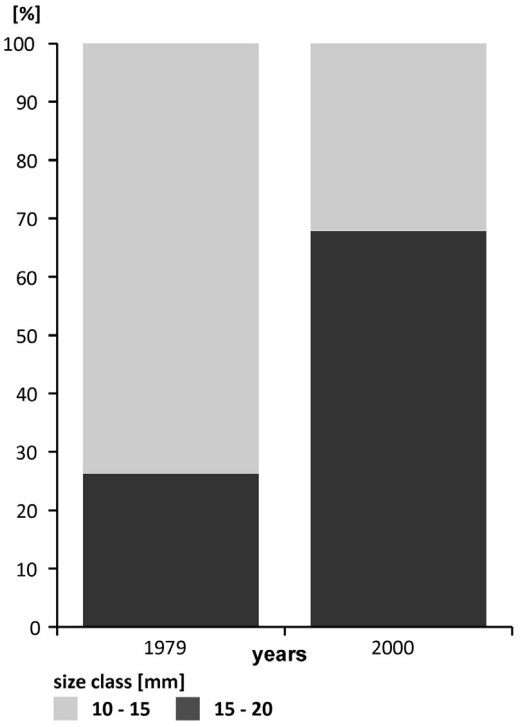

Figure 7 Contribution of two *Limecola balthica* size classes, most abundant in the samples, to the species' population in 1979 and 2000.

values of abundance and biomass reported may not have been consistent.

Noteworthy are the abundances and biomasses of *L. balthica* in 2014, much higher than those found in 1979. One may thus conclude that the environmental conditions were not favourable for the macrobenthos as early as in 1979. The available dissolved oxygen content values at the time (Fig. 6) may suggest that relatively low abundances and biomasses in 1979 were caused by hypoxia.

The nature of changes in the structure of macrozoobenthic communities, a rapid faunal reduction followed by recolonisations, changes in the dominance structure (an increased contribution of polychaetes and a reduced share of crustaceans) point to periodic oxygen deficiencies in the near-bottom water layer (Pearson and Rosenberg, 1978; Rumohr et al., 1996). The role of hypoxia is suggested also by the available data on oxygen content (Fig. 6), the high organic load (maximum about 17%), and results of chemical sediment assays regarding, e.g. the presence of methane (Brodecka et al., 2013; Reindl and Bolałek, 2012). The abundance and biomass of macrobenthos at muddy bottom in the eastern part of the Outer Puck Bay was found to be reduced as early as in the 1990s (Janas and Szaniawska, 1996; Janas et al., 2004; Włodarska-Kowalczuk et al., 1996). The authors mentioned ascribed the changes they observed to oxygen deficiency and the resultant presence of hydrogen sulphide in the sediment. Studies carried out in 2000 showed reduction in the number of species, abundance and biomass on almost the entire area of the muddy bottom in the outer Puck Bay (Warzocha et al., 2001).

Information from shallower areas (30—35 m) with a muddy bottom, where the macrozoobenthos had been reduced by 2000, shows *L. balthica* to have survived at abundances sufficient for the analysis of the population structure used as an indicator of the condition at the study site (Fig. 7). The analysis demonstrated that in 1979 the population included much more numerous younger individuals, whereas the contribution of the oldest individuals increased after the reduction of the population size in 2000. The change in the size structure of the bivalve population constituting an important fish diet item may have also impacted the predators' food resources (e.g. Barnes et al., 2010).

Summing up: The structure of the muddy bottom macrobenthos in the Outer Puck Bay has been undergoing substantial changes in the several recent decades. A drastic reduction of the fauna observed in the area in 2000 may have been indicative of oxygen deficiency in the near-bottom water. The re-appearance of the species following the reduction did not lead to any complete recovery of the community, which may suggest a permanent alteration of sediment characteristics.

Changes in the biomass observed (particularly the reduction in the crustacean biomass) may have adverse consequences for food availability for higher trophic levels, although the biomass of the bivalve *Limecola balthica*, one of the major diet components for the flounder and sea ducks, has recovered in recent years. On the other hand, preliminary observations indicate a change in the size structure of the bivalve population resulting from a higher mortality of younger individuals, in the periods when reduction of macrofauna was observed. The polychaete *Marenzelleria*, a new immigrant, changed the community structure, but did not affect the total macrozoobenthos biomass in any substantial way.

Conclusions

Long-term changes in the distribution and structure of the macrozoobenthos occurring on the muddy bottom of the

outer Puck Bay point towards adverse effects of abiotic conditions, most probably oxygen deficiency resulting from eutrophication, on the functioning of the benthic community. Those effects may impinge, permanently or periodically, upon the availability of food for demersal fish and wintering waterfowl. As the adverse drastic changes, especially in the abundance and biomass of crustaceans, have been observed since 2000, it would be difficult to directly relate them to an impact of a concrete anthropogenic intervention, except for the discharge of sewage which, in progress for many years, has doubtless induced an increase in the area's trophic status and sediment organic load. In light of the data collected, it appears important to combine the environmental impact assessment of a development and the relevant monitoring data with results of long-term research.

Acknowledgements

The paper is based on data collected in several statutory projects supported by the Ministry of Science and Higher Education, Republic of Poland. We are grateful to Professor Teresa Radziejewska for comments on the manuscript.

References

Barnes, C., Maxwell, D., Reuman, D.C., Jennings, S., 2010. Global patterns in predator—prey size relationships reveal size dependency of trophic transfer efficiency. Ecology 91 (1), 222—232.

Brodecka, A., Majewski, P., Bolałek, J., Klusek, Z., 2013. Geochemical and acoustic evidence for the occurrence of methane in sediments of the Polish sector of the southern Baltic Sea. Oceanologia 55 (4), 951—978, http://dx.doi.org/10.5697/oc.55-4.951.

Demel, K., 1935. Investigations on the bottom fauna and its occurrence in the southern Baltic. Arch. Hydrob. Ryb. IX (3—4), 237—311, (in Polish).

HELCOM, 2014. Manual for the Marine Monitoring in the COMBINE Programme of HELCOM. Soft bottom macrozoobenthos. Annex C-8, 277—287.

Janas, U., Szaniawska, A., 1996. The influence of hydrogen sulphide on macrofaunal biodiversity in the Gulf of Gdańsk. Oceanologia 38 (1), 127—142.

Janas, U., Wocial, J., Szaniawska, A., 2004. Seasonal and annual changes in macrozoobenthic populations of the Gulf of Gdańsk with respect to hypoxia and H_2S. Oceanologia 46 (1), 85—102.

Mulicki, Z., 1937. Note of the quantitative distribution of the bottom fauna near the Polish coast of Baltic. Bull. Stac. Mor. Helu 1, 74—101, (in Polish).

Pearson, T.H., Rosenberg, R., 1978. Macrobenthic succession in relation to organic enrichment and pollution of the marine environment. Oceanogr. Mar. Biol. Ann. Rev. 16, 229—311.

Reindl, A.R., Bolałek, J., 2012. Methane flux from sediment into near-bottom water in the coastal area of the Puck Bay (southern Baltic). Oceanol. Hydrobiol. Stud. 41 (3), 40—47.

Rumohr, H., Bonsdorff, E., Pearson, T.H., 1996. Zoobenthic succession in Baltic sedimentary habitats. Arch. Fish. Mar. Res. 44 (3), 179—214.

Šiaulys, A., Daunys, D., Bučas, M., Bacevičius, E., 2012. Mapping an ecosystem service: a quantitative approach to derive fish feeding ground maps. Oceanologia 54 (3), 491—505, http://dx.doi.org/10.5697/oc.54-3.491.

Słomianko, P., 1974. Physical condition of the region. Perspective of the economic development of the region. Stud. i Mater. Oceanol. 5, 7—30, (in Polish).

Warzocha, J., 1995. Classification and structure of macrofaunal communities in the southern Baltic. Arch. Fish. Mar. Res. 42 (3), 225—237.

Warzocha, J., Grelowski, A., Bolałek, J., Białkowska, I., 2001. The response of soft bottom benthic macrofauna to environmental changes in the Gulf of Gdańsk in 2000—2001. In: 3rd Int. Symp. "Functioning of coastal ecosystems in various geographical regions", 19—22 June 2001, Gdynia, Poland, (abstracts), p. 72.

Winkler, H.M., 1996. Is the polychaete *Marenzelleria viridis* an important food item for fish? In: Proc. of the 13th Symposium of the Baltic Marine Biologists. 147—151.

Włodarska-Kowalczuk, M., Janas, U., Szaniawska, A., 1996. Hydrogen sulphide and other factors influencing the macrobenthic community structure in the Gulf of Gdańsk. Oceanologia 38 (3), 379—394.